Copyright

by

Bo Ren

2017

The Dissertation Committee for Bo Ren Certifies that this is the approved version of the following dissertation:

Local Capillary Trapping and Permeability-Retarded Accumulation during Geologic Carbon Sequestration

Committee:

Larry W. Lake, Supervisor

Steven L. Bryant, Co-Supervisor

David A. DiCarlo

Hugh C. Daigle

Timothy A. Meckel

Local Capillary Trapping and Permeability-Retarded Accumulation during Geologic Carbon Sequestration

by

Bo Ren

Dissertation

Presented to the Faculty of the Graduate School of

The University of Texas at Austin

in Partial Fulfillment

of the Requirements

for the Degree of

Doctor of Philosophy

The University of Texas at Austin

August 2017

Dedication

To my parents, my wife, and my baby for their love and support

Entities must not be multiplied beyond necessity.

John Punch, 1639

Acknowledgements

I would like to express great thanks to my supervisor Dr. Larry Lake and my co-supervisor Dr. Steven Bryant for their guidance during my Ph.D. study. This dissertation is impossible without their encouragement, support and criticisms. I really benefit a lot from their knowledges, ways of thinking, and the attitudes toward scientific research. I would also like to thank my dissertation committee members Dr. David DiCarlo, Dr. Hugh Daigle, and Dr. Tip Meckel for their valuable comments, which are essential in the completion of my dissertation.

I am grateful to the current and former faculty members in the Department of Petroleum and Geosystems Engineering for being supportive during my study. I would also like to thank the staff in the PGE department, Amy Steward, Jin Lee, Diane Landeros, John Cassibry, Frankie Hart, and Gabby Banales for their help. I would also extend my gratitude to Joanna Castillo and Sophia Ortiz for their assistance with conference posters and presentations.

A special thank goes to Ehsan Saadatpoor. His work establishes the foundation of this dissertation. I would also like to thank Hoonyoung Jeong for access to the connectivity analysis code used in this work.

I would also like to thank all my officemates, Brian Lee, Arin Raina, Zhong Pan, Behzad Eftekhari, Yun Wu, Philip Thomas, Nuntha Naudomsup, Ryan Leung, and Bin Liang for their friendliness, discussion and help during my study. I would also like to thank my Chinese friends Wei Yu, Jun Lu, Kan Wu, Weiwei Wu, Yongcun Feng, Weiwei Wang, and Chunbi Jiang for their help and encouragement.

Special thanks are due to Subhash Thakur and Nigel Jenvey for giving the internship opportunity in their carbon solution team. Their mentorship, professionalism, and enthusiasm have greatly inspired me.

This work was partially supported by the Office of Fossil Energy, National Energy Technology Laboratory of the United States Department of Energy (DOE) under Award Number DE-FE0004956. We are grateful to the sponsors of Geologic CO_2 Storage Industrial Affiliates

Project (IAP) at The University of Texas at Austin: BP, Chevron, ExxonMobil, Foundation CMG, Statoil, and USGS. I would also like to extend my thanks to the CO_2 IAP industrial representatives Gary Teletzke (ExxonMobil), Sean Brennan (USGS), Qiang Xu (Chevron), and Bamshad Nazarian (Statoil) for their feedback during the annual review meetings.

Local Capillary Trapping and Permeability-Retarded Accumulation during Geologic Carbon Sequestration

Bo Ren, Ph.D.

The University of Texas at Austin, 2017

Supervisor: Larry W. Lake

Co-Supervisor: Steven L. Bryant

Safe storage of CO_2 in saline aquifers depends on CO_2 migration rate, accumulation, and trapping inside saline aquifers that have intrinsic heterogeneity. This heterogeneity can be in both capillary entry pressure and permeability. The former heterogeneity causes local capillary trapping while the latter results in permeability-retarded accumulation. A main objective of this dissertation is to understand how both local capillary trapping and permeability-retarded accumulation secure CO_2 storage.

We establish a fast simulation technique to model local capillary trapping during CO_2 injection into saline aquifers. In this technique, modeling efforts are decoupled into two parts: identifying trapping in a capillary entry pressure field and simulating CO_2 flow in a permeability field. The former fields are correlated with the latter using the Leverett j-function. The first part describes an extended use of a geologic criterion originally proposed by Saadatpoor (2012). This criterion refers to a single value of 'critical capillary entry pressure' that is used to indicate barrier or local traps cells during *buoyant flow*. Three issues with the criterion are the unknown physical critical value, the massive overestimation of trapping, and boundary barriers. The first two issues are resolved through incorporating *viscous flow* of CO_2. The last issue is resolved through creating periodic boundaries. This creation enables us to study both the amount and clusters of local capillary traps in infinite systems, and meanwhile the effects of reservoir

heterogeneity, system size, aspect ratio, and boundary types are examined. In the second part, we adapt a connectivity analysis to assess CO_2 plume dynamics. This analysis is then integrated into the geologic criterion to evaluate how injection strategies affect local capillary trapping in reservoirs. We demonstrate that reservoir heterogeneity affects the optimal injection strategies in terms of maximizing this trapping.

We conduct analytical and numerical modeling of CO_2 accumulations caused by both permeability hindrances and capillary barriers. The analytical model describes CO_2 buoyant migration and accumulation at a low permeability region above a high-permeability region. In the limiting case of zero capillary pressure, the model equation is solved using the method of characteristics. The permeability-retarded accumulation is illustrated through CO_2 saturation profiles and time-distance diagrams. Capillary trapping is subsequently accounted for by graphically incorporating the capillary pressure curve and capillary threshold effect. The relative importance of these two types of accumulations is examined under various buoyant source fluxes and porous media properties. Results demonstrate that accumulation estimate that account for only capillary trapping understates the amount of CO_2 accumulated beneath low permeability structures during significant periods of a sequestration operation.

Table of Contents

List of Tables

List of Figures

Chapter 1: Introduction

1.1 PROBLEM DESCRIPTION

Carbon capture and storage (CCS) is the most promising technology to mitigate greenhouse gas emission and global warming (IPCC 2005). After CO_2 is captured from a large source (e.g., a power plant), it is transported to an injection site and then injected into a porous medium for geological storage. Among the possible storage media, e.g., saline aquifers, depleted/depleting oil and gas reservoirs, and coalbed methane, storage in a saline aquifer is considered the most promising choice in terms of its large storage capacity and wide accessibility in sedimentary basins (Bachu 2008).

During storage, it is essential to understand CO_2 migration, accumulation and trapping in geologic formations under the effects of complicated interplaying forces (namely buoyancy, capillary pressure, and viscous force), geologic characteristics and operating conditions, so that CO_2 can be stored in a manner that is secure and environmentally acceptable.

Typically, CO_2 can be trapped in the subsurface with the following mechanisms: stratigraphic/structural trapping, dissolution trapping, residual gas trapping and mineral trapping (IPCC 2005). Among these mechanism, dissolution, residual phase and mineral trapping are considered as the safest way of immobilizing CO_2, while the remaining CO_2 (as free gas) mostly in the stratigraphic and structural traps are potentially mobile and most likely could escape from the storage body should leakage occur.

Recently, a new trapping mechanism – local capillary trapping (refer to Fig. 1-1a) – was proposed (Saadatpoor 2009, 2012). It occurs during buoyancy-driven migration of bulk phase CO_2 within a saline aquifer exhibiting spatially varying properties (permeability and capillary entry pressure). Its benefit, applied specially to CO_2 storage, is that saturation of stored CO_2 will be larger than the saturation predicted for residual gas saturation. Also, in a case of leakage, local capillary trapping will not escape from the storage formation (Saadatpoor, 2009, refer to Fig. 1-1b). This is the most important benefit of local capillary trapping relative to structural or stratigraphic trapping.

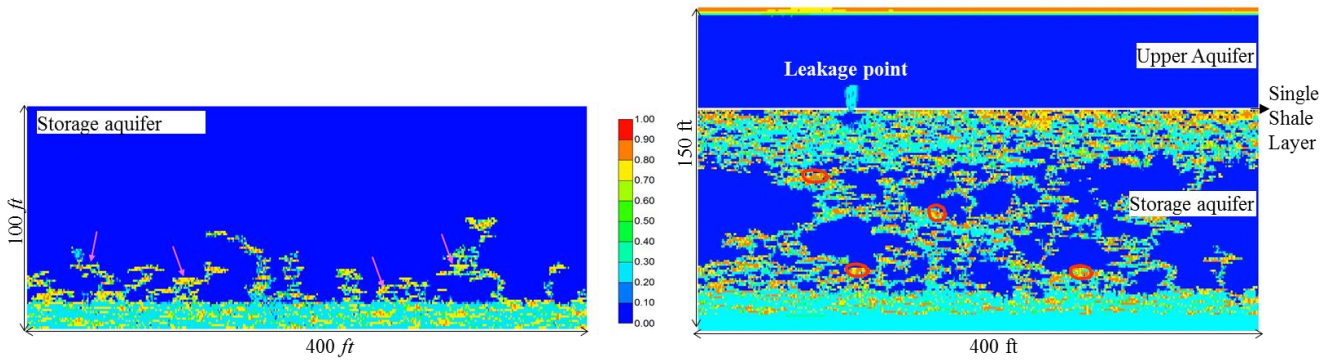

(a) (b)

Fig. 1-1 (a) CO_2 saturation field at 25 yrs of buoyant flow. Initial condition was that a uniform saturation (0.5) of CO_2 was emplaced at the bottom of a domain with a height of 12 ft. Size of grid block was 1×1 ft. Capillary pressure curves are scaled to local permeability using the Leverett j-function. The scaling causes many grid blocks to have large values of entry pressure and thus act as complete barriers to CO_2. Large CO_2 saturations build up under these local barriers but do not migrate. The distribution shown is almost at steady state. Pink arrows show the CO_2 accumulation with large saturations, and they are local capillary trapping. Adapted from Saadatpoor (2009). (b) CO_2 saturation profile at 100 yrs after a leak opens in the top seal of the storage domain. A high permeability formation was immediately above the top seal layer. The leak was located at a 110 ft distance from the left boundary. The leak was assumed to emerge instantaneously after 25 yrs of buoyant flow. At the beginning of buoyant flow, a uniform CO_2 saturation (0.5) was emplaced at the bottom with a height of 62 ft. Red circles indicate regions where local capillary trapping has immobilized CO_2. Adapted from Saadatpoor (2009).

Local capillary trapping is analogous to other well-known phenomenon in the context of multiphase flow through porous media. It is equivalent to the large-scale "fill and spill" process used in charging hydrocarbon reservoirs (refer to Fig. 1-2). It is also analogous to the pooling of dense non-aqueous phase liquid spilled onto soils (Van Valkenburg and Annable, 2002). Several mechanisms would create local capillary trapping within the saline aquifer, such as grain size variation (Sun 2014, see Fig. 1-3), changes in depositional environments over time, and non-uniform/uneven diagenetic alteration (Lasseter et al. 1986).

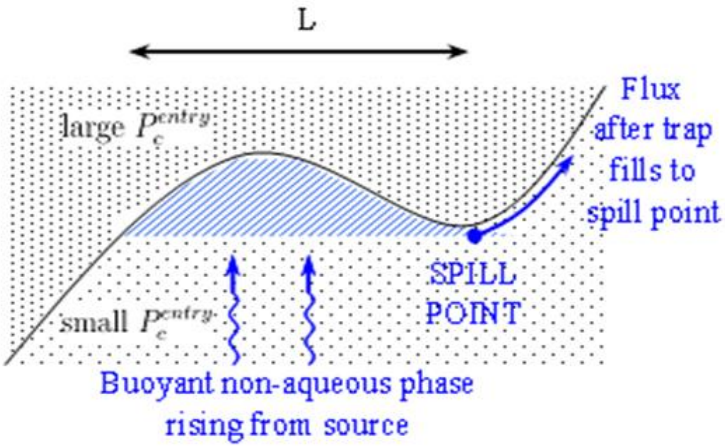

Fig. 1-2 The schematic illustration of local capillary trapping. CO_2 rises through an area with small capillary entry pressure (P_c^{entry}) and then accumulates below the area with high capillary entry pressure. CO_2 accumulation will continue until its thickness reaches the spill point as determined by the geometry of large capillary entry pressure area. The accumulation is local capillary trapping. Characteristic length (L) for a hydrocarbon reservoir is ~10^3 m, while the scale of local capillary trapping is on the order of 10^{-1} to 10^2 m. (Source: Saadatpoor, 2012).

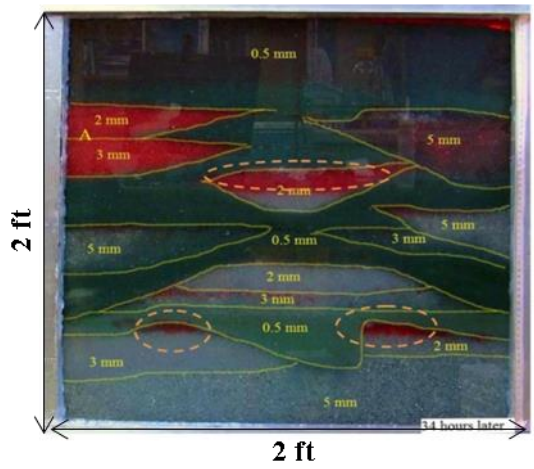

Fig. 1-3 End state of the buoyant flow of a non-wetting phase (red). This phase was initially emplaced at the bottom of a heterogeneous domain. Yellow text indicates grain size in each region. The non-wetting phase accumulates beneath regions of higher capillary entry pressure (smaller grain size). Adapted from Sun (2014).

Previous work (Saadatpoor 2009, 2012) indicates that 10-50% of local capillary traps get filled during the buoyancy-driven drainage (*simply emplace CO_2 at the bottom of a storage*

domain). However, it is still not clear that, with the injection period included, how large local capillary trapping capacity can be. Additionally, local capillary trapping is caused by capillary barriers. Since capillary pressure is correlated with permeability, capillary barriers would also act as permeability hindrances. Nevertheless, it is still unknown how capillary-barriers interact with permeability-hindrances in terms of CO_2 migration and trapping. In summary, the following questions are proposed in this dissertation.

(1) What are the influential parameters of local capillary trapping when including the injection period?

(2) How to model local capillary trapping at reservoir/field scale?

(3) How to maximize local capillary trapping during geologic carbon sequestration?

(4) How does the interplay between the capillary barrier and permeability retardation influence CO_2 migration, accumulation and trapping?

1.2 HYPOTHESIS, OBJECTIVE, AND TASKS

The *hypothesis* of this dissertation is

If a storage reservoir exhibits heterogeneity, then both local capillary trapping and permeability-retarded accumulation will largely influence CO_2 storage performance during both injection and post-injection sequestration periods.

The overall objective of this research is to determine the extent and capacity of local capillary trapping in a typical storage formation, maximize local capillary trapping amount during CO_2 injection, and evaluate the effects of both capillary barriers and permeability hindrances on CO_2 accumulation during geologic carbon sequestration. To accomplish the overall objective, the following tasks are focused.

(1) Conduct full-physics simulations on local capillary trapping under various geologic characteristics, rock/fluid properties, and injection scenarios;

(2) Develop a reduced-physics simulation technique to model local capillary trapping during CO_2 injection;

(3) Develop strategies to optimize local capillary trapping storage capacity during CO_2 injection;

(4) Determine the degree to which capillary barriers and permeability hindrances delay CO_2 upward migration.

1.3 ORGANIZATION OF THIS DISSERTATION

Chapter 2 reviews experimental observations and numerical simulations of local capillary trapping presented in the literature. Further remarks are made on the numerical challenges of modeling local capillary trapping. Beside numerical models, the analytical and semi-analytical models of predicting CO_2 migration and trapping are also summarized briefly.

Chapter 3 presents a systematic evaluation of local capillary trapping using full-physics simulations. We study the effects of reservoir heterogeneity, injection strategies, and rock/fluid properties on local capillary trapping, and compare local capillary trapping to other trapping mechanisms, i.e., residual and dissolution trapping.

Chapter 4 adapts a geologic criterion-based algorithm to predict local capillary trapping that occurs when a finite injection period occurs. The algorithm was developed by Saadatpoor (2012) to model local capillary trapping during *buoyant flow*. We extend it to model local capillary trapping that occurs when *viscous flow* is added through injection.

Chapter 5 aims to estimate local capillary trapping capacity in effectively infinite domains. By introducing a periodic boundary condition into the geologic criteria algorithm. We apply the improved algorithm to both synthetic media and realistic geological samples. We explore the effects of reservoir heterogeneity and boundary types on local capillary trapping volume.

Chapter 6 focuses on the influence of reservoir heterogeneity on the properties of local capillary trapping clusters, including clusters size, number and lateral extent.

Chapter 7 presents an integrated model to simulate local capillary trapping during CO_2 injection. The integrated model consists of a geologic criterion algorithm and a connectivity

analysis. The former is used to predict local capillary traps, while the latter is used to predict CO_2 plume. We employ the integrated model to evaluate injection strategies on local capillary trapping.

Chapter 8 extends the model of describing the secondary oil migration proposed by Siddiqui and Lake (1992) to characterize CO_2 upward migration and backfilling under countercurrent flow. We present a self-similar solution of CO_2 saturation wave without capillary pressure and a traveling wave solution with capillarity added. The extended model shows a good match with field observation.

Chapter 9 presents a one-dimensional analytical and numerical study on the interplay between capillary barriers and permeability hindrances of rising CO_2 during buoyant countercurrent flow. We demonstrate that both capillary-barriers and permeability hindrances result in CO_2 accumulations. The accumulations are separated into capillary-barrier trapping and permeability-retardation. The relative importance of these two are examined.

Chapter 10 summarizes current work and recommends future work.

Chapter 2: Literature Review

The literature review focuses on trapping in CO_2 disposal in aquifers, characteristics of local capillary trapping phenomenon, and the mathematical modeling of local capillary trapping and CO_2 migration.

2.1 TRAPPING PROCESSES IN AQUIFER DISPOSAL

Carbon dioxide (CO_2) can be stored in a saline aquifer by various means through several physical and chemical trapping mechanisms. After CO_2 injection, CO_2 can be dissolved into brine water; this is solubility trapping. As time proceeds, the dissolved CO_2 changes into carbonate and becomes mineral trapping. Such trapping is considered as the safest mechanism of storing although the process is very long (hundreds to thousands of years) (Pruess et al. 2003, Zhang et al. 2011).

The distance that CO_2 rises depends on the uniformity of displacement front and the CO_2 saturation behind the front (Bryant et al. 2008). CO_2 flow can be impeded by physical low-permeability barriers, which can be intra-reservoir inter-bedded shales (Krevor et al. 2011, Singh et al. 2010) or overlying caprock (Woods and Espie 2012). In the short-term, most of CO_2 resides in stratigraphic or structural traps if no flow path is available.

Many authors have presented the evolution of the above trapping mechanisms (Doughty 2007, Kumar et al. 2005, Juanes et al. 2006, Taku Ide et al. 2007, Mo and Akervoll 2005, Saadatpoor 2009). Overall, their relative importance depends on several factors, including the geometry of formations, reservoir permeability and its spatial distribution, injection rate, and wettability. As storage continues, the amount of CO_2 in safe storage modes (residual gas and solubility trapping) increases, and meanwhile the fraction of free CO_2 decreases.

To speed up the safe storage of CO_2, an important endeavor is to accelerate solubility trapping and residual gas trapping. Different injection strategies have been proposed accordingly. One way is the “inject low and let rise” approach, in which, CO_2 is injected only into the bottom part of an aquifer (Kumar et al. 2005). Another way is to inject CO_2 into the bottom part of an

aquifer, and meanwhile, brine is injected in the upper part of an aquifer to accelerate CO_2 entrapment (Leonenko and Keith 2008, Anchliya et al. 2012, Hassanzadeh et al. 2009, Javaheri and Jessen 2011, Nghiem et al. 2010, Nghiem et al. 2009). Additionally, some work specifically focuses on increasing residual gas trapping (Na et al. 2011, Qi et al. 2009, Nghiem et al. 2010) and dissolution trapping (Tao and Bryant 2014).

2.2 LOCAL CAPILLARY TRAPPING

Saadatpoor et al. (2009a) employed the Leverett j-function (Leverett 1941) to scale the capillary pressure curve for each grid block in a heterogeneous domain and found that capillary pressure heterogeneity gives rise to local capillary trapping during CO_2 buoyant flow in saline aquifer. In a buoyancy-dominated flow regime, the magnitude of the buoyant force is comparable to that of capillary pressure, so CO_2 moves along highly-ramified flow paths with small capillary entry pressure. When rising CO_2 plume encounters a region where capillary entry pressure is large, CO_2 accumulates beneath the region. These accumulations constitute local capillary trapping.

Local capillary trapping differs from structural/stratigraphic trapping in that much of the accumulated CO_2 will not escape, even if the integrity of seal overlying a storage aquifer is compromised (Saadatpoor et al. 2010). Local capillary trapping differs from residual phase trapping in that the accumulated saturation can be much larger than the residual phase saturation for a rock (Saadatpoor et al. 2009a).

Table 2-1 summarizes the main differences between local capillary trapping and residual phase trapping. Residual phase trapping refers to the immobilization of fluid as disconnected blobs or ganglia caused by local capillary forces (Roof, 1970). Once these gas bubbles or ganglia are trapped, they are stable against pressure gradient induced by, for example, gravity, fluid injection or extraction, and injected volume. However, recent pore-scale imaging through micro-CT suggests that, over time after imbibition, the disconnected CO_2 ganglia would be reconnected

by the surrounding mobile CO_2, thus, residual CO_2 trapping may be remobilized if these ganglia coalesce is large enough (Garing et al., 2016).

Table 2-1. Local capillary trapping vs. residual gas trapping

Property	Local capillary trapping	Residual gas trapping
Origin	Intra-reservoir capillary barriers	Snap-off, pore doublet model
Porous media	Heterogeneous	Homogeneous and heterogeneous
Flow regime	Buoyant flow	Viscous flow
Displacement type	Drainage	Imbibition
Trapped CO_2 saturation	Larger than the maximum residual gas saturation	Smaller than the maximum residual gas saturation
Scale of trapping	10^{-2}~10^{+2} meter	~μm, pore scale
Influential parameters	Gas column height, capillary entry pressure, reservoir heterogeneity	Wettability, pore structure and connectivity

Moreover, local capillary trapping is different from CO_2 accumulation caused by intra-layer (Hesse and Woods 2010) or inter-layer shale (Chadwick et al. 2009) in terms of numerical modeling techniques. In the standard industry practice of reservoir numerical modeling, shale is represented by null-blocks with zero transmissibility (Arts et al. 2004). On the contrary, local capillary trapping originates from capillary heterogeneity and it is realized by assigning different capillary pressure curves to each grid block. In this sense, local capillary barriers are still permeable compared to shale barriers.

Experimentally, local capillary trapping has been observed in core flooding using a high-resolution CT scanner (Krevor et al. 2011, Wei et al. 2014). In a micro-model (Zhao et al., 2014), capillary blunting is observed, in which, capillarity at drainage front causes buoyant non-wetting current to thicken. This is essentially local capillary trapping. Additionally, local capillary trapping has been observed in bench-scale experiments on CO_2 buoyant plume (Sun 2014) and on CO_2 flow with the injection-period incorporated (Trevisan et al. 2014). All these experimental

results provide important qualitative and quantitative insights on the role of local capillary trapping on CO_2 flow and distribution in porous media.

2.3 MATHEMATICAL MODELING OF LOCAL CAPILLARY TRAPPING AND CO_2 MIGRATION

2.3.1 Full-physics simulations

Several full-physics modeling efforts have been directed towards exploration of the impact of capillary heterogeneity (Saadatpoor 2009, Kong et al. 2014, Krause et al. 2011, Wei et al. 2014, Lengler et al. 2010) on CO_2 movement, saturation distribution and trapping in brine-saturated porous media. However, the full-physics simulation suffers from drawbacks of computational intensity and time-step limitations. Resolving the discontinuity of capillary pressure and saturation (caused by different capillary pressure-saturation curves assigned to each grid block) introduces convergence problems in numerical simulation, which requires the use of small time-step size. Additionally, transport dynamics under the influences of viscous, buoyant, and capillary forces can be very complicated because of spatial variations of permeability, porosity, and the capillary-pressure-saturation relationship (Li et al. 2012). Consequently, modeling local capillary trapping using conventional reservoir simulation would be computationally intensive or even intractable at the field scale.

2.3.2 Physics-proxy simulations

The above full-physics simulation suffers from computational intensity. Thus, inexpensive approximations or proxies have been developed that allow us to rapidly evaluate local capillary barriers and their effect on CO_2 flow response. They are upscaling, geologic criteria method, and invasion percolation.

2.3.2.1 Upscaling

Several work have been dedicated to upscale CO_2 upward migration with heterogeneous capillary pressure effect in 1D (Mouche et al. 2010) and 2D (Saadatpoor et al. 2009b, Rabinovich et al. 2015, Behzadi and Alvarado 2012) systems. Different physics at a fine grid are

upscaled to achieve equivalent gas travel time, or equivalent trapped CO_2 saturation, and/or equivalent leakage flux at a coarse-grid simulation. For example, Saadatpoor et al. (2009) found that a coarse-grid simulation that upscales only heterogeneity (single-phase upscaling) is inaccurate to capture the above equivalent behaviors. They manipulate the maximum residual gas saturation using post-processed simulations to get an equivalent leakage flux. Physically, single phase upscaling is unreasonable as it does not capture dynamic properties, e.g., relative permeability and capillary pressure curves. Considering this, Behzadi and Alvarardo (2012) proposed a two-phase upscaling procedure that accounts for the spatial connectivity of flow paths; this gives more realistic rock-fluid pseudo-functions and captures the effect of local capillary trapping on CO_2 upward migration. However, since coarse-grid simulations always smear small-scale heterogeneity, representing local capillary trapping in a coarse model would be difficult, particularly, the spatial distribution of local capillary trapping would never be accounted for in any upscaling simulations.

2.3.2.1 Geologic criterion method

The method of geologic criterion (Saadatpoor 2012) is a novel concept of identifying local capillary trapping based on a given geologic model without flow dyanmics. The method assumes that a single value of critical capillary entry pressure could describe all the clusters of local capillar traps in a capillary entry pressure field. This critical capillary entry pressure is used to determine whether a given cell is a flow path or a flow barrier. Then the algorithm finds clusters of flow paths that are surrounded by clusters of flow bariers, these flow paths are local capilary traps. The concept of CCEP has been demonstrated to be a physical approximation of the local capillary traps filling process (Saadatpoor 2012). Since CCEP is a static indicator of the flow path or the flow barrier, the geologic algorithm did not consider the process of dynamic filling and spilling or the complicated change of CO_2 saturation in local capillary traps. It directly approximates local capillary trapping capacity from a capillary entry pressure field rather than mimics buoyant flow under the interaction of buoyance and capillary pressure.

2.3.2.2 Invasion percolation

Invasion percolation (IP) applies to the problem of fluid-fluid immiscible displacement in a porous medium under the action of capillary forces. It follows a dynamic rule of "*advancing the interface at the point of least resistance as opposed to advancing all interfaces up to some chosen threshold resistance*" (England et al. 1987, Lenormand et al. 1988). The flow condition required by the above application is corrresponding to a combination of large mobility ratio and small capillary number (Lenormand et al. 1988).

The IP approach allows for cellular automata modeling, and this enables a regional simulation at a high resolution (Carruthers and van Wijngaarden 2000). The resolution of grid cell can be just a few meters, which allows for an accurate representation of subtle features such as high well densities. Considering the advantage, this approach has been applied to study the regional hydrocarbon migration, the local hydrocarbon charging process (Carruthers and Ringrose 1998, Carruthers 2003, 1998, Luo 2011), and water and contaminant transport in porous media (Glass et al. 2000, Glass and Yarrington 2003).

For gelogical carbon sequestration in a saline aquifer, buoyancy and capillary forces dominate viscous forces within hundreds of meters of injection wells (Ren et al. 2014). For carbon sequestration projects of Sleipner (Singh et al. 2010), In Salah (Cavanagh and Ringrose 2011) and Weyburn (Cavanagh and Rostron 2013), the capillary number (C_a) for CO_2 plume is small enough (C_a < 1E-07) to satisfy the criteria of using IP simulation to approximate plume behavior. IP has been applied to CO_2 storage to predict field-scale migration behavior (Singh et al. 2010, Cavanagh and Ringrose 2011), characterize CO_2 saturation resulting from buoyant flow (Meckel et al. 2015, Trevisan et al. 2017), and assess leakage risk from wellbores (Cavanagh and Rostron 2013). Gavanagh and Rostron (2013) compared IP technique and conventional reservoir simulation. Invasion percolation are significantly different in behavior from conventional Darcy flow solvers in that the former simulations are sensitive to capillary threshold pressures and interfacial tension rather than permeability and viscosity. However, both IP models and

conventional reservoir simulation need to close the gap in terms of addressing both the final detail and the large scale of reservoir simulation models.

2.3.3 When and how to model capillary pressure heterogeneity

It is subject to discussion about when and how to consider the small-scale capillary pressure heterogeneity. At a potential storage site, the effort in considering small-scale heterogeneity along with the geometry and spatial distribution of facies appears not be justified for a short time scale and a first-time site assessment. Nevertheless, it is recommendable to evaluate the impact of small-scale heterogeneity when assessing storage capacity (Lengler et al. 2010). From a practical point of view, the capillary pressure effect is often negligible when simulating field-scale displacement, especially when the characteristic capillary length is much smaller than grid resolution (Aziz and Settari 1978, Spiteri and Juanes 2006). Under a typical reservoir condition, the capillary length between CO_2 and water is ~ 4 mm (0.013 ft). For reported simulation work on capillary pressure heterogeneity, the grid block size was in a range of 0.0029 ft to 3 ft (Kuo et al. 2010, Saadatpoor 2009, Lengler et al. 2010). Whether these sizes are representative of the characteristics of heterogeneous capillary pressure is still unknown. Nevertheless, it should be clear that here is about modeling *capillary pressure*, rather than purely modeling *capillary entry pressure*. Modeling *capillary pressure* (with capillary transition zone) indeed requires small-size grids, as grid size influences saturation gradient and capillary pressure gradient numerically. However, modeling *capillary entry pressure* does not necessarily require such small cells, as long as each cell is assigned to different capillary entry pressure. This might echo why field-scale simulations using invasion percolation method employs large grid blocks with a range of 1-50 m (Cavanagh and Ringrose 2011, Singh et al. 2010).

2.4 ANALYTICAL AND SEMI-ANALYTICAL MODELING OF CO_2 MIGRATION

Beside the numerical models, another major category of predicting CO_2 migration and trapping is analytical and semi-analytical models. These simple models are essential for engineering design in terms of their fast prediction of CO_2 plume evolution.

Published analytical and semi-analytical models can be categorized into two types: (1) vertical equilibrium (VE) models; (2) fractional flow models (FFM). The VE model assumes large aspect ratio and good vertical communication, these assumptions can be satisfied for many reservoirs (Lake et al. 2014), particularly for laterally-extensive saline aquifers in sedimentary basins. Also, the assumption can be relaxed while maintaining the computational efficiency using a multiscale framework (Guo et al. 2014). When a capillary transition zone is absent, the VE model reduces to a sharp interface model. There is vast literature on sharp-interface models (Nordbotten et al. 2005) with further considering residual phase trapping (Hesse et al. 2008), solubility trapping (MacMinn et al. 2011), capillary trapping and formation dip with regional ground water flow (MacMinn et al. 2010), buoyancy-dominated condition (Dentz and Tartakovsky 2009) and compressibility (Vilarrasa et al. 2010). They are useful and accurate to analyze and predict CO_2 plume behavior when applied within appropriate length and time scales (Court et al. 2012, Swickrath et al. 2016).

The second category is the fractional flow model (FFM), the advantage of the FFM over VE & sharp interface models is that the former accounts for the tempo-spatial evolution of CO_2 saturation. Notable developments have been made to improve the applicability of FFM for simulating geological carbon sequestration. The progress includes incorporating the dry region into FFM (Burton et al. 2009), coupling geochemistry into FFM (Noh et al. 2007), considering non-Darcy flow (Mijic and LaForce 2012), as well as miscibility and gas compressibility (Mijic et al. 2014), accounting for buoyancy driven floating with simultaneous dissolution (Saripalli and McGrail 2002), gravity effect (Hayek et al. 2009), and permeability heterogeneity (Ren et al. 2015). Generally, good agreement is observed between these analytical models and full-physics simulations (Oruganti and Mishra 2013, Jeong and Srinivasan 2016).

2.5 SUMMARY

We conduct an intensive literature review on local capillary trapping and the relevant modeling techniques. Other analytical and semi-analytical models of predicting CO_2 migration and trapping are also summarized briefly.

Chapter 3: Modeling Local Capillary Trapping Using Conventional Reservoir Simulation[1]

Previous work (Saadatpoor 2009, 2012) on local capillary trapping indicates that 10-50% of local capillary traps in a storage formation get filled during buoyancy-driven flow. However, the previous work assumed a limiting-case initial distribution of CO_2 in a storage formation; the injection process was ignored and the stored CO_2 was simply assumed to be present in a storage reservoir at the beginning of simulation. It remains to be determined whether more realistic distributions of CO_2 saturation for buoyancy-driven migration, namely, the CO_2 distribution at the end of a long-term injection period, affect the extent of local capillary trapping. In addition, it is necessary to examine the effects of both fluid/rock properties (e.g., permeability anisotropy and residual gas saturation) and operating parameters (e.g., injection rate and injector type) on local capillary trapping during CO_2 injection and storage processes.

To achieve this, we conduct reservoir numerical simulation (with the injection period included) to evaluate the local capillary trapping amount and spatial distribution. A series of two-dimensional synthetic domains were built and these domains are representative of typical storage formations. Different factors are examined, including injection parameters and reservoir static properties. Particularly, a wide range of buoyancy numbers (i.e., ratio between buoyant force and viscous force) are considered. At the end of post-injection, a leak conduit is manually introduced along a wellbore to evaluate the effect of local capillary trapping on storage security. The understanding thus obtained will provide insights into post-injection leakage behaviors while the injection period is simulated realistically.

[1]Parts of this this chapter has been presented in the following conference: Ren, B., Sun, Y., Bryant, S. 2014. Maximizing Local Capillary Trapping During CO_2 Injection. Presented at the 12th International Conference on Greenhouse Gas Control, Austin, TX, USA, 5-9 October.

3.1 APPROACH

The simulator used in the study CMG-GEM (2012) is an efficient, multidimensional, equation-of-state compositional simulator. It can simulate all the important mechanisms controlling CO_2 sequestration into a saline aquifer.

3.1.1 Reservoir properties

The base reservoir model is almost the same as Saadatpoor (2012). The initial reservoir pressure is 2265.6 psi with a constant reservoir temperature of 140 °F. A 2D vertical model (Fig. 3-1a) is built with the dimensions of 400×100 and the cell size of 1×1 ft.

Permeability fields (Fig. 3-1b) are generated using a fast Fourier transform technique (Jennings and Ward 2000). The advantages of the method are speed and global conditioning. It can be applied in any number of dimensions. We detail the procedures of generating the field in Appendix B.

Porosity is correlated with permeability by Eq. 3.1 (Holtz 2002). In Eq. 3.1, the unit of permeability is mD.

$$\phi = \left(\frac{k}{7E + 7} \right)^{1/9.61} \tag{3.1}$$

Capillary entry pressure fields (Fig. 3-1c) are generated using the Leverett j-function (Leverett 1941) that links permeability, porosity, and capillary entry pressure. The Leverett j-function is in Eq. 3.2.

$$J(S_w) = \frac{p_c(S_w)}{\sigma_{g/w} \cos\theta} \sqrt{\frac{k}{\phi}} \tag{3.2}$$

In Eq. 3.2, p_c is capillary pressure, σ is the interfacial tension between CO_2 and brine, θ is contact angle, k is permeability, ϕ is porosity. To scale the capillary pressure curve for each grid block in the model, we assume that the interfacial tension and contact angle do not vary spatially. We also assume that the shape of capillary pressure curve does not vary spatially. Thus for arbitrary grid blocks i and j, we can transform Eq. 3.2 into Eq. 3.3.

$$p_{ci}(S_w) = p_{cj}(S_w)\sqrt{\frac{k_j}{k_i} * \frac{\phi_i}{\phi_j}} \tag{3.3}$$

Subscript j denotes properties of the rock, for which we know the capillary pressure curve, and we call it the reference rock. ϕ_j and k_j are the reference permeability and porosity, respectively. We assign the reference capillary pressure curve to grid blocks with the mean permeability (reference permeability), and capillary pressure curves for other cells are calculated using Eq. 3.3. Table 3-1 summarizes the properties of the base geologic model.

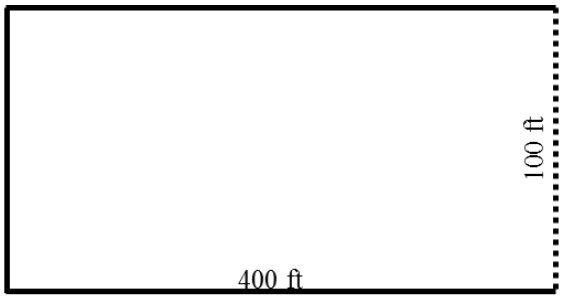

(a) 2D storage domain

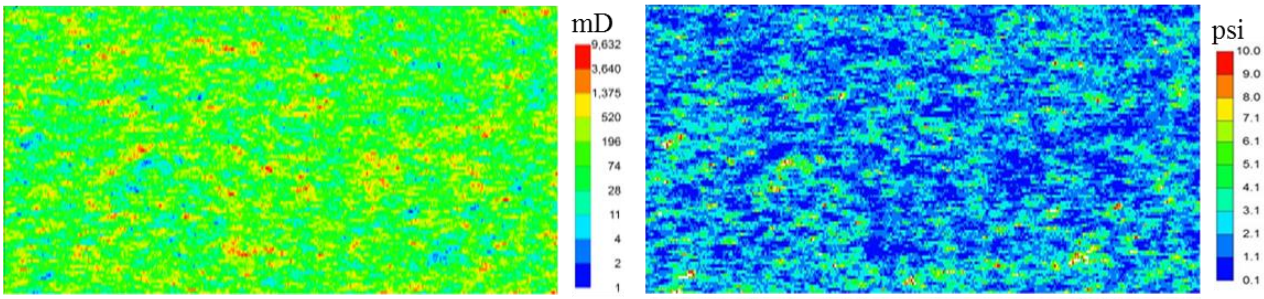

(b) 2D permeability field

(c) 2D capillary entry pressure field

Fig. 3-1 A 2D aquifer model. Dotted lines in (a) represents cells with a large volume modifier (1E+7), which is used to create an open aquifer.

Table 3-1. Properties of the base geologic model (corresponding to Fig. 3-1)

Model parameters	2D
Model size, ft	400×100
Grid block size, ft	1×1
Permeability frequency distribution	lognormal
Autocorrelation length, ft	(5, 0)
Arithmetic mean of permeability, mD	194
Anisotropy of permeability field	isotropic
Standard deviation of permeability, mD	339
Mean of porosity	0.27
Mean of capillary entry pressure, psi	2.07
Standard deviation of capillary entry pressure, psi	1.36

In this model, the pore volume of cells in the right boundary is adjusted to mimic different types of aquifers (i.e., an open aquifer and a closed aquifer). This is realized by using the keyword VOLMOD in CMG-GEM (2012). The magnitude of VOLMOD is chosen based on the magnitude of injected CO_2 volume. An extremely large VOLMOD (1.0E+7) is assigned to the right boundary cells to mimic an open boundary condition. This boundary is convenient because it prevents pressure buildup during injection without perturbing the injection flow field. On the other hand, a small (1E+4) VOLMOD is used to mimic a closed aquifer system, which enables study of the effect of pressure buildup on local capillary trapping.

The above base storage model is varied in terms of permeability anisotropy, dip angle, and heterogeneity. Permeability fields are set to be anisotropic by considering the vertical component of permeability to be a tenth, hundredth, and thousandth of the horizontal component. Three formation dip angles (0, 5 and 25 degree) are examined; they represent horizontal, moderately-deviated, and highly-deviated formations, respectively. Different horizontal auto-

correlation lengths and standard deviations of permeability are also considered. Table 3-3 summarizes settings of these parameters.

Following the storage model, a leakage model is built and schematically shown in Fig. 3-2. The lower formation in Fig. 3-2 is the same as the storage domain in Fig. 3-1. A shale barrier and an upper saline aquifer are added above the storage formation. A leaking conduit is assumed to have a large permeability of 20.0 Darcy with a width of 4 ft. The upper saline aquifer has a uniform permeability of 20.0 Darcy and porosity of 0.3. The main difference compared with previous work (Saadatpoor 2012) is the right boundary condition settings; previous work employs a closed boundary (VOLMOD=1), but here an open boundary condition is created through using a large VOLMOD (1E+7).

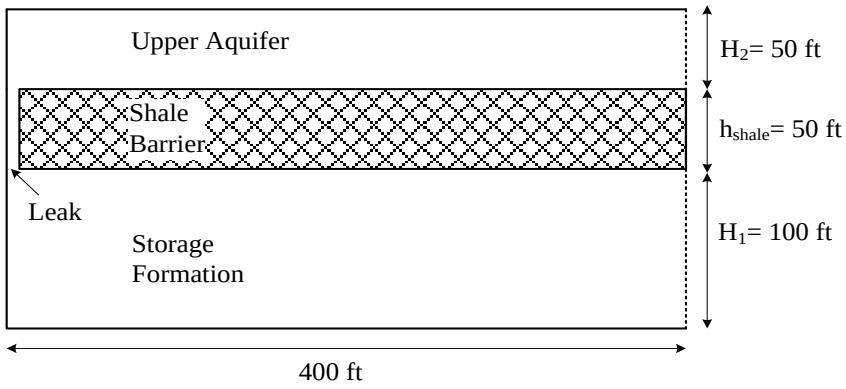

Fig. 3-2 A 2D schematic aquifer leakage model. The schematic diagram is adapted from Saadatpoor (2012). Changes are made on the right boundary cells as indicated by dotted lines.

3.1.2 Components and Rock-fluid properties

Component properties are the same as those in previous work (Kumar et al. 2005, Saadatpoor 2012). In the simulator CMG-GEM, the brine phase is set as "oil" and CO_2 as "gas", and the Peng-Robinson equation of state is tuned to the experimental data on CO_2/brine solubility (Kumar et al. 2005).

The Brooks-Corey models of relative permeability and capillary pressure are employed to describe rock-fluid interactions (Brooks and Corey 1966). The Land trapping model is employed to describe residual gas trapping (Land 1968). Figures 3-3 and 3-4 are the relative permeability curves and the capillary pressure curves, respectively. The hysteresis in both the relative permeability and capillary pressure curves are considered. Settings of other parameters can be found in an example of CMG-GEM input file in Appendix A.

The above settings of components and rock-fluid properties indicate that both dissolution trapping and residual phase trapping are modeled in the simulation. Mineral trapping is not considered.

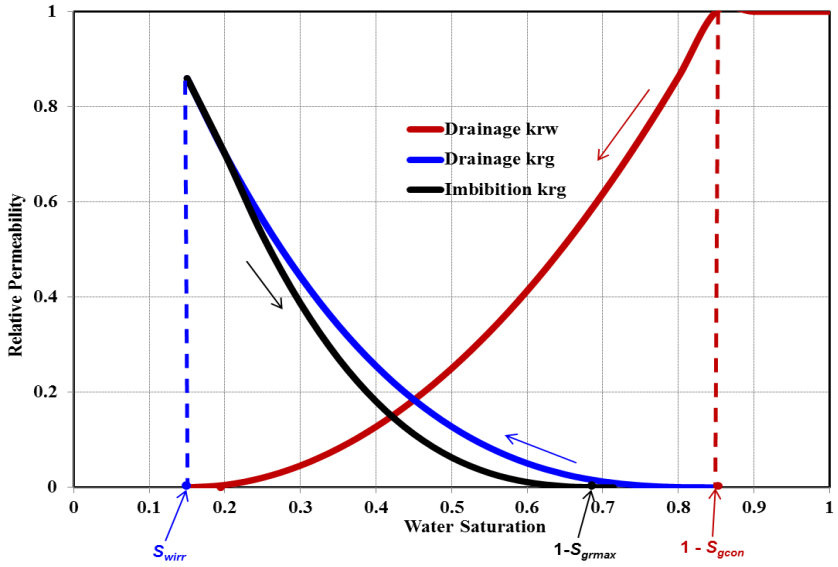

Fig. 3-3 Relative permeability curves. Adapted from Saadatpoor (2012)

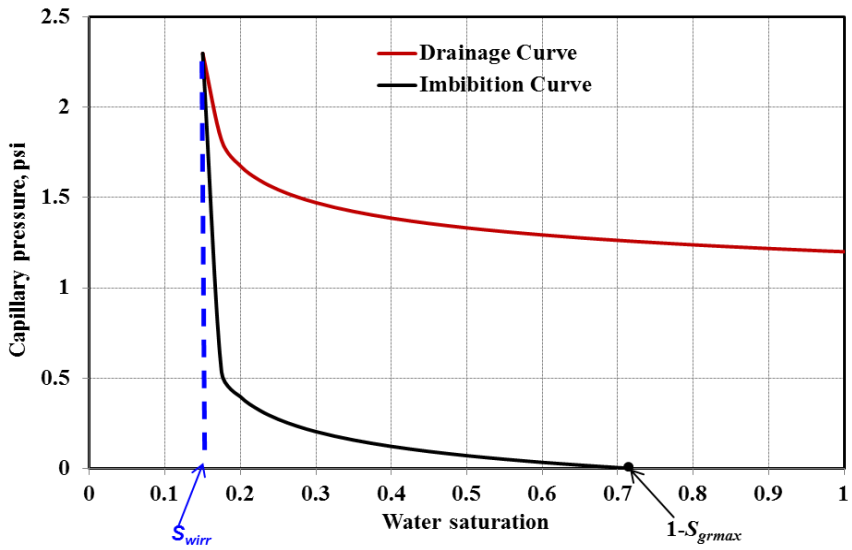

Fig. 3-4 Capillary pressure curves for the reference grid blocks.

3.1.3 Injection and leakage simulation schemes

We introduce a buoyancy number to describe the influence of gravity on CO_2 migration; the number is a dimensionless ratio of buoyancy to viscous force that drives CO_2 migration. Several definitions of the buoyancy number are possible. Here, we use the ratio of a nominal speed of vertical flow u_v to a nominal speed of horizontal flow u_h, combined with the ratio of reservoir horizontal length L, thickness H, and formation dip angle α.

The nominal vertical flux (u_v) depends on the mean vertical permeability k_v, buoyant driving force ($\Delta\rho$), and CO_2 viscosity (μ):

$$u_v = \frac{k_v \Delta \rho g}{\mu} \tag{3.4}$$

The nominal horizontal flux (u_h) is the volumetric flux (volume per unit area per unit time) from an injection well:

$$u_h = \frac{Q}{A} \tag{3.5}$$

Here Q is the well injection rate (at the bottomhole conditions of pressure and temperature; for convenience these are taken to be reservoir temperature and initial reservoir pressure). A is surface area of the perforated section of a wellbore (i.e. $A = 2\pi r_w L_{perf}$ for the wellbore of radius r_w that has been perforated along an interval of length L_{perf}).

Finally, we write the buoyancy number (N_{gr}) following the definition by Shook et al. (1992):

$$N_{gr} = \frac{\Delta\rho g k_v H \cos\alpha}{u_h \mu L} \tag{3.6}$$

In the above, $\Delta\rho$ is the density difference between brine water and CO_2, g is the gravitational acceleration, μ is CO_2 viscosity at reservoir condition, α is formation dip angle with respect to the horizontal direction, L is reservoir horizontal length, H is the perforation length. Under the reservoir condition (2265.6 psi, 140 °F), CO_2 density is determined to be 618.7 kg/m^3, brine density is 1024.6 kg/m^3, and CO_2 viscosity is 0.0486 cp.

All terms, except for u_h, in the above expression are fixed for a given storage reservoir and well completion. u_h varies with injection rate. Thus, N_{gr} is essentially a dimensionless injection rate (a reciprocal injection rate). Small values of N_{gr} (10^{-2}) correspond to large injection rates, with correspondingly minimal influence of buoyancy on CO_2 plume movement. Large values of N_{gr} (~10^2) correspond to small injection rates and the CO_2 plume movement is dictated by buoyancy. For commercial injection rates, N_{gr} is small in the portion near the wellbore. This is the region of primary interest in this study. Table 3-2 shows injection rates used in this study.

Table 3-2. Injection simulation scheme in 2D domains

Injector types	Injection rate, Scf/d	Flux entering formation from wellbore, ft/d	Injection duration, yr	N_{gr} along the wellbore*, (Eq. 3.6)	Dominant force
Vertical	490	0.06	20	20	Buoyant force
Vertical	4900	0.6	2	2.0	Transition
Vertical	49,000	6	0.2	0.2	Transition
Vertical	490,000	60	0.02	0.02	Viscous force
Point	1.2	0.6	26	2.0	Transition
Point	120	60	0.26	0.02	Viscous force

*the buoyancy number is calculated for isotropic permeability fields.

The injected amount is chosen to exactly fill the pore volume (PV) of the domain excluding the right boundary cells. This is determined to be 190 tonnes (1 PV). The same mass is injected under different injection rates, this yields injection periods shown in Table 3-2. The injected CO_2 occupies only a little of the pore volume of the whole domain (i.e. including the right boundary cells). Therefore, the injected CO_2 would cause negligible pressure buildup.

For configurations of injectors, Fig. 3-5 shows a schematic illustration of well types, perforation lengths, and well locations. Two types of injector are examined: a vertical injector and a point injector. The purpose of using a point injector is to mimic injection from a horizontal well; the point injection could be considered a vertical slice of a horizontal injector. Well injection rates are calculated using both the CO_2 flux entering the formation from a wellbore (refer to Table 3-2) and the perforation length. For example, for the point injector, CO_2 flux at the wellbore is 60 ft/day for the smallest N_{gr} (refer to Table 3-2), the well injection rate (q_{rc}) under the reservoir condition is

$$q_{rc} = u \times L_{perf} \times \Delta_y = 60\ ft/d \times 2\ ft \times 1\ ft = 120\ ft^3/d \tag{3.7}$$

The injected CO_2 is 1PV, then, the injection period (T_{ij}) is

$$T_{inj} = L \times H_{res} \times \phi / q_{rc} = 399\ ft \times 100\ ft \times 0.286 / 120\ ft^3/d = 0.26\ yr \tag{3.8}$$

In the above, Δy is the grid size in the y-direction, ϕ is the reservoir porosity. H_{res} is the reservoir thickness. The definitions of other terms are the same as above.

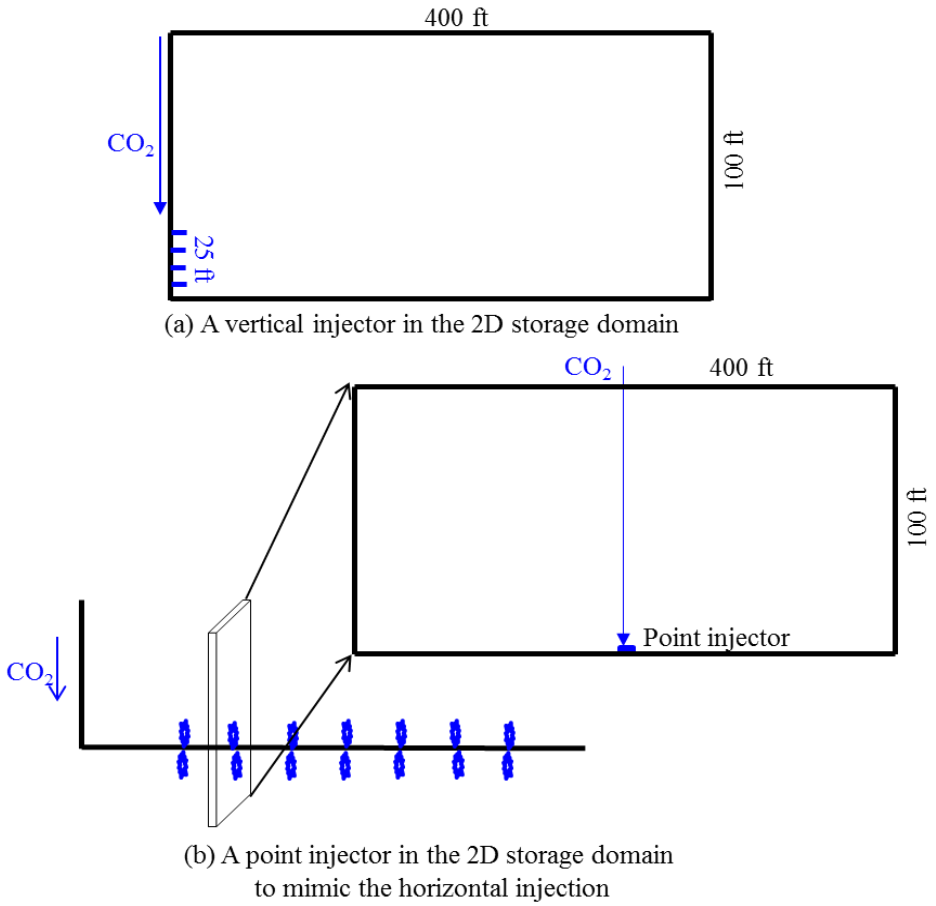

(a) A vertical injector in the 2D storage domain

(b) A point injector in the 2D storage domain to mimic the horizontal injection

Fig. 3-5 A schematic illustration of injectors. (Upper) a vertical well is located in the middle left boundary of the domain with perforation intervals represented by small blue bars. (Lower) a point injector is located in the middle bottom of the domain, and the blue dots represent perforation intervals.

The flow simulation consists of three sequential processes: (1) an injection period; (2) a post-injection storage process; and (3) a leakage period. Injection and post-injection lasts for a total of 50 yrs. At the end of post-injection, a leak conduit is manually introduced to represent a caprock breach induced by geochemical processes or by stress/strain variations within the caprock. The leakage lasts for another 50 yrs.

Table 3-3 summarizes all cases studied with different settings of conditions. In these cases, parameters are divided into three groups: injection parameters, reservoir static properties, and rock/fluid interaction parameters. The first group consists of well injection rate (indicated by N_{gr}), injected volume (in multiples of pore volume or PV), and injection well type. The second group is comprised of permeability anisotropy (k_v/k_h), formation dip angle (α), horizontal auto-correlation length (λ_x), coefficient of variation (C_v), and aquifer type (i.e., the closed or open aquifer). The third group parameters are residual gas saturation (S_{gr}), relative permeability hysteresis, and capillary pressure hysteresis. We report how these parameters affect LCT spatial extent and mass fraction at the end of each process (i.e., injection, post-injection, and leakage). LCT mass fraction is defined as the ratio of LCT mass over the total CO_2 mass injected.

In the following quantification, CO_2 saturation associated with local capillary trapping is defined in the range between residual gas saturation (S_{gr}) to 100%. That is, CO_2 in cells with gas saturation above residual are categorized as local capillary trapping. LCT mass is calculated using the following equation (Saadatpoor 2012):

$$m_{LCT} = \sum_{S_g > S_{gr}}^{PV<1} (PV \cdot (S_g - S_{gr}) \cdot \rho_{g,molar} \cdot Y_{CO_2} \cdot MW_{CO_2}) \tag{3.9}$$

Where, PV is pore volume, S_g is CO_2 saturation, S_{gr} is residual CO_2 saturation, $\rho_{g,molar}$ is CO_2 mole density, Y_{CO2} is CO_2 mole fraction, and MW_{CO2} is CO_2 molecular weight (44 g/mole).

Table 3-3. Summary of conditions for simulations

λ_x, ft	C_v	N_{gr}	Leak	Injected volume, PV	Injector type	Right boundary type	k_v/k_h	Formation dip angle	Residual gas saturation	Capillary pressure hysteresis	Relative permeability hysteresis	Figure
5	0.66	0.02-20	No	1	Vertical	Open	1	0	0.29	No	Yes	3-6
5	0.66	0.02-20	Yes	1	Vertical	Open	1	0	0.29	No	Yes	3-7
5	0.66	0.02	No	0.1~1	Vertical	Open	1	0	0.29	No	Yes	3-10
5	0.66	0.02, 2.0	No	1	Point	Open	0.001, 1	0	0.29	No	Yes	3-11
5	0.66	0.2	No	1	Vertical	Open	0.001~1	0	0.29	No	Yes	3-12
5	0.66	0.02, 20	No	1	Vertical	Open	1	0, 5, 25	0.29	No	Yes	3-14
200	0.66	0.02~20	No	1	Vertical	Open	1	0	0.29	No	Yes	3-15
200	0.66	0.02~20	Yes	1	Vertical	Open	1	0	0.29	No	Yes	3-16
5	0.66, 0.14	0.02	No	1	Vertical	Open	1	0	0.29	No	Yes	3-17
5	0.66	0.02	Yes	1	Vertical	Open, closed	1	0	0.29	No	Yes	3-18, 3-19
5	0.66	0.02	NA	1	Vertical	Open	1	0	0.18~0.44	No	Yes	3-20
5	0.66	0.02	NA	1	Vertical	Open	1	0	0.29	No	No	3-21
5	0.66	0.2, 0.02	NA	1	Vertical	Open, constant pressure	0.001, 1	0	0.29	Yes	No	3-22

3.2 RESULTS

3.2.1 Injection parameters

3.2.1.1 Effect of injection rate on LCT

Figure 3-6 shows CO_2 saturation fields at the end of injection under different injection rates. The injection eliminates the transition zone observed during buoyant flow under an initial emplacement (Saadatpoor 2012). This elimination occurs at least near the wellbore for an isotropic domain. In the following section of the anisotropy effect, we show such a transition zone occurs when using very anisotropic media.

At a large injection rate (N_{gr}=0.02), the immiscible displacement is "compact"; CO_2 goes almost everywhere during injection. This compact displacement leads to a widespread residual gas trapping during water imbibition into the tail edge of CO_2 plume during the post-injection period. Also, the residual phase trapping surrounds local capillary trapping. However, when a small injection rate is employed (N_{gr}=20), CO_2 mostly follows channels of auto-correlated larger-than-average permeability, and saturation distributions for the immiscible displacement are ramified. As injection rates decrease, buoyancy stands out as the main driving force and gravity segregation is pronounced.

Notably, for a small injection rate (N_{gr}=20), the injected CO_2 flows into the storage domain from only the upper portion of a perforated interval. This is because, for the lower portion, CO_2 pressure along the wellbore is less than reservoir hydrostatic pressure, which prevents CO_2 in the wellbore from flowing into the reservoir. The phenomenon disappears as injection rate increases (N_{gr}=0.02). This observation necessitates the optimization of perforation intervals when using different injection rates (Kumar and Bryant 2008).

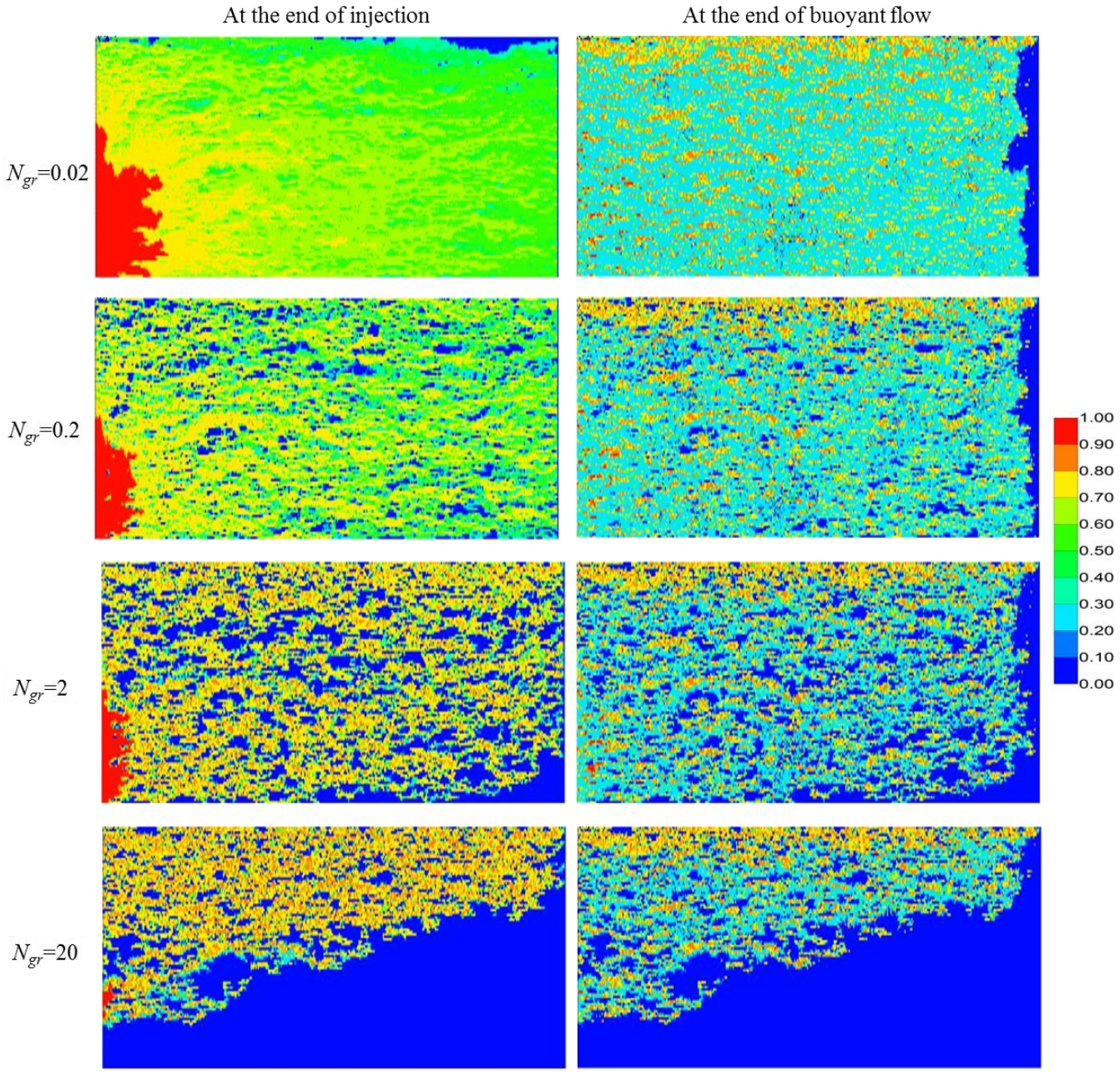

Fig. 3-6 CO_2 saturation fields at the end of injection (left column) and at the end of post-injection (right column) for decreasing injection rates from top to bottom. 190 tonnes (equivalent to 1PV) of CO_2 was injected. At the end of injection (left column), the CO_2 mass staying in the storage domain was 148, 106, 92, and 58 tonnes from top to bottom. The difference between the injected CO_2 masses and the remaining has entered the column of very large cells on the right side of the domain.

Obviously, among the four injection rates, the largest N_{gr} gives the least filling of local capillary traps in the domain. In other works, the filling efficiency of local capillary traps

decreases as a transition from compact displacement to capillary channeling flow, i.e. as injection rates decrease.

On the other hand, the filling of local capillary traps within the region invaded during injection is essentially the same for all injection rates. That is, if a region contains CO_2 at the end of injection and that region corresponds to a local capillary trap, then, at steady state, that trap will contain locally trapped CO_2 at a large saturation, regardless of buoyancy numbers during injection. This makes sense since local capillary trapping is an equilibrium phenomenon. In other words, while the buoyancy number strongly influences the fraction of the reservoir into which CO_2 flows during injection (essentially 100% at the smallest buoyancy number and falling to about 50% at the largest buoyancy number in the left column of Fig. 3-6), the migration that fills traps to a large saturation occur after injection ends. Hence, the structures of local capillary trapping are independent of the buoyancy number.

Meanwhile, it is instructive to verify that the steady state post-injection CO_2 distribution occupies local capillary traps. Consider, take the largest injection rate (N_{gr}=0.02, left column of Fig. 3-6) for example, CO_2 displaces water in every cell of the domain by the end of injection because viscous forces are large throughout this 2D domain. Obviously, CO_2 has invaded all the regions corresponding to local capillary traps. CO_2 has also invaded all the regions corresponding to capillary barriers. This is to be expected: the definition of a barrier is with respect to capillary forces, not to viscous forces. None of cells have zero permeability, and thus when viscous pressure is sufficient to overcome capillary entry pressure, CO_2 can and does invade the entire domain. The detailed structure of heterogeneous reservoir can still be detected in the fine-scale variation of saturation fields in the left column of Fig. 3-6. As an aside, this is the reason that simulation of conventional reservoir processes, in which flow at commercial rates is driven by production and injection wells throughout a hydrocarbon reservoir, routinely ignores the heterogeneity of capillarity (Lake et al. 2014). In these cases, the solution, in terms of where injected and reservoir fluids go, is dictated by the structure of a permeability field, and this can be determined with sufficient accuracy by ignoring capillarity. However, for geologic CO_2

sequestration, the onset of buoyancy-dominated migration and displacement is a crucial portion of a storage process. This buoyant behavior cannot be described correctly unless the heterogeneity of capillary pressure is explicitly included.

The widespread filling of local capillary traps under the large rate case is similar to behaviors observed in the large-emplaced volume limit of the buoyancy-driven storage scenario (Saadatpoor 2012). In the latter scenario, all the local capillary traps get filled as the rising CO_2 forms a gas cap and then backfills non-barrier regions downward from the reservoir seal. During the injection with large rates, viscous forces enable CO_2 to fill all the rock volume. In both cases, essentially all the traps are filled.

The next step of the storage process, when injection ceases, is that the injected CO_2 and the remaining native brine are free to rearrange themselves in response only to buoyant force. Since CO_2 saturation is greater than its residual saturation, we expect significant migration to occur. The right column of Fig. 3-6 confirms this expectation and it demonstrates that CO_2 with large saturations accumulate within local capillary traps - even when the saturation in the trap at the end of injection was a moderate value. To see this note how many of the yellow/red pixels in the right column correspond to green pixels in the left column of Fig. 3-6. Evidently, post-injection migration enables CO_2 to build to the drainage curve limit in local capillary traps. Meanwhile, in regions that are neither traps nor barriers, CO_2 present at the end of injection migrates until it leaves residual saturation behind (cyan pixels). Thus, local capillary traps in the near-well region are filled during injection, and they remain filled after post-injection buoyancy-driven flow ends.

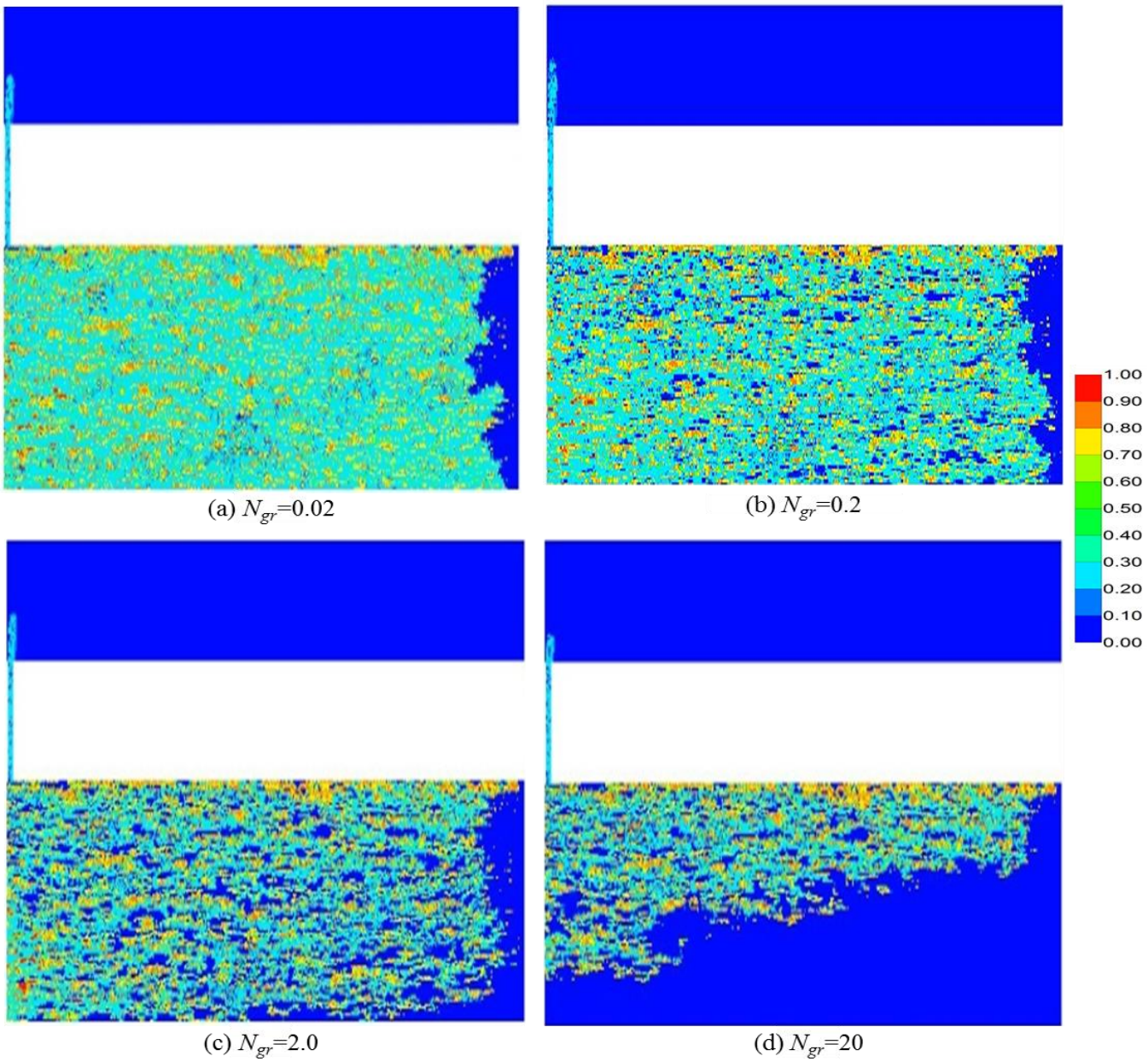

Fig. 3-7 CO_2 saturation fields at the end of leakage. The initial condition of leakage modeling corresponds to right column in Fig. 3-6.

To examine the robustness of local capillary trapping in the case of leakage, a sudden leaking conduit is introduced along the wellbore at the end of the post-injection period and then another 50 yrs of leakage modeling is conducted to look into the change of CO_2 saturation inside local capillary trapping under buoyant flow. CO_2 saturation fields at the end of leakage are in Fig. 3-7. Most of the local capillary trapping (bright yellow pixels) remain in place. This

demonstrates that local capillary trapped CO_2 is stable and robust. What leaks from the formation is the CO_2 in flow paths that are connected to the leakage conduit.

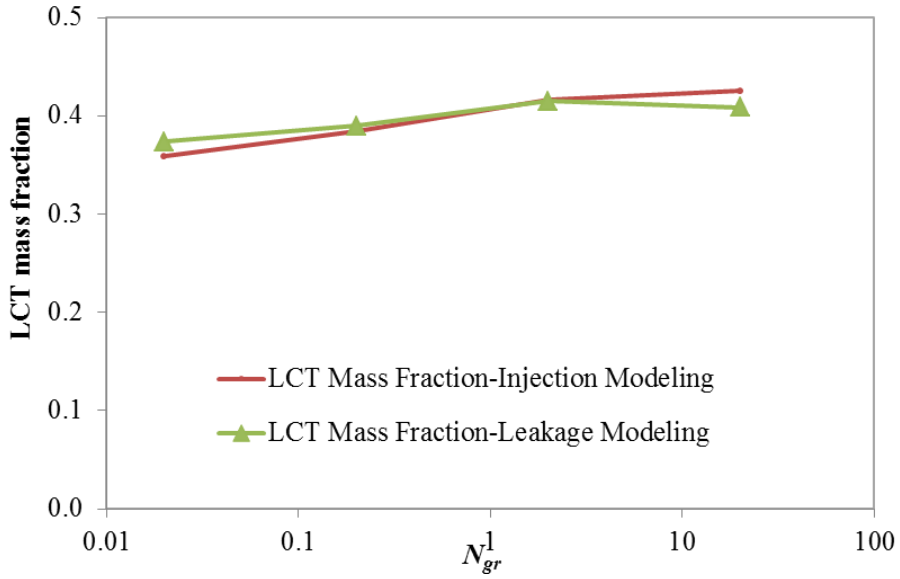

Fig. 3-8 The variation of LCT mass fraction with the buoyancy number at the end of post-injection and at the end of leakage. Recall, LCT mass fraction is defined as the CO_2 mass in local capillary traps divided by the CO_2 mass remaining in the storage domain (i.e., 399×100 cells). The 400th column of cells acts as a boundary condition (recall a very large VOLMOD is applied to the column) and thus is not included in LCT calculation.

Next, we quantify the LCT mass fraction for the above cases. Figure 3-8 shows the variation of LCT mass fraction along with buoyancy numbers. The red curve is measured at the end of post-injection (corresponding to the right column in Fig. 3-6). The green curve is computed at the end of leakage (corresponding to Fig. 3-7). The LCT mass fraction was about 40%. This fraction is almost insensitive to injection rates, although varying injection rates causes different displacement patterns and filling efficiencies of local capillary traps. The unchanged mass fraction is because local capillary traps are intrinsic to a geologic model.

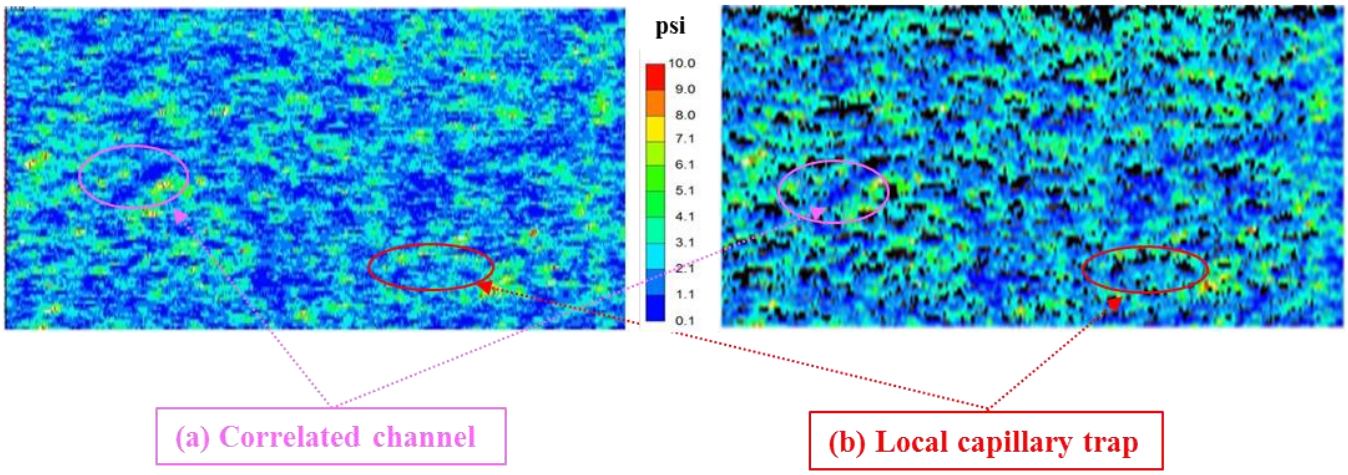

Fig. 3-9 (a) The capillary entry pressure field used for the above storage modeling. Blue regions are correlated flow channels with small capillary entry pressure. (b) The same capillary entry pressure map with CO_2 above-residual saturation map from Fig. 3-7a overlaid as black pixels. The prevalence of black regions beneath warm colors shows that essentially all of local capillary traps in the entire reservoir fill.

Overlaying the above residual saturations of Fig. 3-7a as black pixels on the capillary entry pressure map (Fig. 3-9a) yields the right panel in Fig. 3-9b. This figure confirms that CO_2 has filled essentially every local capillary trap. Blue regions still exist in the right panel, as they did in the emplacement storage scenario (Saadatpoor 2012). However, these regions contain no CO_2 in the emplacement scenario, whereas, in the case of high-rate injection, these regions contain residual CO_2.

3.2.1.2 Effect of injected volume on LCT

Figure 3-10 shows CO_2 saturation fields at the end of the post-injection period. Obviously, as the injected CO_2 volume increases, more local capillary traps become filled. The injected CO_2 mass does not affect the extent of local capillary trapping; the bright yellow pixels common in the four cases have the same spatial distribution. This again indicates that local capillary traps are intrinsic to a capillary entry pressure field.

Similar to the behavior (refer to Fig. 3-6) observed at different buoyancy numbers, Fig. 3-10 shows that CO_2 occupies all the local capillary traps within the region swept by CO_2. Thus, the essential question during injection is what fraction of the reservoir volume "sees" the injected

CO_2. The gravity driven fluid movement after injection ends enables CO_2 to fill local traps in the swept region to a large saturation.

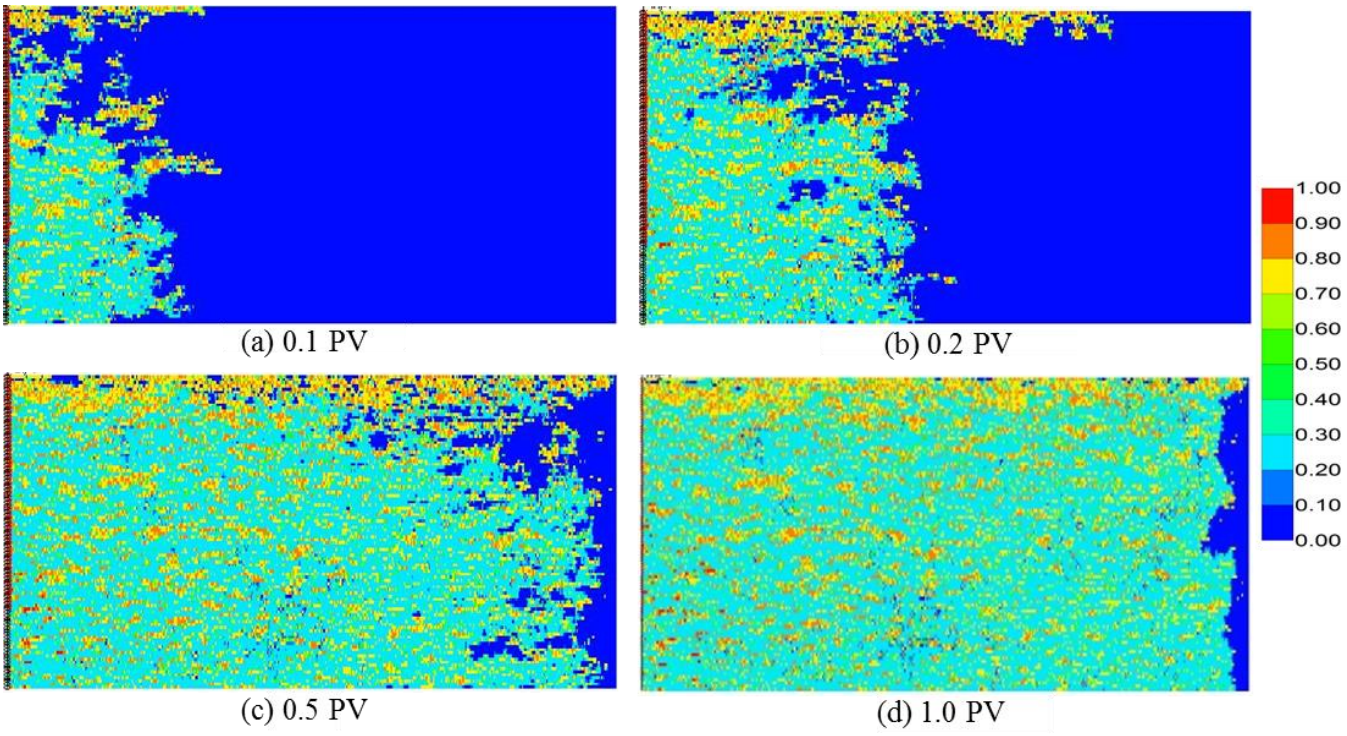

Fig. 3-10 CO_2 saturation fields at the end of post-injection. Different volumes were injected under a fixed injection rate (N_{gr}=0.02). From (a) to (d), the injected CO_2 were 0.1, 0.2, 0.5, 1.0 PV with the corresponding injection durations of 0.002, 0.004, 0.01, and 0.02 yrs, respectively.

3.2.1.3 Effect of well types on LCT

A vertical injector is used in the above analysis. In this section, we employ a point injector at the middle bottom of the domain, to mimic a vertical slice of horizontal injection. Figure 3-11a and 3-11b show CO_2 saturation in the *isotropic* (k_v/k_h=1) field at the end of injection for a small, and a large injection rate (refer to Table 3-2), respectively. Figures 3-11c and d show CO_2 saturation in the *anisotropic* (k_v/k_h=0.001) field at the end of injection using the above two rates. Overall, as the decrease of the buoyancy number (either by increasing injection rate or by

decreasing vertical permeability), capillary fingering gets suppressed and displacement becomes compact. This is favorable to the filling of local capillary traps.

Compared to the vertical injector scenario, point injector gives more dispersed CO_2 flow. This is easy to understand: when the vertical injector is used, CO_2 flow velocity across the 2D domain changes negligibly. However, for the point injector, the velocity is decreased as CO_2 migrates away from the middle injection point. The resultant impact on CO_2 flow is similar to that of decreasing injection rates in terms of channeling (refer to Fig. 3-6). Figures 3-11e and f show CO_2 saturation at the end of post-injection, which correspond to Fig. 3-11b and c. Injection well types do not alter the extent of local capillary trapping, whereas, they largely influence the filling of local capillary traps.

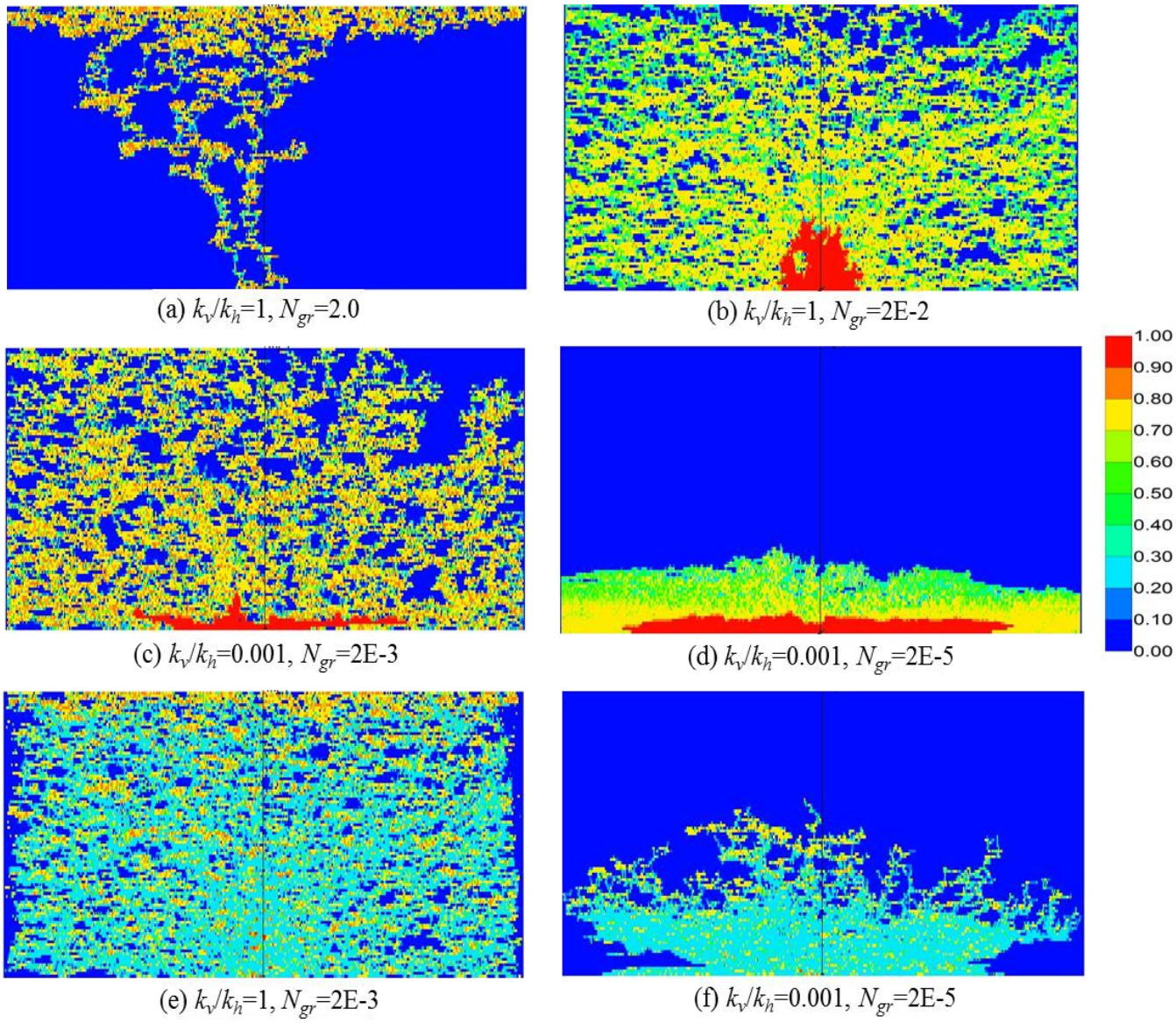

Fig. 3-11 CO_2 saturation fields created through a point injector in the middle bottom of the domain. 1PV of CO_2 is injected and the remainder of CO_2 not shown in the figures goes into the lateral boundary cells. The upper row is CO_2 saturation fields at the end of injection for the isotropic permeability field using two different injection rates (reflected by the buoyancy number). The middle row is CO_2 saturation fields at the end of injection for the very anisotropic permeability field under the same injection rates as the upper row. The lower row is CO_2 saturation fields at the end of post-injection following CO_2 distribution shown in the middle row. The anisotropy is increased by decreasing the vertical permeability. Recall both the injection rate and vertical permeability are considered in the definition of the buoyancy number.

3.2.2 Reservoir static properties

3.2.2.1 Effect of anisotropy on LCT

As stated earlier, injection of large quantities of CO_2 eliminates transition zones in an isotropic formation, even when perforations are only in the bottom quarter of the domain. On the other hand, such transition zones are an important feature of CO_2 migration from an initial emplacement of CO_2 at the bottom of a storage domain (Saadatpoor 2012). Therefore, it is important to determine if transition zones arise during long-term injection under other conditions. The condition most likely to lead to this situation is permeability anisotropy as shown in the effect of well types on LCT.

Here, we set k_v/k_h to be 0.1, 0.01, and 0.001 by decreasing the vertical permeability. We inject the same amount of CO_2 (1PV, 190 tonnes) using the largest injection rate in Table 3-2. Figure 3-12 shows the CO_2 saturation fields at the end of injection. As k_v/k_h decreases (anisotropy increases), CO_2 tends to flow along the bottom of the domain. When k_v/k_h decreases to be 0.001, the injected CO_2 is mainly restricted at the bottom at the end of injection. This CO_2 becomes the source CO_2 zone for the post-injection buoyant flow, during which, transition zones and gas caps are generated. The right column of Fig. 3-12 shows CO_2 saturation at the end of post-injection, which confirms the formation of transition zones.

In the right column (at the end of post-injection) of Fig. 3-12, structures and distributions of local capillary trapping (yellow pixels) are similar in the flooded areas common for four anisotropies. However, CO_2 saturations are a little different. The first three fields have a higher CO_2 saturation in local capillary traps than the highest anisotropic field does. This is because the first three have relatively large mass of CO_2 left in the storage domain: as calculated for the left column of Fig. 3-12, the mass of CO_2 staying in the storage domain were 106, 110, 97, and 69 tonnes, respectively.

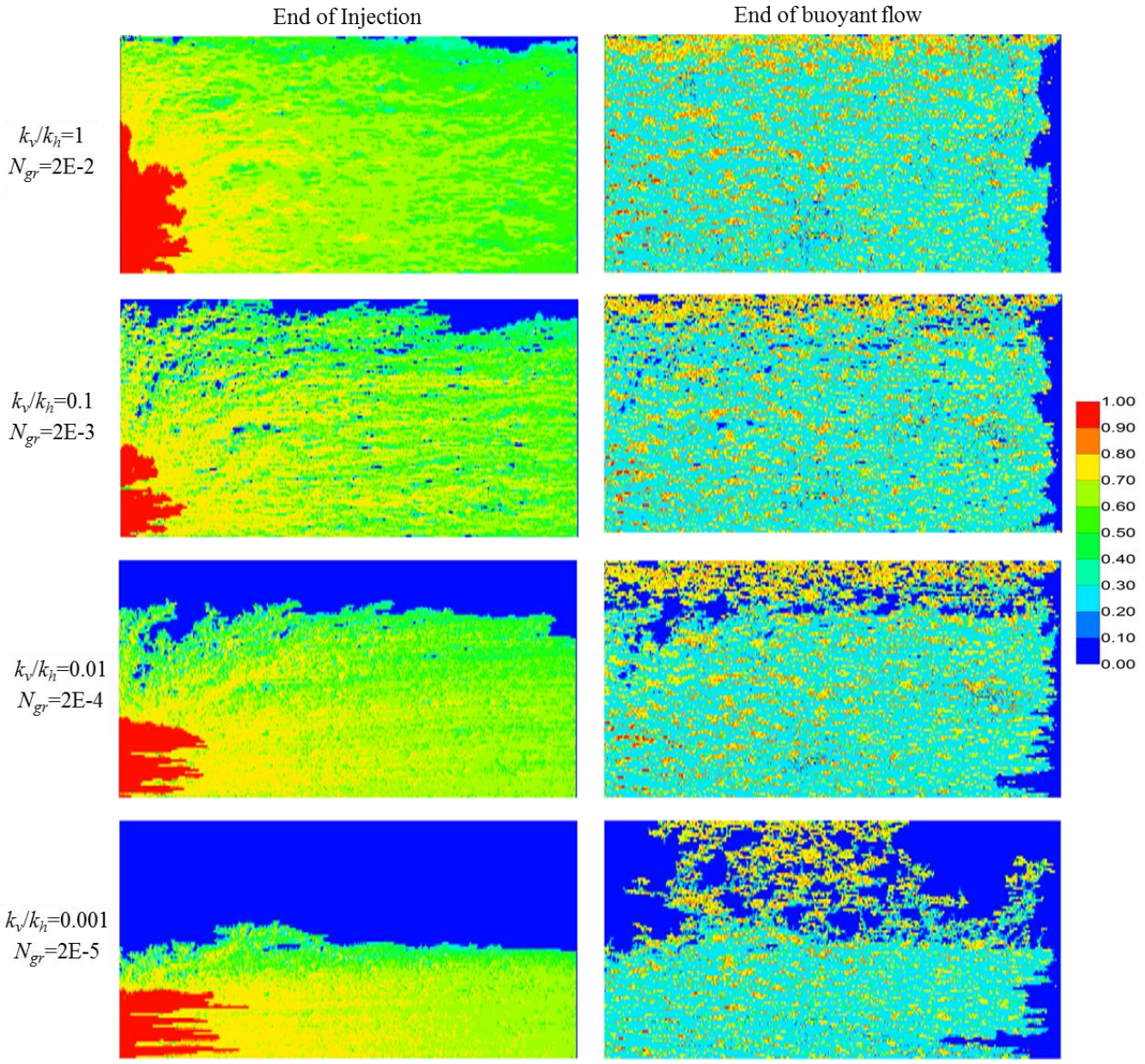

Fig. 3-12 CO_2 saturation fields at the end of injection (left column) and at the end of post-injection (right column).

In the transition zones (refer to the right column of Fig. 3-12), CO_2 migrates along some of the flow paths to reach the top seal but leaves a large gas saturation in the flow path. Large CO_2 saturations accumulate below the top seal but not uniformly. Notably, for the most anisotropic field, almost half of the upper portion of the domain is uninvaded by CO_2. Obviously, the local capillary traps in the portion are not filled.

The previous research by Saadatpoor (2012) employs a hydrostatic reservoir pressure for the initial condition and a closed domain for the boundary condition. However, reservoir pressure close to injectors increases during injection. Thus, the assumption of hydrostatic pressure gradient is not realistic. One possible remedy would involve simulating injection phase as shown above. Recall that we can generate transition zones using a very anisotropic field, and for this field, the corresponding CO_2 saturation at the end of injection is reproduced in Fig. 3-13a. Meanwhile, we choose the same amount of CO_2 as that in Fig. 3-13a, and emplace CO_2 at the bottom of the domain by tuning the initial CO_2 saturation to be 0.76. The initial CO_2 saturation field is in Fig. 3-13b. Pressure buildup induced by injection was about 690 kPa in Fig. 3-13a, so we use this pressure field as the initial pressure in Fig. 3-13b. After 100 yrs of flow, both the injection and emplacement scenarios approaches to a steady state and the corresponding CO_2 saturation is in Fig. 3-13c and Fig. 3-13d, respectively. These figures show that injection into storage reservoirs with large anisotropies yields essentially the same behavior as the emplacement storage scenario when the same initial pressure condition is used. The emplacement volume corresponds to the thickness of the perforated interval. Thus, we conclude that local capillary trapping is essentially independent of CO_2 storage modes (i.e., injection or emplacement) in highly anisotropic reservoirs.

Otherwise, if we do not consider injection-induced pressure, the simulation shows that it takes a long time (400 yrs) for CO_2 to achieve a similar spatial distribution. For this case, the CO_2 saturation is in Fig. 3-13e. Therefore, injection-induced pressure affects both CO_2 plume dynamics and local capillary traps filling.

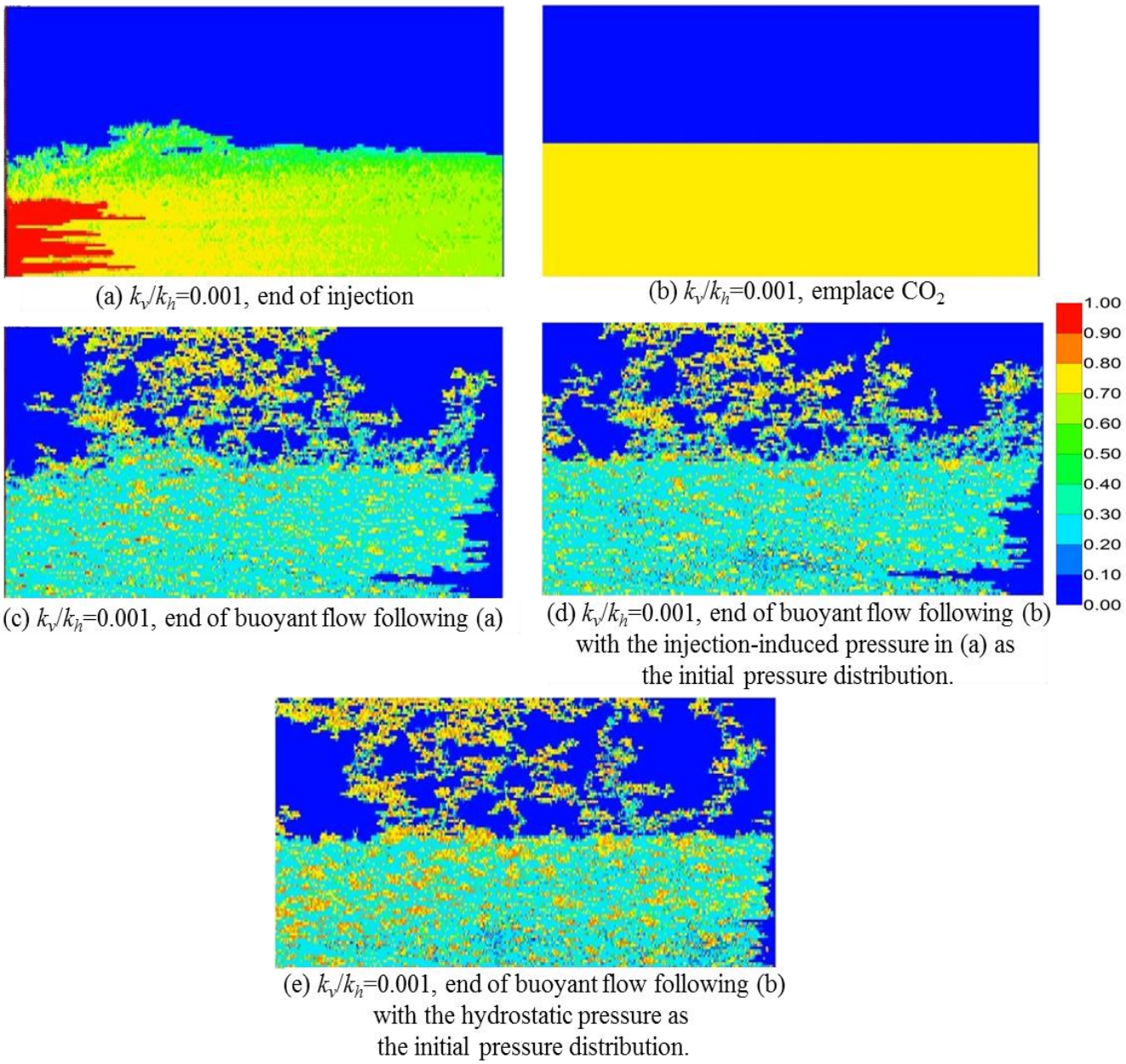

(a) k_v/k_h=0.001, end of injection

(b) k_v/k_h=0.001, emplace CO_2

(c) k_v/k_h=0.001, end of buoyant flow following (a)

(d) k_v/k_h=0.001, end of buoyant flow following (b) with the injection-induced pressure in (a) as the initial pressure distribution.

(e) k_v/k_h=0.001, end of buoyant flow following (b) with the hydrostatic pressure as the initial pressure distribution.

Fig. 3-13 (a) CO_2 saturation fields at the end of injection in a highly anisotropic (k_v/k_h=0.001) formation. The injected CO_2 is 190 tonnes (1PV) using the largest injection rate listed in Table 3-2. The mass of CO_2 remaining in the storage domain was 67.5 tonnes. (b) The same amount (67.5 tonnes) of CO_2 is emplaced in the same portion of the domain as the initial state of buoyant flow. (c) CO_2 saturation distribution at the end of post-injection following (a). (d) CO_2 saturation distribution at the end of post-injection following (b), the injection-induced pressure in (a) is used as the initial state in (b). (e) CO_2 saturation distribution with hydrostatic pressure assigned as the initial state.

3.2.2.2 Effect of formation dip angle on LCT

Fig. 3-14 shows CO_2 saturation in formations with dip angles of 0°, 5°, and 25°. For each dip angle, both the smallest and largest injection rates (refer to Table 3-2) are employed. For the largest injection rate, the mass of CO_2 staying in the storage domain (the 399×100 ft portion) at the end of post-injection for the three dip angles was 147.6, 147.73, and 148 tonnes, respectively. Whereas, for the smallest injection rate, the mass of CO_2 remaining in the storage formation at the end of post-injection was 57.6, 48.6, and 25.8 tonnes, respectively. Thus, formation dip angle tends to have a greater impact on stored mass of CO_2 inside a fixed area under small injection rates (N_{gr}~20).

In a moderate dip (5°) formation, structures of local capillary trapping are similar to those in the horizontal formation. However, when the formation becomes highly inclined (25°), LCT structures tend to be parallel to the formation inclination. Notably, when the injection rate is smaller for the highly-deviated formation, CO_2 migration tends to be dominated by several of the capillary channels. For this scenario, obviously, most of the local capillary traps cannot be flooded. The laterally extensive local capillary traps become convenient conduits for moving CO_2 rapidly to the right boundary.

However, for the smallest injection rate (Right column in Fig. 3-14); LCT filling efficiency in the horizontal formation is better than that in the inclined formation. This suggests, if small injection rates have to be employed (because of, e.g., small formation fracturing pressure), it would be better to choose a horizontal saline aquifer to enhance local capillary trapping.

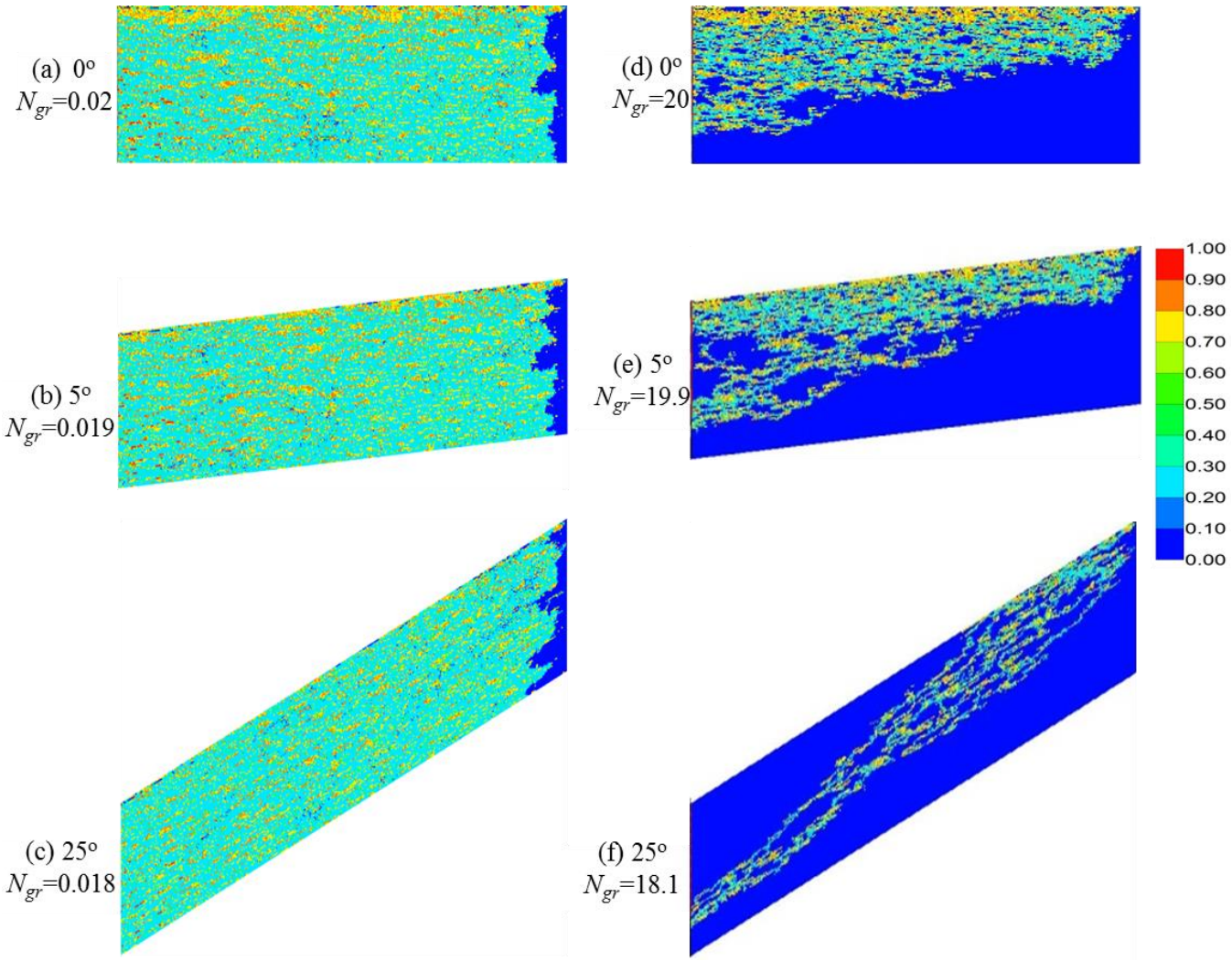

Fig. 3-14 CO_2 saturation fields at the end of post-injection for the largest (left column) and smallest injection rate (right column). Recall the buoyancy number includes the parameter of formation dip angle, so the number changes slightly with dip angles.

3.2.2.3 Effect of auto-correlation length on LCT

Figure 3-15 shows CO_2 saturation at the end of injection and at the end of post-injection in the 2D domain with a large horizontal auto-correlation length of 200 ft. Recall, the base case uses a horizontal auto-correlation length of 5 ft. The large horizontal auto-correlation length enhances lateral migration of CO_2, and gives rise to remarkable distribution patterns of CO_2.

For large injection rates, CO_2 sweeps the whole domain and therefore, all the local capillary traps are filled. However, for small injection rates, auto-correlated structures with relatively small capillary entry pressure determine CO_2 preferential flow paths, so large

horizontal auto-correlation suppresses the upward migration of CO_2. This is further reflected in Fig. 3-16 that shows CO_2 saturation fields at the end of leakage. For the small injection rate, all the injected CO_2 stays inside the storage formation, and no CO_2 leaks out. However, for the large injection rate, both capillary barriers and flow paths are flooded. This causes some of CO_2 to move toward the wellbore and subsequently escape from the storage formation.

Through comparing Fig. 3-15 (λ_x=10 ft) to Fig. 3-6 (λ_x=5 ft), a large horizontal auto-correlation length yields: (1) a large LCT structure; (2) a large LCT mass fraction (it increased from 36% to 48 as λ_x increased from 5 to 10 ft). Additionally, in the case of leakage, a large horizontal auto-correlation yields less leakage of CO_2 along the wellbore (Fig. 3-16 vs. Fig. 3-7). This is because large horizontally auto-correlated flow paths cause CO_2 to migrate laterally, rather than upward.

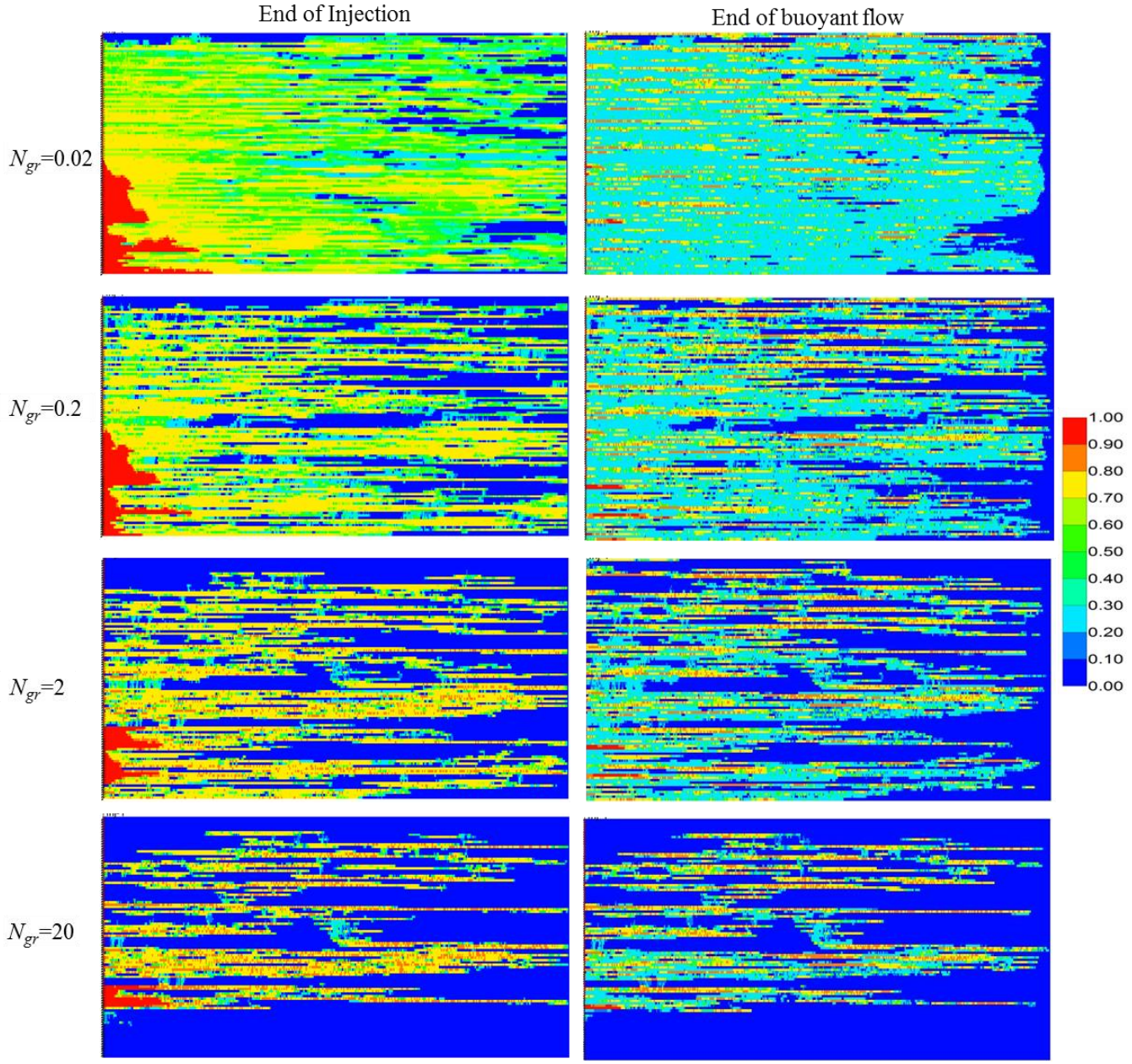

Fig. 3-15 CO_2 saturation fields at the end of injection (left column) and at the end of post-injection (right column).

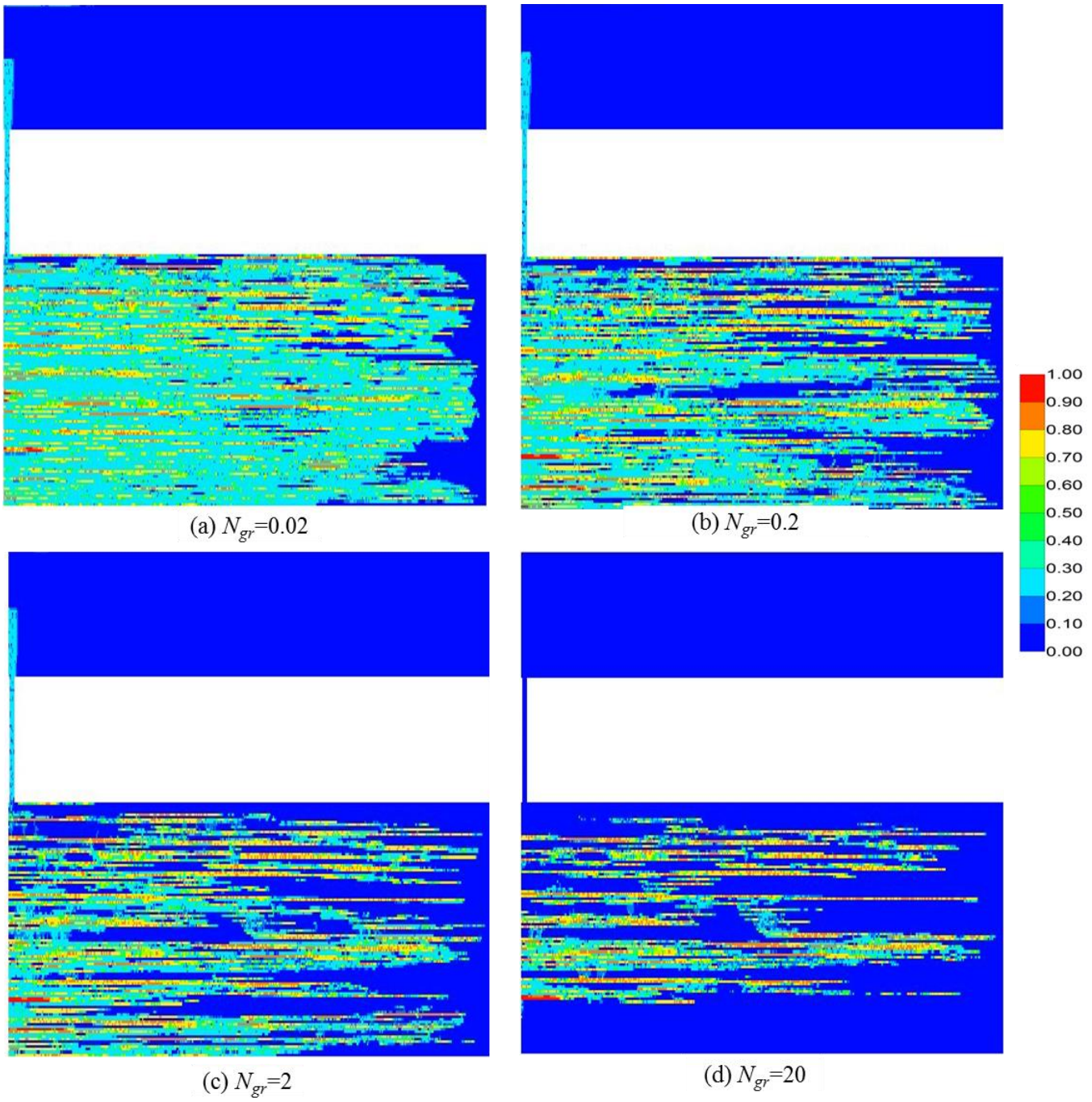

(a) N_{gr}=0.02 (b) N_{gr}=0.2

(c) N_{gr}=2 (d) N_{gr}=20

Fig. 3-16 CO_2 saturation fields after 50 yrs of leakage simulation following the right column of Fig. 3-15.

3.2.2.4 Effect of standard deviation of capillary entry pressure on LCT

The above analysis demonstrates the spatial heterogeneity or auto-correlated structures of capillary entry pressure determine LCT amount and distribution. In this part, we study another indicator of heterogeneity – the standard deviation. Figure 3-17 shows CO_2 saturation fields at the end of post-injection for capillary entry pressure fields with different coefficient of variations (C_v). C_v is the ratio of the standard deviation to the mean of capillary entry pressure. Larger C_v gives rise to a denser distribution of LCT (the yellow and red pixels). Quantification shows the LCT volume fraction increased from 22 to 28% as C_v increased from 0.66 to 1.14.

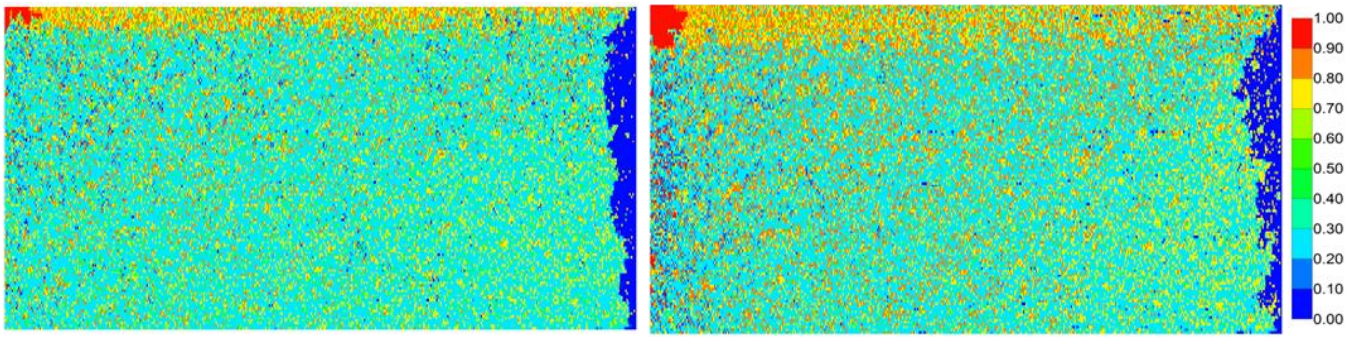

(a) C_v =0.66 (b) C_v =1.14

Fig. 3-17 CO_2 saturation fields at the end of post-injection for the capillary entry pressure fields with two coefficients of variation (C_v).

3.2.2.5 Effect of aquifer types on LCT

All the above studies are limited to the effect of buoyant force on LCT robustness in an open system where aquifer pressure has almost no change during the storage period; it increased by only 5 psi at the end of post-injection. However, pressure build-up would be encountered in a closed aquifer (Ehlig-Economides and Economides 2010). Thus, during leakage, viscous flow would be created, which is driven by the relaxation of pressure build-up of a storage aquifer into the still hydrostatic pressure of an upper aquifer. We study the effect of viscous flow on local capillary trapping through modelling leakage from a closed aquifer. The domain configuration is the same as before except that a small VOLMOD (1.0E+4) is employed to the right boundary cells. Meanwhile, the injected CO_2 mass is kept as 190 tonnes (1PV). Thus, the finite size of the

domain was noticeable for the volume of CO_2 injected, and consequently the fluid pressure in the domain will increase during injection. At the moment of leakage or at the end of post-injection, the average pressure build-up relative to the original reservoir pressure was about 2000 psi. Hence, this is helpful to examine the robustness of local capillary trapping under viscous flow.

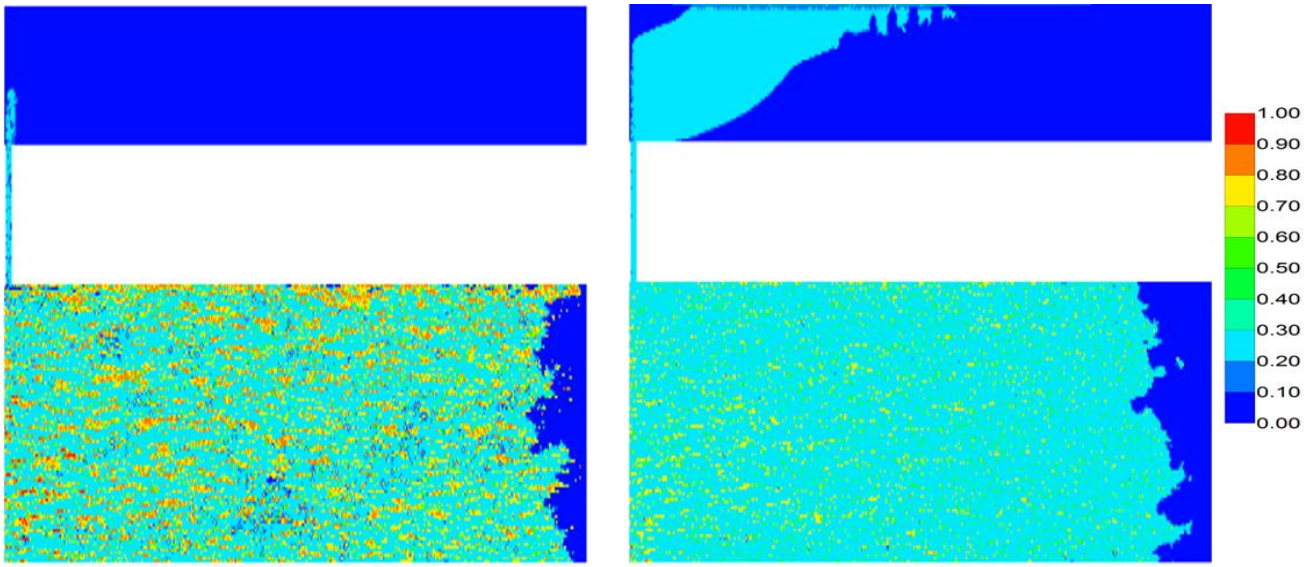

(a) Buoyant flow during leakage (b) Viscous flow during leakage

Fig. 3-18 CO_2 saturation fields after 50 yrs of leakage modeling in an open aquifer (a) and in a closed aquifer (b). The largest injection rate (N_{gr}=0.02, refer to Table 3-2) is used.

Under viscous flow (Fig. 3-18b), the size of local capillary trapping (dispersed bright yellow) and magnitude of associated LCT saturations become small, as compared to the local capillary trapping under buoyant flow of leakage (Fig. 3-18a). However, many small patches of local capillary trapping remain in the former case even after 50 yrs of leakage.

Next, we quantify the mass of local capillary trapping and then compare it to residual and dissolution trapping. Figure 3-19 shows the variation of trapped CO_2 mass fraction along time (injection, post-injection, and leakage) for both closed and open aquifers. Many studies have examined the fraction change of CO_2 in forms of residual phase trapping, dissolution trapping, and free state (e.g., Doughty 2007, Kumar et al. 2005, Taku Ide et al. 2007). Their analyses are restricted to the injection and post-injection periods. However, here we focus on the post-

injection and leakage periods, because LCT takes the effect on safe storage of CO_2 during these periods. During the post-injection period, LCT decreases while residual phase trapping increases: the former is converted into the latter as water imbibes into the trail of CO_2 plume. During leakage, CO_2 flows toward to the leak point and then escapes from the formation in a short time period. After that, buoyant flow approaches to a steady state, and the mass fraction of CO_2 in different forms keeps almost constant. LCT immobilizes more CO_2 than dissolution trapping in the closed aquifer, while for the open aquifer, LCT can play as significant role as residual phase trapping in storing CO_2. It should be noted that those mass fractions are measured in a small (~5 ft) horizontally auto-correlated domain. They would change with horizontal auto-correlation lengths.

Specifically, at the end of leakage, the LCT mass fraction was 0.37 for the open aquifer, and it was 0.15 in the closed aquifer. This indicates that viscous force compromises LCT during leakage, and LCT is sensitive to aquifer pressure. This finding is consistent with laboratory experiments (Sun 2014), in which local capillary trapping of the buoyant non-wetting phase remain intact when system pressure is hydrostatic, but when forcing imbibition occurs (driven by imposing a gradient in hydraulic potential in aqueous phase in the domain), much of the locally trapped phase is displaced.

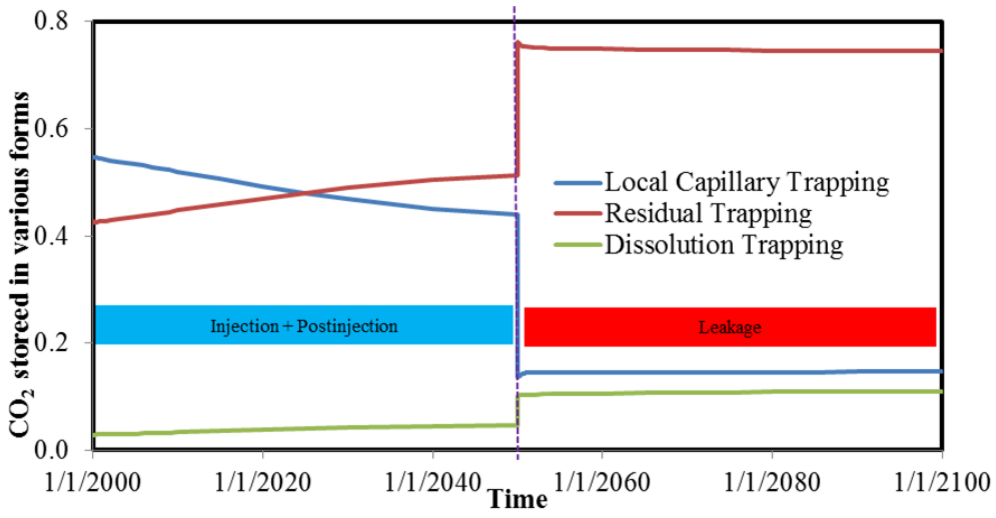

(a)

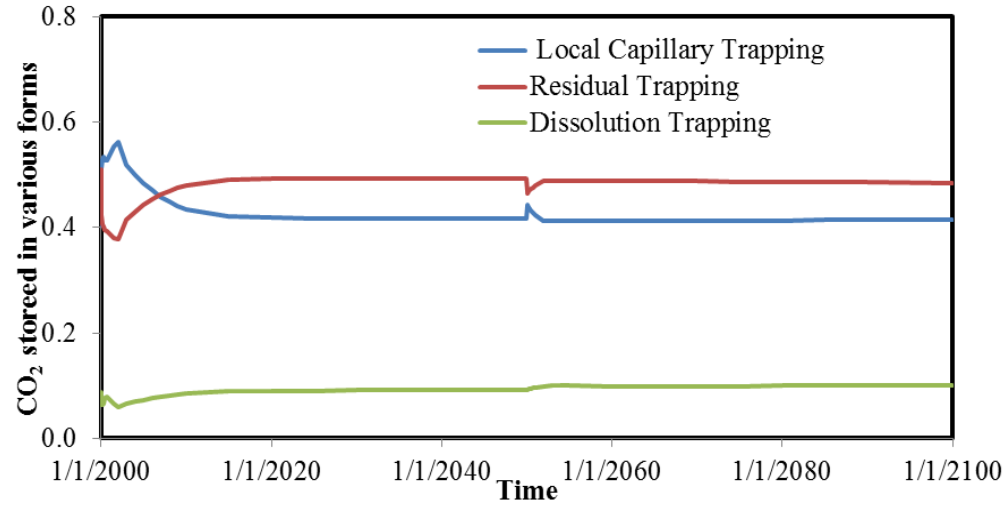

(b)

Fig. 3-19 Variation of CO_2 mass fraction stored by local capillary trapping, residual gas, and dissolution along with time. (a) is for a closed aquifer, (b) is for an open aquifer.

3.2.3 Rock/fluid interaction parameters

3.2.3.1 Effect of residual gas saturation on LCT

Recall the base case sets the residual gas saturation to be 0.29. Here, we change the residual gas saturation from 0 to 0.44. This range is representative of sandstone/sand-packs (Iglauer et al. 2011). Figure 3-20 shows the mass fraction of LCT, residual phase trapping, and dissolution trapping at both the end of post-injection and the end of leakage. These mass

fractions change little during leakage, thus, curves almost overlap at the two measured times. As residual gas saturation increases, the LCT mass fraction decreases significantly, and meanwhile, dissolution trapping decreases slightly. Local capillary trapping and residual phase trapping compete with each other.

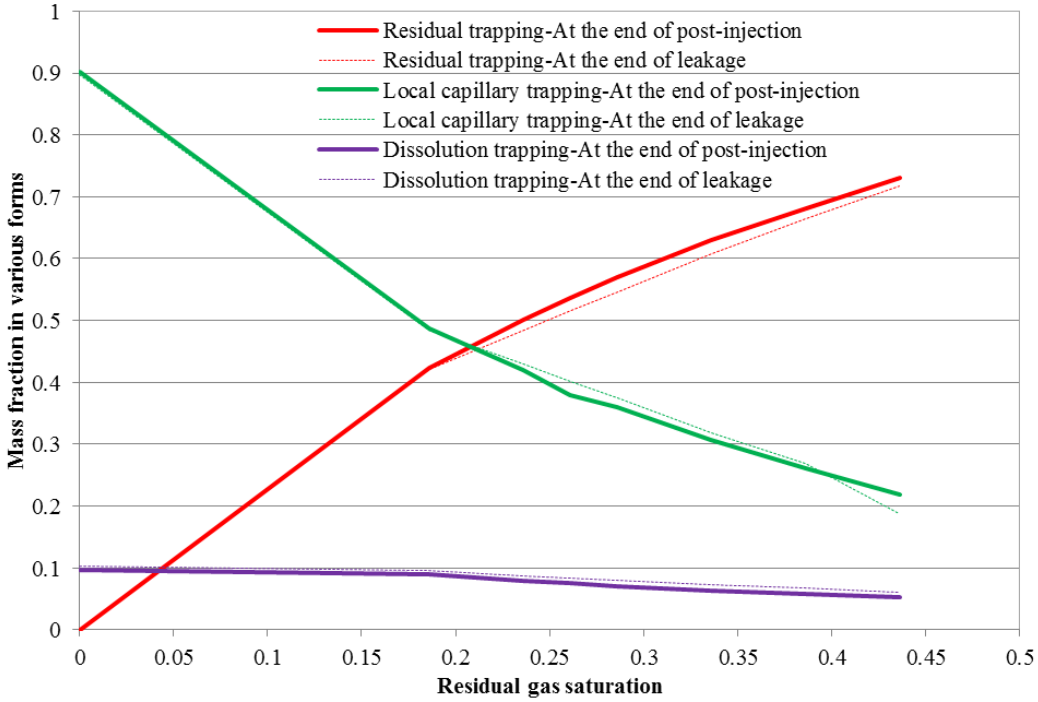

Fig. 3-20 Variation of CO_2 mass fraction in different forms with residual gas saturation. 1PV of CO_2 is injected using the largest injection rate (refer to Table 3-2, N_{gr}=0.02).

3.2.3.2 Effect of relative permeability hysteresis on LCT

Figure 3-21a shows CO_2 saturation fields with relative permeability hysteresis added (base case); the hysteresis is the reason for widespread residual gas (cyan color) inside the domain. Without hysteresis, residual phase trapping does not occur (Fig. 3-21b). However, local capillary trapping still occurs. In addition, its structures and saturations are similar to the case with hysteresis. This means that the hysteresis in relative permeability has no effect on LCT. Additionally, this observation indicates that local capillary trapping is different from residual phase trapping in terms of underlying mechanisms: the former trapping is resulted from the

heterogeneity of capillary entry pressure at a large or representative element volume scale, whereas, the latter is caused by snap-off (Roof 1970) at a pore-scale.

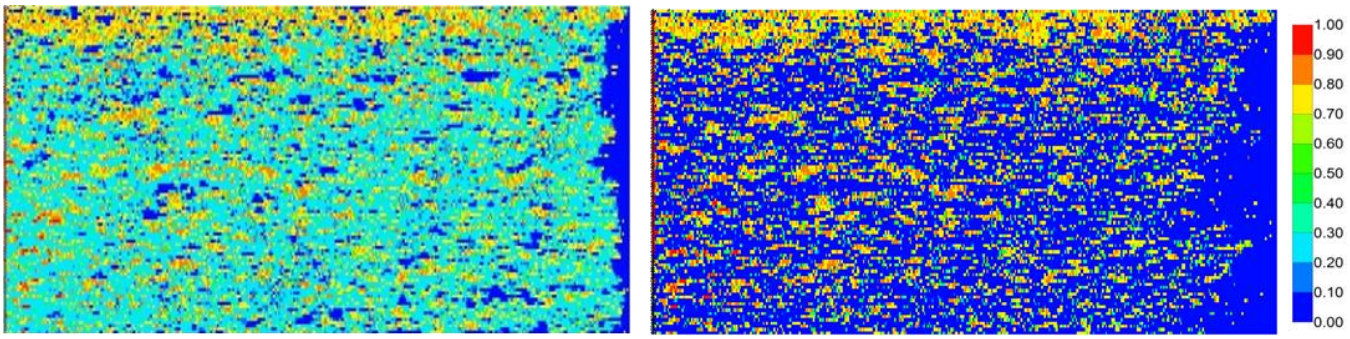

(a) w/ hysteresis of relative permeability (b) w/o hysteresis of relative permeability

Fig. 3-21 CO_2 saturation fields at the end of the post-injection. 1PVof CO_2 is injected under the largest injection rate in Table 3-2.

3.2.3.3 Effect of capillary hysteresis on LCT

Figure 3-22a and b show CO_2 saturation at the end of post-injection in an isotropic field for CO_2 flow without and with capillary hysteresis, respectively. With capillary hysteresis, most of the CO_2 inside local capillary traps have been displaced, and the remaining CO_2 saturation after imbibition was around 0.4~0.5 (see scattered green pixels in Fig. 3-22b). Recall the residual gas saturation is 0.29, so the remaining saturation is still larger than the residual gas saturation. The right open boundary condition creates "a very large aquifer". This supplies enough water for the imbibition. Even after the complete imbibition, CO_2 inside local capillary traps cannot be entirely displaced to the residual level even after 50 yrs of buoyant flow.

To further examine the effect of water amount on local capillary trapping, the right open boundary is changed into a constant pressure boundary. For such a boundary condition, local capillary trapping is robust under the influence of capillary hysteresis (Fig. 3-22c and 3-22d). This observation means that the amount of water for the imbibition is a key; for the constant pressure boundary, most of the brine water has been displaced out of the storage domain during injection so the rest is not enough for the subsequent imbibition during buoyant flow. It should

be aware that those observations of local capillary trapping are in the compact displacement region where CO_2 goes everywhere.

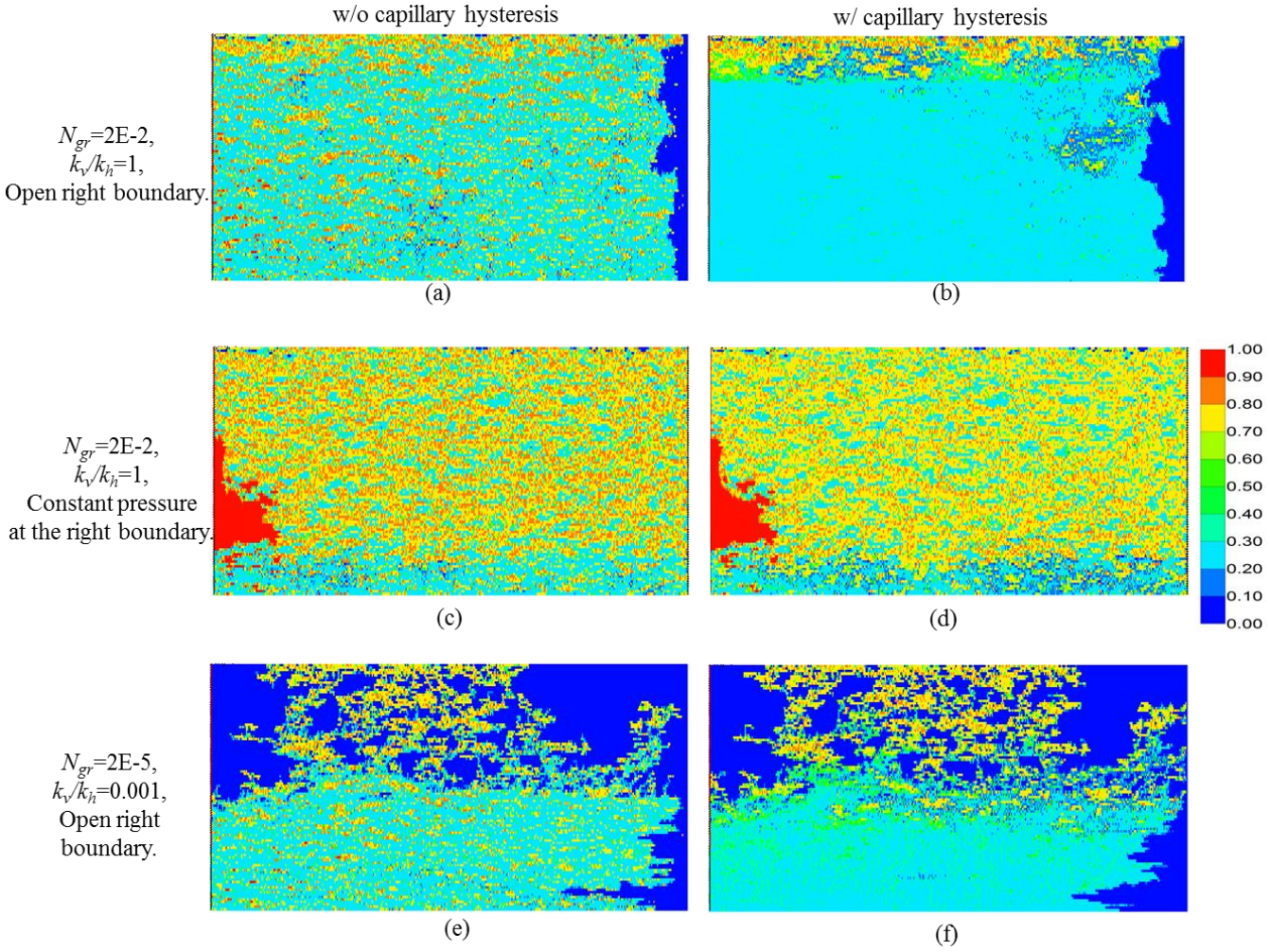

Fig. 3-22 Effect of capillary hysteresis on local capillary trapping under different anisotropies and boundary conditions. The largest injection rate in Table 3-2 is employed with N_{gr} 0.02.

However, in transition zones, local capillary trapping is robust irrespective of the amount of surrounding water. Figure 3-22e and f show CO_2 saturation fields at the end of injection in the very *anisotropic* domain for cases without and with capillary hysteresis, respectively. The yellow pixels with high CO_2 saturation are local capillary trapping. They are not compromised by capillary hysteresis, even if surrounded by water with high saturation.

The above boundary conditions apply to geologic carbon sequestration. Open boundary conditions or open aquifers would be encountered frequently in a sedimentary basin (Cavanagh et al. 2010). Constant pressure boundaries would be introduced if a producer were employed to pump saline water out of a storage formation in order for pressure management (Birkholzer et al. 2015), or if fluid flow encounters a fault boundary with a constant fault opening pressure (Guglielmi et al. 2015).

3.3 DISCUSSION

The auto-correlated structures of capillary entry pressure determine the extent of local capillary trapping. Such trapping determines the final distribution of CO_2 in a storage aquifer. Therefore, the amount of CO_2 that is trapped locally changes with the spatial heterogeneity of capillary entry pressure fields.

Moreover, local capillary traps in the near well region can be fully filled (CO_2 invades all the traps and establishes a large saturation) during injection in an isotropic domain when the corresponding N_{gr} is less than 2. Moreover, they remain filled after post-injection buoyancy driven flow ends. The next question would be how large this "near-well region" can be in a typical injection scenario in a 3D domain. Here, we estimate the size of this region. Consider a vertical CO_2 injector in an open aquifer, the aquifer thickness is 390 ft, and the vertical perforation interval is in the lower quarter part. CO_2 is injected at the rate of 5.0E+7 Scf/d. The average vertical permeability is 20 mD. The properties of brine and CO_2 are the same as described above. The calculated near-well region is around tens of meters. Therefore, such a "near-well region" is very small for typical injection rates.

For leakage modeling, a single leakage conduit along a wellbore is used to model the most probable leakage scenario of CO_2 (Tao 2012). Admittedly, local capillary trapping would be influenced by settings, including the number of leakage points, leakage time, and the connection between leakage points and local capillary traps. Thus, the mass fraction of local capillary trapping calculated above would be changed as well.

3.4 SUMMARY AND CONCLUSION

In this chapter, we employ a commercial reservoir simulator CMG-GEM to study the influential parameters of local capillary trapping (LCT). The examined parameters are categorized into three groups: reservoir static parameters, injection parameters, and rock/fluid interaction parameters. The main purpose is to investigate how these parameters alter the extent and amount of local capillary trapping. In addition, we compare LCT to other widely-accepted trapping mechanisms (i.e., residual and dissolution trapping) in different types of aquifers.

For the reservoir static parameters, the heterogeneity of permeability/capillary entry pressure fields essentially determines the LCT amount and structure. This means that local capillary traps are intrinsic to a capillary entry pressure field. This also suggests that local capillary traps can be directly identified from a capillary entry pressure field. We will show such an identification method in chapter 4.

The injection parameters (i.e., injection rate and injected volume) influence only the filling efficiency of local capillary traps. This suggests that local capillary trapping can be maximized through manipulating injection strategies. We will show this point in chapter 7.

The rock/fluid interaction parameters (e.g., hysteresis in relative permeability and capillary pressure curves) affect CO_2 saturation in local capillary trapping, but not the spatial configurations of local capillary trapping.

Overall, through full-physics simulation, we demonstrate that local capillary trapping is one of the most important trapping mechanisms during geological carbon sequestration in a saline aquifer. Therefore, in the future CO_2 sequestration projects, local capillary trapping should be considered during the design and optimization of trapping processes.

Chapter 4: Local Capillary Trapping Identification Using a Geologic Criterion[2]

The last chapter employed a commercial reservoir numerical simulator CMG-GEM to model local capillary trapping and identify the main influential parameters. The main issue of these simulations is that they are computationally intensive because of the incorporation of small-scale capillary pressure heterogeneity. For example, a 2D model with dimensions of 400×100 and grid size of 1×1 ft takes ~30 hours of CUP time to complete on a 2.8 GHz processor. Thus, modeling LCT will be intractable at the large/field scale using the above full-physics simulator. Alternatively, physics-proxy simulations reduce modeling complexities in both numerical and mathematical aspects; therefore, they might be promising in modelling local capillary trapping.

A geologic criterion (Saadatpoor 2012) is one such method. The method is developed for a fast prediction of LCT distribution and capacity based on a capillary entry pressure field. The method was used to predict local capillary trapping during purely *buoyant flow* (i.e., emplace CO_2 at the bottom of a domain and let it rise). In this work, we extend it to predict local capillary trapping that occurs during *viscous flow*.

In the following, we first describe the geologic criterion algorithm and its implementation on a capillary entry pressure field. Then, we model local capillary trapping using CMG-GEM, in which *viscous flow* is incorporated through using a large injection rate. Next, we compare CMG-GEM results to the geologic criterion algorithm in terms of local capillary trapping distribution and amount. Finally, we discuss advantages and limitations of the two methods.

[2]Parts of this this chapter has been presented in the following conference: Ren, B., Bryant, S.L., Lake, L.W. 2015. Quantifying Local Capillary Trapping Storage Capacity Using Geologic Criteria. Paper CMTC-439489-MS presented at Carbon Management Technology Conference, Sugar Land, Texas, USA, 17-19 November.

4.1 DESCRIPTION OF THE GEOLOGIC CRITERION METHOD

This section summarizes the geologic criterion algorithm developed by Saadatpoor (2012). Differences introduced by this work are so noted; otherwise, the concepts are those of Chapter 6 and 7 from his dissertation. The algorithm takes three steps to find local capillary traps. The following subroutines can be applied to both 2D and 3D capillary entry pressure fields, which are the inputs to the method.

(1) Given a value of critical capillary entry pressure (CCEP), find all cells in a domain that have capillary entry pressure exceeding this value. These cells are defined as barriers. The other cells are non-barriers or flow paths. For example, Fig. 4-1a shows a sample 2D capillary entry pressure field. Figure 4-1b shows barrier grid blocks in yellow that have capillary entry pressure larger than CCEP (=2 psi).

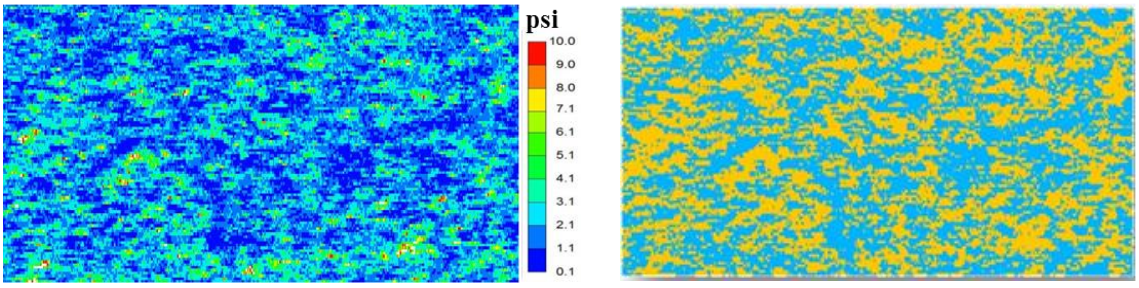

(a) (b)

Fig. 4-1 (a) a 2D heterogeneous capillary entry pressure field. (b) Yellow cells have capillary entry pressure larger than CCEP (2 psi in this example) and are considered barriers.

(2) Find all the clusters of barriers in the set of cells from step 1. The right plot in Fig. 4-2 is the zoom-in of a small patch of barrier clusters. Red cells are the clusters of barriers.

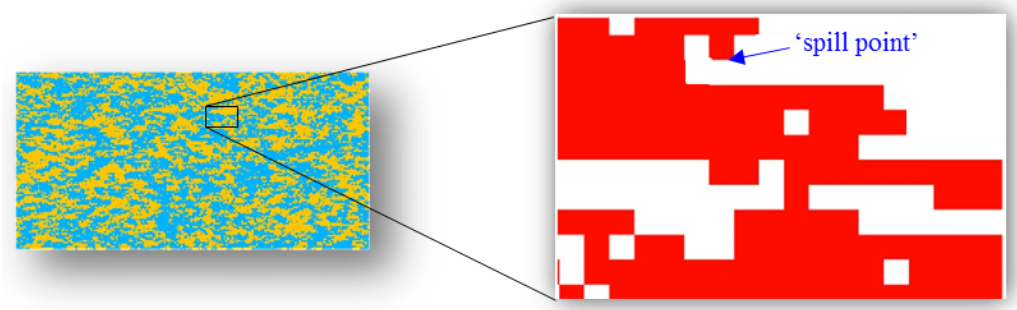

Fig. 4-2 The clusters of barriers are shown in red cells on right. The blue arrow indicates an example of spill points determined by the geometry of barriers.

(3) Find clusters of the flow paths that are surrounded by the set of clusters of barriers identified in step 2. This is realized by removing the flow paths a cluster that are connected to the cells in the top layer, meanwhile also keeping the flow paths that are surrounded by barriers. This procedure is repeated for every cluster of flow paths that are connected to the top layer. After doing this, the flow paths kept inside the domain are assured to be surrounded by local capillary barriers from both the top and sides. This statement implicitly means that the so-called "spill point" in the large-scale hydrocarbon accumulation is accounted for in these small-scale local capillary traps, in other words, the structurally lowest point in a cluster of local capillary trap is resolved. As seen from Fig. 4-2, a cluster of barriers has a spill point indicated by a blue arrow. Correspondingly, in Fig. 4-3, the circled cell is a local capillary trap that is determined by the geometry of a cluster of barriers. Other green cells (flow paths) are also surrounded by red barrier cells. All these green cells are local capillary traps.

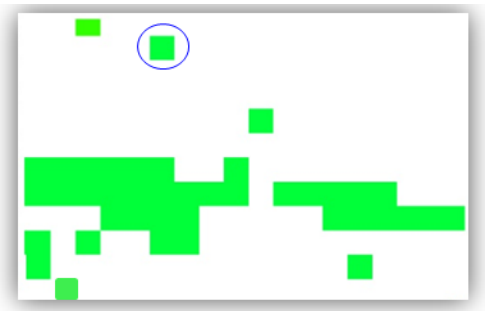

Fig. 4-3 Green cells are local capillary traps. The blue-circled cell is an example of local capillary traps, which are controlled by the spill point of a cluster of barriers.

4.2 ISSUES WITH THE METHOD

Saadatpoor (2012) has tested the above algorithm through full-physics simulation on *buoyancy-driven flow* of CO_2. The author observed that the number of local capillary traps shows a threshold as critical capillary entry pressure value is increased, and that this threshold value is not equal to the arithmetic mean of capillary entry pressure. There are two main issues with the geologic criterion method:

(1) For the detection of local capillary trapping, the arithmetic mean of capillary entry pressure predicts unrealistically large amounts of local capillary trapping.

(2) It is unknown that how to select a physical value of CCEP that gives the same results as the flow simulations.

These two issues motivate this study. For the first issue, the main reason is that CO_2 does not fill all the local capillary traps during buoyancy-driven flow; instead, CO_2 migrates along only paths with the least resistance (small capillary entry pressure). Therefore, some of the local capillary traps cannot be invaded. The corresponding solution, as suggested by chapter 3, is to create *viscous flow* through CO_2 injectors. During injection, the viscous force enables CO_2 to invade much of the pore space near the wellbore regardless of capillary heterogeneity. During post-injection, local capillary traps remain filled as shown in chapter 3. Thus, by introducing viscous flow, the problem of local capillary traps filling encountered during purely buoyant flow can be addressed. Then, we strictly test whether the geologic criterion algorithm give a good

prediction of local capillary trapping. By trying different CCEPs, we suggest a choice of selecting the most physically representative CCEP in the following.

4.3 SYNTHETIC GEOLOGIC MODELS

Following the procedures described in section 3.1.1, we synthesize both 2D and 3D base geologic models. Model dimensions and properties are listed in Table 4-1. Figure 4-4 shows the generated 2D permeability field, the capillary entry pressure field, and its histogram. Figure 4-5 is for the 3D.

Table 4-1. Properties of 2D and 3D base geologic models

Model parameters	2D	3D
Model dimensions	400×100	64×32×32
Grid block size, ft	1×1	1×1×1
Permeability field	lognormal	lognormal
Autocorrelation length, ft	(5, 0)	(5, 5, 0)
Arithmetic mean of permeability, mD	194	403
Anisotropy of permeability field	isotropic	isotropic
Standard deviation of permeability, mD	339	774
Porosity, constant	0.27	0.27
Mean of capillary entry pressure, psi	2.07	2.13
Standard deviation of capillary entry pressure, psi	1.36	1.43

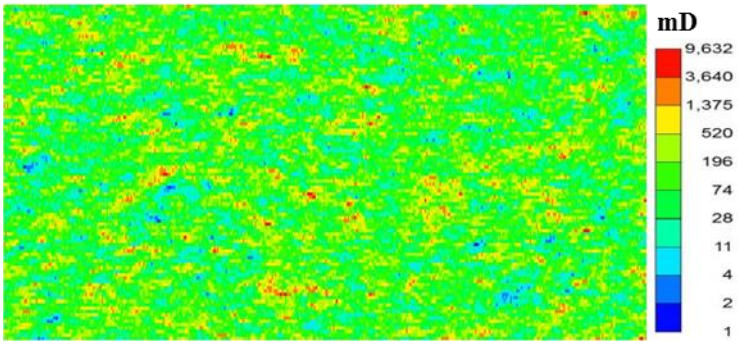

(a)

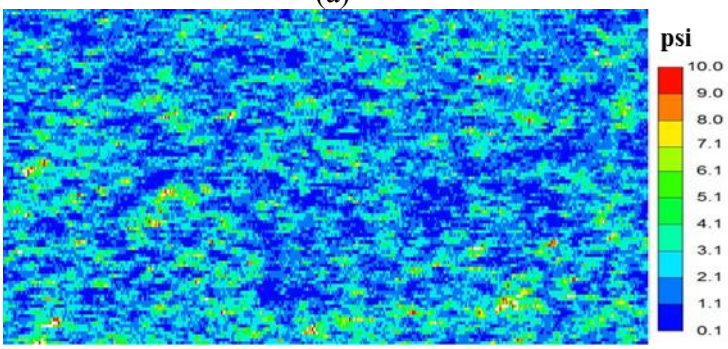

(b)

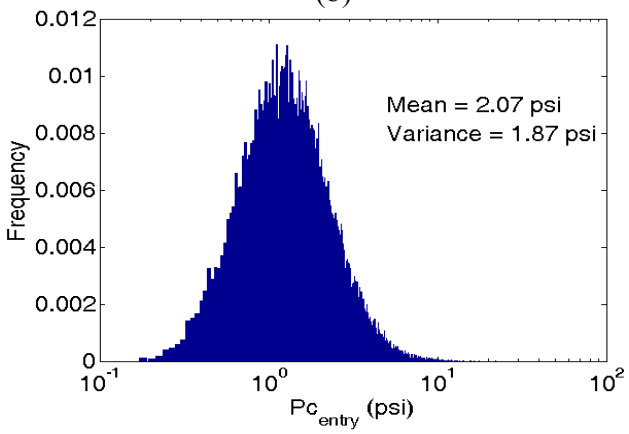

(c)

Fig. 4-4 (a) 2D permeability field, (b) 2D capillary entry pressure field, (c) capillary entry pressure histogram for (b).

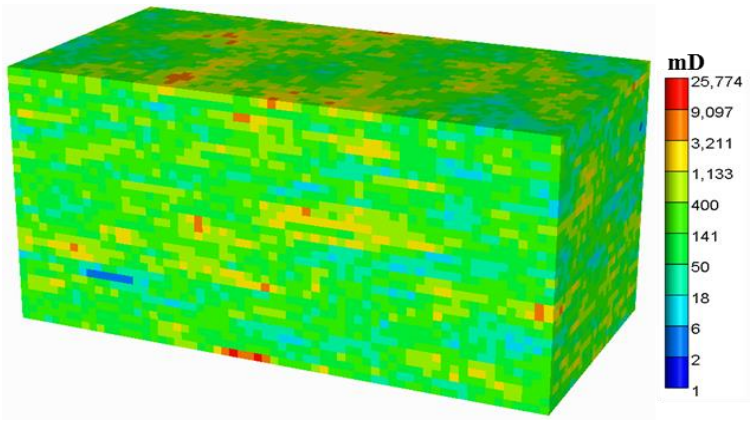

(a)

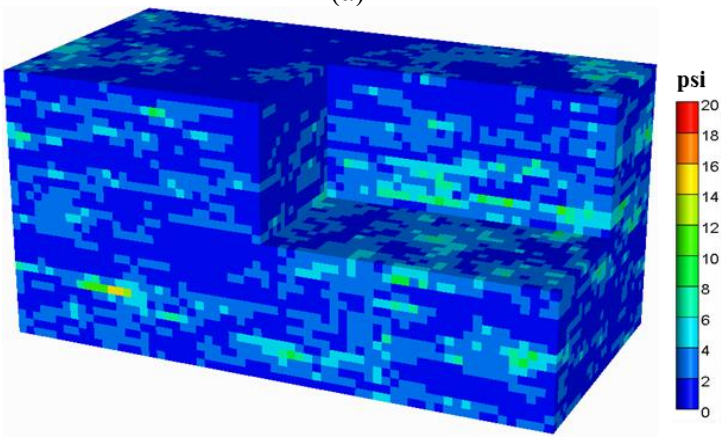

(b)

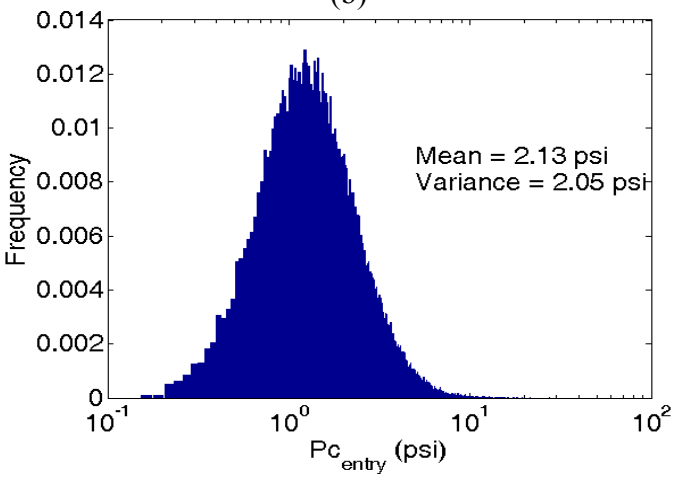

(c)

Fig. 4-5 (a) 3D permeability field, (b) 3D capillary entry pressure field, (c) capillary entry pressure histogram for (b).

4.4 FLOW SIMULATION SETTINGS IN CMG-GEM

We employ CMG-GEM (2012) to conduct CO_2 flow simulations. Properties of components, the relative permeability curve, and capillary pressure curve are the same as described in chapter 3. However, hysteresis was not considered here; the hysteresis of capillary pressure has almost no impact on local capillary trapping as shown in chapter 3.

The values of injection parameters are in Table 4-2. In CMG-GEM, a very large VOLMOD (1.0E+7) is assigned to the right boundary cells to mimic an open aquifer. The injected volume is selected to sufficiently fill the pore space of a *storage domain*, but it accounts for little (4.2E-5) pore volume fraction of the *entire domain*. Here, the pore volume of the entire domain consist of two parts: one part is the storage volume; the other is the volume of right boundary cells with large VOLMOD. Injection periods are short because the storage domain is small. After injection, flow simulation is continued to model buoyant flow. The period during injection and post-injection lasts for 50 yrs in total.

Table 4-2. Settings of injection simulation in CMG-GEM

Parameters	2D	3D
Well type	Vertical	Vertical
Perforation interval	Left lower quarter	Left middle lower half
Perforation length, ft	25	16
Injection rate, Scf/d	4.9E+5	3.1E+7
Injection period, day	73	0.7
Simulation period, yr	50	50
Buoyancy number along wellbores	0.1	0.05

For settings on well injection rates (Table 4-2), CO_2 inlet flux entering the formation in both 2D and 3D domains is set to be 60 ft/day. This magnitude is enough to create a compact displacement near the wellbore (refer to chapter 3). Well injection rate is then calculated for a

given perforation interval and wellbore radius. The buoyancy number along an injector is calculated using Eq. 4.1 and shown in Table 4-2.

$$N_{gr} = \frac{\Delta\rho g k_v H \cos\alpha}{u \mu L} \tag{4.1}$$

In the above, N_{gr} is the buoyancy number, $\Delta\rho$ is the density difference between brine (1024.6 kg/m^3) and CO_2 (405.9 kg/m^3), g is the gravitational constant, k_v is the mean vertical permeability (see Table 4-1), u is CO_2 flux penetrating a storage formation, $u = q/(2\pi r_w H)$, μ is the viscosity of CO_2 (0.049 cp), L is the horizontal length of a storage reservoir, H is the perforation length, α is the formation dip angle. As seen from Table 4-2, N_{gr} is much smaller than one. This means viscous-dominated flow would prevail around the wellbore. Thus, all the local capillary traps inside the model would be filled by viscous flow.

4.5 TWO-DIMENSIONAL RESULTS

4.5.1 Local capillary trapping from the geologic criterion algorithm

As mentioned, local capillary traps are surrounded by cells with large capillary entry pressure. Thus, intuitively, the physically representative CCEP will be very close to the median of capillary entry pressure; since the number of flow path cells will be the same as that of the barrier cells if the median value is an input CCEP. On the other hand, equating flow path and barrier cells is not enough to warrant local capillary traps because the spatial configuration of these cells is not accounted for. As a trial, we simply select several values of CCEP around the median entry pressure (1.72 psi) from 0.60 to 2.30 psi with an interval of 0.05 psi.

Figure 4-6a shows the variation of LCT volume fractions at different CCEPs in the 2D capillary entry pressure field. Here, the LCT volume fraction is defined as the number of LCT cells divided by the total number of cells in a storage domain. The CCEP is normalized by the mean and standard deviation of capillary entry pressure. Generally, the LCT volume fraction first increases with CCEP followed by a decrease. The increasing part is simply because as CCEP increases, more cells become flow paths instead of barriers, and since most of the cells are barriers at small CCEP, the additional flow paths are additional LCT. However, increasing the

CCEP also decreases the number of barrier grid blocks, which is necessary to surround LCT cells, and eventually, the number of local capillary traps must decrease. Therefore, a threshold value of CCEP exists that yields the maximum LCT volume fraction. In this example, the *threshold* CCEP was 1.80 psi and the corresponding LCT volume fraction was 0.45 (refer to Table 4-1 for other parameters of the capillary entry pressure field).

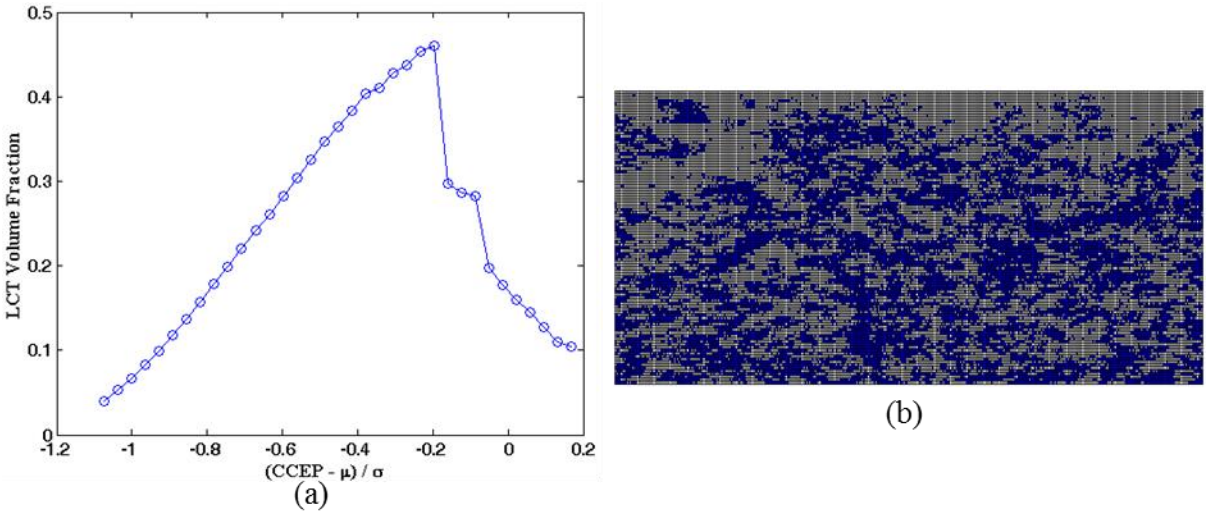

Fig. 4-6 (a) LCT volume fraction versus CCEP for a 2D capillary entry pressure field, μ=2.07 psi, σ=1.36 psi. (b) Distribution of LCT cells at the threshold CCEP (1.8 psi) identified in (a). The qualitative behavior in (a) is similar to that in the previous work (Saadatpoor, 2012). The difference is that a small interval (0.05 psi) of CCEP was used in this study. A subtle change of CCEP around the threshold causes a large change of LCT volume fractions. Thus, a small CCEP intervalgives accurate predictions of both the maximum LCT volume fraction and the threshold CCEP.

Figure 4-6b shows the LCT spatial distribution at the threshold CCEP (1.8 psi). The local capillary traps in the domain are comprised of many clusters with different sizes. We will systematically analyze cluster properties (e.g., numbers and size) in chapter 6. This chapter focuses on the total amount and spatial distribution of local capillary trapping. In the following, we test different CCEP values and identify the physically representative CCEP, under which, the predicted local capillary trapping show a good match with those from CMG-GEM.

4.5.2 Local capillary trapping from CMG-GEM

Figure 4-7a shows CO_2 saturation fields at the end of injection. CO_2 is in a compact displacement (i.e., CO_2 displaces brine almost everywhere), though CO_2 saturations are not the same. Clearly, all the local capillary traps are filled at the end of injection. This can be clearly seen from the CO_2 saturation fields at the end of buoyant flow (Fig. 4-7b), yellow and red color grid blocks with high CO_2 saturations are the local capillary trapping.

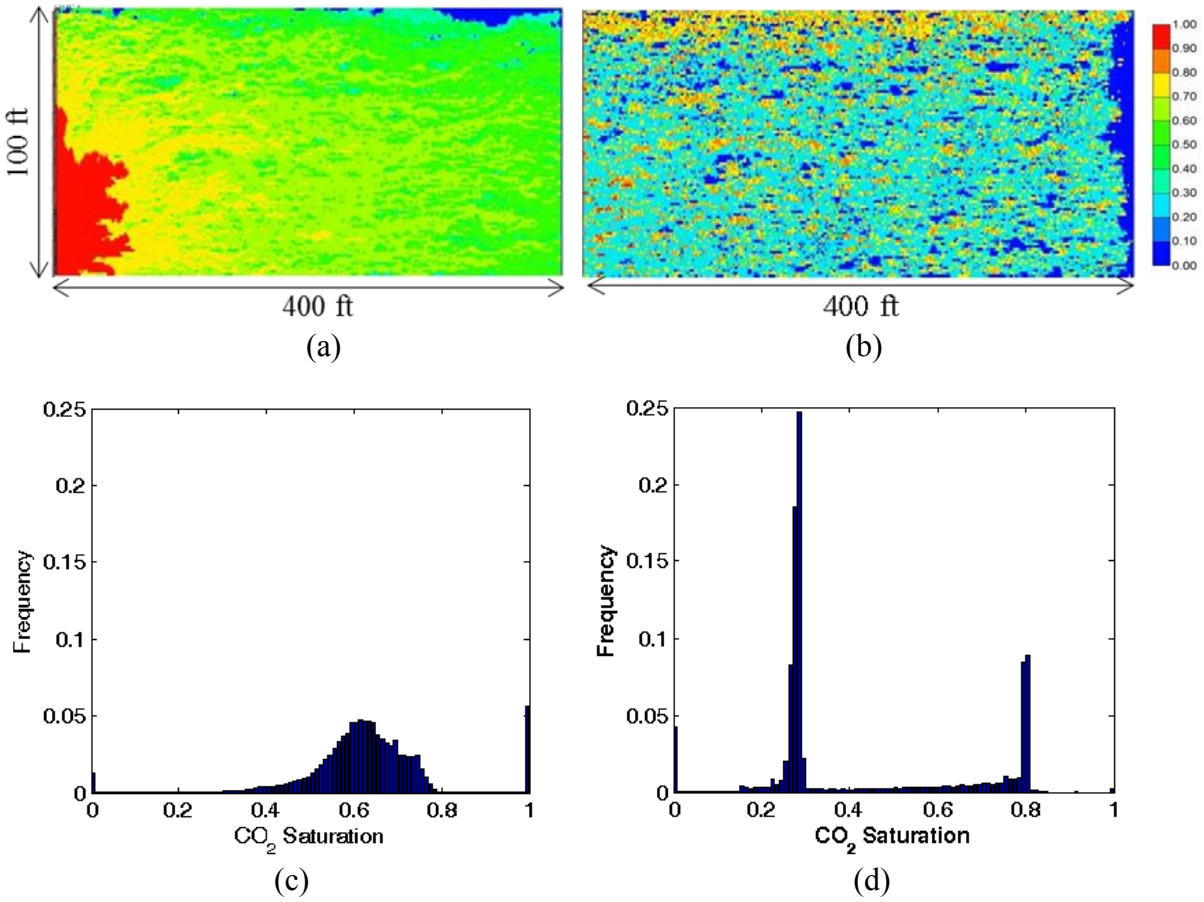

Fig. 4-7 (a) CO_2 saturation field at the end of injection. (b) CO_2 saturation field at the end of buoyant flow. (c) CO_2 saturation histogram for (a). (d) CO_2 saturation histogram for (b).

Figures 4-7c and d show the histograms of CO_2 saturation corresponding to Fig. 4-7a and b. At the end of injection, the CO_2 saturation histograms follow a normal distribution. This is

consistent with experimental observations from core flooding (Kong et al. 2014, Krause 2012). At the end of buoyant flow, however, two peaks of saturation frequency are observed, one is around residual gas saturation (S_{gr}=0.287), and the other peak is around 0.8 (1-S_{wirr}). The latter peak corresponds to local capillary trapping.

Moreover, some cells with gas saturation in between are observed. One reason is that 50 yrs of buoyant flow simulation is not long enough for CO_2 to completely achieve the "steady-state"; the average CO_2 saturation in the reservoir was 0.419 at 40 yrs, and it was 0.418 at 50 yrs. One would expect that longer-time simulation would minimize the number of these cells, and that CO_2 inside them would become either residual phase trapping or local capillary trapping.

4.5.3 Comparison of LCT between the geological criterion and CMG-GEM

After we obtain CO_2 saturation fields from CMG-GEM, we extract LCTs from saturation fields and compare them to the predictions from the geologic criterion algorithm.

We define a match index (Eq. 4.5) to search for a physically representative CCEP. It is defined as the ratio of the cell numbers predicted from both methods divided by the sum of cells predicted only from CMG-GEM and those predicted only from the geologic criterion (GC). Therefore, the match index ranges from 0 to 1. The worst match has an index equal to zero, which means the algorithm cannot predict any LCT cells. The best match approaches one, and this means all the LCT cells predicted from CMG-GEM are identified by the algorithm. A physically representative CCEP would correspond to the maximum match index.

$$M.I = \frac{\text{LCT from both methods (\# green grid)}}{\text{LCT from both methods (\# green grid)} + \text{LCT from CMG-GEM only (\# red grid)} + \text{LCT only from GC only (\# blue grid)}} \quad (4.2)$$

The change of the match index with CCEP is in Fig. 4-8. The CCEP at the maximum match index was 1.15 psi. At this CCEP, the comparison of LCT between the two methods is in

Fig. 4-9a. Green cells are the LCTs predicted from both methods. Red and blue cells are the LCTs predicted only from CME-GEM and only from the geologic criterion, respectively. The LCT volume fraction was 0.25 from the geologic criterion while it was 0.20 as predicted from CMG-GEM. Some blue cells exist in Fig. 4-9a, which means that some cells are identified as LCTs in the geologic criterion but not in CMG-GEM. Meanwhile, many red cells appear in Fig. 4-9a, this means that the spatial distribution of LCT cells are not successfully identified by the geologic criterion. Thus, the CCEP at the maximum match index is not a good choice.

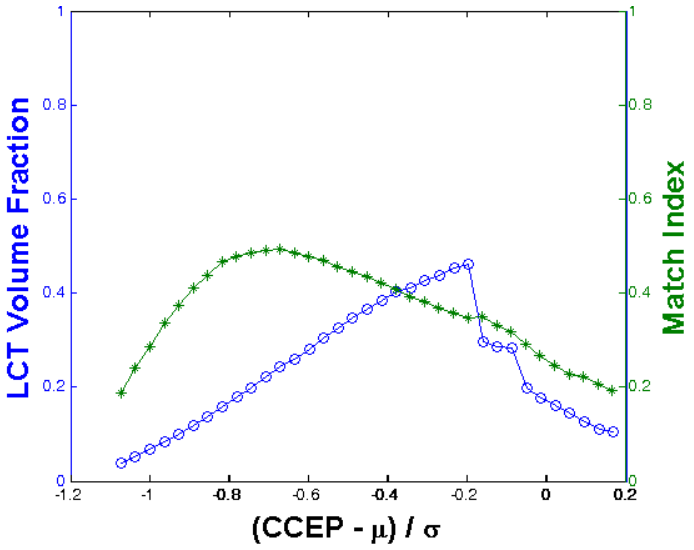

Fig. 4-8 Change of LCT volume fraction and match index with CCEP in a 2D capillary entry pressure field. μ=2.07 psi, σ=1.36 psi.

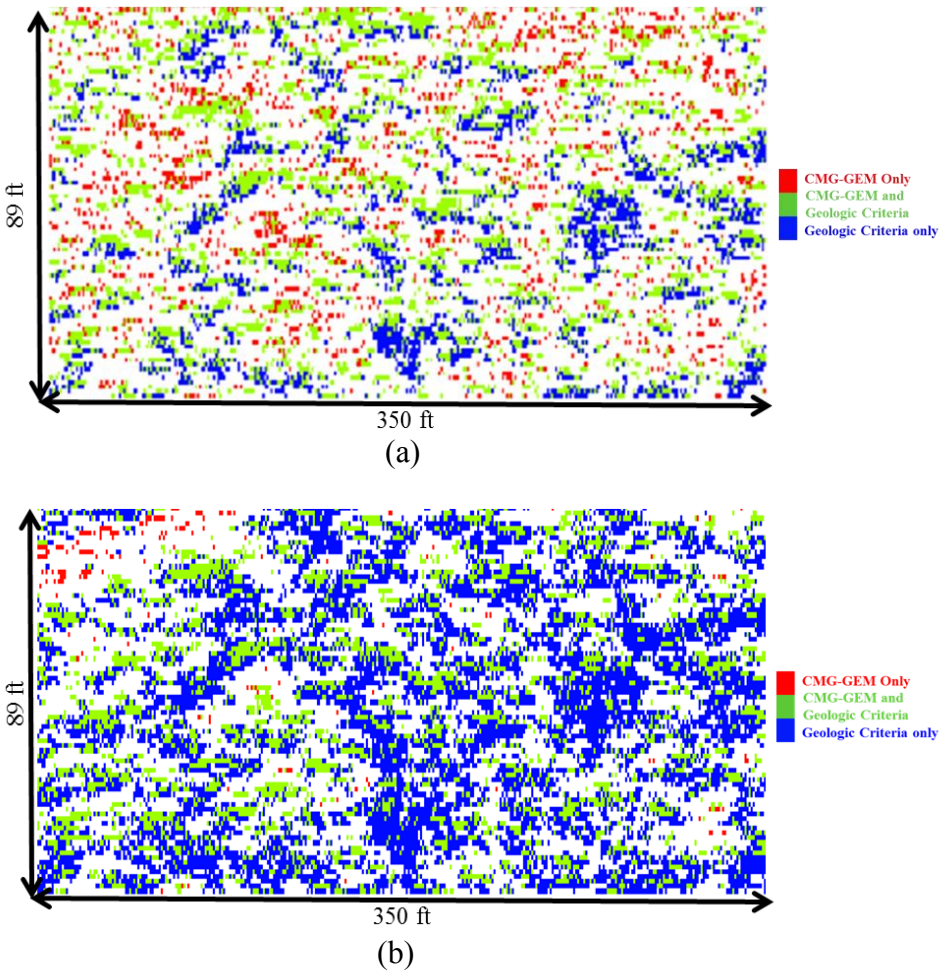

Fig. 4-9 Comparison of LCT prediction between CMG-GEM and the geologic criterion. (a) A CCEP (1.15 psi) at the maximum match index was used. (b) A threshold CCEP (1.80 psi) was used. For comparison, the top 11 layers with high saturation CO_2 accumulation beneath the seal and the right 50 columns were excluded to remove boundary effects. The previous study (Saadatpoor 2012) on purely buoyant flow suggests that an input CCEP of 1.0 psi determines an upper limit of local capillary trapping capacity, and the predicted LCT volume fraction was 0.17. However, in this study, the flow simulation considering injection periods shows the LCT volume fraction was 0.20. Thus, the threshold CCEP (1.80 psi) is suggested as a physically representative CCEP to determine an upper bound of local capillary trapping capacity, and the predicted volume fraction was 0.45.

Thus, we abandon the concept of maximum match index. Instead, we identify a CCEP at which the algorithm will predict all the LCT cells identified in CMG-GEM. The intuitive choice would be the threshold CCEP as this CCEP yields the maximum amount of local capillary traps.

We compare the CMG-GEM results with the geologic criterion at the threshold CCEP, and the result is in Fig. 4-9b. As expected, the threshold CCEP is feasible in reproducing the spatial distribution of local capillary trapping; negligible red cells were observed. Nevertheless, many false blue cells (only predicted from the geologic criterion algorithm) were observed. Thus, the maximum LCT fraction at the threshold CCEP should be considered as an upper bound. The next question will be that is the upper bound close to the true value? We examine this point in the following by using different heterogeneous capillary entry pressure fields.

4.5.4 Effect of reservoir heterogeneity on LCT comparison

We conduct a sensitivity study to examine the effect of capillary entry pressure heterogeneity (i.e., auto-correlation length and standard deviation) on the LCT comparison between CMG-GEM and the geologic criterion. In the following, the constant porosity and permeability are 0.269 and 194 mD, respectively. The mean of capillary entry pressure is constant at 2.07 psi (same as the base case). Model dimensions are 512×128 with grid size of 1×1 ft. We vary the standard deviation and auto-correlation length of capillary entry pressure, since these parameters determine the final distribution of CO_2. The detailed settings of these parameters are listed in Table 4-3. Other simulation settings in CMG-GEM are the same as the 2D base case above. The considerations in using the geologic criterion algorithm, including a small interval of CCEP, are the same as before.

Table 4-3. 2D capillary entry pressure fields

Case #	λ_x, ft	λ_z, ft	σ, psi	C_v
1	0	0	0.86	0.41
2	0	0	1.36	0.66
3	0	0	1.86	0.90
4	0	0	2.36	1.14
5	5	0	1.36	0.66
6	20	0	1.36	0.66
7	50	0	1.36	0.66
8	0	5	1.36	0.66
9	0	20	1.36	0.66
10	0	50	1.36	0.66

First, we study the effect of standard deviation on the LCT comparison between the two methods. The vertical and horizontal auto-correlation lengths are set to be zero. Standard deviation changes from 0.86 to 2.36 psi, which yields different coefficients of variation (refer to case 1-4 in Table 4-3). Figure 4-10 shows CO_2 saturation fields from CMG-GEM. We compare the LCT amount between CMG-GEM and the geologic criterion in which threshold CCEPs are used. Overall, The LCT volume fraction increases as the frequency distribution of capillary entry pressure becomes wide. The fraction predicted from the algorithm is close to that from CMG-GEM; the former is about 0.12 larger than the latter.

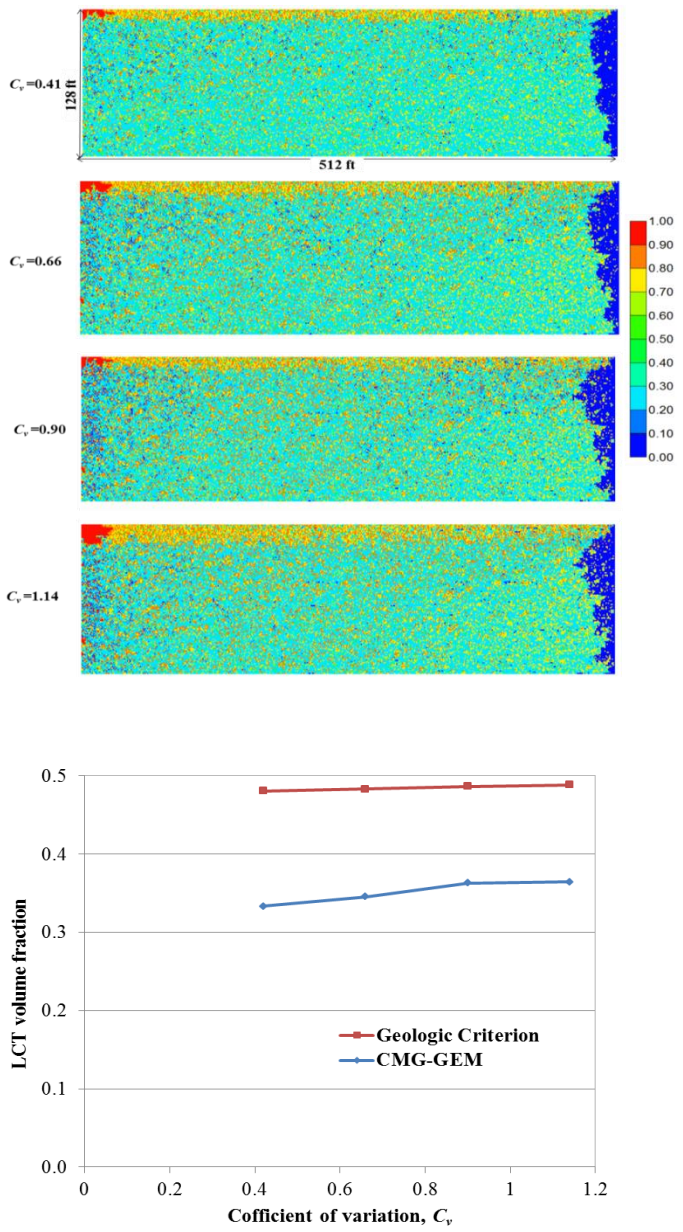

Fig. 4-10 Comparison between CMG-GEM and the geologic criterion for capillary entry pressure fields with different C_v. The upper four plots are CO_2 saturation fields after 50 yrs of buoyant flow modeled by CMG-GEM, and the lowest plot is the LCT volume fraction comparison between CMG-GEM and the geologic criterion algorithm. For comparison, the upper 28 layers were excluded to remove CO_2 accumulation below the upper closed boundary, and the right 200 column cells were excluded to remove dissolved CO_2.

Next, we analyze the effects of horizontal and vertical auto-correlation on the LCT comparison. Results are in Figs. 4-11 and 4-12. Auto-correlation lengths are made dimensionless

(λ_{Dx}, λ_{Dz}) by dividing system lengths in the corresponding direction. As the horizontal auto-correlation increases, the LCT volume fraction increases, whereas the vertical auto-correlation length shows the opposite trend. The geologic criterion produces these trends and the predicted LCT fraction was about 0.1 higher than that from CMG-GEM. Thus, the algorithm gives an upper bound estimation of the LCT amount at threshold CCEPs.

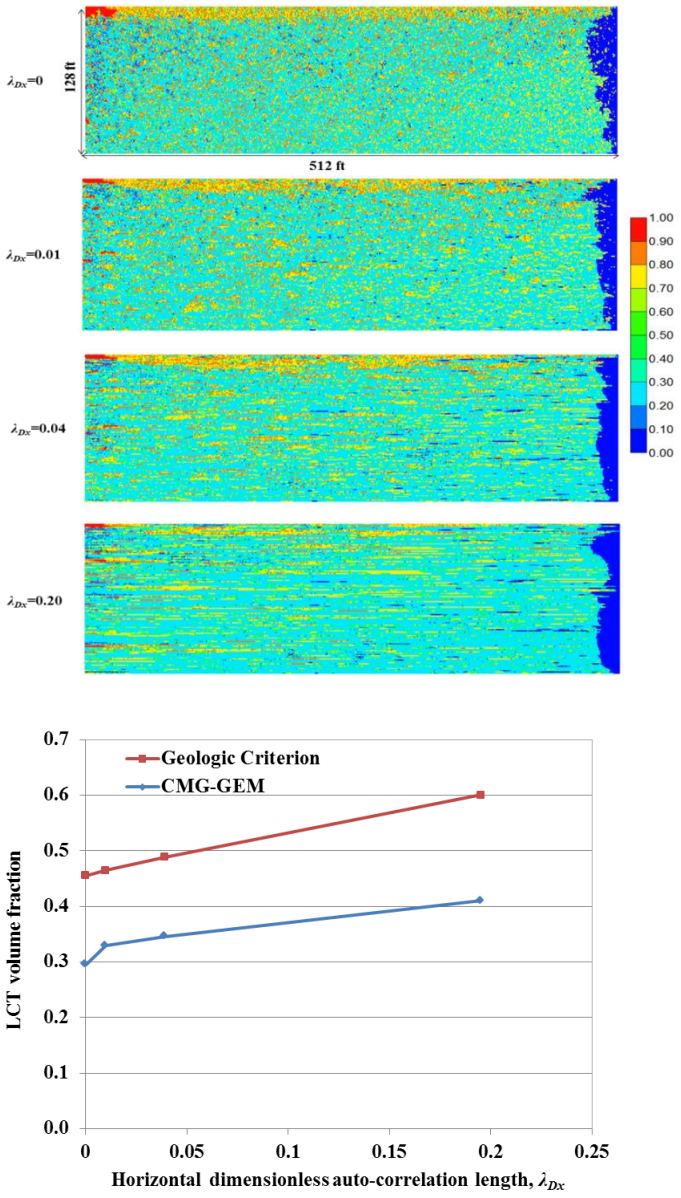

Fig. 4-11 Comparison between CMG-GEM and the geologic criterion for capillary entry pressure fields with different λ_{Dx}. The upper four plots are CO_2 saturation fields after 50 yrs of buoyant flow modeled by CMG-GEM, and the lowest plot is the LCT volume fraction comparison between CMG-GEM and the geologic criterion.

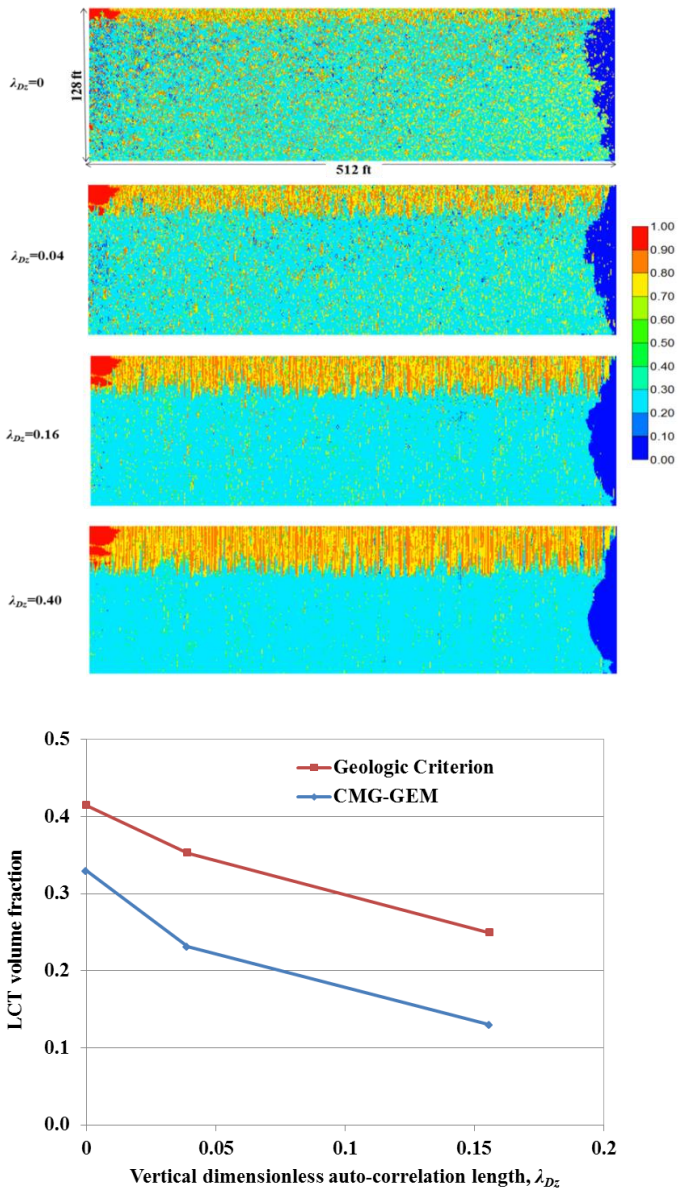

Fig. 4-12 Comparison between CMG-GEM and the geologic criterion for capillary entry pressure fields with different λ_{Dz}. The upper four plots are CO_2 saturation distribution after 50 yrs of buoyant flow modeled by CMG-GEM, and the lowest plot is the LCT volume fraction comparison between CMG-GEM simulator and the geologic criterion algorithm.

4.6 THREE-DIMENSIONAL RESULTS

4.6.1 Local capillary trapping from the geologic criterion algorithm

Figure 4-13a shows the LCT~CCEP curve for the 3D capillary entry pressure field (refer to Fig. 4-5). The threshold CCEP was 1.1 psi, and the corresponding maximum LCT volume fraction was 0.165. Figure 4-13b shows the spatial distribution of local capillary trapping.

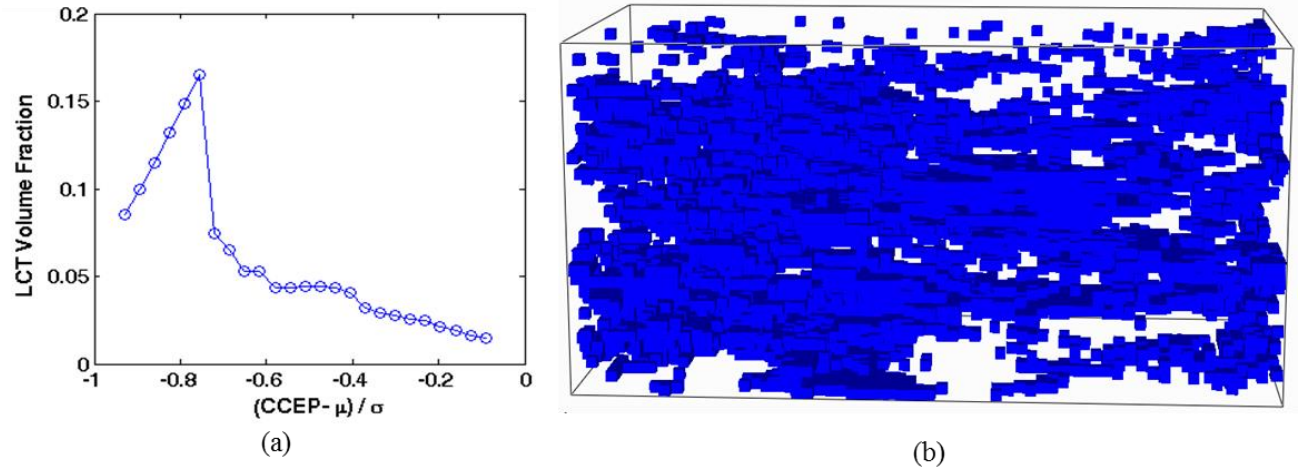

Fig. 4-13 (a) Change of the LCT volume fraction with CCEP for the 3D capillary entry pressure field, μ=2.13 psi, σ=1.43 psi. The threshold CCEP was 1.1 psi. (b) The spatial distribution of local capillary traps at a threshold CCEP of 1.1 psi. Compared to the previous study by Saadatpoor (2012), a small CCEP interval 0.05 psi was used in this study to accurately identify the maximum LCT volume fraction and the threshold CCEP.

4.6.2 Local capillary trapping from CMG-GEM

Figure 4-14 shows CO_2 saturation fields and the corresponding saturation histograms. Specifically, the average gas saturation was 0.307 at 50 yrs of buoyant flow, and it was 0.309 at 40 yrs. This means that CO_2 saturation field approaches a steady state. The yellow and red cells in Fig. 4-14b are local capillary trapping, and the percentage of cells with gas saturation around 0.8 (1-S_{wirr}) was about 4% (refer to Fig. 14d). Recall that in 2D, this can be as high as 10%. Therefore, it can be expected that the LCT amount in 3D would be about half of that in 2D, this is confirmed in the following comparison.

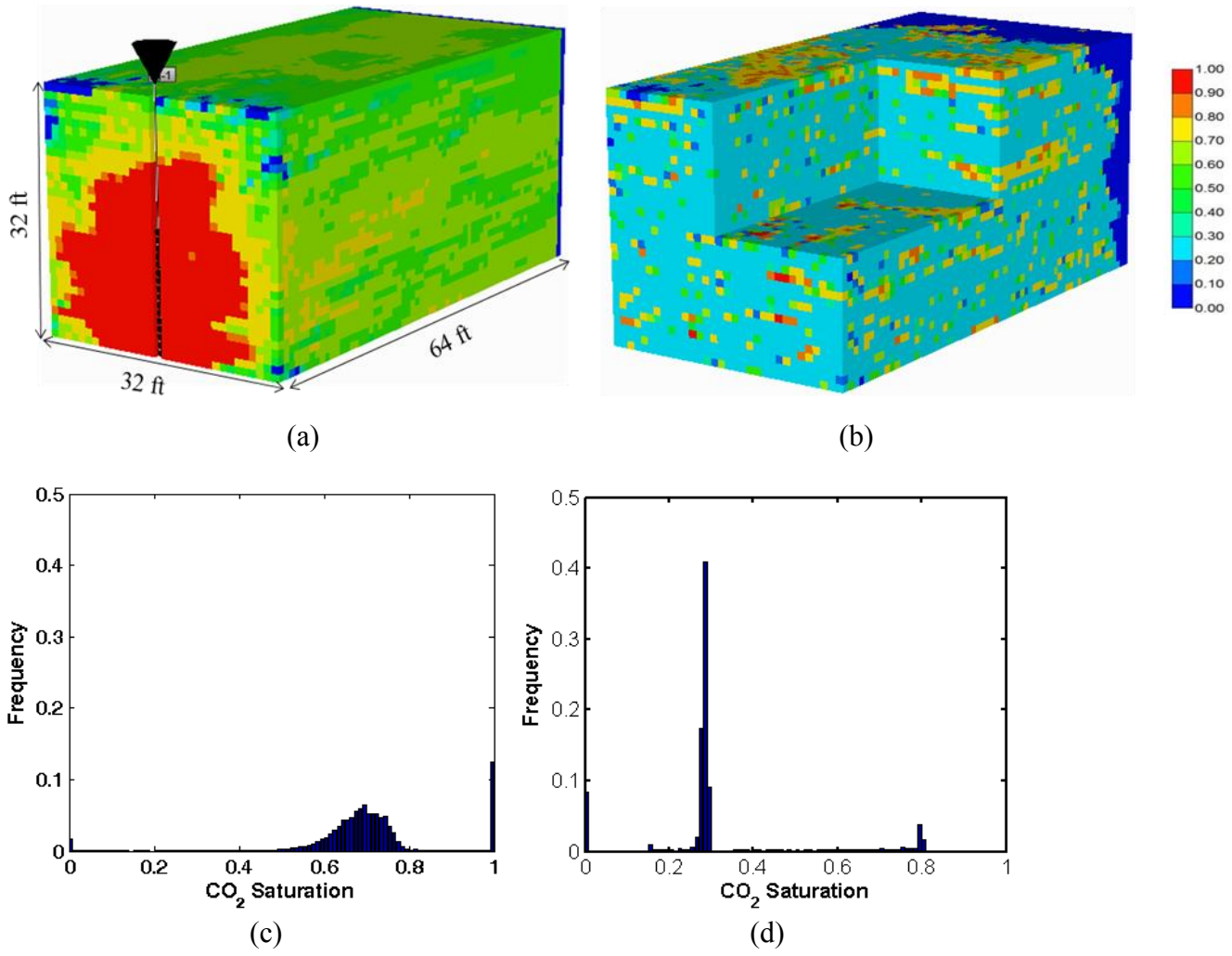

Fig. 4-14 (a) CO_2 saturation field at the end of injection. (b) CO_2 saturation field at the end of buoyant flow. (c) CO_2 saturation histogram for (a). (d) CO_2 saturation histogram for (b).

4.6.3 Comparison of LCT between the geological criterion and CMG-GEM

As learned from 2D, the threshold CCEP gives a close upper bound estimation of the LCT amount, also, the prediction of spatial distribution of LCT is trustworthy. Therefore, in the 3D analysis, we directly make a comparison of LCT between CMG-GEM and the geologic criterion at a threshold CCEP. Figure 4-14 shows the comparisons in several layers of the reservoir. The geologic criterion reproduces most of the LCT predicted by CMG-GEM. Meanwhile, similar to 2D, the algorithm overestimates the LCT amount (see blue cells). The

LCT volume fraction from the algorithm was 0.15 while it was 0.09 as predicted from CMG-GEM.

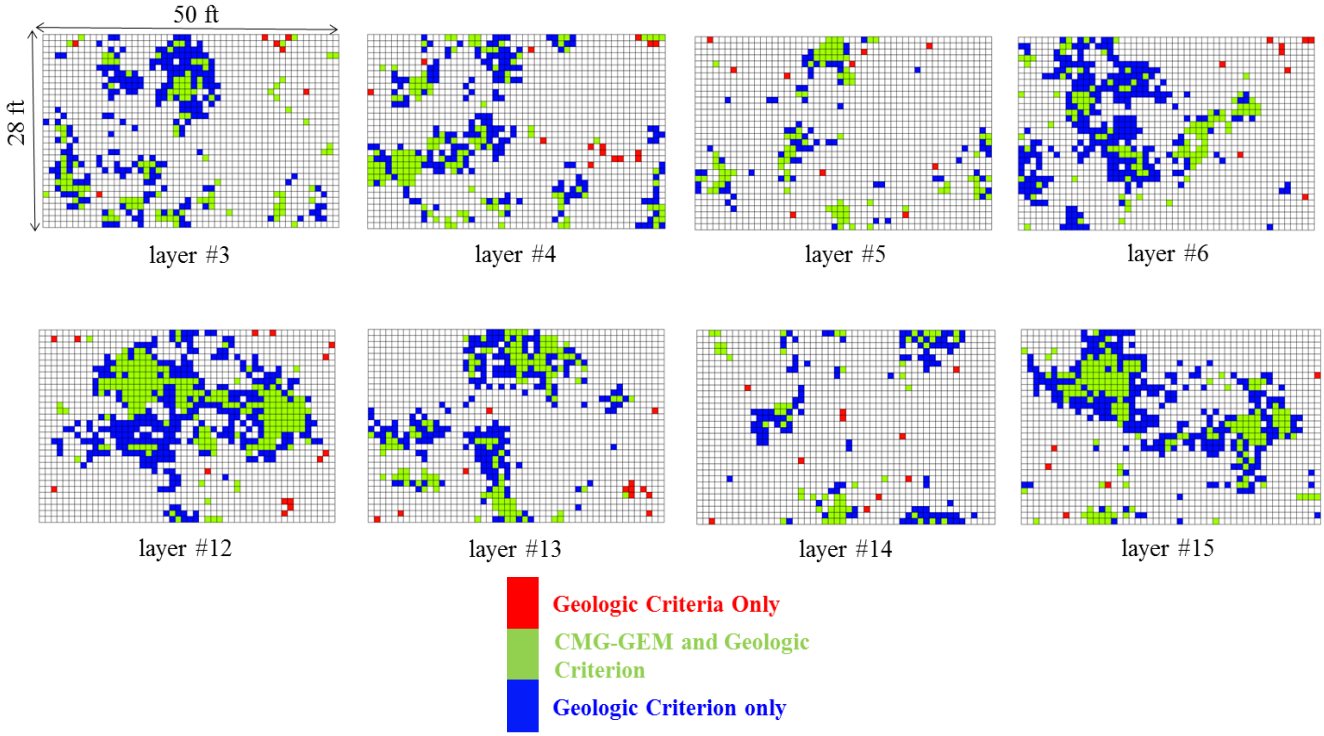

Fig. 4-15 Comparison of LCT predictions between CMG-GEM and the geologic criterion at a threshold CCEP of 1.1 psi. For comparison, the top four layers with CO_2 accumulation beneath the seal and the right fourteen columns were excluded. In a previous study (Saadatpoor 2012) on *buoyant flow*, CCEP at 1.0 psi was shown to give a good prediction of the LCT amount, but the prediction of LCT locations are bad. However, this study shows that, the threshold CCEP (1.1 psi) gives a good prediction of local capillary trapping amount as well as its spatial distribution, as compared to CMG-GEM with *viscous flow* incorporated.

The above LCT comparison is for a 3D capillary entry pressure field with a fixed auto-correlation length. As demonstrated in 2D, both standard deviation and auto-correlation influence the LCT amount. More 3D sensitivity studies on these parameters might be necessary to further examine the geologic criterion.

However, 3D numerical simulations using CMG-GEM is computationally intensive; it takes about 119 hours to complete the above 3D run. Additionally, convergence problem occurs more frequently in 3D runs than in 2D, mainly because more discontinuities of phase pressure

and saturation are involved in 3D. Additionally, the complicated dynamics of buoyant flow and reservoir heterogeneity also increase computational intensity. Thus, we did not conduct sensitivity studies in 3D, but this should not compromise the extended application of the geologic criterion. This is because the controlling physics on LCT hold the same in 2D as in 3D; the added one more dimension mainly enhances the connectivity of LCT clusters as demonstrated in chapter 6.

4.7 COMPARISON OF COMPUTATIONAL TIME BETWEEN CMG-GEM AND THE GEOLOGIC CRITERION

Table 4-4 shows CPU seconds used to find LCT cells for the two methods: CMG-GEM and the geologic criterion. The geologic criterion finds LCT cells much faster than CMG-GEM: The cost of the geologic criterion was around 20 sec in identifying LCT for both 2D and 3D, whereas, the cost of CMG-GEM is about four orders of magnitude longer. The computational advantage of the geologic criterion is pronounced in 3D models with more grid blocks involved.

Table 4-4. CPU seconds used for finding LCT for 2D and 3D models

Parameter	2D	3D
Model dimensions	400 × 100	64 × 32 × 32
Grid block size, ft	1 × 1	1 × 1 × 1
CMG-GEM CPU time, *sec*	10800	428400
Geologic criterion CPU time, *sec*	12.5	22.2

The fast computation of the geologic criterion algorithm is attributed to the reduced physics considered in establishing local capillary trapping. The geologic criterion identifies flow paths and flow barriers using a static indicator (i.e., CCEP). Instead, CMG-GEM models both viscous and buoyant dynamic flow, and meanwhile the processes of filling local capillary traps and possible spilling are simulated as well. Overall, the geologic criterion achieves a cost-effective approximation of LCT capacity.

4.8 DISCUSSION

The discrepancy in LCT predictions between CMG-GEM and the geologic criterion is further discussed here. It can be explained in three aspects: (1) time-scale, (2) relevant physics, and (3) boundary conditions.

(1) In CMG-GEM, local capillary trapping cells are extracted from a CO_2 saturation field at 50 yrs of buoyant flow. At this time, average CO_2 saturation still changes with time at a speed of 0.001~0.002/yr as quantified above. Thus, local capillary trapping identified from CMG-GEM is at a quasi-equilibrium state. However, the geologic criterion models the equilibrium state of local capillary trapping at an infinite time.

(2) Since *CCEP* is a static indicator of a flow path or a barrier, the geologic criterion is able to approximate LCT capacity directly from a given capillary entry pressure field. After detecting the clusters of LCT cells surrounded by barriers, the algorithm identifies the possible spill point determined by the topology of a cluster of barriers (recall step 3 of the algorithm). Nevertheless, whether this cluster of barriers is capable of sustaining the whole column of a LCT cluster is unknown, in other words, this LCT column might create a buoyant force that is larger than the capillary entry pressure of the surrounding barriers. Instead, CMG-GEM mimics the slow buoyant flow under the interaction of buoyancy and capillary pressure, and it captures the dynamic filling and spilling processes and the complicated change of CO_2 saturations in local capillary trapping.

(3) In CMG-GEM, the right boundary is set to be open while the other boundaries are closed. However, the geologic criterion assumes a closed boundary, this means boundaries act as barriers. This can cause an overestimation of LCT. We will elaborate this point in chapter 5.

4.9 SUMMARY

Full-physics simulation on viscous and buoyant flow incorporating capillary heterogeneity is computationally intensive. A fast geologic criterion algorithm developed by Saadatpoor (2012) is extended here to predict the amount and distribution of local capillary

trapping. The algorithm assumes a critical capillary entry pressure (CCEP) and searches for the clusters of local capillary traps in a storage domain. However, the previous study by Saadatpoor (2012) shows that the algorithm predicts 'false' local capillary trapping as compared to full-physics simulation of *buoyant flow*. Additionally, the previous study did not provide a guidance of selecting CCEP. This chapter addresses the two issues by introducing *viscous flow* into the CO_2/brine displacement dynamics through an injector.

In this chapter, we first employ CMG-GEM to conduct flow simulation. A large CO_2 injection rate (N_{gr}~0.05) is used to assure CO_2 fully sweeps a storage domain. The following post-injection period is long enough to allow for a complete charging of local capillary traps. Then, we extract LCT in a CO_2 saturation field and compare them to the LCT predicted from the geologic criterion. This permits identifying a physically representative CCEP. We demonstrate that a threshold CCEP in the algorithm gives a close upper bound estimation of local capillary trapping amount. The small overestimation of local capillary trapping by the algorithm is attributed to factors of time-scale, relevant physics, and boundary conditions. More importantly, at threshold CCEPs, the algorithm gives a good prediction of local capillary trapping locations.

Overall, we extend the applicability of the geologic criterion in identifying local capillary trapping that occurs when *viscous flow* is incorporated into CO_2 sequestration modeling.

Chapter 5: Local Capillary Trapping Capacity in Infinite Systems

In the last chapter, the geologic criterion treats the lateral sides of a domain as impermeable barriers for local capillary trapping. This treatment causes an overestimation of the LCT amount. One way of removing the boundary artifact is to employ a large-size system, but it is unknown that how large the system should be. The other way is to employ a 'periodic LCT boundary' to mimic an effectively infinite domain. The periodic LCT boundary means, when a LCT cluster exits from one side of the domain, it is connected to the LCT cluster exiting from the other side correspondingly. This is a general way of mimicking behaviors of the infinite system, and it has been traditionally used in the fields of percolation theory (Wilkinson 1984, Behseresht et al. 2009) and molecular dynamics (Wang et al. 2016).

We adopt both methods, but our analysis will be mainly restricted to the period LCT boundary. We examine the impact of LCT boundary types on the LCT amount in both 2D and 3D synthetic domains. By measuring LCT amounts in a series of systems with the increasing size, we identify the representative system size that is completely unaffected by boundary conditions. Then, we demonstrate that the interaction between boundary types and auto-correlation lengths largely affects LCT volume.

Next, we apply the above algorithm (with the periodic LCT boundary) to realistic geologic fabrics. We estimate the range of LCT capacities in various types of facies typical of clastic storage domains. Based on this, we develop a comprehensive LCT capacity predictor representing a wide range of facies and fabrics. Finally, we compare our results to the published invasion percolation results and discuss the differences and common features.

5.1 CLOSED VS. PERIODIC LCT BOUNDARY

When the lateral boundaries are treated as barrier cells, it causes an artifact of flow barriers to CO_2. We call this type of boundary as a 'closed LCT boundary'. In this study, we remove this artifact by introducing a 'periodic LCT boundary'. Figure 5-1 shows a schematic explanation of the difference between the closed LCT and periodic LCT boundaries. Recall using

the geologic criterion requires three steps to find LCT cells. Step 1 is the same for both boundary types and not shown in the figure. Changes occur in step 2 and 3.

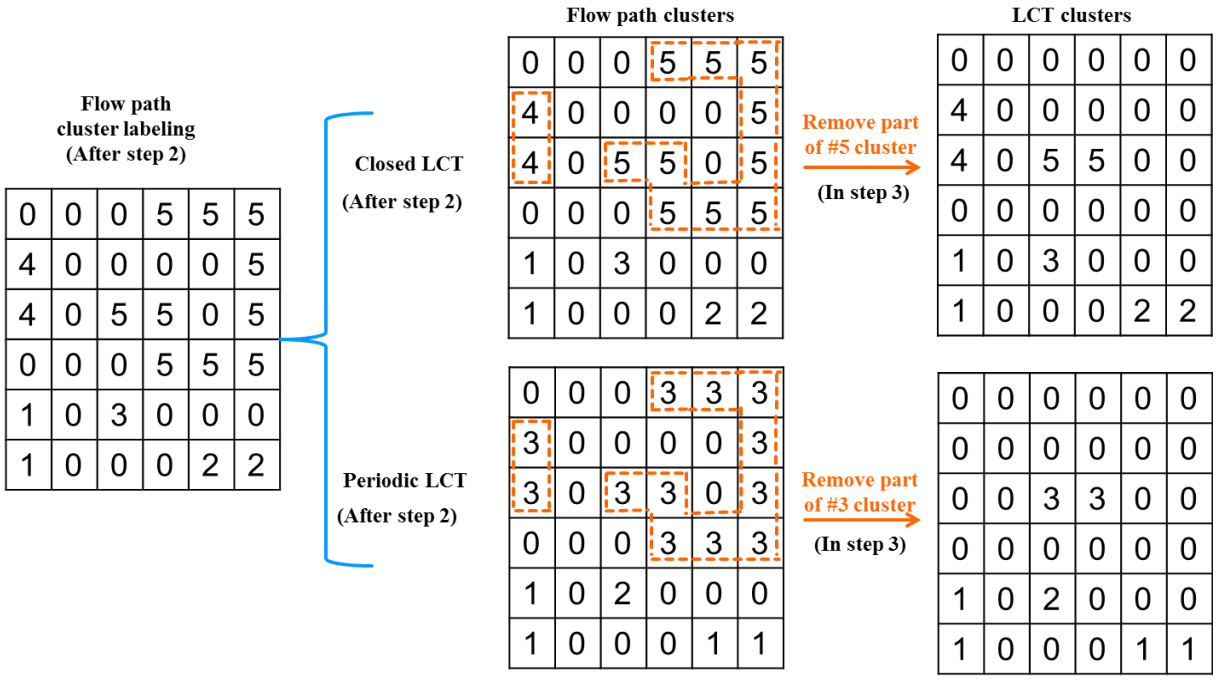

Fig. 5-1 Schematic illustration of the differences between the closed and periodic LCT boundaries. Dashed lines show the numbering change of flow path clusters connected to the cells in the top layer, when the closed LCT boundary is changed into the periodic one.

In step 2, the algorithm identifies the clusters of flow paths. In Fig. 5-1, the number '0' represents a cell of flow barrier, and the other non-zeros represent flow paths. The number of non-zero labels the ID of a cluster, and the corresponding counting represents the size of this cluster. Take the closed LCT boundary for example, a total of five clusters of flow paths are identified and the cluster ID is labeled from one to five in step 2.

In step 3, LCT cells are identified through removing all the flow path cells connected to the top layer meanwhile also keeping the cells surrounded by barriers from both the top and sides. For example, in the case of closed LCT boundary, some cells in the flow-path cluster #5 are discarded because they are connected to the top layer. Meanwhile, other cells of the cluster

are left inside the domain because they are surrounded by barriers. These remaining cells are local capillary traps.

For the periodic boundary, three changes have been made compared to the closed LCT boundary:

(1) In step 2, the flow path cluster exiting from the right boundary is correspondingly connected to the cluster exiting from the left boundary. These two clusters become one. For example, clusters #4 and #5 in the closed LCT boundary become one single cluster (#3, dashed lines) in the periodic LCT case, cluster #1 and #2 are also merged together. Thus, a total of three clusters of connected flow paths are identified for the periodic LCT boundary, whereas, five clusters are observed for the closed LCT boundary.

(2) In step 3, the number of flow path cells that are removed is different for the two boundary types. For example, cluster #4 is a flow path cluster and also act as a LCT cluster for the closed LCT boundary. However, in the periodic LCT, this flow path cluster is merged into a large cluster #3, which is connected to the top layer. Thus, parts of the cluster #3 in the periodic case (corresponding to the cluster #4 in the closed case) are removed and cannot act as LCTs.

(3) In step 3, both LCT cluster size and numbering are altered when LCT boundaries are changed. For example, in the closed LCT boundary, the flow path clusters #1 and #2 become two different LCT clusters in step 3. However, in the periodic LCT, they are merged as one single flow path cluster #1 in step 2, and then act as one single LCT cluster #1 in step 3.

Based on the above analysis, one would expect that, compared with a closed LCT boundary, a periodic LCT boundary would yield (1) a less LCT volume; (2) a small number of LCT clusters; (3) a possible larger size of LCT clusters. The periodic LCT is created only on the lateral boundaries (i.e., left, right, front, and back faces).

5.2 GENERATION OF CAPILLARY ENTRY PRESSURE FIELDS

5.2.1 Purely synthetic capillary entry pressure fields

We employ a fast Fourier transformation (FFT) technique (Jennings and Ward 2000) to directly generate capillary entry pressure fields. One of the main disadvantages of the method is that realizations have periodic boundaries. This means that the boundaries in the opposite directions are artificially auto-correlated. The natural system should be closed, i.e., without spatial auto-correlation between boundaries. A closed system is obtained through making a field realization larger than required and discarding boundary regions. Such a sub-sampled field might not exactly maintain the original values of geostatistical parameters (i.e., mean, standard deviation, and auto-correlation length), but they are very close.

Figure 5-2 shows one realization example of a series of capillary entry pressure fields with different horizontal auto-correlation lengths. Figure 5-3 shows capillary entry pressure fields auto-correlated in both horizontal and vertical directions. Table 5-1summarizes the properties of the simulated capillary entry pressure fields. These properties are system sizes, standard deviation (σ), horizontal dimensionless auto-correlation length (λ_{Dx}), and vertical dimensionless auto-correlation length (λ_{Dz}). The auto-correlation length (λ) is made dimensionless by scaling it to the system length in the corresponding direction. λ measures how well neighboring values of capillary entry pressure are related to each other. With increasing λ, the spatial distribution of a capillary entry field becomes auto-correlated with long-range features, and sedimentary formations become layered. Qualitatively, λ relates to depositional facies and environments (Waggoner et al. 1992). For example, a high-energy environment, such as valley fills, would create small horizontal auto-correlation length (λ_x), whereas, a low-energy environment, such as marine bar, tends to have large λ_x (Exum and Harms 1968). An example in between is the shallow-water platform, which gives a short-range of λ_x (Jennings and Ward 2000). λ_{Dx} can be as large as 2. The typical λ_{Dz} is about 0.05. Grid size is 1×1 ft, and the mean of capillary entry pressure (μ) is constant at 3.0 psi. In two-dimensional systems, three realizations are generated for both uncorrelated and auto-correlated capillary entry pressure fields.

Table 5-1. Properties of synthetic capillary entry pressure fields

Model	N_x	N_y	N_z	λ_{Dx}	λ_{Dz}	σ, psi	Figure
2D	256	1	256	0	0	2.0	5-8
2D	256	1	256	0.125	0	2.0	5-9
2D	32	1	32	0	0	2.0	5-10
2D	128	1	128	0	0	2.0	5-10
2D	512	1	512	0	0	2.0	5-10
2D	256	1	128	0	0	2.0	5-11
2D	256	1	64	0	0	2.0	5-11
2D	256	1	32	0	0	2.0	5-11
3D	16	16	16	0	0	2.0	5-12
3D	64	64	64	0	0	2.0	5-12
3D	128	128	128	0	0	2.0	5-12
2D	256	1	256	0	0	0.4~3.6	5-13
2D	256	1	256	0~0.5	0	2.0	5-14~5-18
2D	256	1	256	0~0.5	0.25	2.0	5-19
3D	128	128	128	0~0.25	0	2.0	5-20
3D	128	128	128	0~0.25	0.125	2.0	5-21
2D	256	1	256	0	0~0.5	2.0	5-22
2D	256	1	256	0.25	0~0.5	2.0	5-23, 5-24

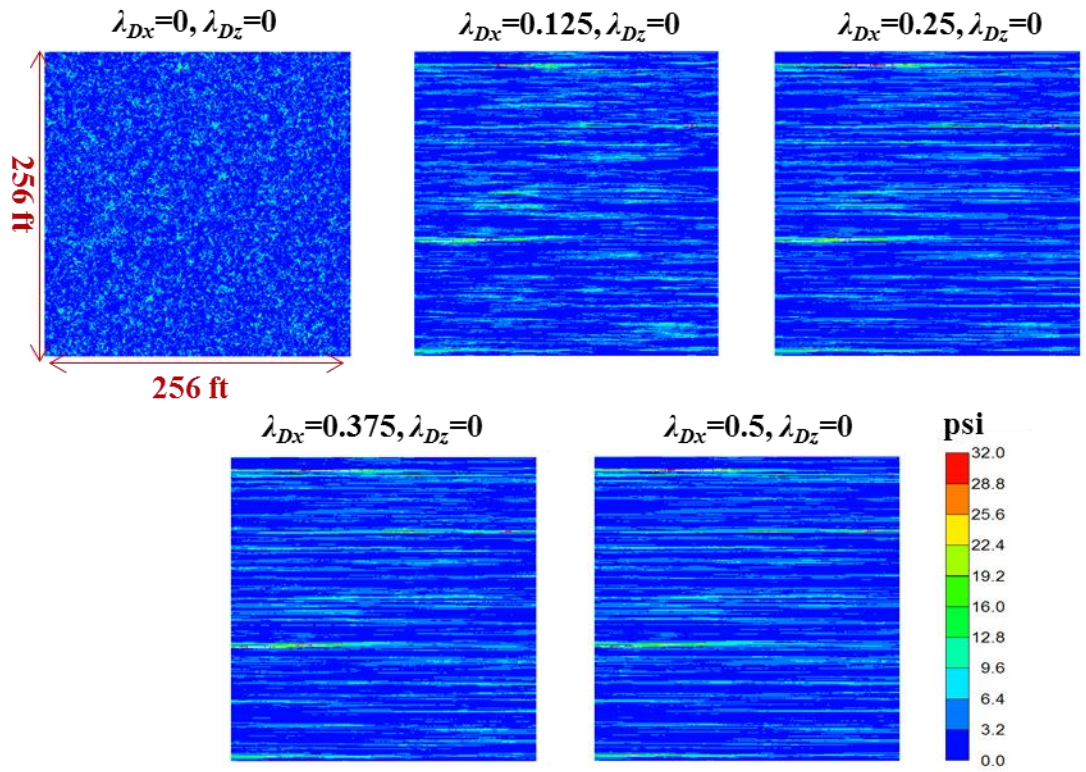

Fig. 5-2 Capillary entry pressure fields with zero vertical auto-correlation lengths and different horizontal auto-correlation lengths. μ=3 psi, σ=2 psi.

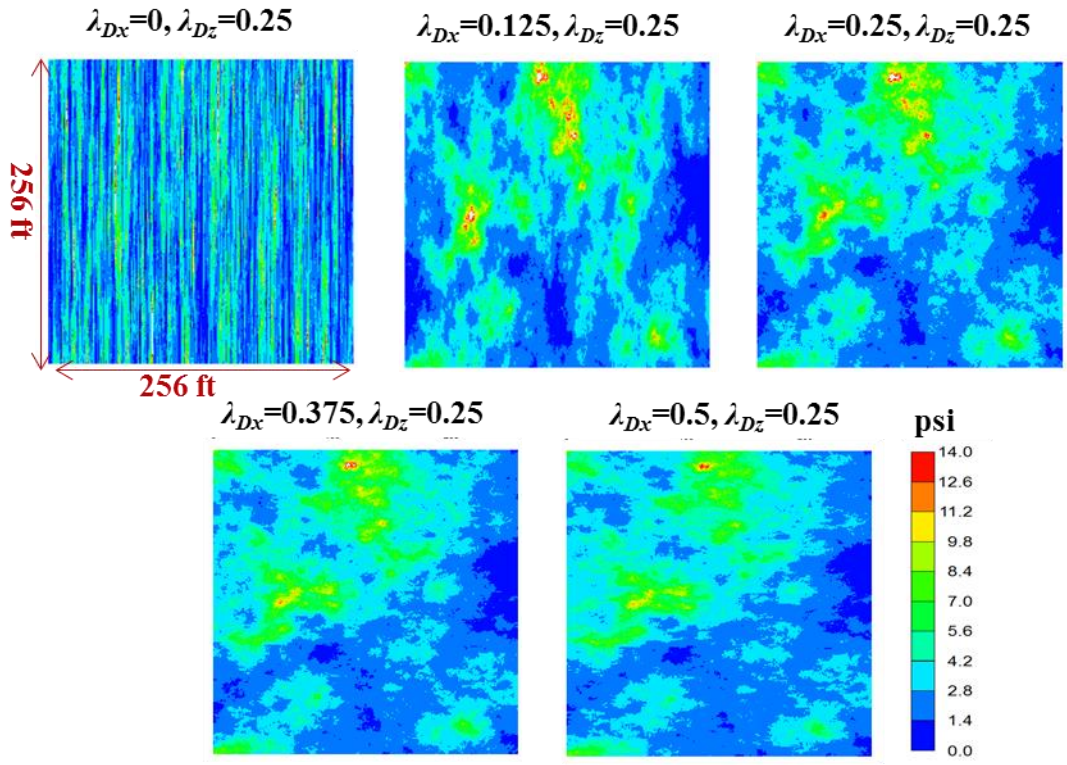

Fig. 5-3 Capillary entry pressure fields with a constant vertical auto-correlation and different horizontal auto-correlation lengths. μ=3 psi, σ=2 psi.

5.2.2 Realistic geologic fabrics

Two types of realistic geologic media (Meckel et al. 2015, Ganesh 2012) are studied: (1) fabrics are generated geostatistically, and then assigned with real sedimentary facies typical of clastic reservoirs; (2) a digital capillary entry pressure fields converted from a real field peel sample.

5.2.2.1 Synthetic fabrics with real sedimentary facies assigned

Figure 5-4 shows synthetic fabrics with different horizontal auto-correlation lengths. System dimensions are 200×200 with cell size of 1×1 ft. Vertical auto-correlation length is set as the cell size. White and black colors represent the relative magnitude of capillary entry pressure, and the spatial distribution of colors is controlled by the horizontal auto-correlation length.

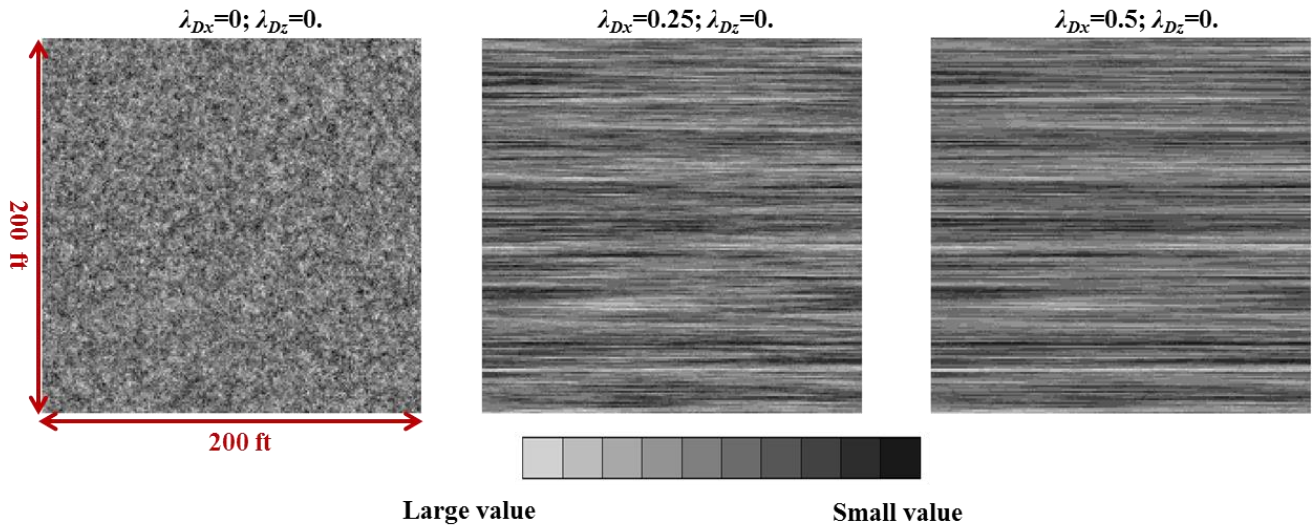

Fig. 5-4 Geostatistical model fabrics with different horizontal auto-correlation lengths. The relative light brightness represents different values of a given parameter (e.g., capillary entry pressure). The black area represents a high value while the light white area has a low value.

Next, real textures are assigned to each fabric (Ganesh 2012). The Beard and Weyl (1973) table is used to generate the real different textures. They represent a wide range of clastic depositional processes and environments. The table is embedded in Fig. 5-5 with a column representing a grain size and a row recording a sorting factor. Sorting factors are given in terms of the Trask coefficient (S_o) and krumbein phi scale (φ). As the Trask coefficient increases, or from the upper to the bottom of the table, the texture moves from the extremely well-sorted to the very poorly-sorted. The grain size decreases from the left to the right column, meanwhile, the classification changes from the coarse upper sand to the coarse upper silt.

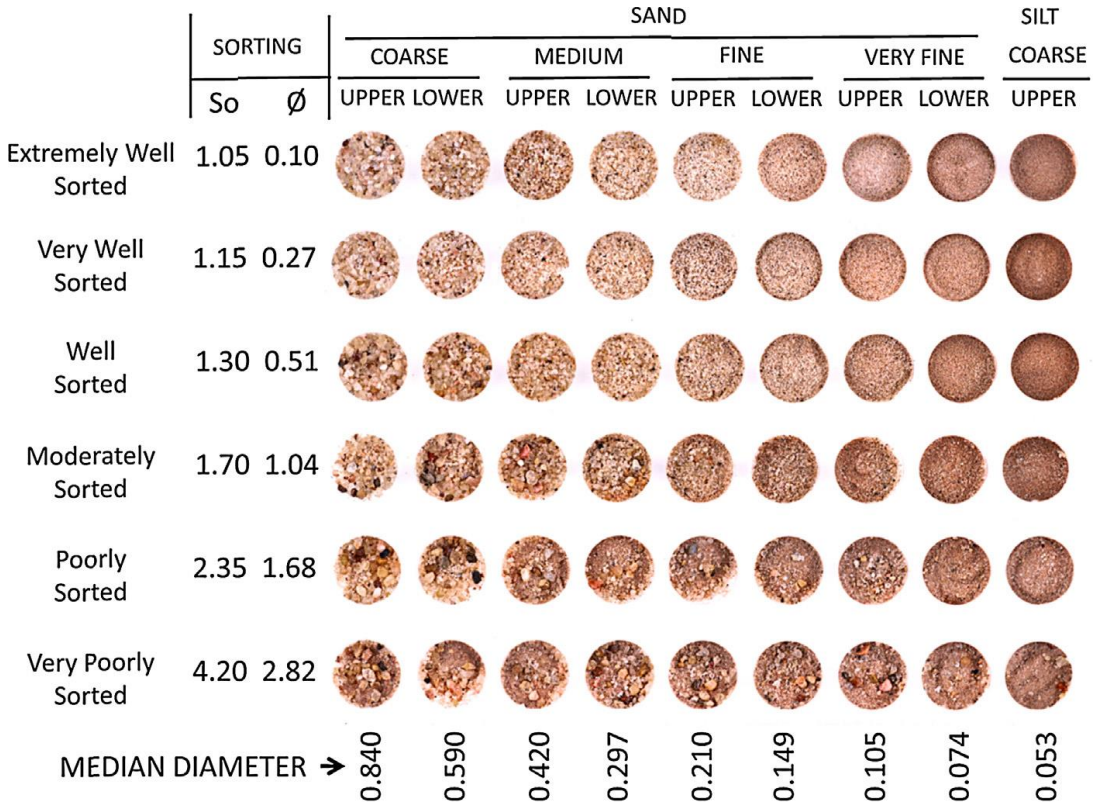

Fig. 5-5 54 modeled facies comprised of nine different grain sizes and six sorting factors. These facies are characteristic of a wide range of clastic depositional processes and environments. For example, several textures in the upper right corner represent the point bar sedimentary facies. S_o is the Trask sorting coefficient, $S_o=(D_{75}/D_{25})^{0.5}$, D_{75} is the grain diameter corresponding to the cumulative grain size frequency of 75% while D_{25} is at the cumulative frequency of 25%. φ is the Krumbein phi scale defined as the negative log base 2 of the grain diameter in mm (Beard and Weyl 1973, Meckel et al. 2015).

To use the table, a grain size should be converted into a capillary entry pressure. We use the simple Berg equation (Berg 1975) to calculate capillary threshold pressure. $P_c = 16.3 \times IFT/D$. In the above, *IFT* is interfacial tension (N/m), *D* is the grain diameter (mm). The *IFT* between CO_2 and brine water was set to be 30 mN/m. Details of generating grain size distributions and capillary threshold pressure fields have been described in the previous work (Ganesh 2012).

Table 5-2 summarizes properties of the 54 facies grouped by sorting factors. Each facies is assigned onto three geologic fabrics, so a total of 162 geologic models are generated. Figure 5-

6 shows the examples of capillary threshold pressure fields for the very poorly-sorted upper-coarse sand and extremely well-sorted upper-coarse silt. These fields have different anisotropies. The anisotropy here is defined as the ratio of horizontal to vertical auto-correlation lengths.

Table 5-2. Properties of 54 facies. The left column shows abbreviated names for the 54 facies. For example, EWUCSa represents the **e**xtremely **w**ell-sorted **u**pper **c**oarse **s**and. VPUCSi is the **v**ery **p**oorly-sorted **u**pper **c**oarse **s**ilt. The top row lists the statistical parameters of a capillary threshold field. P_{thmax} is the maximum capillary entry pressure, P_{thmin} is the minimum, $<P_{th}>$ is the arithmetic mean, ΔPth is the difference between the maximum and minimum, σP_{th} is the standard deviation of capillary entry pressure.

SampleName	Sorting mid ø	Sorting upper ø	Sorting lower ø	Pthmax	Pthmin	<Pth>	ΔPth	σPth
EWUCSa	0.1	0.19	0	0.696	0.486	0.582	0.21	0.0133
EWLCSa	0.1	0.19	0	0.992	0.693	0.828	0.299	0.019
EWMUSa	0.1	0.19	0	1.393	0.973	1.163	0.42	0.027
EWMLSa	0.1	0.19	0	1.971	1.376	1.645	0.595	0.0375
EWFUSa	0.1	0.19	0	2.787	1.946	2.327	0.841	0.053
EWFLSa	0.1	0.19	0	3.928	2.742	3.279	1.186	0.075
EWVFUSa	0.1	0.19	0	5.574	3.891	4.653	1.683	0.106
EWVFLSa	0.1	0.19	0	7.909	5.522	6.6025	2.387	0.1504
EWUCSi	0.1	0.19	0	11.0422	7.709	9.219	3.3332	0.21
VWUCSa	0.27	0.36	0.19	0.974	0.348	0.582	0.626	0.038
VWLCSa	0.27	0.36	0.19	1.387	0.495	0.828	0.892	0.055
VWMUSa	0.27	0.36	0.19	1.948	0.696	1.163	1.252	0.077
VWMLSa	0.27	0.36	0.19	2.755	0.984	1.645	1.771	0.1085
VWFUSa	0.27	0.36	0.19	3.896	1.392	2.326	2.504	0.154
VWFLSa	0.27	0.36	0.19	5.491	1.962	3.279	3.529	0.216
VWVFUSa	0.27	0.36	0.19	7.791	2.784	4.652	5.007	0.307
VWVFLSa	0.27	0.36	0.19	11.055	3.95	6.601	7.105	0.436
VWUCSi	0.27	0.36	0.19	15.436	5.515	9.217	9.921	0.608
WUCSa	0.51	0.66	0.36	1.53	0.222	0.583	1.308	0.074
WLCSa	0.51	0.66	0.36	2.178	0.315	0.83	1.863	0.105
WMUSa	0.51	0.66	0.36	3.059	0.443	1.166	2.616	0.148
WMLSa	0.51	0.66	0.36	4.3262	0.627	1.649	3.6992	0.209
WFUSa	0.51	0.66	0.36	6.119	0.886	2.332	5.233	0.295
WFLSa	0.51	0.66	0.36	8.623	1.249	3.287	7.374	0.416
WVFUSa	0.51	0.66	0.36	12.237	1.772	4.665	10.465	0.5904
WVFLSa	0.51	0.66	0.36	17.363	2.515	6.619	14.848	0.838
WUCSi	0.51	0.66	0.36	24.243	3.511	9.242	20.732	1.17
MUCSa	1.04	1.36	0.66	4.108	0.083	0.594	4.025	0.165
MLCSa	1.04	1.36	0.66	5.848	0.118	0.845	5.73	0.235
MMUSa	1.04	1.36	0.66	8.215	0.165	1.188	8.05	0.33
MMLSa	1.04	1.36	0.66	11.617	0.233	1.679	11.384	0.467
MFUSa	1.04	1.36	0.66	16.43	0.33	2.375	16.1	0.66
MFLSa	1.04	1.36	0.66	23.156	0.465	3.347	22.691	0.93
MVFUSa	1.04	1.36	0.66	32.86	0.66	4.75	32.2	1.32
MVFLSa	1.04	1.36	0.66	46.625	0.937	6.74	45.688	1.872
MUCSi	1.04	1.36	0.66	65.099	1.308	9.411	63.791	2.614
PUCSa	1.68	1.95	1.36	13.532	0.025	0.622	13.507	0.337
PLCSa	1.68	1.95	1.36	19.265	0.036	0.886	19.229	0.48
PMUSa	1.68	1.95	1.36	27.063	0.05	1.245	27.013	0.674
PMLSa	1.68	1.95	1.36	38.271	0.071	1.76	38.2	0.953
PFUSa	1.68	1.95	1.36	54.126	0.1002	2.489	54.0258	1.348
PFLSa	1.68	1.95	1.36	76.286	0.141	3.508	76.145	1.9
PVFUSa	1.68	1.95	1.36	108.253	0.2004	4.979	108.0526	2.696
PVFLSa	1.68	1.95	1.36	153.602	0.284	7.064	153.318	3.825
PUCSi	1.68	1.95	1.36	214.463	0.397	9.863	214.066	5.341
VPUCSa	2.82	3.42	1.95	114.793	0.003	0.743	114.79	1.406
VPLCSa	2.82	3.42	1.95	163.434	0.004	1.058	163.43	2.001
VPMUSa	2.82	3.42	1.95	229.585	0.0059	1.486	229.5791	2.811
VPMLSa	2.82	3.42	1.95	324.666	0.00835	2.101	324.6577	3.976
VPFUSa	2.82	3.42	1.95	459.171	0.0118	2.972	459.1592	5.623
VPFLSa	2.82	3.42	1.95	647.153	0.0166	4.189	647.1364	7.925
VPVFUSa	2.82	3.42	1.95	918.341	0.0236	5.944	918.3174	11.246
VPVFLSa	2.82	3.42	1.95	1303.05	0.0335	8.434	1303.017	15.957
VPUCSi	2.82	3.42	1.95	1819.35	0.047	11.776	1819.303	22.2793

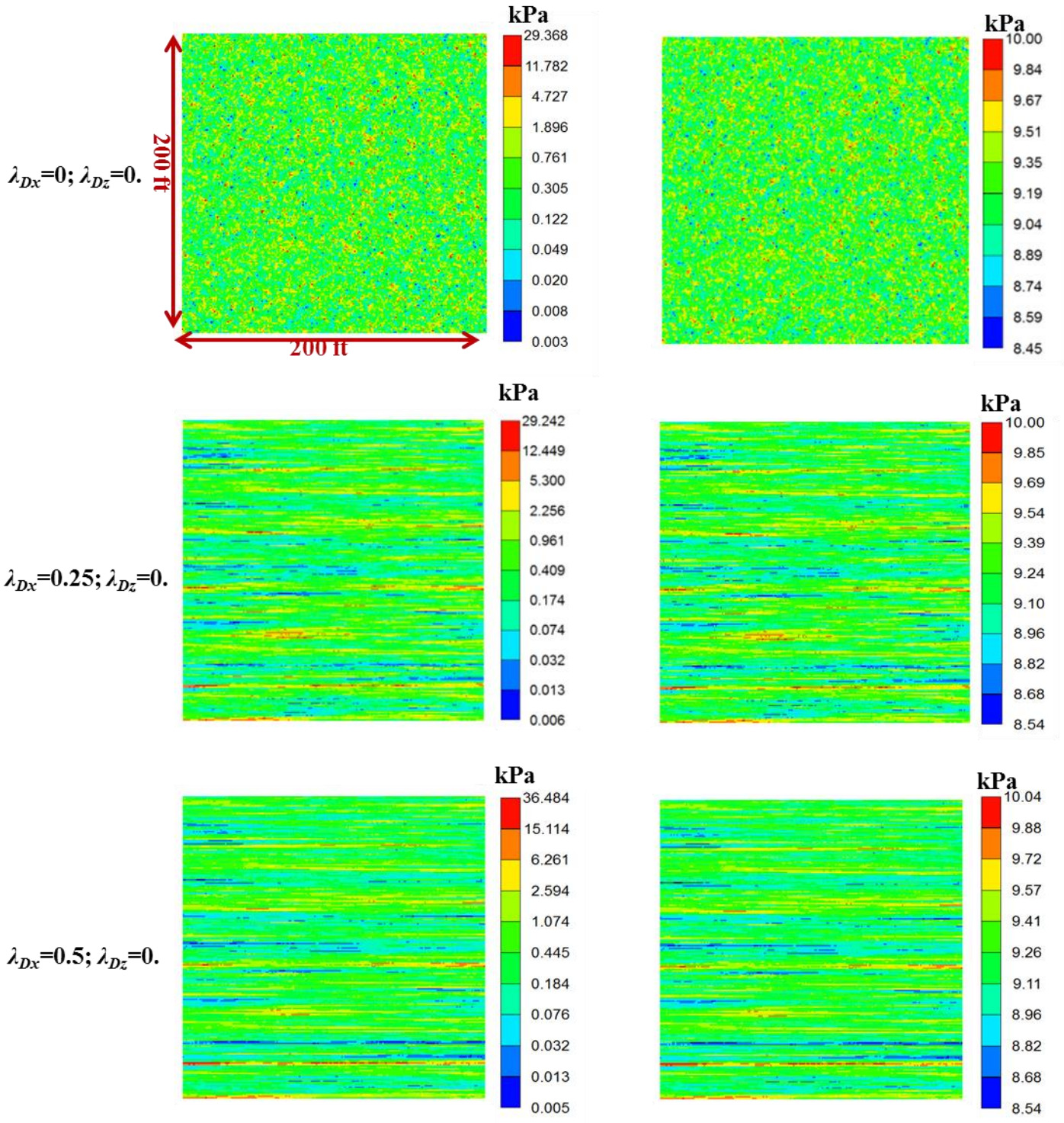

Fig. 5-6 Examples of capillary threshold pressure fields for the very poorly-sorted upper-coarse sand (left column) and extremely well-sorted upper-coarse silt (right column).

5.2.2.2 Digital capillary entry pressure field

A digital or real capillary entry pressure field has been extracted from a naturally occurring geologic field sample (Meckel 2013). This sample (Fig. 5-7a) is from a fluvial sedimentary environment. It broadly consists of centimeter-scale ripple laminated well-sorted lower fine to lower very fine sands. The peel is oriented perpendicular to the dominant depositional flow direction. More information of the sample can be found from Meckel (2013).

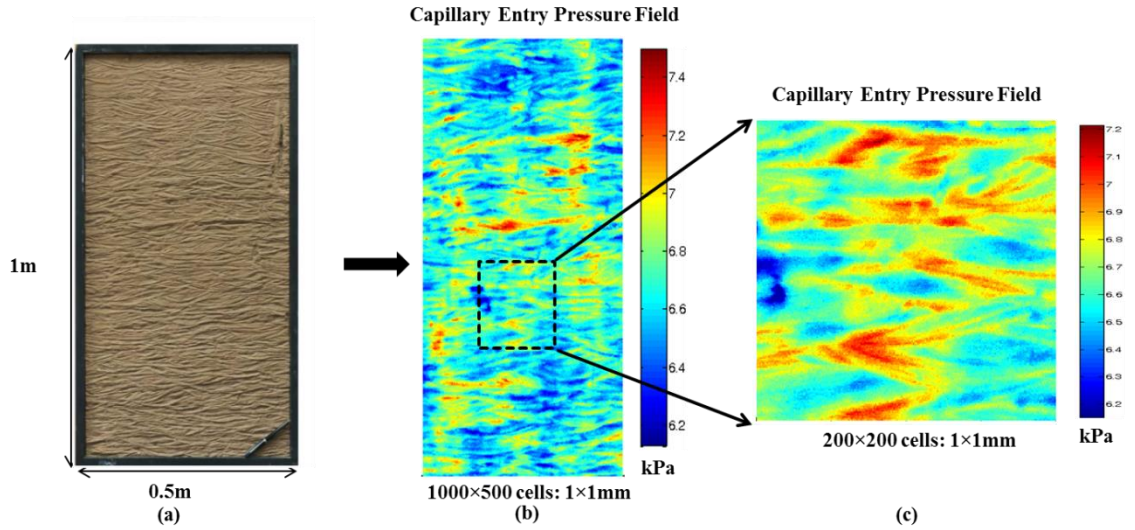

Fig. 5-7 Convert a real geologic sample into a digital simulation model: (a) the real geological peel sample; (b) the converted digital capillary entry pressure field; (c) the subsampled field used for simulations. Adapted from Ganesh (2012).

Next, the geologic peel sample is converted into a digital simulation model. Details of procedures and implementations have been described in the previous work (Ganesh 2012, Meckel 2013). Figure 5-7b shows the converted capillary entry pressure field. The digital model is highly resolved to the depositional resolution with the cell size of 1×1 mm. From the digital field, small-scale crossbedding structures can be clearly observed. We subsample from the whole field and employ a relatively small domain (Fig. 5-7c) to simulate local capillary traps using the geologic criterion algorithm. The domain has the dimensions of 200×200, which are the same as

the above models with real textures. The subsampled capillary entry pressure field conforms to a normal distribution with the mean of 6.70 psi and standard deviation of 0.02 psi. The horizontal and vertical auto-correlation lengths were 26 mm and 14 mm, respectively.

5.3 RESULTS FROM PURELY SYNTHETIC MEDIA

Most of the following analysis will be restricted on 2D systems. Differences between 3D and 2D are highlighted.

5.3.1 Effect of multiple realizations on the LCT amount

Figure 5-8 shows the impact of multiphase realizations of a capillary entry pressure field on the LCT amount in uncorrelated systems. Figure 5-9 shows the results in auto-correlated systems.

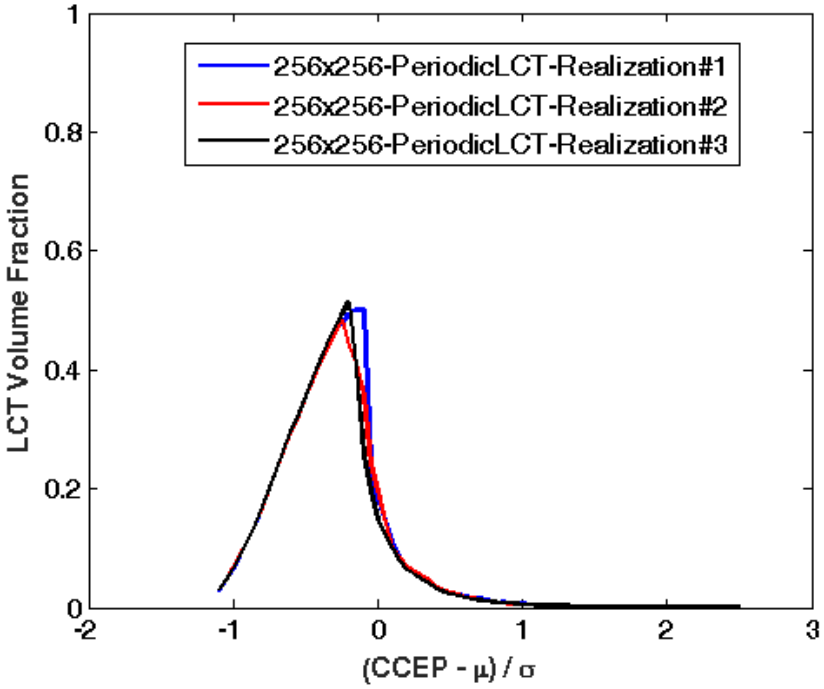

Fig. 5-8 Change of LCT volume fraction with CCEP for the three realizations of a capillary entry pressure field. μ=3 psi, σ=2 psi, λ_{Dx}=0, λ_{Dz}=0.

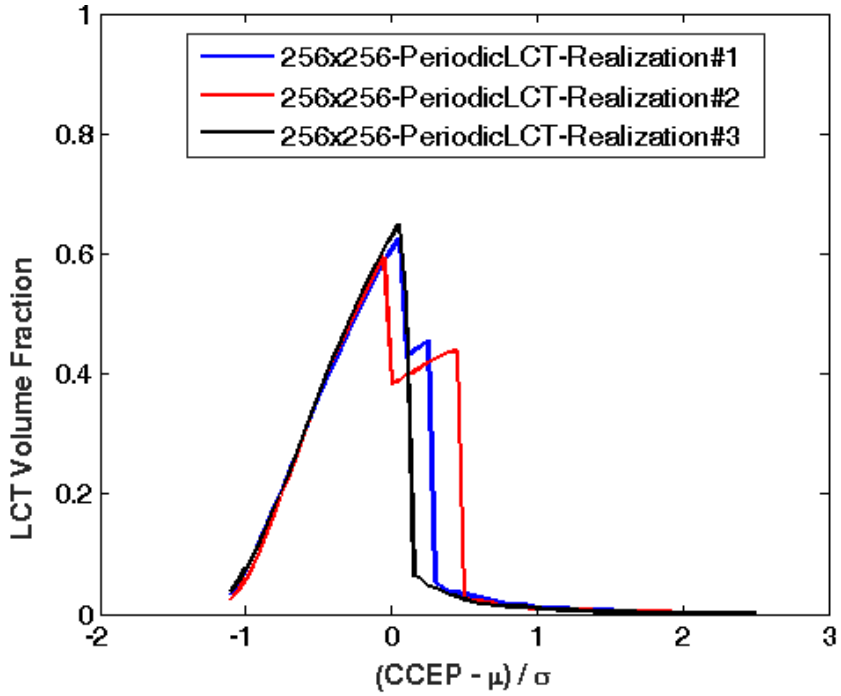

Fig. 5-9 Change of LCT volume fraction with CCEP for the three realizations of a capillary entry pressure field. μ=3 psi, σ=2 psi, λ_{Dx}=0.125, λ_{Dz}=0.

In the uncorrelated media, LCT~CCEP curves overlap for different realizations. This means different realizations have a negligible impact on the LCT volume fraction.

For the auto-correlated media, the LCT amount is subject to the spatial distribution of auto-correlated structures, particularly when CCEP is around a threshold point. At that threshold, flow path structures get connected around a threshold CCEP, and these structures follow the pattern dictated by auto-correlation lengths. As analyzed in section 5.1, the auto-correlated structures of flow paths in the middle part of the domain are more likely to become LCT cells than those close to boundary cells. This results in slightly different LCT capacities for different realizations. As CCEP increases beyond the threshold, the added flow paths become LCTs. As a result, a slight increase in LCT fraction is observed. However, when CCEP becomes much large, more cells become clusters of flow paths. The effect of auto-correlation length on the LCT amount fades, and LCT~CCEP curves for different realizations finally overlap.

Since multiple realizations show a negligible effect on the LCT amount, we employ a single realization in the following study.

5.3.2 Effect of system size on the LCT amount

Figure 5-10 shows the change of LCT amounts with CCEP in uncorrelated systems with different sizes. The solid and dashed lines are for the periodic LCT and closed LCT, respectively. For the 32×32 domain, the closed LCT boundary predicts a slightly larger LCT volume fraction than the periodic LCT does in the large CCEP interval. This is because the boundary cells act as barriers in the closed LCT case. This observation also confirms the schematic analysis in the above section 5.1 that closed LCT boundary overestimates the LCT amount in a small domain.

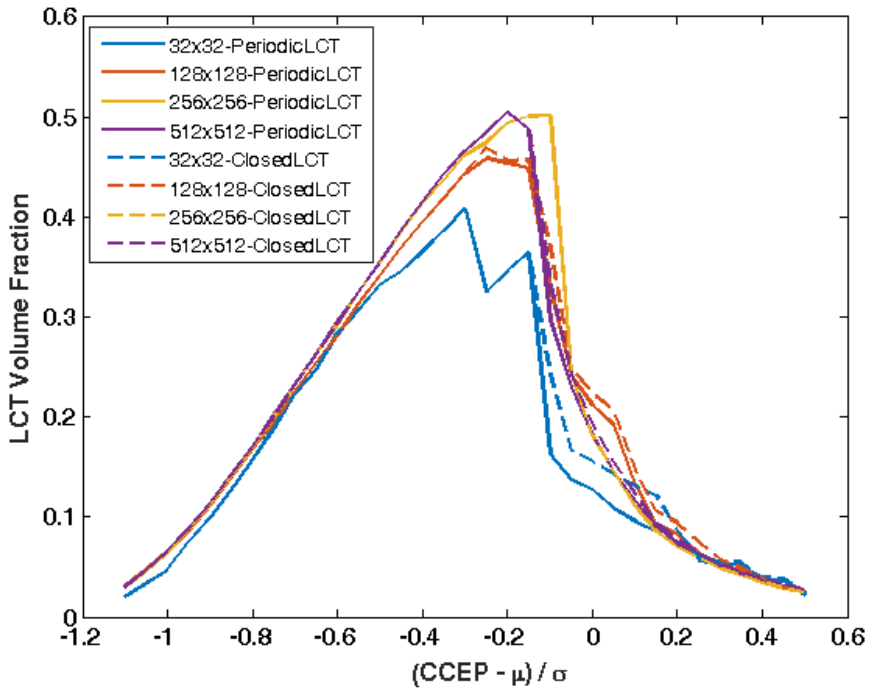

Fig. 5-10 Change of LCT volume fraction with CCEP for 2D uncorrelated media with different sizes. μ=3 psi, σ=2 psi, λ_{Dx}=0, λ_{Dz}=0.

However, as the domain size increases to 256×256 (Fig. 5-10), the periodic LCT curve overlaps the closed LCT curve. This suggests that (1) creating a periodic LCT structure achieves

a similar effect as increasing a system size; and (2) the dimensions of 256×256 was large enough to remove the boundary effect, and therefore, can be used as a 'unit cell'.

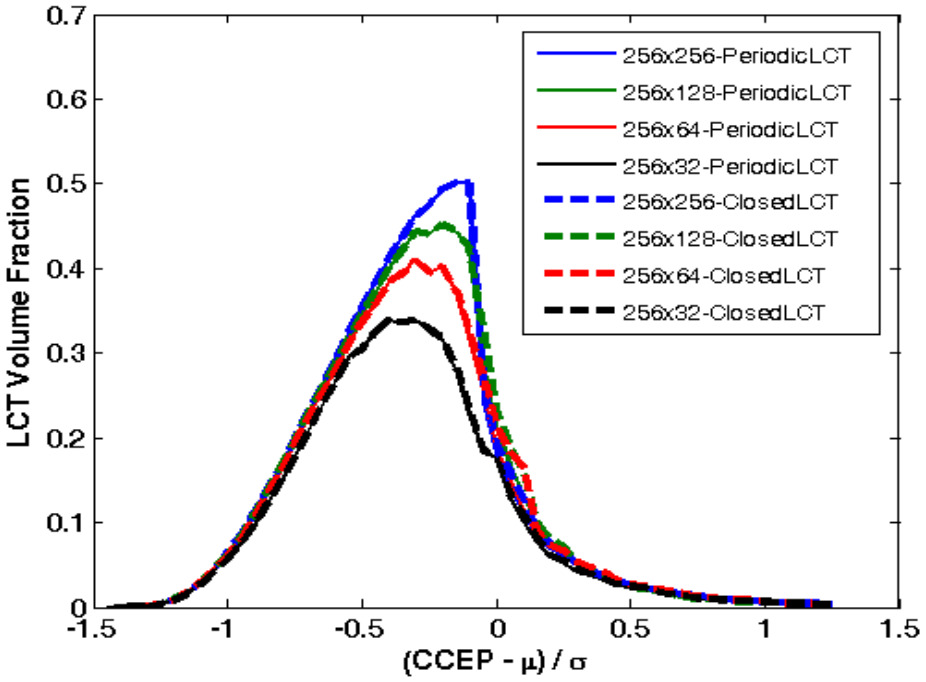

Fig. 5-11 Change of LCT volume fractions with CCEP for 2D uncorrelated media with different domain aspect ratios. μ=3 psi, σ=2 psi, λ_{Dx}=0, λ_{Dz}=0.

Next, the effect of domain aspect ratio on LCT amounts is studied through decreasing the system vertical length. The result is in Fig. 5-11. As the aspect ratio (system horizontal length / system vertical length) increases, the threshold CCEP becomes small, and meanwhile, the maximum LCT volume fraction decreases. The decreased system vertical length causes the connected flow path to percolate at small CCEP, and this small CCEP give rises to a small number of local capillary traps.

For the three-dimensional systems (refer to Fig. 5-12), the representative "unit cell" size can be identified as 128×128×128. Compared to the two-dimensional uncorrelated cases, three main changes occur to LCT~CCEP curves for the three-dimensional cases: (1) the accessible LCT capacity decreases: the maximum fraction was only about 0.17 in 3D, whereas, the fraction

was around 0.5 in 2D; (2) the threshold CCEP becomes small in three-dimensional systems. This is because the added one more dimension enhances the connectivity of LCT clusters; (3) in 3D systems, LCT boundary affects LCT~CCEP curves before CCEP approaches to a threshold point for a small system, whereas, in 2D cases, this boundary effect appears after a threshold point (refer to Fig. 5-10). This is again attributed to a better connectivity of flow path clusters introduced by one more dimension, this, in fact, enables the periodic LCT boundary to act on the LCT amount at small CCEPs.

As one might realize that, the above comparison and explanation invoke part of the percolation theory (Stauffer and Aharony 1992). In the discussion part, we clarify the similarity to and difference from the ordinary percolation theory.

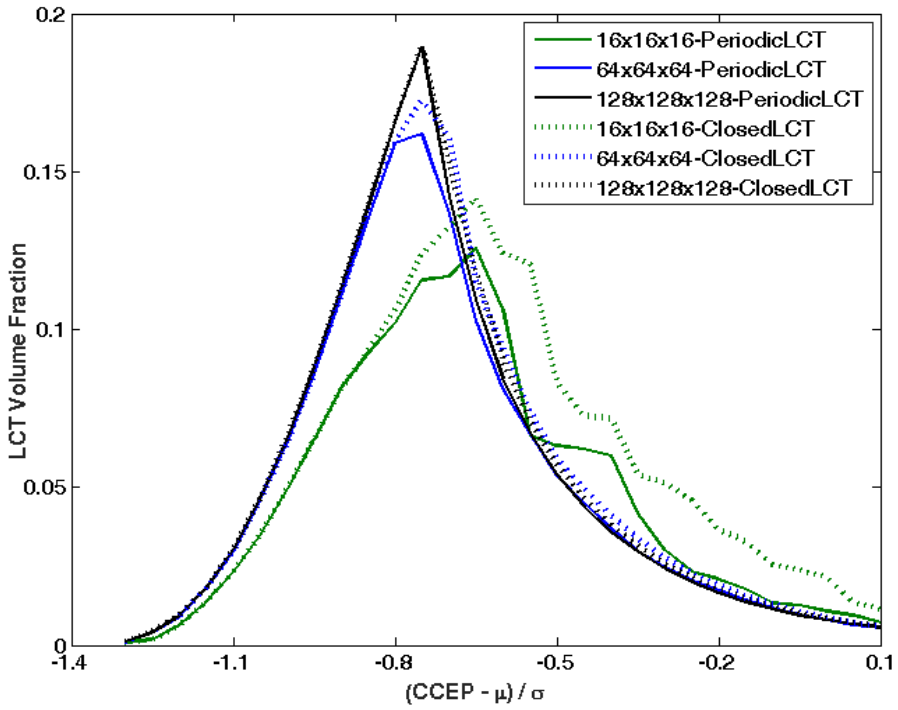

Fig. 5-12 Change of LCT volume fractions with CCEP for 3D uncorrelated media with different system dimensions. μ=3 psi, σ=2 psi, λ_{Dx}=0, λ_{Dz}=0.

5.3.3 Effect of standard deviation of capillary entry pressure on the LCT amount

Figure 5-13 shows the effect of standard deviation on the LCT amount in two-dimensional systems. The maximum point moves to the right as a capillary entry pressure field becomes homogeneous. An increase in standard deviation causes more values smaller than the mean to appear throughout a domain. This increases the possibility that, at small CCEPs, a connected path of flow path cell becomes LCTs. However, standard deviation has a negligible impact on the maximum LCT volume fraction (with small decrease as the decrease in standard deviation), which is always less than 0.50. This value will be discussed later.

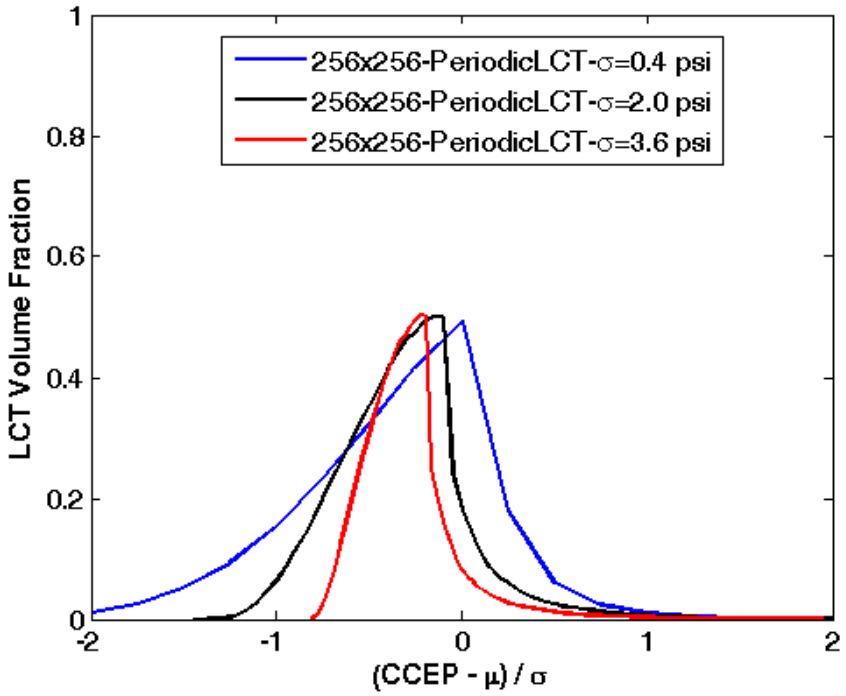

Fig. 5-13 Change of LCT volume fractions with CCEP in uncorrelated systems with different standard deviations of capillary entry pressure. μ=3 psi, λ_{Dx}=0, λ_{Dz}=0.

5.3.4 Effect of the interplay between LCT boundaries and horizontal auto-correlations on LCT

Figure 5-14 shows LCT~CCEP curves for a series of capillary entry pressure fields with different horizontal auto-correlation lengths. When a CCEP is small, all the curves coincide irrespective of auto-correlation lengths. This is because small CCEP give rise to the limited

amount of flow paths and LCT cells, and these flow paths reside inside a domain and have not connected to the top layer.

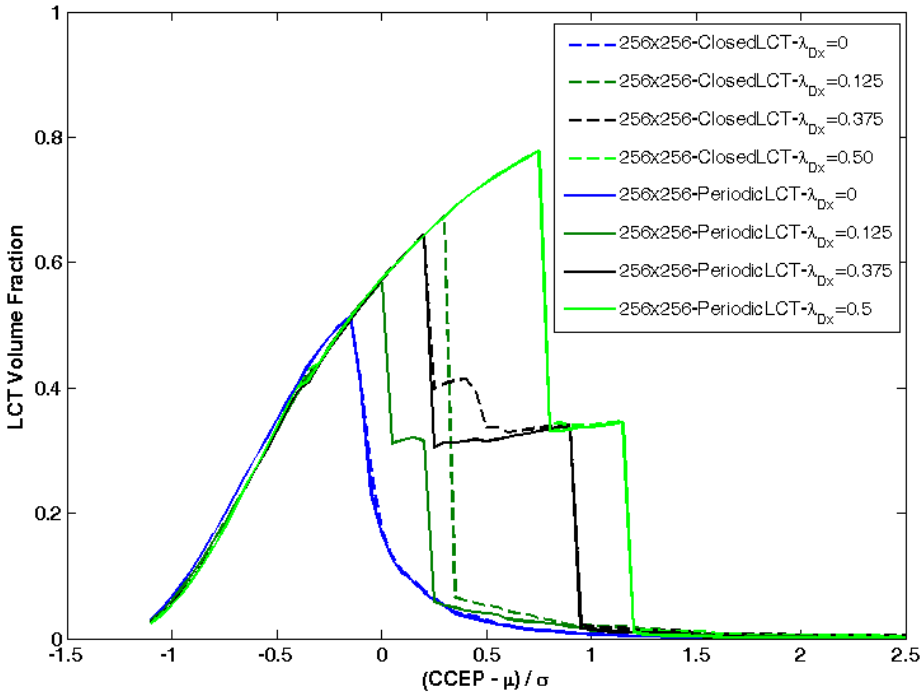

Fig. 5-14 Change of LCT volume fraction with CCEP in auto-correlated systems with different horizontal auto-correlation lengths. μ=3 psi, σ=2 psi, λ_{Dz}=0.

Although the LCT amounts are the same, the spatial distributions of LCT cells are different. This can be directly observed from Fig. 5-15; the locations of LCT cells have already been influenced by auto-correlations even when CCEPs are small.

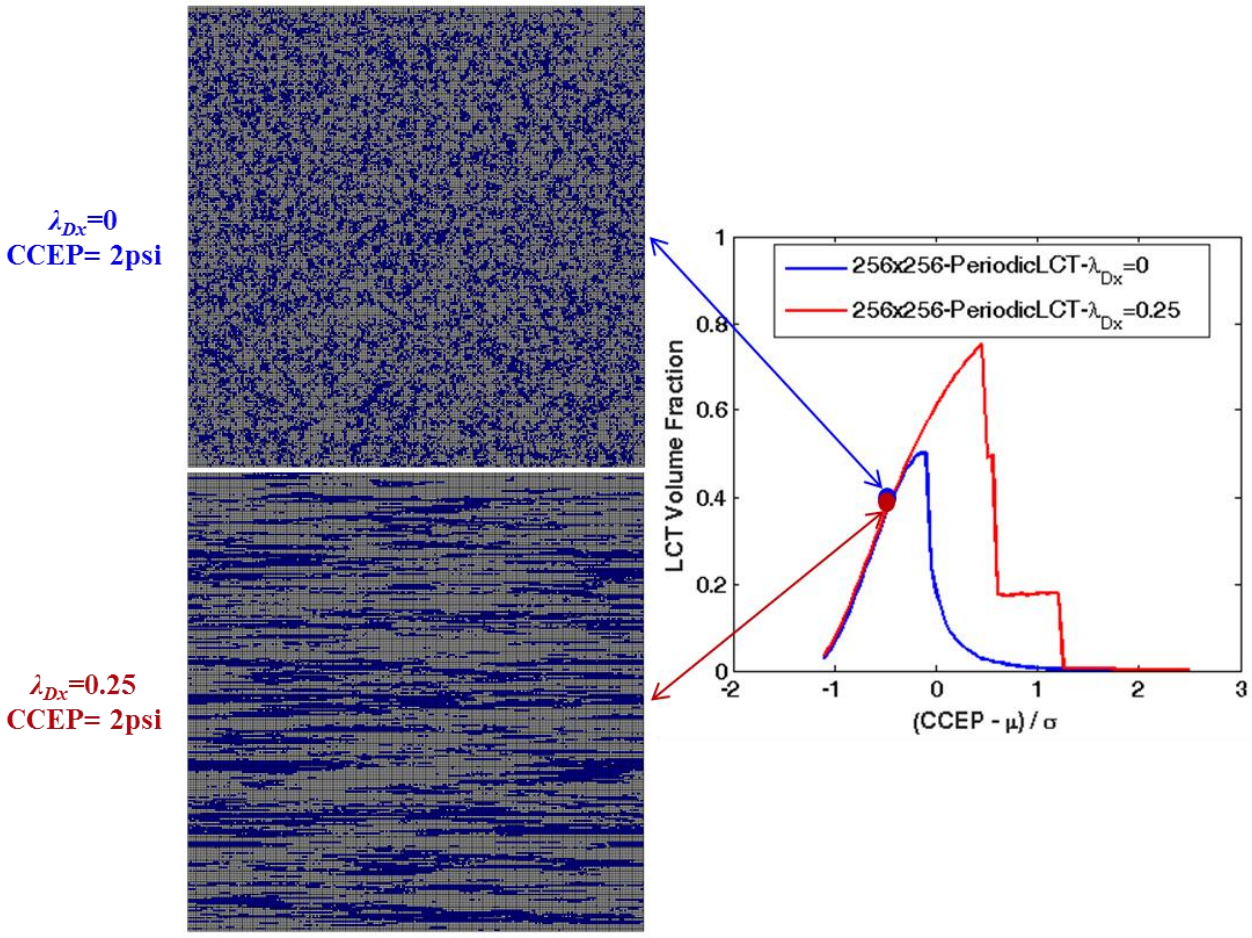

Fig. 5-15 Distributions of LCT cells in capillary entry pressure fields with two different horizontal auto-correlation lengths. μ=3 psi, σ=2 psi, λ_{Dz}=0.

As CCEP approaches a threshold point, the effect of auto-correlation on the LCT volume fraction becomes significant (refer to Fig. 5-14). Two main observations can be made from this figure: (1) the maximum point moves to the right as the horizontal auto-correlation increases. This is because the larger auto-correlation requires more cells to form LCT clusters; and (2) the LCT volume capacity increases with the horizontal auto-correlation length. Such an increase is because auto-correlation creates a layering effect that yields many LCT cells. This can be directly observed from Fig. 5-16; in the auto-correlated systems, both the LCT and barrier cells laterally extend like layers as horizontal auto-correlation length increases, thus, a possible single barrier layer at the top of the domain renders all the flow path cells into LCT cells.

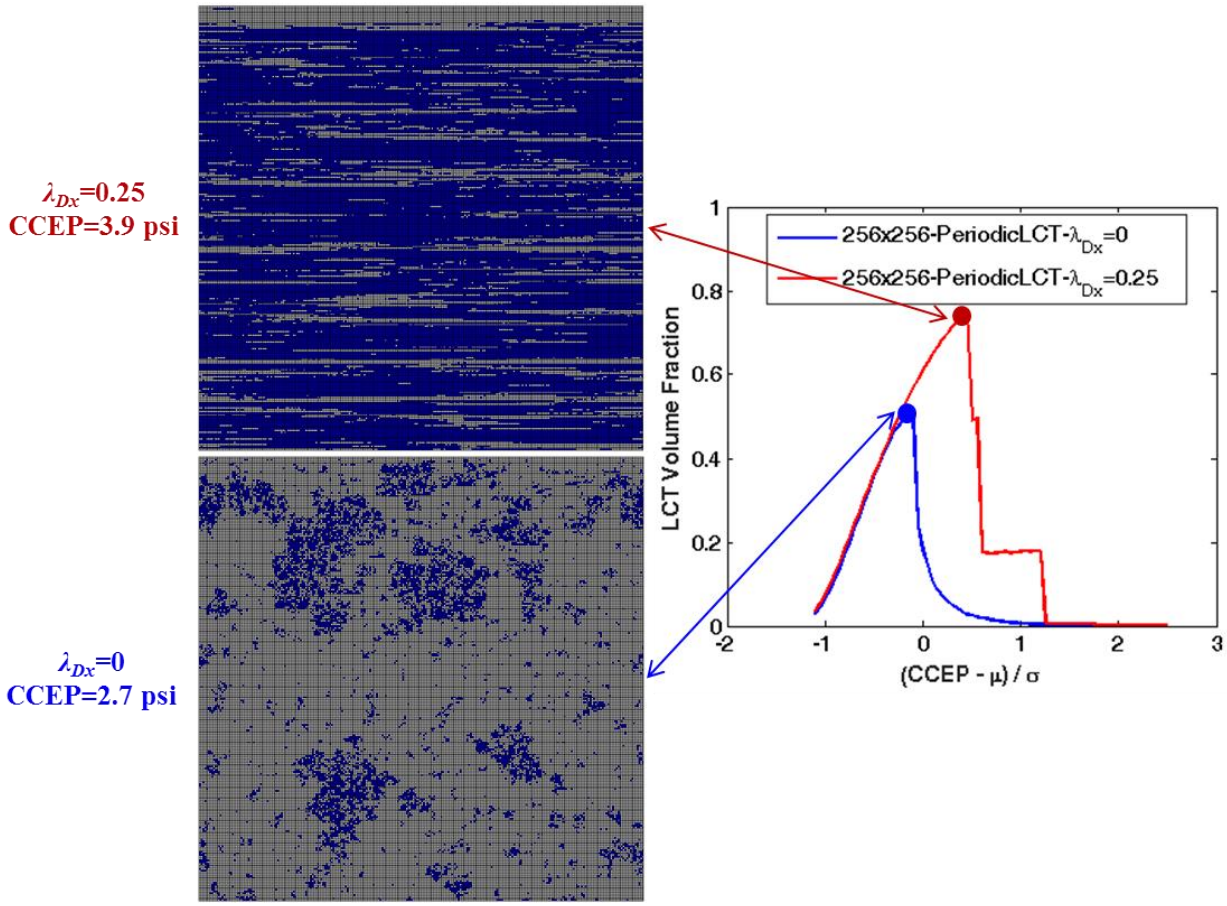

Fig. 5-16 The distribution of periodic LCT at the maximum point of LCT~CCEP curve for two different auto-correlation lengths periodic systems. μ=3 psi, σ=2 psi, λ_{Dz}=0.

Notably, in Fig. 5-16, LCT volume rapidly decreases with increasing CCEP after the maximum point. Such a decrease is pronounced in the auto-correlated systems. This observation can be explained by the spatial distribution of LCT cells at two different CCEPs (refer to Fig. 5-17). Magnitudes of the two CCEPs were very close, one was at the maximum point (CCEP=3.9 psi), and the other was slightly larger (CCEP=4.2 psi). When CCEP is 3.9 psi, barriers spatially separate LCT clusters. However, these barriers are converted into flow paths with a small increase in CCEP, and suddenly flow path clusters become connected to the top layer. Thus, they cannot act as LCTs, which causes a sharp decrease in the LCT amount.

Following the rapid decline, the LCT-CCEP curve shows a plateau. In other words, increasing CCEP has a negligible impact on the LCT amount. This is because the added flow path cells caused by CCEP increasing are connected to the top layer meanwhile.

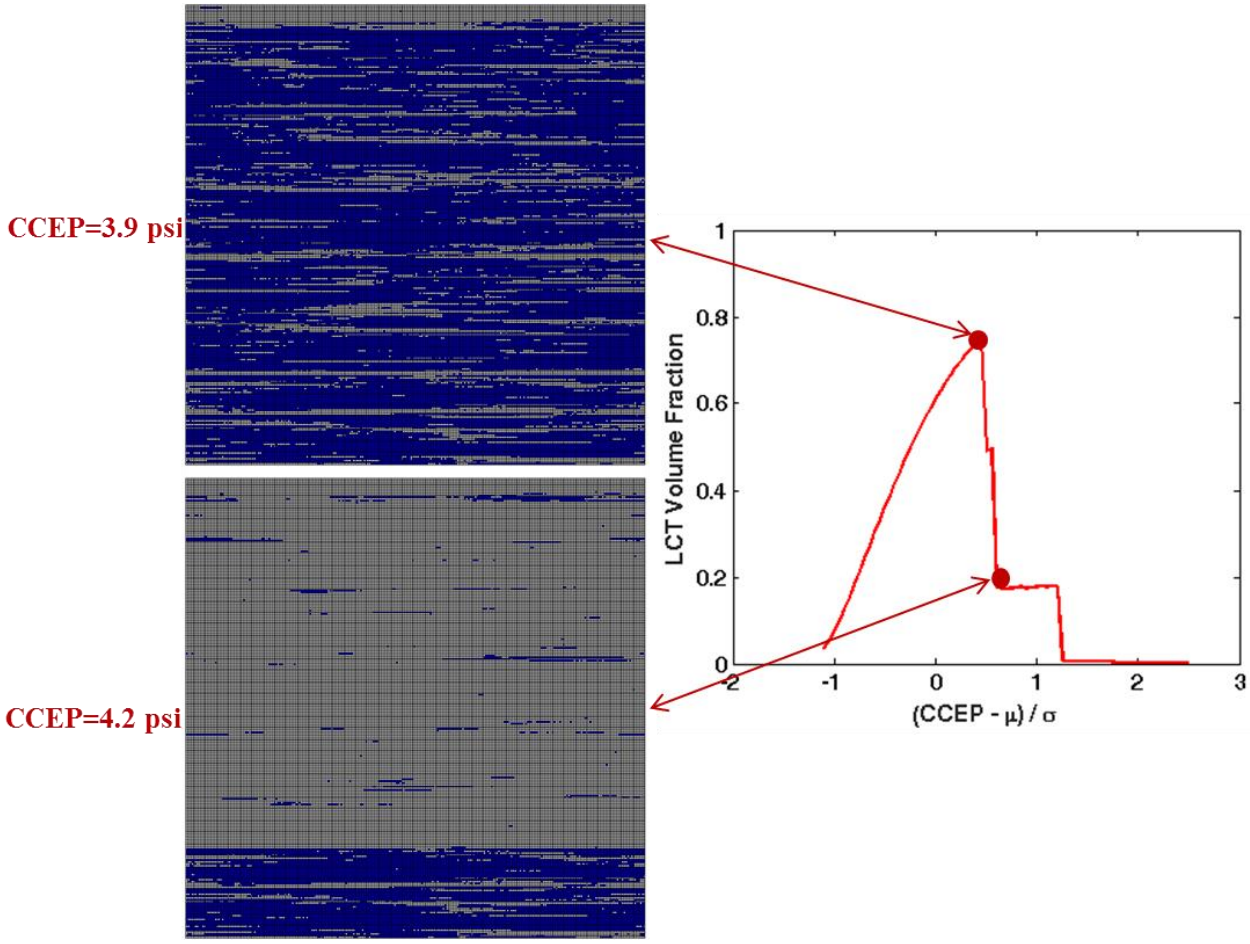

Fig. 5-17 The distributions of periodic LCT cells at two selected CCEPs in a horizontally auto-correlated system. μ=3 psi, σ=2 psi, λ_{Dx}=0.25, λ_{Dz}=0.

Finally, when the CCEP becomes large, most of the cells become flow paths. The auto-correlation effect on the LCT amount is diminished, and all the curves collapse to one in Fig. 5-14.

For the LCT boundary effect, periodic LCT curves overlap the closed LCT ones if a medium is uncorrelated (λ_{Dx}=0) or moderately auto-correlated (λ_{Dx}=0.5). On one extreme with

zero auto-correlation, we already demonstrate that a system size of 256×256 is enough to remove the closed boundary artifact. On the other extreme with λ_{Dx} 0.5, this moderate auto-correlation length creates a layering effect on LCT clusters, and such an effect is equivalent to the periodic LCT boundary. Thus, the CCEP-LCT curves for the closed LCT boundary overlap those for the periodic LCT.

Between the two extremes is the system with small (λ_{Dx}=0.12~0.2) horizontal auto-correlation lengths. In these systems, a closed LCT boundary causes an estimation of LCT volume fractions: the overestimated fraction can be as high as 0.2. Such an overestimation is non-negligible compared to the true LCT volume fraction. This indicates the importance of employing periodic LCT boundaries in quantifying LCT.

The reason of the overestimation is explored here. Figure 5-18 shows the spatial distribution and cluster size frequency of LCT at the maximum point of LCT~CCEP curves for both the closed and periodic LCT boundaries. The frequency $n(s)$ is defined as the ratio of the number of LCT clusters with a specific size s to the cells inside a domain. The spatial configuration of LCT cells for the closed LCT boundary looks qualitatively similar to that for the periodic LCT. However, the sizes of the largest LCT are different: the largest LCT cluster owned 43403 cells in the former boundary condition, whereas, it had 20078 cells in the latter. This is the main reason for the overestimation.

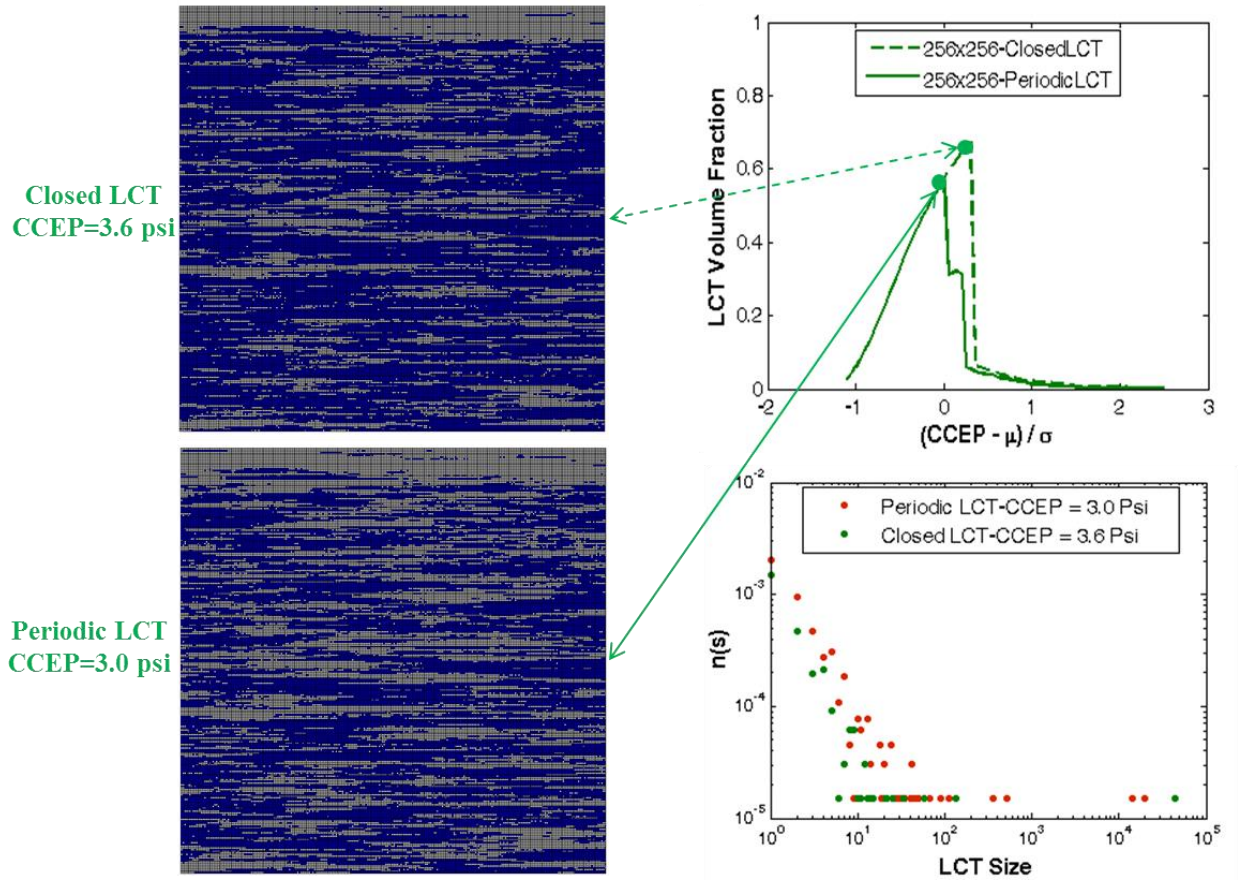

Fig. 5-18 The spatial distribution and cluster size frequency of the closed and periodic LCT cells at the maximum point of LCT~CCEP curves. μ=3 psi, σ=2 psi, λ_{Dx}=0.125, λ_{Dz}=0.

If a medium is spatially auto-correlated in both vertical and horizontal directions, the interactions among CCEP, boundary types and auto-correlation length become complicated. Figure 5-19 shows LCT~CCEP curves for capillary entry pressure fields with different λ_{Dx} and a constant λ_{Dz}. Notable changes caused by the added vertical auto-correlation can be observed by comparing Fig. 5-19 to Fig. 5-14. In Fig. 5-19, at small CCEPs, LCT~CCEP curves separate for different λ_{Dx}. Interestingly, a small λ_{Dx} yields a large LCT volume fraction. This is because, for the vertically auto-correlated system (λ_{Dz}=0.25), the larger λ_{Dx} would enable more flow path cells to be connected to the top layer, so these cells cannot act as local capillary traps. This observation is different from that in the purely horizontally auto-correlated system (left sides in

Fig. 5-14), for which, the horizontal auto-correlation length has no impact on the LCT amount at small CCEPs.

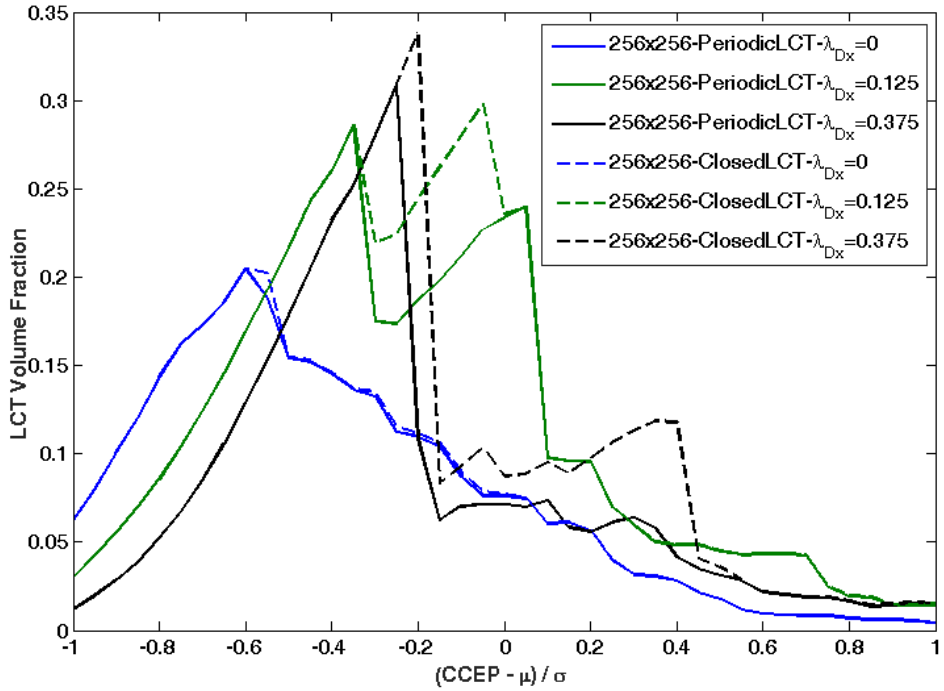

Fig. 5-19 Change of LCT volume fraction with CCEP in auto-correlated systems with different horizontal auto-correlation lengths. μ=3 psi, σ=2 psi, λ_{Dz}=0.25.

However, as CCEP approaches a threshold value, the effect of horizontal auto-correlation lengths on the LCT amount overrides the vertical auto-correlations, and larger λ_{Dx} results in more LCT cells. Meanwhile, the separation point between a closed LCT curve and a periodic LCT curve moves to the right as λ_{Dx} increases. The enhancement of connectivities in the horizontal direction causes more LCT cells to be accumulated.

Additionally, a mixed auto-correlated system encounters an overestimation of LCT capacity in a wider range of horizontal auto-correlation lengths than the purely horizontally auto-correlated systems. Even when λ_{Dx} increases to 0.375, this overestimation still exists in the former systems (refer to Fig. 5-19). In the latter systems, however, such an overestimation is removed as seen from Fig. 5-14. The added vertical auto-correlation offsets the horizontal auto-

correlation in creating a layering effect. This causes a pronounced effect of closed LCT boundaries on the overestimation in a mixed auto-correlated system.

The above analysis is for the two-dimensional systems, observations from the three-dimensional systems are briefly summarized here. Figures 5-20 and 5-21 show the interplay between LCT boundaries and horizontal auto-correlations in purely horizontally auto-correlated systems, and mixed auto-correlated systems, respectively. Overall, 3D observations of LCT~CCEP behaviors are qualitatively similar to 2D because mechanisms of interaction among CCEP, auto-correlation length, and LCT boundaries are the same. Nevertheless, the extra third dimension in 3D also causes some quantitative differences in aspects of the threshold CCEP, LCT capacity, and the overestimated LCT amount.

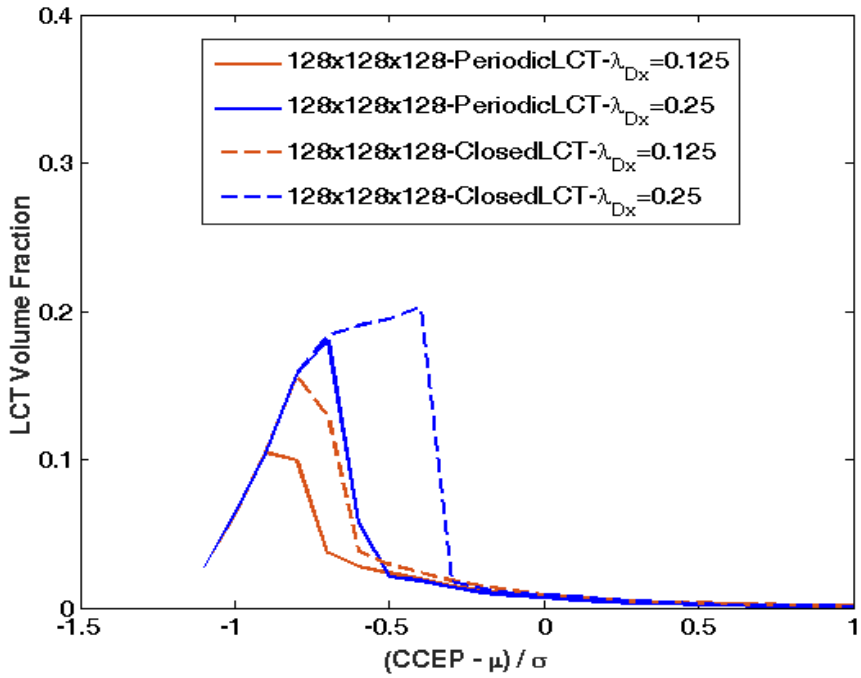

Fig. 5-20 Change of LCT volume fractions with CCEP in auto-correlated systems with different horizontal auto-correlation lengths. μ=3 psi, σ=2 psi, λ_{Dz}=0.

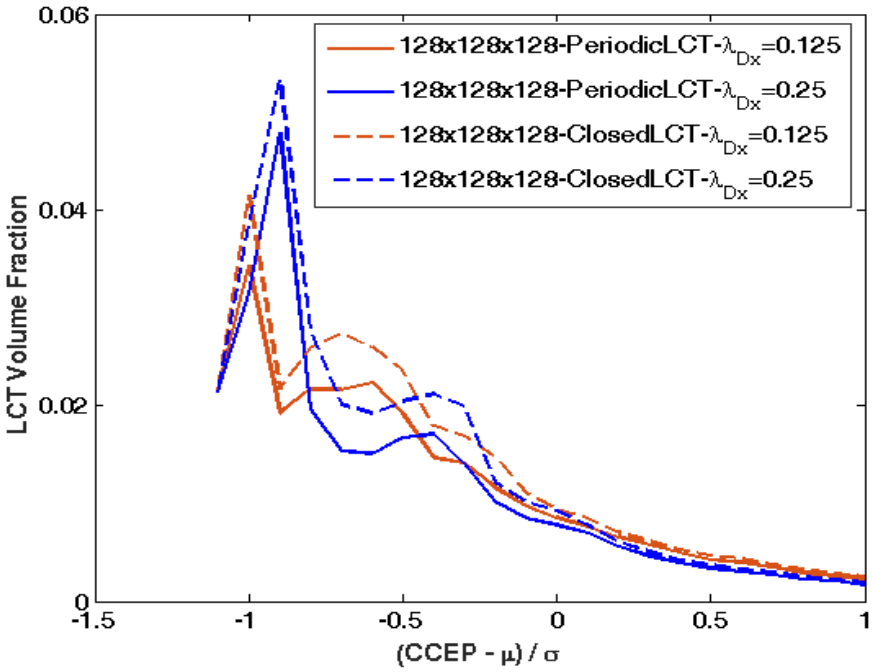

Fig. 5-21 Change of LCT volume fractions with CCEP in 3D systems with different horizontal auto-correlation lengths. μ=3 psi, σ=2 psi, λ_{Dz}=0.125.

5.3.5 Effect of the interplay between LCT boundaries and vertical auto-correlations on LCT

Figure 5-22 shows LCT~CCEP curves for purely vertically auto-correlated systems. A closed LCT boundary gives the same LCT amount as a periodic LCT does. Only lateral boundaries are set as periodic (recall periodic setting in the algorithm, refer to section 5.1).

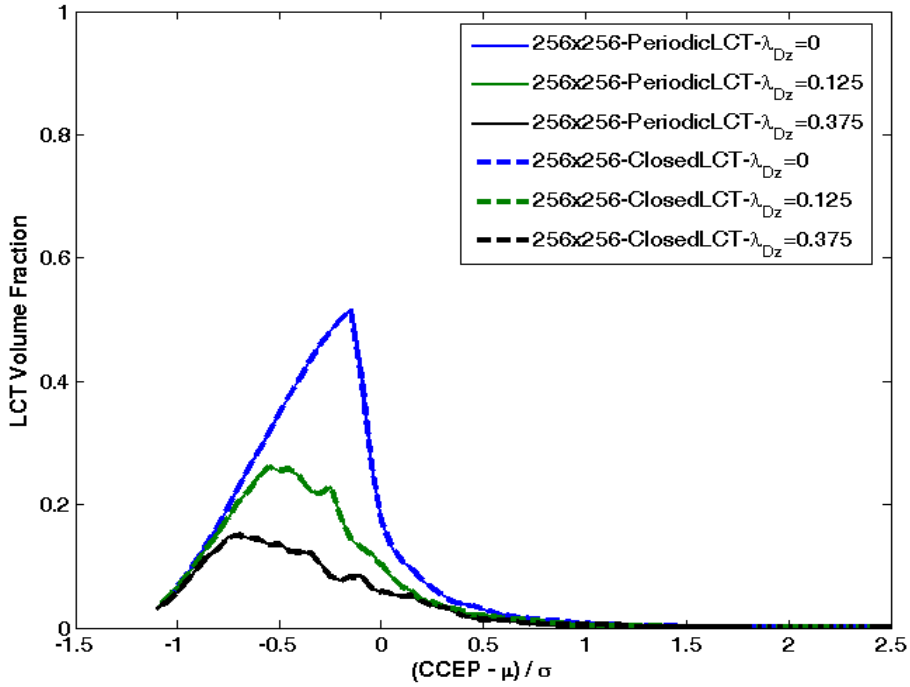

Fig. 5-22 Change of LCT volume fraction with CCEP in 2D systems with different vertical auto-correlation lengths. μ=3 psi, σ=2 psi, λ_{Dx}=0.

However, once the horizontal auto-correlation is added, the LCT boundary effect is introduced as shown in Fig 5-23. First, closed LCT boundaries cause an overestimation of the LCT amount. This can be explained by the LCT spatial distribution and cluster size frequency (Fig. 5-24). At the maximum point of LCT~CCEP curves, the LCT distribution for the periodic LCT boundary is different from that for the closed boundary. In the former case, the threshold CCEP was 2.8 psi. At this CCEP, flow path clusters have been spatially constrained by the auto-correlation length, but they have not got connected to the top layer yet. Therefore, LCT cells appear across the system from top to bottom. When CCEP increased to 3.2 psi, more flow path cells are added into clusters, and these clusters become connected to the top layer under the periodic LCT boundary condition. This causes a sharp decrease of the LCT volume. However, this does not occur in the closed LCT boundary because it creates a poor connectivity of flow path clusters than the periodic boundary does, so the added flow path cells can still act as LCTs. Therefore, dense LCTs are observed in the lower part of the storage domain. This is also

reflected from the cluster size distribution (Fig. 5-24); more numbers of large LCT clusters (cell#>1000) are observed in the closed LCT system than the periodic LCT system.

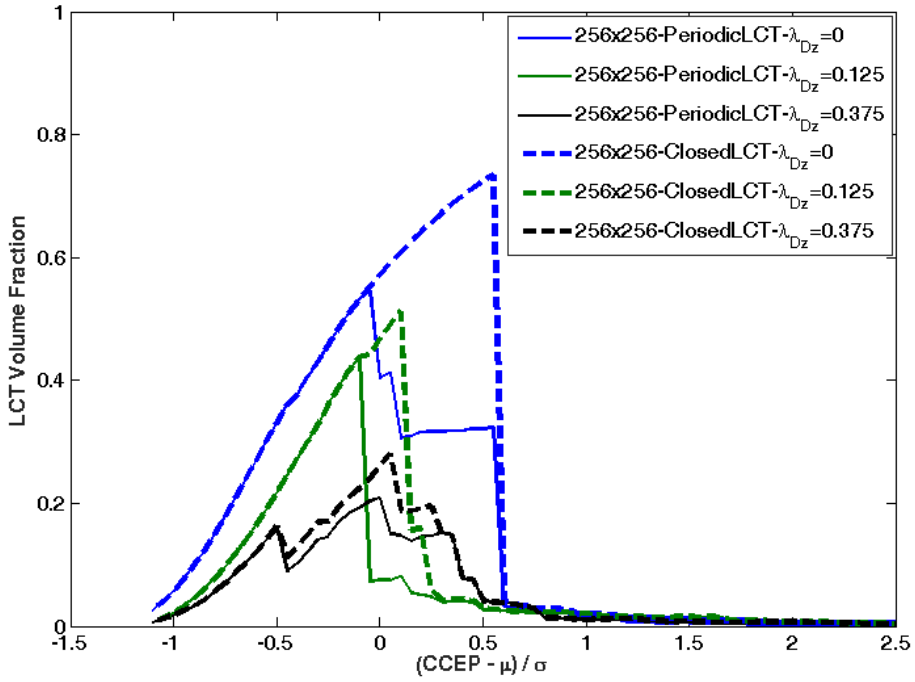

Fig. 5-23 Change of LCT volume fractions with CCEP in the mixed auto-correlated systems with different vertical auto-correlation lengths. μ=3 psi, σ=2 psi, λ_{Dx}=0.25.

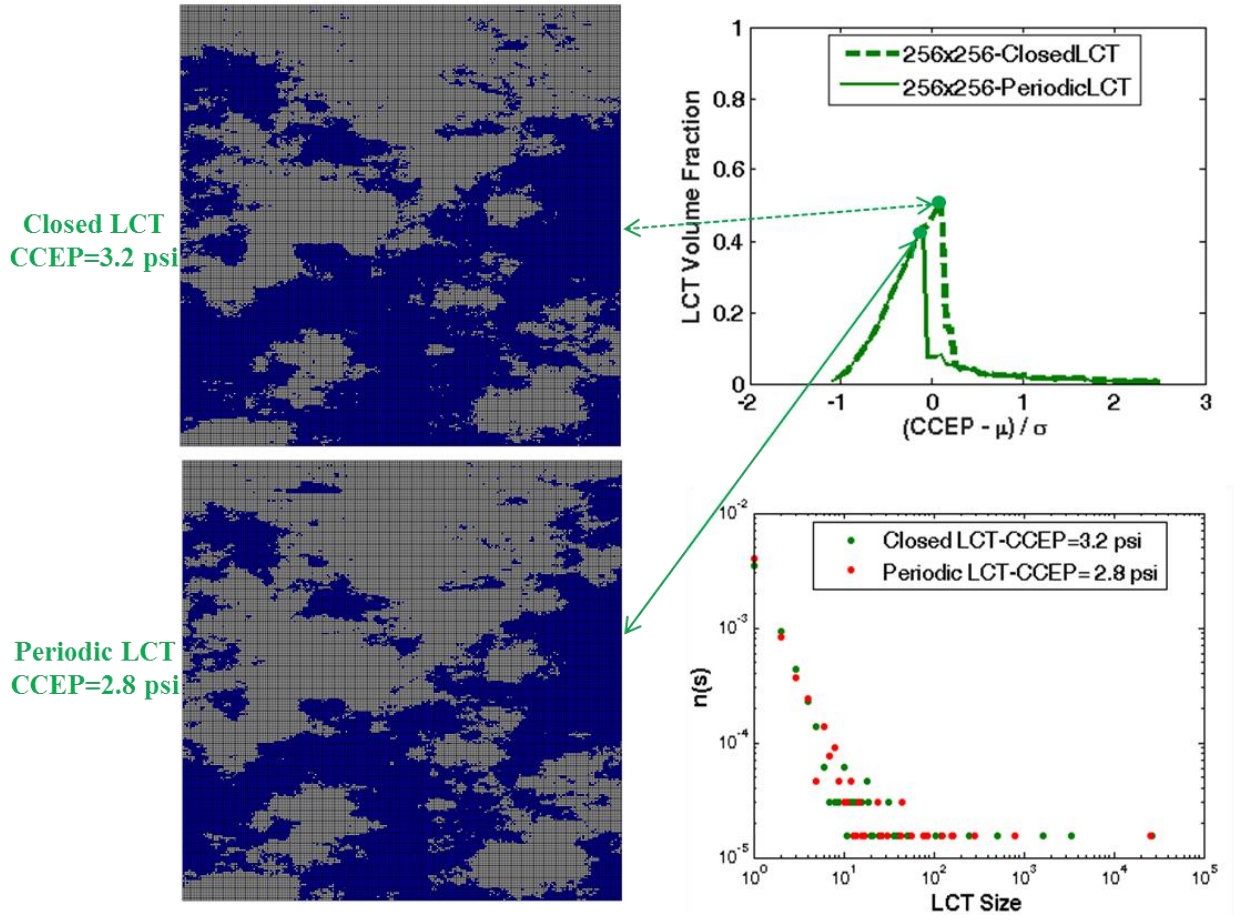

Fig. 5-24 The spatial distribution and cluster size frequency of closed and periodic LCT at the maximum points of the LCT~CCEP curves for mixed auto-correlated systems. μ=3 psi, σ=2 psi, λ_{Dx}=0.25, λ_{Dz}=0.125.

Second, the overestimation of the LCT fraction decreases as λ_{Dz} increases. This is because: when λ_{Dz} becomes large, the LCT volume fraction is mainly determined by the vertical rather than horizontal auto-correlation. Since periodic LCT boundaries are set only in the lateral faces (in the horizontal direction), large vertical auto-correlation lengths overrun the lateral LCT boundaries in affecting the LCT fraction.

5.4 RESULTS FROM REALISTIC GEOLOGIC FABRICS

We directly apply the periodic LCT boundary algorithm to realistic geologic fabrics. The main purpose is to estimate ranges of local capillary trap capacities in various types of sedimentary facies. The result is restricted to 2D models.

We plot the changes of LCT capacities with the statistical properties (i.e., mean, standard deviation, and anisotropy) of the 162 capillary threshold pressure fields. Recall the maximum point on a LCT~CCEP curve correspond to the LCT capacity or the maximum LCT volume fraction. Figure 5-25 shows the LCT capacities for the three fabrics, nine average grain sizes, and six sorting factors. 54 points defining each horizontal plane correspond to the capillary entry pressure distributions of the 54 facies (refer to Table 5-2). In each horizontal plane, the six sorting factors define the six dotted lines. Each line consists of nine points representing nine grain sizes. As seen, the anisotropy or fabric mainly influences the LCT capacity, whereas, the texture shows a minor effect. This is consistent with the above results from purely synthetic media that the standard deviation of capillary entry pressure has a negligible impact on the LCT capacity.

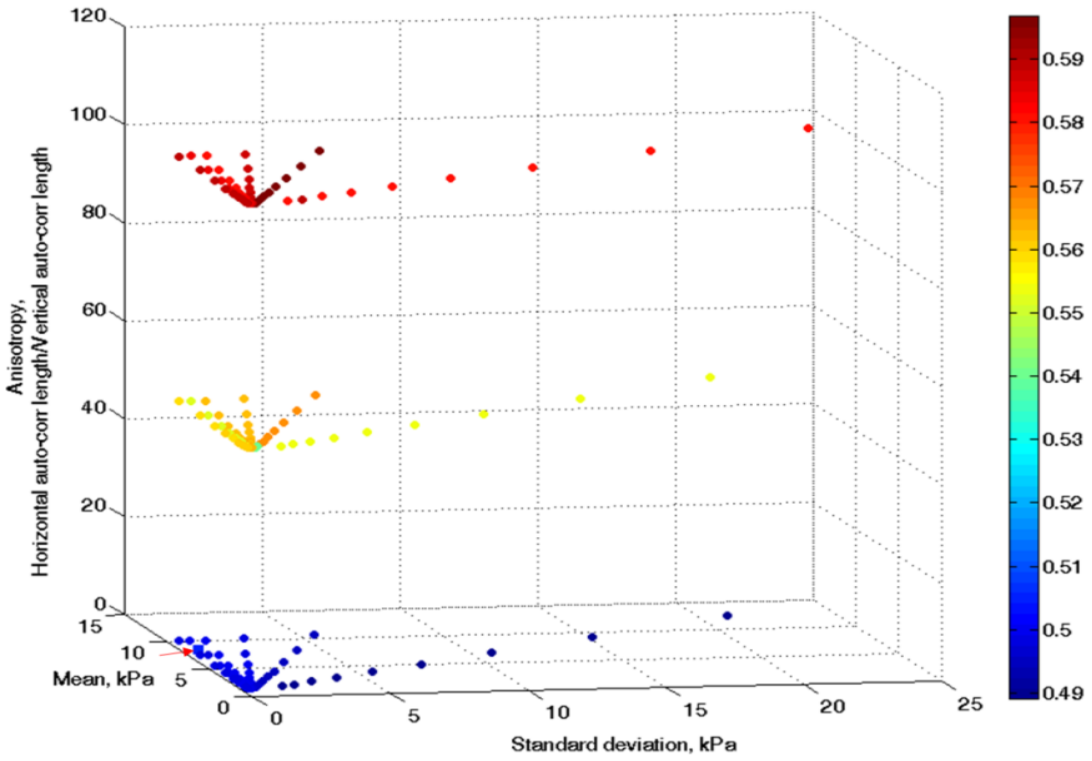

Fig. 5-25 Summary results of LCT capacities for both the 162 fields and the digital field. The lower left square indicated by the red arrow represents the result from the digital model. The color bar shows the maximum LCT volume fraction or the LCT capacity.

Additionally, the LCT capacity from the digital capillary entry pressure field is integrated into the results of the above 162 models (see the red arrow in Fig. 5-25). The former can be well fit into the latter. Considering a fabric mainly determines LCT capacities, it would be helpful to employ capillary entry pressure fields with large-scale structures (large auto-correlation length) to examine the robustness of the LCT capacity predictor. Unfortunately, such structures are less likely to obtain in the lab.

5.5 DISCUSSION

5.5.1 Implications of LCT capacities for engineering operations

As stated earlier, the critical capillary entry pressure (CCEP) determines whether a given cell is a barrier or a flow path for CO_2. This meaning is physically equivalent to CO_2 column height: if a column of CO_2 creates buoyant force greater than the capillary entry pressure of a cell, then this cell cannot act as a barrier, otherwise, this cell can be a barrier. This statement suggests a way of maximizing LCT volume during CO_2 injection: if we manipulate the height of a CO_2 column in a storage formation to render the corresponding buoyancy equal to the threshold CCEP as determined from the geologic criterion, then local capillary traps would be fully utilized.

This can be achieved using the water alternating gas (WAG) injection. WAG is typically employed in CO_2 enhanced oil recovery to improve the conformance profile (Lake et al. 2014). It can be adapted here to disconnect a CO_2 stream into columns with the height determined from CCEP. This disconnection can be easily realized by adjusting WAG ratios for different heterogeneous storage formations. For example, formations with strong horizontal auto-correlation lengths would need a small WAG ratio (i.e., less water and more CO_2), as the threshold CCEPs in such formations are large and allow for high CO_2 columns.

5.5.2 Comparison to the percolation theory

Saadatpoor (2012) compared the behavior in local capillary trapping to that described by the percolation theory (Broadbent and Hammersley 1957). This comparison is made in uncorrelated capillary entry pressure fields. For these fields, the cumulative distribution function evaluated at a threshold CCEP is found to be close to the site percolation thresholds in both 2D square lattices and 3D cubic lattices. However, only one standard deviation of capillary entry pressure is tested. Therefore, the finding is not applicable to the capillary entry pressure fields with small standard deviation.

Here, we thoroughly compare local capillary trapping to the percolation process for both uncorrelated and correlated fields. As analyzed below, several features of the percolation process are involved in the local capillary trapping phenomenon.

For local capillary trapping, a threshold CCEP arises from the competition between clusters of barriers and clusters of flow paths. Parts of the latter clusters become local capillary traps. Additionally, the flow path cluster percolates as CCEP increases. These are similar to the observations of traditional site percolation phenomenon in uncorrelated systems (Broadbent and Hammersley 1957, Frisch and Hammersley 1963). In the site percolation, a site percolation threshold is resulted from the competition between sites and bonds, and a spanning cluster of sites percolates as the site occupation probability increases.

For auto-correlated fields, threshold CCEPs move to the right as horizontal auto-correlation lengths increase. This is similar to the site percolation in auto-correlated systems; the horizontal auto-correlation increases the percolation threshold because it reduces the vertical connectivity of sites relative to the probability in uncorrelated systems.

Thus, the percolation theory provides a good foundation for explaining two factors in a qualitative way: (1) the existence of the maximum LCT in any domains; (2) the influence of heterogeneity (i.e., auto-correlation length and standard deviation) on the movement of threshold CCEPs.

However, local capillary trapping is also different from the percolation process. As schematically shown in Fig. 5-26, a spanning LCT cluster never percolates as defined in the geologic criterion algorithm. Only a cluster of flow paths percolates as CCEP increases. Therefore, the cumulative probability of capillary entry pressure evaluated at a threshold CCEP is different from the site percolation threshold. The former threshold happens before a flow path cluster percolates from bottom to the top of the domain while the latter represents the first spanning cluster of sites from sides to sides. Therefore, theoretically, the former should be smaller than the latter in uncorrelated systems. Table 5-3 confirms this. A site percolation threshold is always larger than the corresponding cumulative probability at a threshold CCEP.

Further, the deviation between these two become large as the standard deviation of capillary entry pressure decreases. This implies that, only when moving away from percolation thresholds, the percolation theory has some relevance with local capillary trapping.

Additionally, the percolation theory cannot explain the maximum LCT fraction and spatial structures of local capillary traps and barriers. Instead, a simple counting argument provides a better way of interpreting them as shown below.

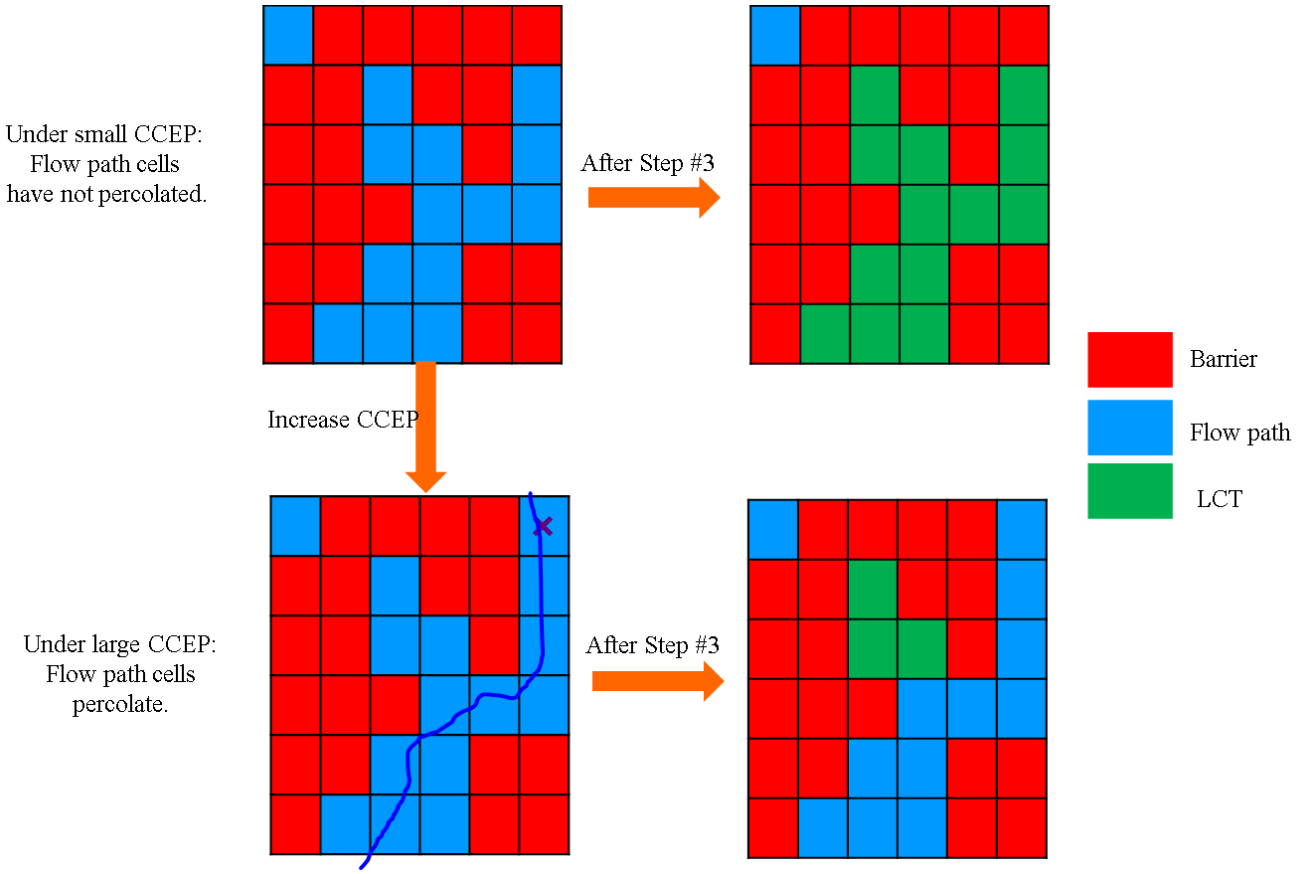

Fig. 5-26 Schematic explanation of the differences between the local capillary trapping phenomenon and the traditional percolation phenomenon. The "x" means, at a large CCEP, a cluster of flow paths percolates.

Table 5-3. Comparison between the cumulative probabilities evaluated at threshold CCEPs to site percolation thresholds in uncorrelated capillary entry pressure fields.

Parameter	2D			3D		
Mean, psi	3.0	3.0	3.0	3.0	3.0	3.0
Standard deviation, psi	0.4	2.0	3.6	0.4	2.0	3.6
Threshold CCEP, psi	3.0	2.65	2.15	2.6	1.5	0.9
Cumulative probability	0.526	0.539	0.548	0.156	0.200	0.211
Site percolation threshold	0.59			0.31		

5.5.3 Interpretation using a simple counting argument

A simple counting argument is used here to interpret the phenomenon of local capillary trapping in both qualitative and quantitative ways.

For a given value of CCEP, a fraction (f) of cells are "occupied flow paths", and 1-f is the fraction of cells that are barriers. Note that f is equal to the cumulative distribution function evaluated at a CCEP value. If a capillary entry pressure field is uncorrelated, the probability that a barrier cell is above any given cell is 1-f. Therefore, the probability that an "occupied" cell is below a barrier cell is $f(1-f)$. This situation is a rudimentary local capillary trap, as it does not account for the occurrence possibility of side barriers around occupied cells.

Similarly, the probability of a cluster of n adjacently "occupied" cells are f^n and the probability of n adjacent barrier cells lie above them is $(1-f)^n$, so the likelihood of a n-cell LCT is $f^n(1-f)^n$. A general scenario would be n adjacent barrier cells above m LCT cells, the corresponding likelihood would be $f^m(1-f)^n$. Figure 5-27 shows an example plot of LCT likelihood versus occupation probability. The LCT likelihood (frequency) first increases followed by a decrease. This trend is similar to that of LCT~CCEP curves.

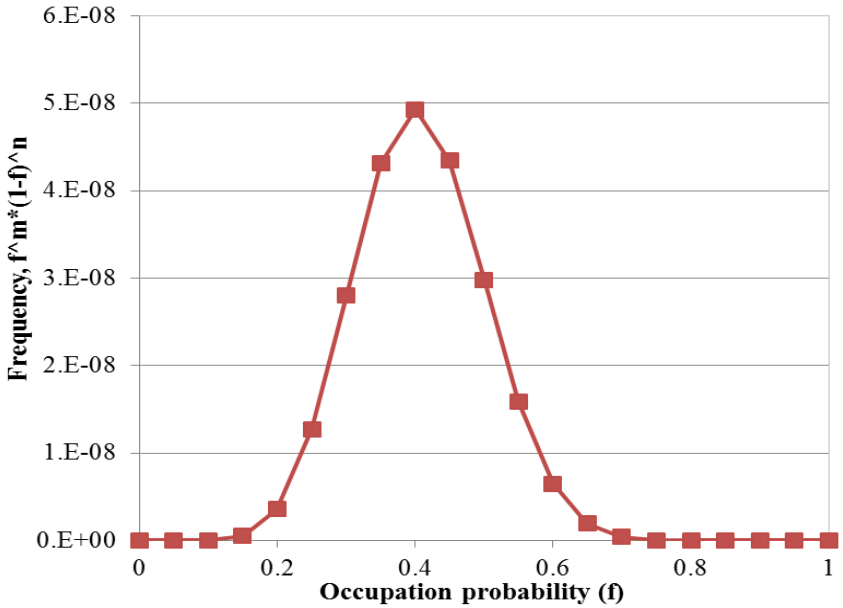

Fig. 5-27 An example frequency using m=10 and n=15. m and n are the number of LCT cells and barrier cells, respectively.

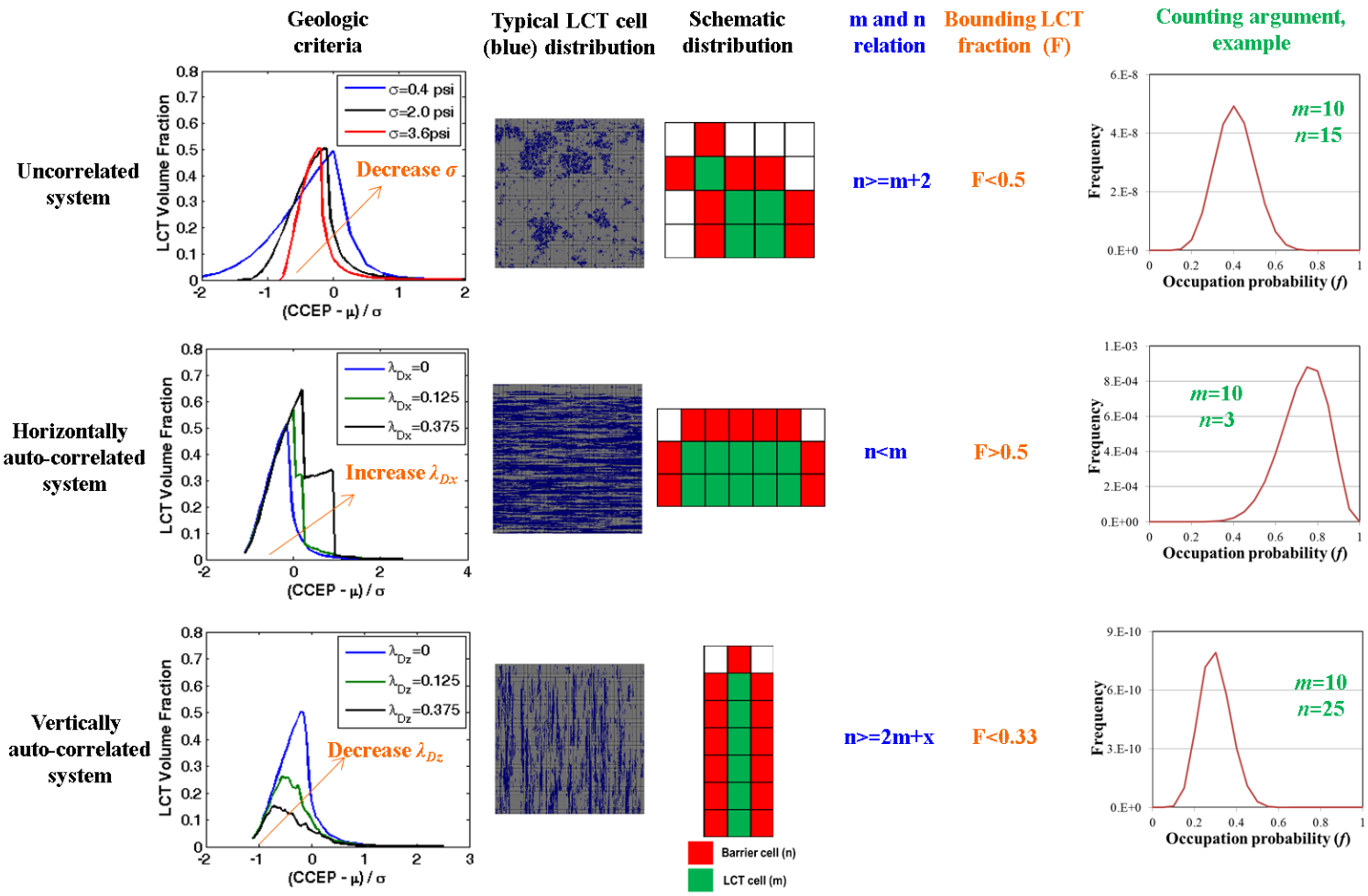

Fig. 5-28 Summary plots of LCT~CCEP curves, typical LCT distributions, schematic configurations of LCT cells and barrier cells, *m* and *n* relationship, limiting LCT fractions, and counting argument examples for uncorrelated, horizontally auto-correlated, and vertically auto-correlated systems. For all the capillary entry pressure fields, system dimensions are 256×256, μ=3 psi. *m* and *n* are the number of LCT cells and barrier cells, respectively. X is an arbitrary number.

Next, we use the counting argument to interpret positions of threshold CCEPs, their movement under the influence of heterogeneity, and observations of limiting LCT fractions. To assist the analyses, we summarize plots of LCT~CCEP curves, typical LCT distributions, schematic configurations of LCTs and barriers, m and n relationship, limiting LCT volume fractions, and counting argument examples for different auto-correlated systems in Fig. 5-28.

In uncorrelated media, the probability of m LCT cells is $f^m(1-f)^n$ according to the above analysis. The first derivative with respect to f gives the position of the largest frequency, and it is calculated to be $f = m/(m+n)$. This means that the maximum LCT volume fraction happens at $f = m/(m+n)$. Based on the possible configuration of LCTs and barriers (refer to the middle column of Fig. 5-28), we can get $n >= m+2$, $f = m/(m+n) <= m/(2m+2) = 1/(2+2/m) < 0.5$. f at 0.5 corresponds to the median of capillary entry pressure. For a lognormal distribution, the mean is less than the median. This explains why a threshold CCEP is smaller the mean of capillary entry pressure in a uncorrelated system (refer to the upper left plot in Fig. 5-28).

In auto-correlated media, spatial configurations of barriers and LCT cells become complicated. In a horizontally auto-correlated medium, the horizontal auto-correlation creates a layering effect; this means that multiple layers of LCTs appear blow a single barrier layer. Thus, m $> n$, $2m > m+n$, $f = m/(m+n) > 0.5$. Therefore, a threshold CCEP should be larger than the median of capillary entry pressure. In addition, as the horizontal auto-correlation length increases, m would be much larger than n, this causes f much higher than 0.5, so a threshold CCEP becomes large. This is consistent with the above observation that a threshold CCEP moves to the right as the horizontal auto-correlation length increases (refer to the middle left plot in Fig. 5-28). A similar analysis can be made for vertically auto-correlated systems.

Next, we explain the observations of limiting LCT volume fractions based on spatial configurations of LCTs and barriers. In an uncorrelated system, the total number of cells is set to be T, and the number of flow path cells excluding LCT cells is p, recall m is the number of LCTs and n is the number of barriers, then $m+n+p = T$. As shown in the middle part of Fig. 5-28, $n \geq m+2$, so $m+n+p \geq 2m+2+p$, that is $T \geq 2m+2+p$. Then the LCT volume fraction (F) can be

expressed as: $F = m/T <= m/(2m+2+p) = 1/(2+2/m+p/m) < 0.5$. This means that the maximum LCT volume fraction should be less than 0.5. This calculation is consistent with the prediction from the geologic criterion algorithm (refer to the upper left plot of Fig. 5-28).

Similarly, the lower bound of LCT volume fractions is determined to be 0.5 in horizontally auto-correlated systems. The upper bound of LCT fractions is 0.33 in vertically auto-correlated systems. All these simple calculations agree with the predictions from the geologic criterion algorithm.

The above 2D analysis can be partially extended to 3D. In 3D, a simple counting argument can also be used to interpret LCT~CCEP trends and the movement of a threshold CCEP in a qualitative manner. However, it is much difficult to estimate the bounds of LCT volume fractions. This is because 3D spatial configurations of LCTs and barriers are complicated, and the relationship between *m* and *n* is less likely to approximate.

Overall, a simple counting argument analysis supports the correctness of the geologic criterion algorithm in both qualitative and quantitative aspects.

5.5.4 Geologic criterion vs. invasion percolation

Invasion percolation simulations on the above 2D realistic geologic fabrics have been conducted using commercial simulator Permedia® (Ganesh 2012, Meckel et al. 2015). They investigated the fraction of domain cells invaded by CO_2 at percolation during buoyant flow. The fraction is defined as 'CO_2 saturation". They found that this CO_2 saturation is influenced by small-scale depositional reservoir heterogeneity (i.e., grain size, capillary threshold pressure distribution, and auto-correlation length anisotropy). The observations are qualitatively similar to the above results of the effect of heterogeneity on LCT capacities. However, the relative influences of these factors on LCT capacities in the geologic criterion algorithm are different from their influences on the CO_2 saturation in the invasion percolation simulation. In the former, the LCT capacity is mainly determined by the auto-correlation length, whereas, in the latter, all the above heterogeneity indicators affect the CO_2 saturation.

This is because the underlying physics behind the two methods are different. Permedia or the invasion percolation simulation is based on the static capillary equation, $P_c=\Delta\rho gh$. When buoyant force created by a CO_2 column exceeds capillary entry pressure of a given cell, CO_2 migrates upward until the next larger capillary barrier is encountered. Before that, CO_2 accumulates to build a high buoyant column as long as the capillary barrier is not overcome. Therefore, the invaded CO_2 follows a path of the least capillary threshold pressure till percolation. Thus, any small changes of mean, standard deviation, and auto-correlation length of capillary threshold pressure definitely influence CO_2 flow path, topologies of CO_2 clusters, and the total number of cells invaded by CO_2 at percolation.

However, in the geologic criterion algorithm, the spatial distribution of LCTs and barriers are changed by adjusting CCEP. The maximum LCT volume is obtained under the optimal spatial configuration of clusters of barriers and clusters of flow paths. Spill points defined by the topology of barrier clusters are also accounted for. These analyses indicate that the spatial distribution (i.e., auto-correlation length) of capillary entry pressure is a key to LCT capacities, rather than histograms (i.e., mean and standard deviation). The latter effect is, in fact, replaced by the input CCEP.

Based on the above comparison, one would expect that there should be overlapping cells between invading CO_2 clusters in the Permedia and LCT clusters in the geologic criterion algorithm, as both of them are related to cells with relatively small capillary entry pressure.

5.6 SUMMARY

In this chapter, we incorporate periodic LCT boundaries into a geologic criterion algorithm. Then we employ the improved algorithm to estimate the LCT amount in both purely synthetic media and realistic geologic fabrics. We demonstrate that interactions among CCEP, auto-correlation, system size, and LCT boundary types influences the LCT amount. We highlight that a simple counting argument is very useful to interpret results from the geologic criterion algorithm.

Chapter 6: Characterization of Local Capillary Trap Clusters

Chapter 5 demonstrated that interactions among CCEP, system sizes, reservoir heterogeneity, and LCT boundary types influence LCT volume fractions in a mixed way. The mechanism underlying the impacts is that these factors control the number, size, and morphology of LCT clusters.

Understanding the morphology of LCT clusters is essential for the injection design of geological carbon sequestration. For example, if the spatial distribution of the largest LCT cluster were identified, it would provide guidance in locating CO_2 injectors. By drilling around the largest LCT cluster, the injected CO_2 would most likely have access to these local capillary traps and then get trapped. Additionally, if most of the LCT clusters were found to extend laterally at the bottom of domains, then, horizontal injectors should be recommended to maximize the contact between the injected CO_2 and local capillary traps. With these efforts, more CO_2 would be safely stored in local capillary traps and therefore the leakage risk is reduced.

Thus, this chapter is aimed to characterize LCT clusters. We explore the mechanisms of how the above factors influence LCT cluster properties, including LCT cluster size, frequency, and extent. Particularly, we analyze (1) the impact of CCEP on the frequency of LCT cluster sizes; (2) properties of the largest LCT cluster; and (3) the impact of reservoir heterogeneity (i.e., standard deviation and auto-correlation length) on cluster properties.

6.1 PARAMETERS USED TO DESCRIBE LCT CLUSTER PROPERTIES

(1) LCT cluster size frequency *n(s)*

$$n(s) = N(s) / N_{cell}$$

N(s) is the number of a LCT cluster with size *s* in cells, N_{cell} is the total number of cells in a model system, *s* is the number of cells.

(2) Contribution to the LCT capacity from the LCT clusters with size *s*

$$m(s) = s * n(s)$$

6.2 SYNTHETIC CAPILLARY ENTRY PRESSURE FIELDS

Table 6-1 summarizes the capillary entry pressure fields for the analysis of LCT cluster properties. System dimensions are $N_x \times N_y \times N_z$, and cell size is 1×1 ft. The mean and standard deviation of capillary entry pressure are μ and σ, respectively. The vertical and horizontal dimensionless auto-correlation lengths of a capillary entry pressure field are λ_{Dx} and λ_{Dz}, respectively.

We employ a periodic LCT boundary in both 2D and 3D synthetic media. In uncorrelated media (i.e., $\lambda_{Dx}=0$, $\lambda_{Dz}=0$), we analyze how standard deviation of capillary entry pressure affects LCT clusters. Then, we analyze the effect of auto-correlation lengths in auto-correlated systems by setting mean and standard deviation to be constant. Some media have multiple realizations for a comprehensive statistical analysis.

Table 6-1. Conditions for simulations

Model	N_x	N_y	N_z	λ_{Dx}	λ_{Dz}	μ, psi	σ, psi	Figure	Note
2D	512	1	512	0	0	3.0	0.4~3.6	6-1	LCT volume fraction
2D	512	1	512	0	0	3.0	0.4~3.6	6-2	n(s)
2D	512	1	512	0	0	3.0	0.4~3.6	6-3	The largest LCT cluster
3D	128	128	128	0	0	3.0	0.4~3.6	6-4	LCT volume fraction
3D	128	128	128	0	0	3.0	0.4~3.6	6-5	The largest LCT cluster
2D	512	1	512	0	0	3.0	2.0	6-6	n(s)
2D	512	1	512	0	0	3.0	2.0	6-7	m(s)
2D	256	1	256	0~0.375	0	3.0	2.0	6-8	LCT volume fraction
2D	256	1	256	0~0.375	0	3.0	2.0	6-9	n(s)
2D	256	1	256	0~0.375	0	3.0	2.0	6-10	The largest LCT cluster
3D	128	128	128	0~0.25	0	3.0	2.0	6-11	LCT volume fraction
3D	128	128	128	0~0.25	0	3.0	2.0	6-12	The largest LCT cluster
2D	256	1	256	0	0~0.375	3.0	2.0	6-13	LCT volume fraction
2D	256	1	256	0	0~0.375	3.0	2.0	6-14	n(s)
2D	256	1	256	0	0~0.375	3.0	2.0	6-15	The largest LCT cluster
3D	128	128	128	0	0~0.25	3.0	2.0	6-16	LCT volume fraction
3D	128	128	128	0	0~0.25	3.0	2.0	6-17	The largest LCT cluster

6.3 RESULTS

Most of the following analysis will be restricted on 2D systems. Differences between 3D and 2D are highlighted.

6.3.1 Effect of standard deviation on cluster properties

Figure 6-1 shows LCT~CCEP curves for uncorrelated systems with different standard deviations. We are not interested in the right part of LCT~CCEP curves in which CCEPs are larger than a threshold. This is because, at such CCEPs, only a small amount of LCT cells is identified at the bottom of the domain (refer to Fig. 5-12 in chapter 5). Instead, we choose a CCEP positioned on the left sides of these curves, and it was 2.05 psi. This value is little smaller than the threshold CCEP for the widest capillary entry pressure distribution.

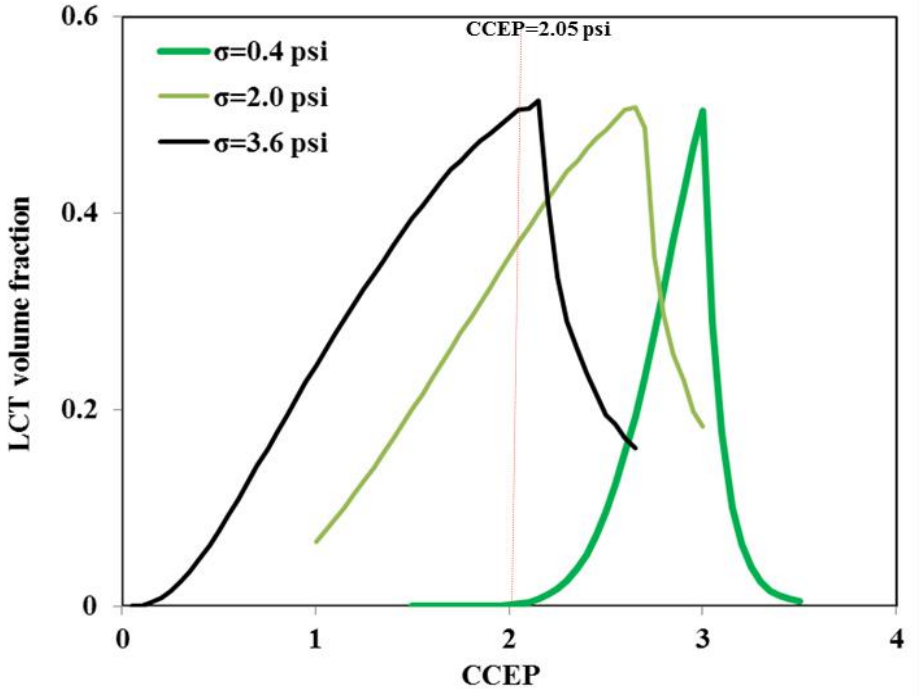

Fig. 6-1 LCT~CCEP curves for several 2D uncorrelated capillary entry pressure fields with different standard deviations. System dimensions are 512×512. μ=3 psi, λ_{Dx}=0, λ_{Dz}=0.

At this CCEP, the impact of standard deviation on LCT cluster size frequency $n(s)$ is in Fig. 6-2. Overall, standard deviation of capillary entry pressure increases both the size and number of large LCT clusters (cell# > 100). For the smallest standard deviation, the chosen CCEP gives several sparse LCT clusters with less than three cells, whereas, the largest LCT cluster for the largest standard deviation contained about 7000 cells (refer to the most right green point in Fig. 6-2).

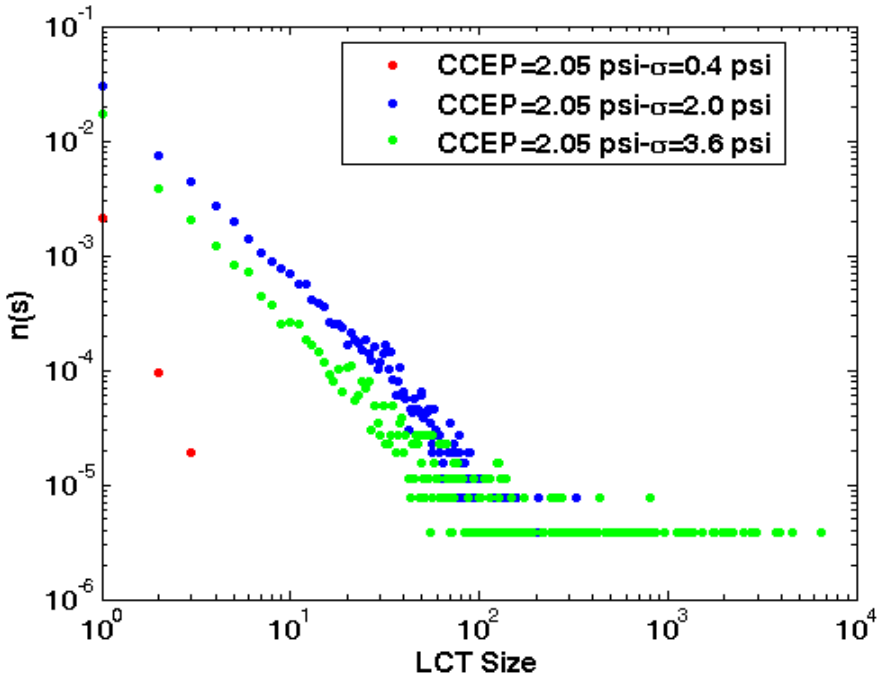

Fig. 6-2 Size frequency of LCT clusters for capillary entry pressure fields with different standard deviations. The chosen CCEP was 2.05 psi. System dimensions are 512×512. μ=3 psi, λ_{Dx}=0, λ_{Dz}=0.

Figure 6-3 shows the numbering of LCT clusters, the largest LCT cluster, and its contribution to the LCT capacity and to the entire domain volume for uncorrelated capillary entry pressure fields. LCT cluster IDs are labeled from the left bottom cell, and colors of cluster labeling are arbitrary. These fields have different standard deviations and a constant mean. Although these fields yield almost the same maximum LCT volume fraction (0.5, refer to Fig. 6-1), the morphology, number, and size of LCT clusters are different. As standard deviation

increases, the size of the largest cluster increases, and meanwhile, the total number of LCT clusters decreases (from 8005 to 7094). When standard deviation was 3.6 psi, the largest LCT cluster accounted for about 33% of the total LCT volume and 17% of the entire domain volume. Such volume fractions are significant. However, the largest cluster does not span a domain from sides to sides.

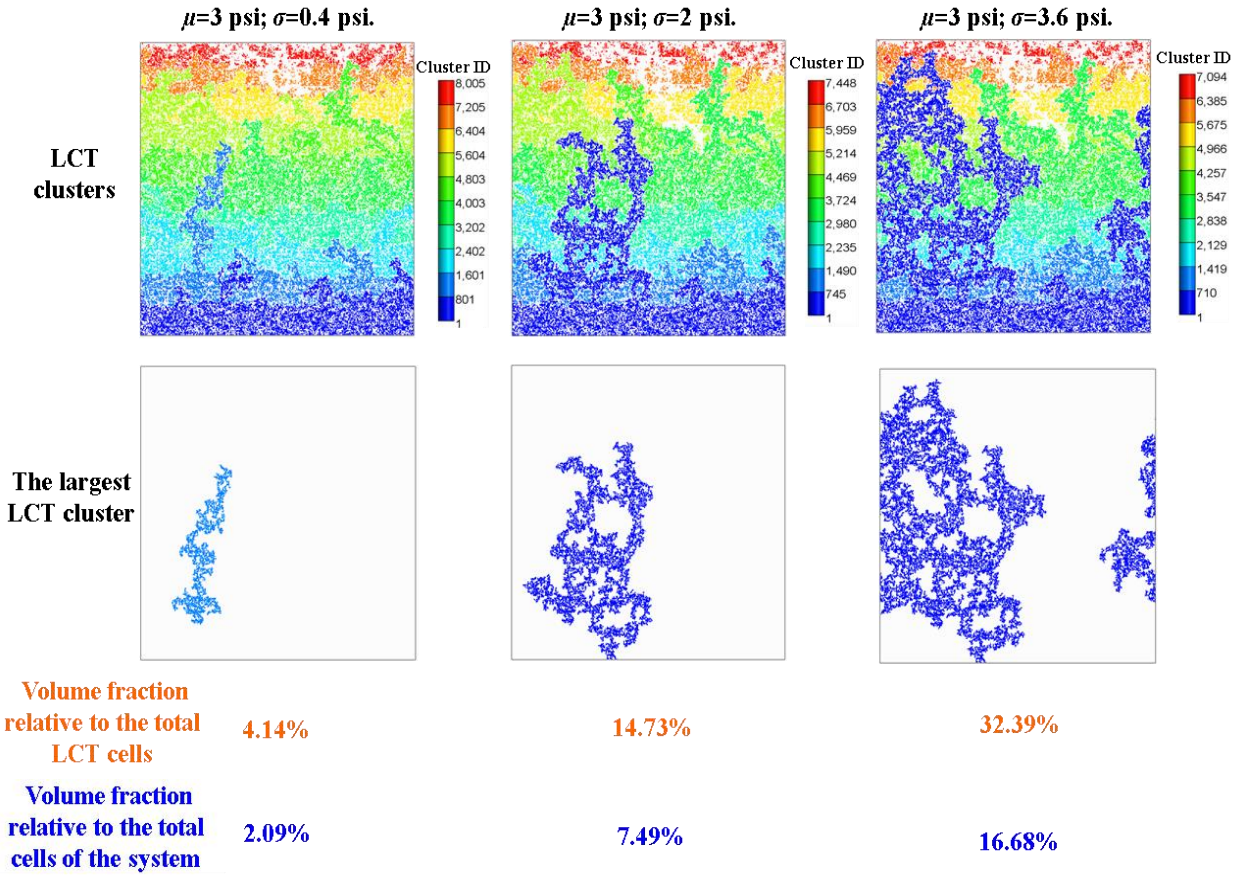

Fig. 6-3 Summary plots of LCT clusters, the largest LCT cluster, its volume fraction relative to the total LCT cells, and its volume fraction relative to the total cells of a domain. CCEP is at the threshold. System dimensions are 512×512. μ=3.0 psi, λ_{Dx}=0, λ_{Dz}=0.

Additionally, one might see that parts of the largest cluster in a field with a narrow distribution become a subset of the largest cluster for a field with a wide distribution. This is

because: the latter field has a smaller threshold CCEP than the former does, so some of LCT cells in the latter are also the LCT cells in the former.

The above analysis is for 2D. In 3D uncorrelated systems, the quantitative differences occur in the largest LCT cluster at threshold CCEP. Figures 6-4 through 6-5 shows LCT~CCEP curves and cluster properties, respectively. In 3D (Fig. 6-5), the largest LCT cluster accounted for only 1.78% of the LCT capacity in a capillary entry pressure field with a standard deviation of 2.0 psi. This fraction can be as high as 14.73% in a 2D field with the same stand deviation (Fig. 6-3). The difference is pronounced as standard deviation increases. These observations means that large LCT clusters are difficult to obtain in a 3D uncorrelated system.

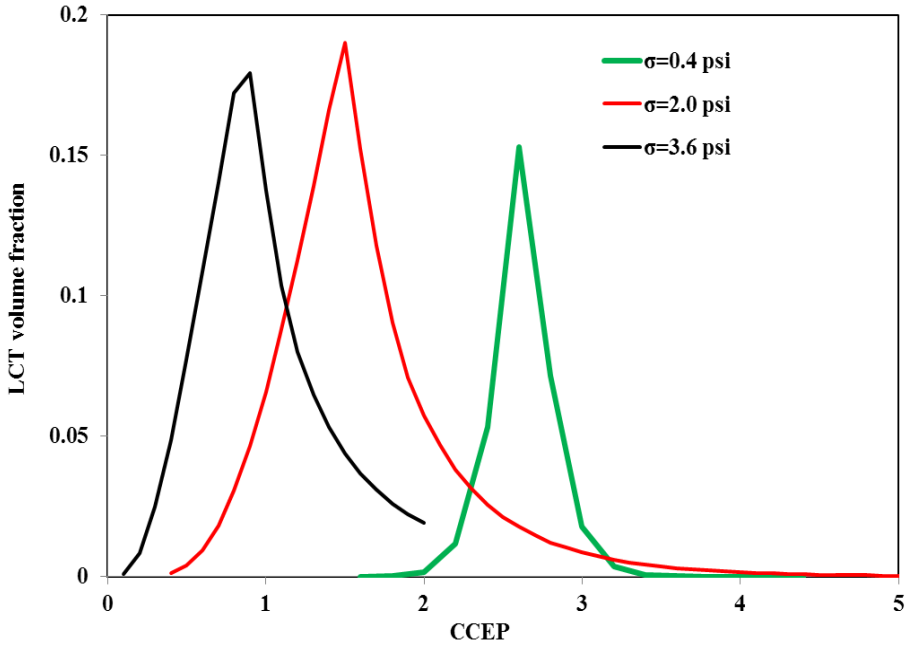

Fig. 6-4 LCT~CCEP curves for 3D uncorrelated systems with different standard deviations. System dimensions are 128×128×128. μ=3 psi, λ_{Dx}=0, λ_{Dz}=0.

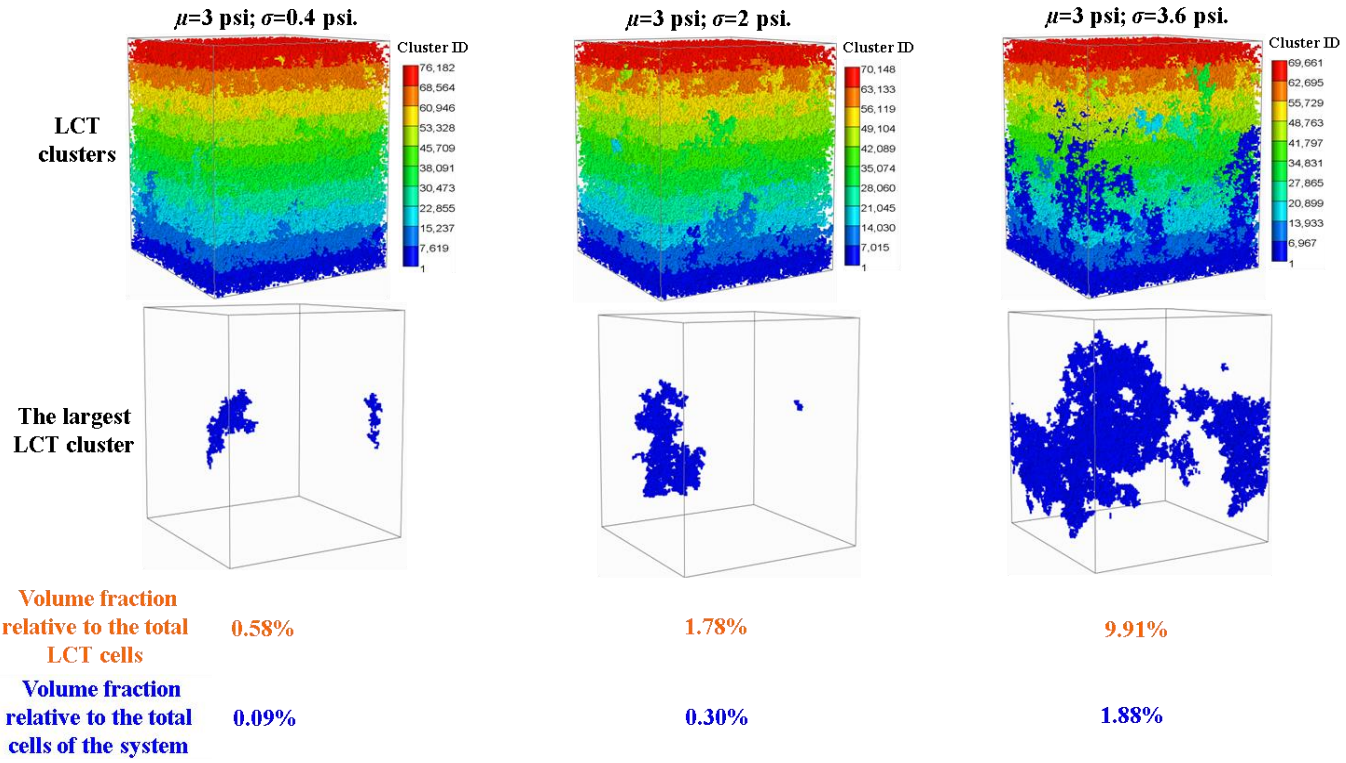

Fig. 6-5 Summary plots of LCT clusters, the largest LCT cluster, its volume fraction relative to the total LCT cells, and its volume fraction relative to the total cells of a domain. CCEPs are selected at thresholds. System dimensions are 128×128×128. λ_{Dx}=0, λ_{Dz}=0.

6.3.2 Effect of CCEP on cluster properties

We choose a two-dimensional capillary entry pressure field (refer to Fig. 6-1) with stand deviation of 3.0 psi to explore the impact of CCEP on the size frequency of LCT clusters. The result is in Fig. 6-6. As CCEP increases, the sparse LCT clusters become connected. This causes both the increasing size of large LCT clusters and the decreasing number of small LCT clusters. Additionally, as the LCT cluster size increases, its number decreases exponentially. This suggests that the contribution to the LCT capacity from the small sizes of LCT clusters cannot be negligible.

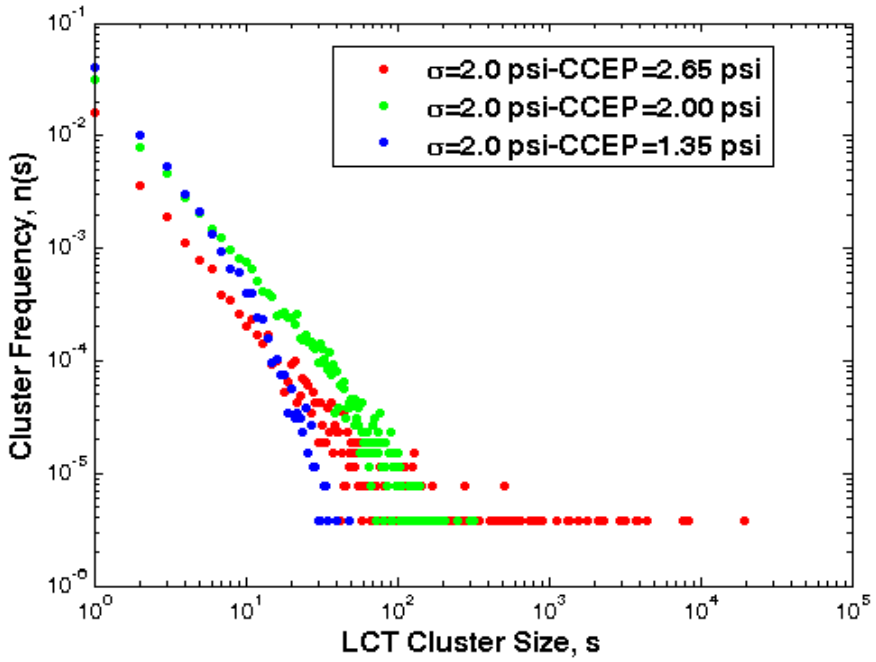

Fig. 6-6 Size frequency of LCT clusters at different CCEPs for a capillary entry pressure field. System dimensions are 512×512. μ=3.0 psi, λ_{Dx}=0, λ_{Dz}=0.

Figure 6-7 supports this deduction. This figure shows the accounting of each size of clusters to the total LCT volume. At a small CCEP of 1.35 psi, most of the LCTs are from clusters with only one cell. As CCEP increases, the contribution to LCTs from clusters with a specific size firstly decreases followed by an increase. This is because of competition between the cluster number and cluster size. When CCEP increases to the threshold of 2.65 psi, small LCT clusters contribute less to the total volume than the large ones. More importantly, the largest LCT cluster contributes the most. Thus, in the following, we make a detailed study on the largest LCT cluster that occurs at threshold CCEP.

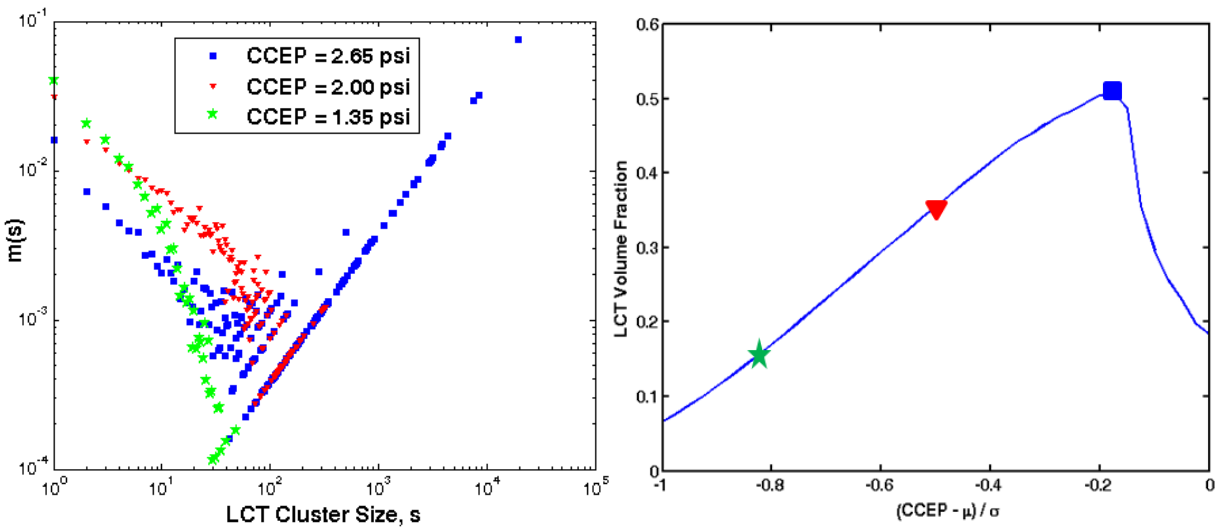

Fig. 6-7 Left: contribution to the LCT capacity from cluster size *s* at different CCEPs in 2D systems. Right: a LCT~CCEP curve with three CCEP points highlighted corresponding to three *m(s)* curves in the left plot. System dimensions are 512×512. μ=3.0 psi, λ_{Dx}=0, λ_{Dz}=0.

6.3.3 Effect of horizontal auto-correlation length on cluster properties

Figure 6-8 shows LCT~CCEP curves for 2D capillary entry pressure fields with different horizontal auto-correlation lengths. We chose CCEP to be 2.0 psi and plot LCT cluster size frequencies for these fields in Fig. 6-9. As the horizontal auto-correlation length increases, the number of small (cell#<10) LCT clusters decreases, whereas, the number of large (cell#>100) LCT clusters increases. This is similar to the effect of CCEP on the LCT amount as shown above.

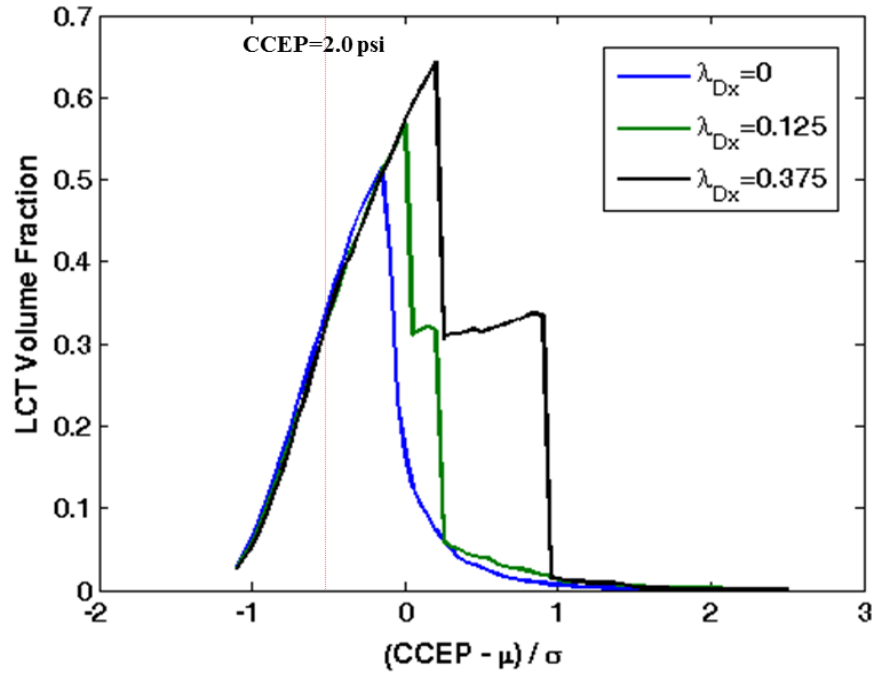

Fig. 6-8 LCT~CCEP curves for 2D systems with different horizontal auto-correlation lengths. System dimensions are 256×256. μ=3.0 psi, σ=2.0 psi, λ_{Dz}=0.

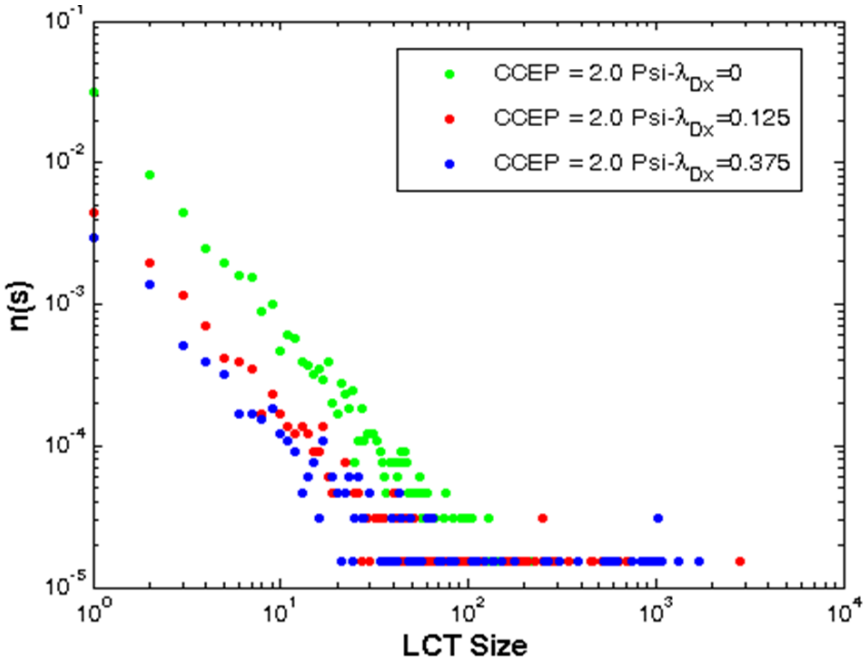

Fig. 6-9 Size frequency of LCT clusters for 2D systems with different horizontal auto-correlation lengths. System dimensions are 256×256. μ=3.0 psi, σ=2.0 psi, λ_{Dz}=0.

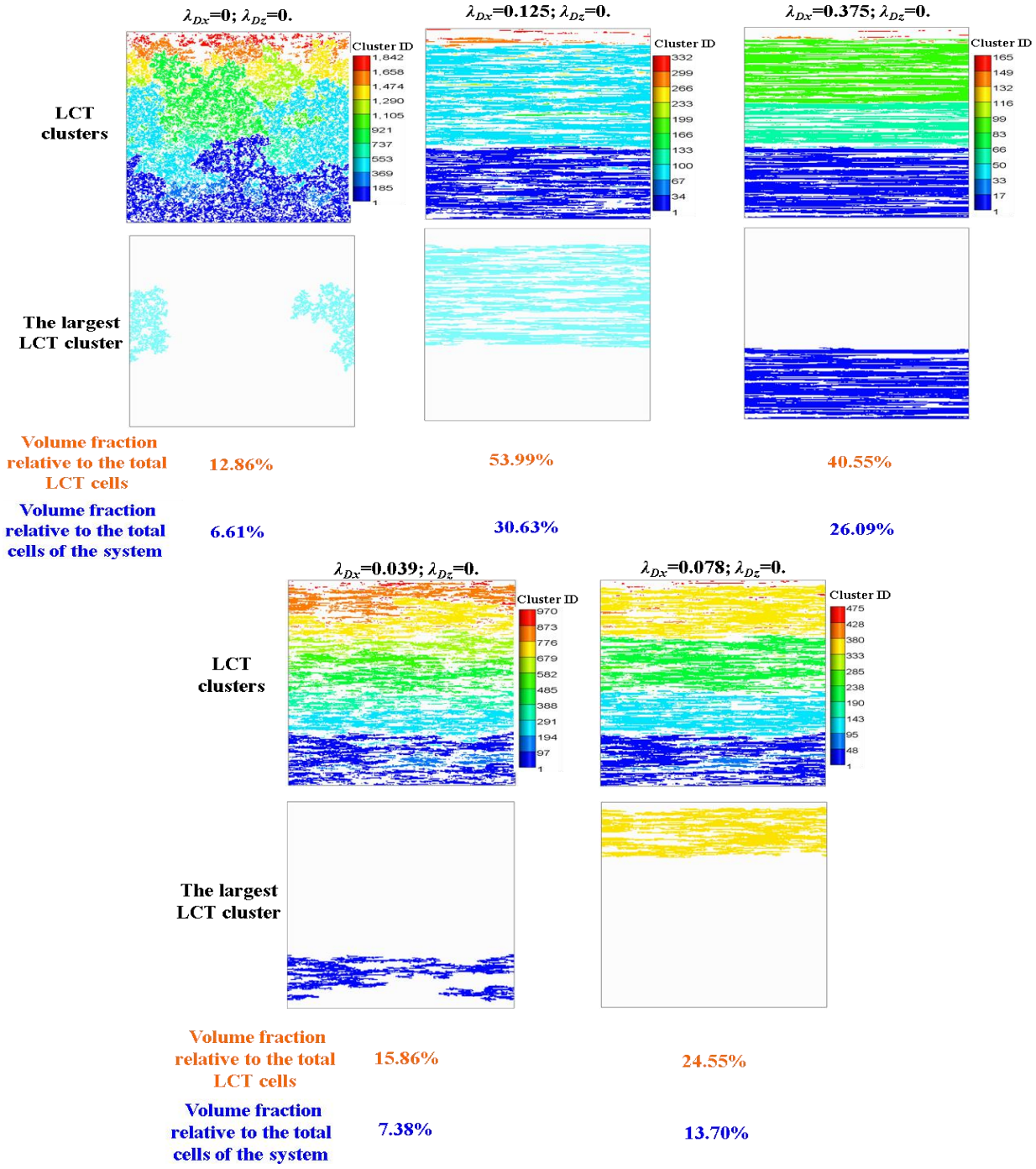

Fig. 6-10 Summary plots of LCT clusters, the largest cluster, and its volume fraction relative to the total LCT cells, and its volume fraction relative to the total cells of a domain. CCEPs are at thresholds. System dimensions are 256×256. μ=3.0 psi, σ=2.0 psi. The uncorrelated system in this figure is different from that in Fig. 6-3 because of different system dimensions.

Figure 6-10 shows the largest LCT cluster at threshold CCEPs for different horizontally auto-correlated systems. One notable thing is the lateral extent of the largest LCT cluster. In the uncorrelated domain (the leftmost panel in Fig. 6-10), the largest LCT is only half width of the domain (recall the cluster is connected via periodic lateral boundaries). However, as λ_{Dx} increases, the largest LCT cluster shows several complete layer-like patterns that laterally spans across the whole system, even when λ_{Dx} is only 1/25 of system width. To make a statistical analysis, we generate 50 realizations with λ_{Dx} equal to 0.039. 47 of them have the largest LCT cluster that spans across systems, and such a cluster contribute to 10~50% of the total LCT volume. Thus, there is a high chance that the largest cluster percolates laterally in a given geologic model, even if λ_{Dx} is very small.

Another notable thing is the size of the largest cluster and its change under the influence of the horizontal auto-correlation length. Although this length always enhances LCT capacity, it does not always increase the size of the largest cluster (Fig. 6-10). At large λ_{Dx}, the enhanced layering effect occurs to both LCT clusters and barriers clusters. The latter clusters tend to suppress the vertical connectivity of LCT cells, which strangles the growth of the largest LCT cluster. It accounted for as high as 54% of the total LCT volume as λ_{Dx} increased to 0.125. However, this volume fraction decreased to 41% at a large λ_{Dx} 0.375.

For 3D horizontally auto-correlated systems, Figure 6-11 and 6-12 shows the impact of horizontal auto-correlation lengths on LCT capacities and cluster properties (i.e., number and size), respectively. A noteworthy thing is the size of the largest LCT cluster. This cluster holds most of the LCT volume: it accounted for as high as 77% of the LCT capacity when λ_{Dx}=0.25 (Fig. 6-12). This large fraction suggests that the largest cluster is well-connected. In contrast, in the 3D uncorrelated system (middle column of Fig. 6-5), the largest cluster held only 1.78% of the LCT volume. This comparison implies that local capillary traps in horizontally auto-correlated fields get filled much easier than those in uncorrelated fields. Thus, a large injection rate would be less imperative in the former field than the latter. In the latter, local capillary traps are surrounded by barriers and these traps are poorly connected. Such spatial configurations

necessitate viscous flow (large injection rates) in order that CO_2 breaches these barriers and fills the surrounding traps. For the former auto-correlated fields, however, the largest LCT cluster is well-connected and extends widely, it can be easily accessed by CO_2, so the injection rate is not the key. Instead, perforation intervals should be optimized to assure that these intervals are connected to the largest LCT cluster.

Additionally, compared to 2D (Fig. 6-10), the added one more dimension in 3D systems weakens the effect of barrier layering on the connectivity of LCT clusters. Thus, the connectivity of LCT clusters in 3D is much better than in 2D, and, the largest cluster contributes more to the LCT capacity (Fig. 6-12 vs. Fig. 6-10).

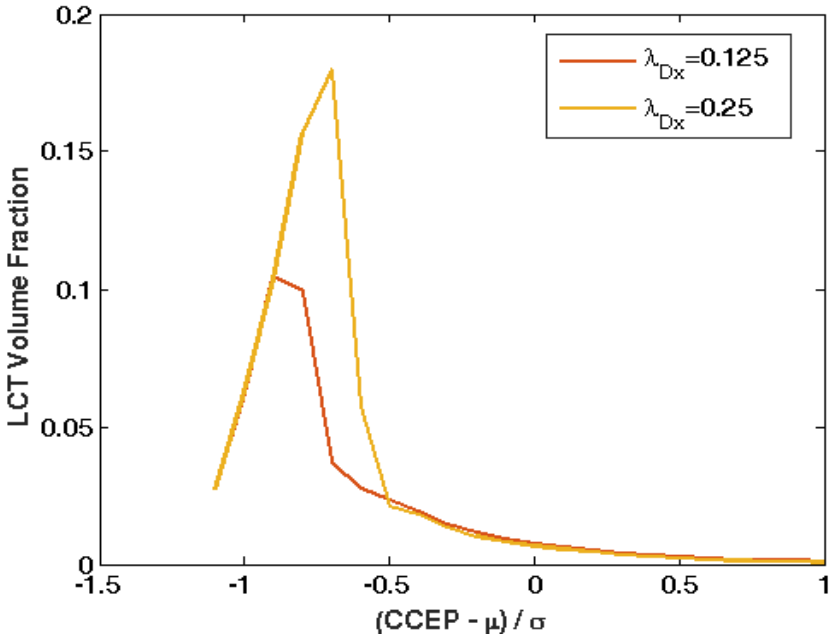

Fig. 6-11 LCT~CCEP curves for 3D horizontally auto-correlated systems. System dimensions are 128×128×128. μ=3 psi, σ=2 psi, λ_{Dz}=0.

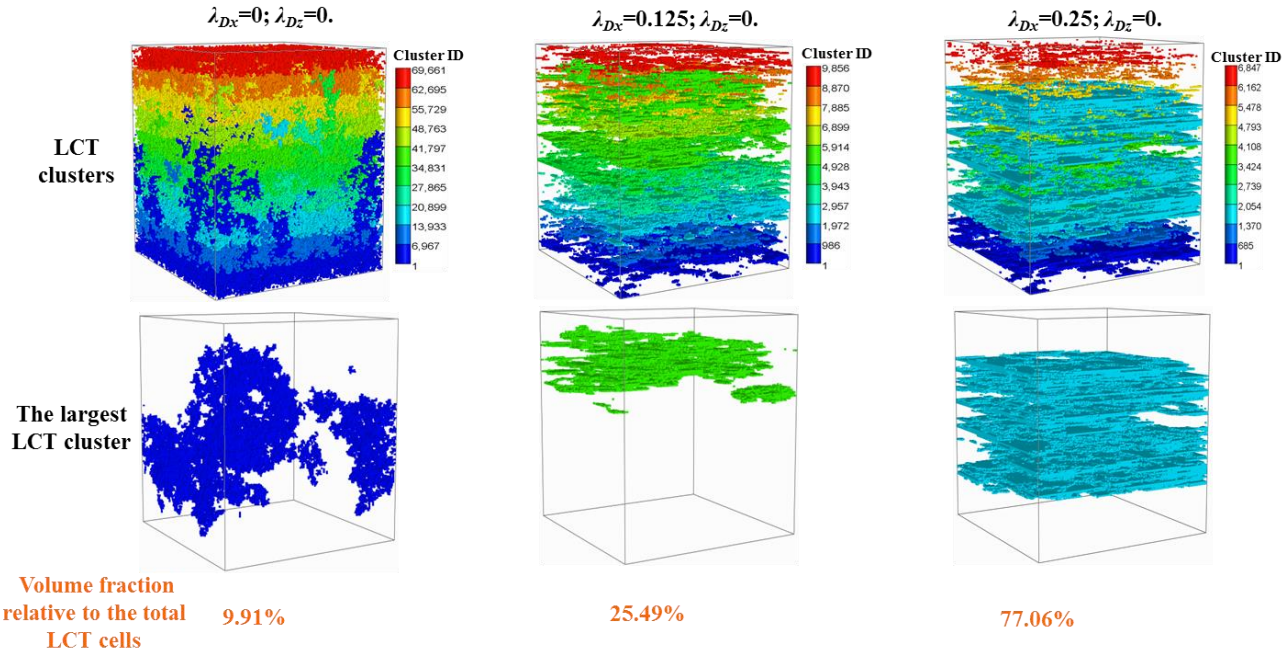

Fig. 6-12 Summary plots of LCT clusters, the largest LCT cluster, and its volume fraction relative to the total LCT cells. CCEPs are selected at thresholds. System dimensions are 128×128×128. μ=3 psi, σ=2 psi. The leftmost column is for an uncorrelated domain, which corresponds to the middle column in Fig. 6-5.

6.3.4 Effect of vertical auto-correlation length on cluster properties

Figure 6-13 through 6-15 shows LCT~CCEP curves, cluster size frequencies, and LCT cluster properties, respectively. Capillary entry pressure fields are vertically auto-correlated. At a small CCEP (1.6 psi, refer to Fig. 6-14), increasing vertical auto-correlation lengths yields more large (cell#>100) LCT clusters. This is easy to understand. The chosen CCEP is less than the threshold. At such a CCEP, flow path clusters have not connected to cells in the top layer and can still act as LCT clusters. Thus, the connectivity of LCT cells would be enhanced as the vertical auto-correlation length increases. This enhancement causes more large LCT clusters.

However, with increasing vertical auto-correlation length, LCT volume fraction decreases (Fig. 6-13). On one hand, the size of clusters increases. On the other hand, the number of clusters decreases (Fig. 6-14). The effect of cluster numbers on the LCT capacity overrides that of cluster size. This causes a decrease in the LCT volume fraction.

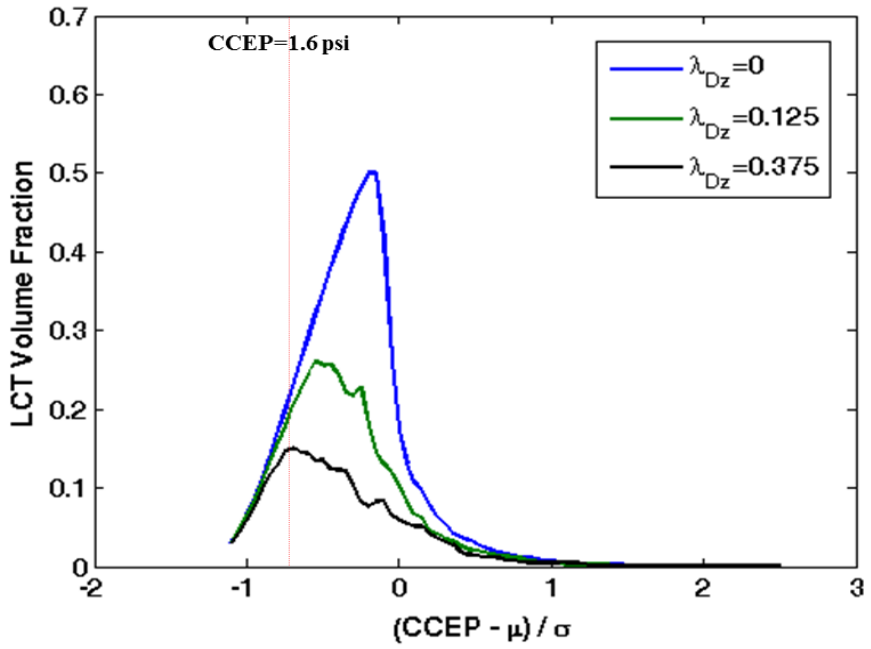

Fig. 6-13 LCT~CCEP curves for several 2D vertically auto-correlated systems with different vertical auto-correlation lengths. System dimensions are 256×256. μ=3 psi, σ=2 psi, λ_{Dx}=0.

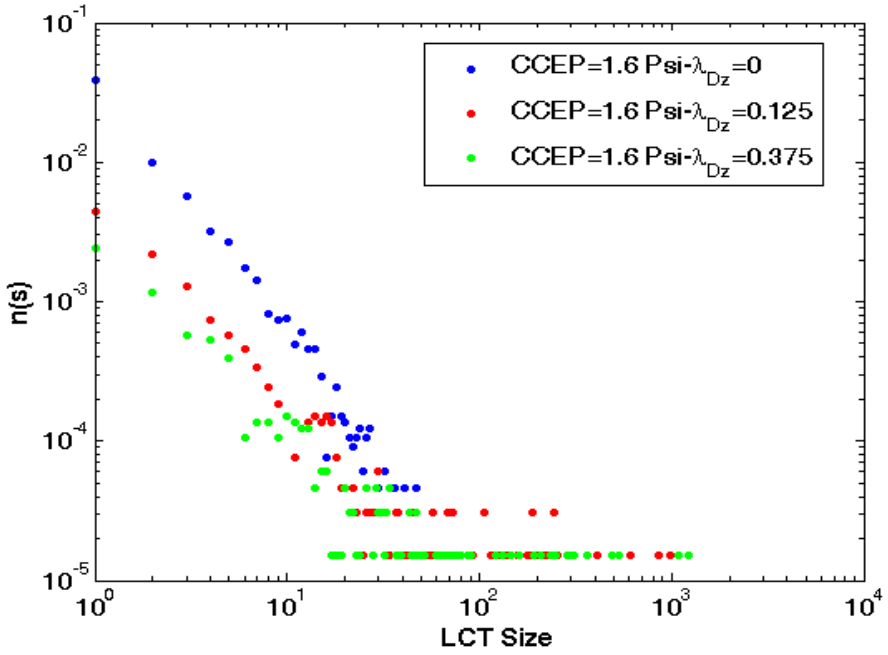

Fig. 6-14 Size frequency of LCT clusters in several 2D systems with different vertical auto-correlation lengths. System dimensions are 256×256. μ=3 psi, σ=2 psi, λ_{Dx}=0.

At threshold CCEPs, the volume fraction of the largest cluster relative to the LCT capacity becomes small as λ_{Dz} increases (Fig. 6-15): this fraction decreased slowly from 12.86% to 12.35% as λ_{Dz} increased from 0 to 0.375. Such an effect is different from the horizontal auto-correlation effect. Rather, the horizontal auto-correlation length heavily influences this fraction; it increased from 12.86% to 40.55% as λ_{Dx} increased from 0 to 0.375 (refer to Fig. 6-10). These observations mean that the size of the largest LCT cluster is more sensitive to λ_{Dx} than λ_{Dz}. However, the LCT capacity is less sensitive to λ_{Dx} than λ_{Dz}; the capacity sharply declined from 50% to 15.1% as λ_{Dz} increased from 0 to 0.375 (Fig. 6-15), whereas, the capacity increased from 50% to only 64.3% as λ_{Dx} increased by the same amount (Fig. 6-8).

The different sensitivities are attributed to an orientation effect of LCT clusters. As defined in the above, LCT clusters are flow paths that are disconnected from cells in the top boundary, rather than in the lateral boundaries. This feature causes a biased-directional effect on LCT cells: the vertical accumulation of flow path clusters is unfavorable to the occurrence of LCT cells, while, the horizontal extending of flow path clusters is favorable to the increase in the LCT cluster size. Thus, the vertical connectivity (λ_{Dz}) of LCT clusters mostly affects LCT capacity while the horizontal connectivity (λ_{Dx}) mainly influences the size of the largest cluster.

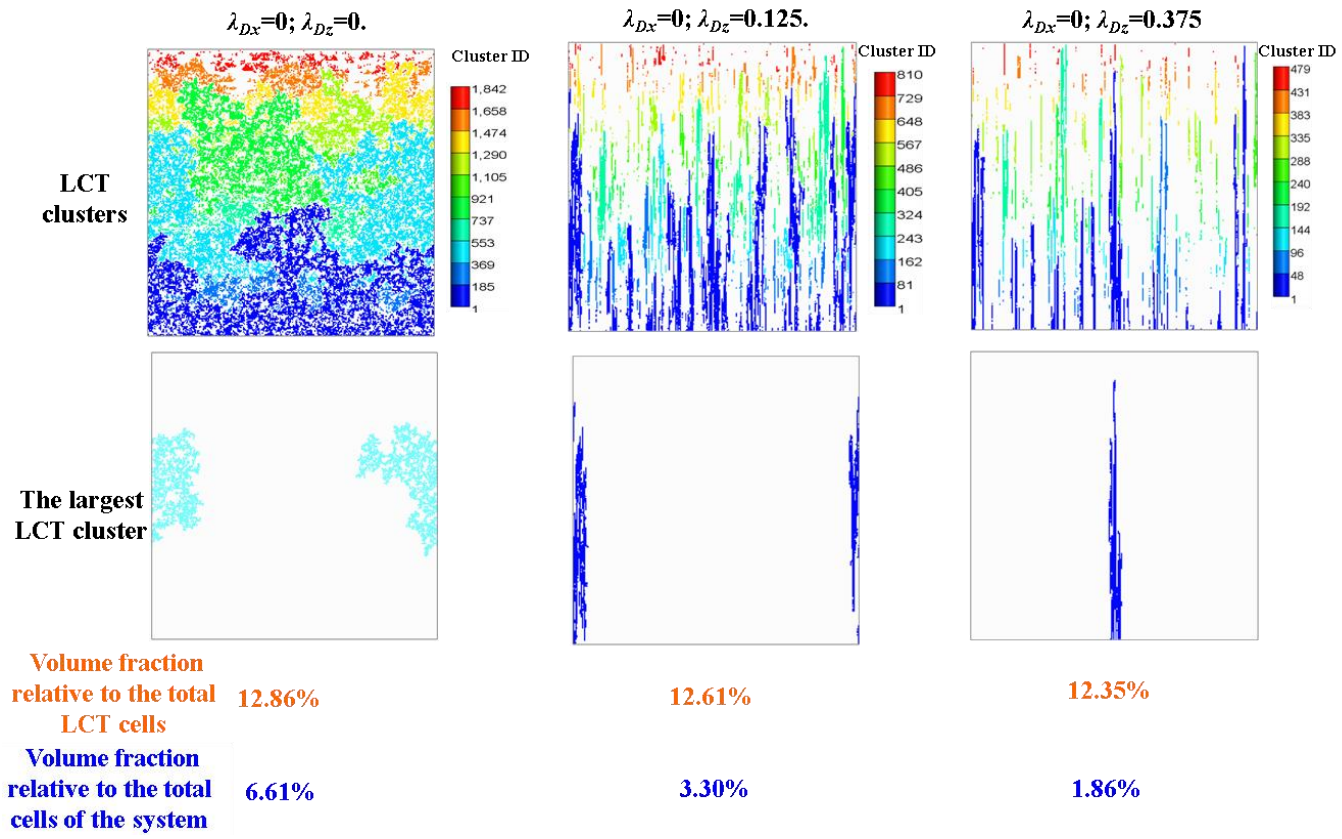

Fig. 6-15 Summary plots of LCT clusters, the largest LCT cluster, its volume fraction relative to the total LCT cells, and its volume fraction relative to the total cells of a domain. Capillary entry pressure fields are auto-correlated in the vertical direction. CCEPs are selected at thresholds. System dimensions are 256×256. μ=3 psi, σ=2 psi.

The following analysis is for 3D. Figures 6-16 through 6-17 show LCT~CCEP curves and the largest LCT cluster properties. Quantitative differences between 2D and 3D exist in the aspects of both the fraction of the largest cluster and the change of this fraction with the vertical auto-correlation length. In 3D, at threshold CCEPs, the fraction sharply decreased from 9.91% to 1.80% as λ_{Dz} increased from 0 to 0.125. In 2D, however, the fraction decreased from 12.86% to only 12.61% (refer to Fig. 6-15). The sharp decrease in 3D is obviously attributed to the enhanced connectivity of flow path clusters introduced by the added one dimension. In 3D, even if a small augment of λ_{Dz}, it would cause vertically-extended flow path clusters to be connected to cells in the top layer, and therefore, these flow path clusters cannot act as LCT clusters.

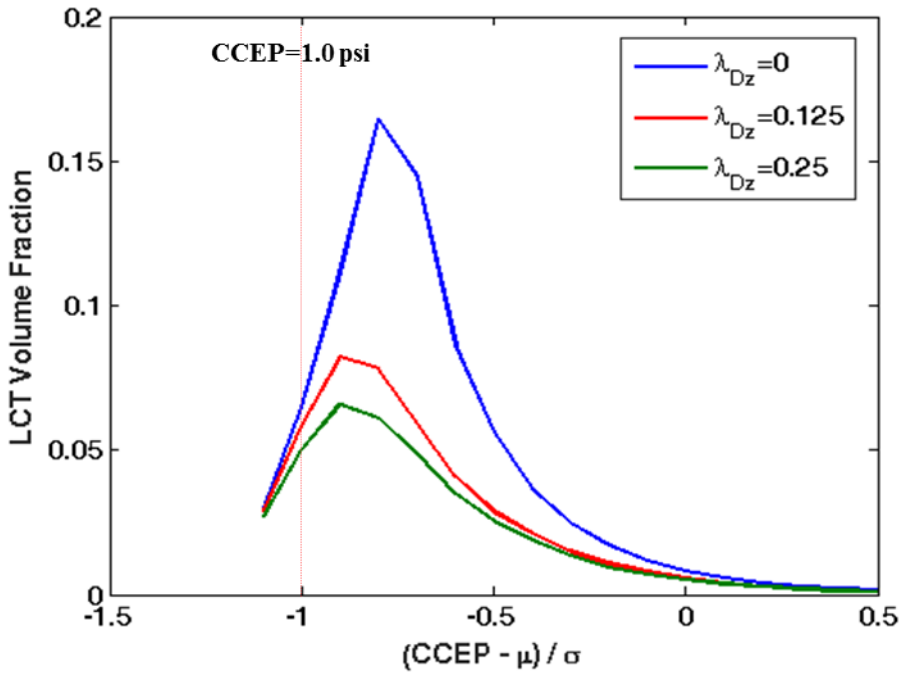

Fig. 6-16 LCT~CCEP curves for vertically auto-correlated systems with different vertical auto-correlation lengths. System dimensions are 128×128×128. μ=3 psi, σ=2 psi, λ_{Dx}=0.

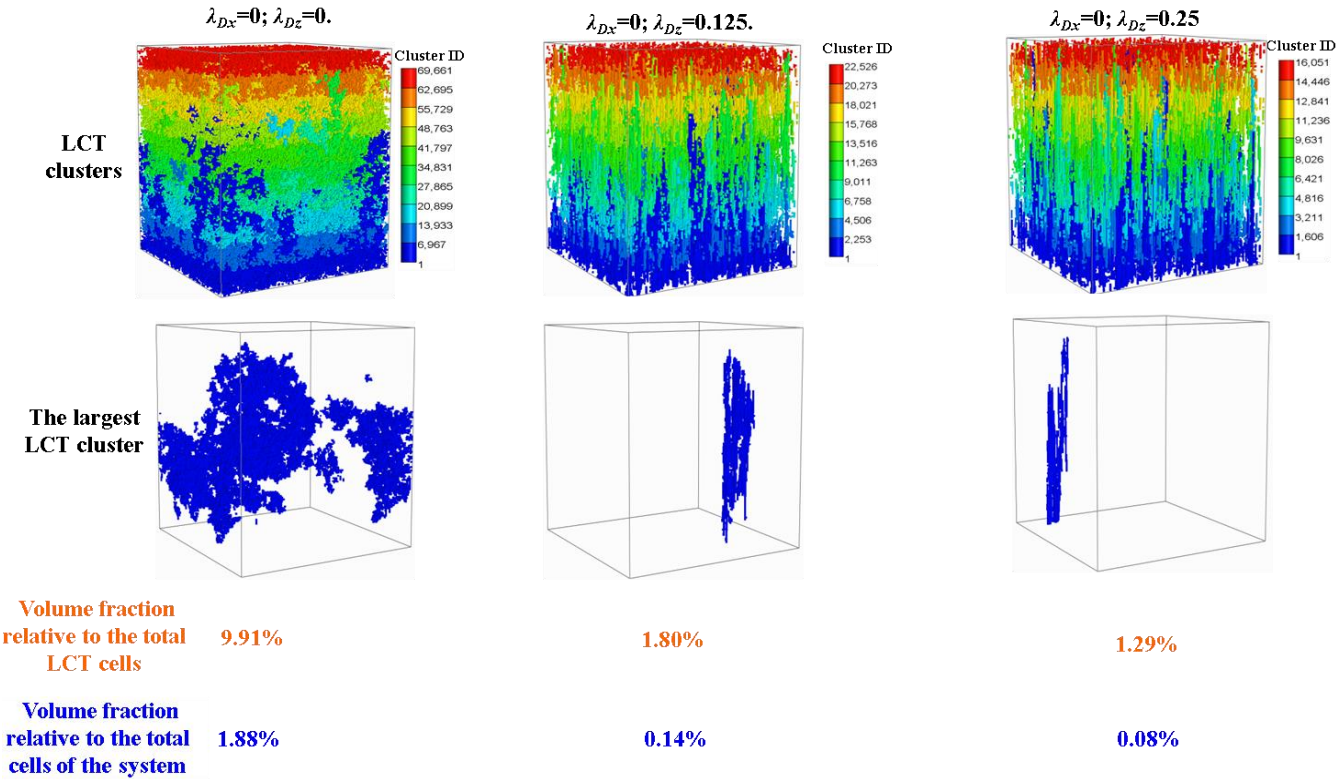

Fig. 6-17 Summary plots of LCT clusters, the largest LCT cluster, its volume fraction relative to the total LCT cells, and its volume fraction relative to the total cells of a domain. The leftmost column is for an uncorrelated domain, which corresponds to the rightmost column in Fig. 6-12. Capillary entry pressure fields are auto-correlated in the vertical direction. CCEPs are at thresholds. System dimensions are 128×128×128. μ=3 psi, σ=2 psi.

6.4 SUMMARY

We conduct a thorough analysis on the local capillary trap (LCT) cluster properties (i.e., cluster size, number, and the largest LCT cluster) in both 2D and 3D capillary entry pressure fields. We examine the influences of CCEP, standard deviation, and the auto-correlation length on the LCT cluster properties. Generally, these influences in 2D are qualitatively similar to those in 3D, but significant quantitative differences are observed. The differences include the connectivity of LCT clusters and the volume fraction of the largest cluster relative to the LCT capacity. The effect of the LCT orientation on both LCT amount and cluster size is highlighted in this chapter.

Chapter 7: Modeling Local Capillary Trapping during CO_2 Injection[3]

Previous chapters employed a geologic criterion algorithm to study local capillary traps in a given geologic model. As local capillary traps are intrinsic to a geologic model, the algorithm uses capillary entry pressure fields as input. Thus, these traps identified by the algorithm are *static*, in other words, the algorithm does not account for CO_2 flow dynamics.

The purpose of this chapter is to rapidly evaluate the injection strategies (i.e., injection rate and injected volume) on *dynamic* local capillary trapping, that is, trapping occurs during CO_2 injection. To do this, we add fluid dynamics into the geologic criterion algorithm. The connectivity analysis originally developed for characterizing well-to-reservoir connectivities is adapted here to simulate CO_2/water immiscible flow. In the analysis, an edge weight is used to describe the connectivity between neighboring grid blocks. This weight accounts for the multiphase flow properties, injection rate, and buoyancy effect.

We employ the integrated methods to quantify the amount of local capillary traps that can be filled during CO_2 injection. We mimic various injection scenarios in storage formations with different levels of heterogeneity. We demonstrate that how injection strategies affect local capillary trapping under the influence of reservoir heterogeneity.

[3]Parts of this this chapter has been presented in the following conference: Ren, B., Bryant, S.L., Lake, L.W. 2015. Fast Modeling Of Local Capillary Trapping During CO_2 Injection into a Saline Aquifer. Paper CMTC-439486-MS presented at Carbon Management Technology Conference, Sugar Land, Texas, 17-19 November.

7.1 USING A CONNECTIVITY ANALYSIS (CA) TO PREDICT CO_2 PLUME

7.1.1 Connectivity and edge weight

According to Hirsch and Schuette (1999), a reservoir geologic model can be considered as a graph, and a grid block in the geologic model is equivalent to a node in the graph. Adjacent nodes are connected with edges that are weighted by reservoir parameters such as porosity and permeability. The physical meaning of the edge weight is the time needed to fill a given pore volume with a fluid of unit viscosity under a unit pressure gradient. Its original definition is for modeling single-phase flow (Hirsch and Schuette, 1999).

Here, following the work by Jeong (2016), we extend the edge weight for modeling two-phase immiscible flow by incorporating the buoyancy effect, relative permeability, and viscous pressure. A new definition is derived based on Darcy's law. The subscript 'g' represents CO_2.

$$q_g = \frac{k k_{rg} A(\Delta P + \rho_g g h)}{\mu_g L} \tag{7.1}$$

If the transmissivity (T) between cells is defined as Eq. 7.2, we can write Eq. 7.1 into Eq. 7.3.

$$T = k \frac{A}{L} \tag{7.2}$$

$$q_g = \frac{T k_{rg} (\Delta P + \rho_g g h)}{\mu_g} \tag{7.3}$$

Equation 7.4 shows the original definition of edge weight for single-phase flow. In two-phase flow, a given cell is assumed to be filled by CO_2 to an average saturation ($\overline{S_g}$). It is equal to the average gas saturation before breakthrough in 1D immiscible displacement, as determined from the fractional flow curve (Lake et al. 2014). Then, the edge weight for two-phase flow can be written as Eq. 7.5.

$$ED1 = \frac{\sqrt{Vp_i * Vp_j}}{T_{ij}} \tag{7.4}$$

$$ED2 = \frac{\sqrt{Vp_i * Vp_j} * \overline{S_g}}{q_g} \tag{7.5}$$

Substituting Eq. 7.3 into Eq. 7.5, we get the final form of edge weight (Eq. 7.6). In this equation, $\overline{k_{rg}}$ is the average relative permeability of CO_2. Applications demonstrate that endpoint gas relative permeability is a better choice than the gas relative permeability at the average gas saturation (Jeong 2016).

$$ED2 = \frac{\sqrt{Vp_i * Vp_j} * \overline{S_g} * \mu_g}{T\,\overline{k_{rg}}(\Delta P + \rho_g g h)} \tag{7.6}$$

In Eq. 7.6, the viscous pressure difference (ΔP) between cells is approximated by the analytical solution (Eq. 7.7) of steady state radial flow in a homogeneous medium.

$$\Delta P = \frac{Q\mu_g}{2\pi \bar{k} H_{re}}\left[Ei\left(-\frac{\phi\mu_g C_t r_2^2}{4\bar{k}t}\right) - Ei\left(-\frac{\phi\mu_g C_t r_1^2}{4\bar{k}t}\right)\right] \tag{7.7}$$

$$Ei(-x) = -\int_x^{\infty} \frac{e^{-y}}{y} dy \tag{7.8}$$

In the above, Q is the well injection rate, μ_g is the viscosity of CO_2, $\bar{k}$ is the geometric average of permeability, H_{re} is the height of a reservoir, C_t is the reservoir compressibility, r is the distance from a wellbore, t is time.

After calculating the edge weight (*ED2*) between adjacent cells, it is scaled by the local minimum (the minimum among the six weights for one cell in 3D) in order that the buoyant behavior of CO_2 can be represented (Jeong 2016). Then, the connectivity between a wellbore cell and any given cell is calculated by summing the scaled edge weight along the shortest path. These connectivities are ranked from low to high. Finally, cells are filled with CO_2 to the average gas saturation in the order of the connectivity until the cumulative volume reaches the desired volume. By doing this, a CO_2 plume shape is predicted.

7.1.2 Applicability of the connectivity analysis

The connectivity analysis gives a good and fast prediction of CO_2 migration during CO_2 injection into a saline aquifer (Jeong 2016). It accounts for many factors on CO_2 plume behavior, including the injection rate, buoyant force, reservoir heterogeneity, topology of storage aquifers, and relative permeability effect. However, the method does not work properly when a saline

aquifer become very homogeneous or when its structure has an overwhelming influence on CO_2 plume migration.

7.2 CONSIDERATION IN USING THE GEOLOGIC CRITERION ALGORITHM

As shown in chapter 4, the geologic criterion algorithm is used to predict local capillary traps in a capillary entry pressure field. This capillary entry pressure field is generated from a permeability realization using the Leverett j-function (Leverett 1941). The success of determining local capillary traps depends on the appropriate selection of critical capillary entry pressure (CCEP). Chapter 4 demonstrated that a threshold CCEP, at which the maximum amount of local capillary traps are identified, gives a good representation of both the LCT amount and spatial distribution. Thus, we will use this CCEP in the following. Additionally, we use closed boundaries for local capillary traps, that is, lateral boundaries are treated as flow barriers.

7.3 APPLICATION OF THE INTEGRATED MODEL

In this part, we will combine the connectivity analysis and the geologic criterion to predict the amount of local capillary trapping during CO_2 injection. The effects of reservoir heterogeneity, injection rate, and injected volume are examined.

We generate nine three-dimensional permeability fields using fast Fourier transform (Appendix B). Field dimensions are 64×64×32, and grid size is 1×1×1 ft. These fields have different levels of heterogeneity, which is measured by the Dykstra-Parsons variation coefficient (Dykstra and Parsons 1950), V_{dp}. The definition of V_{dp} is in Eq. 7.9.

$$V_{dp} = \frac{k_{50} - k_{84.1}}{k_{50}} \tag{7.9}$$

Where k_{50} and $k_{84.1}$ is defined on the log-normal probability graph. Log(k_{50}) is less than 50% of the samples in the log permeability spectrum, whereas, log($k_{84.1}$) is less than 84.1% of the samples, which is one standard deviation from the mean. V_{dp} is a dimensionless number that ranges from 0 to 1. A homogeneous reservoir has a coefficient of permeability variation that approaches 0 whereas an extremely heterogeneous reservoir has a coefficient of permeability

variation that approaches 1. The V_{dp} values for the nine fields are listed Table 7-1, and they are between 0.13 through 0.91. The permeability fields are lognormal, so the mean and standard deviation are dependent (refer to Table 7-1). We purposely vary standard deviation to create different V_{dp} of permeability fields.

Table 7-1. Properties of permeability, porosity and capillary entry pressure fields

Model #	k Mean, mD	k Standard deviation, mD	V_{dp}	ϕ Mean	p_c^{entry} Mean, psi	p_c^{entry} Standard deviation, psi	Threshold CCEP, psi
Hete1	498.9	70.3	0.13	0.29	1.21	0.09	1.1
Hete2	497.9	140.2	0.24	0.29	1.23	0.17	1.05
Hete3	496.9	219.6	0.34	0.29	1.28	0.27	1.00
Hete4	496.2	298.7	0.43	0.29	1.35	0.38	0.95
Hete5	495.0	446.7	0.54	0.28	1.50	0.60	0.95
Hete6	493.2	797.8	0.68	0.27	1.94	1.19	0.95
Hete7	491.7	1335.6	0.76	0.26	2.60	2.12	0.95
Hete8	491.0	3783.0	0.86	0.24	5.04	6.22	1.15
Hete9	496.9	9574.5	0.91	0.22	10.09	16.97	1.45

The other indicator of heterogeneity is the auto-correlation length. Since we have intensively studied the impact of auto-correlation lengths on local capillary traps in chapter 4, here we assume a fixed auto-correlation and focus on the impact of injection strategies on local capillary trapping. The horizontal auto-correlation of the nine permeability fields is set to be 4 ft, and the vertical auto-correlation length is zero.

After generating permeability fields, we correlated permeability with porosity and then correlated the above two parameters with capillary entry pressure following the procedures

described in chapter 3. Properties of these permeability, porosity and capillary entry pressure fields are summarized in Table 7-1. Figure 7-1a shows an example permeability field with V_{dp} equal to 0.54. Figures 7-1b and 7-1c show the corresponding porosity field and capillary entry pressure field, respectively.

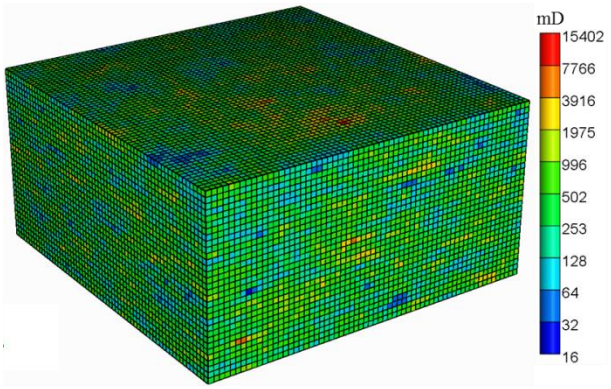

(a)

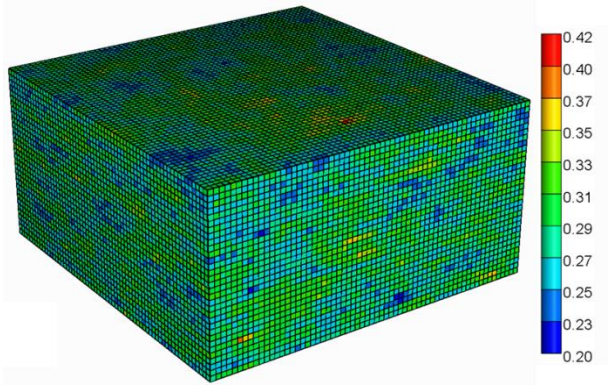

(b)

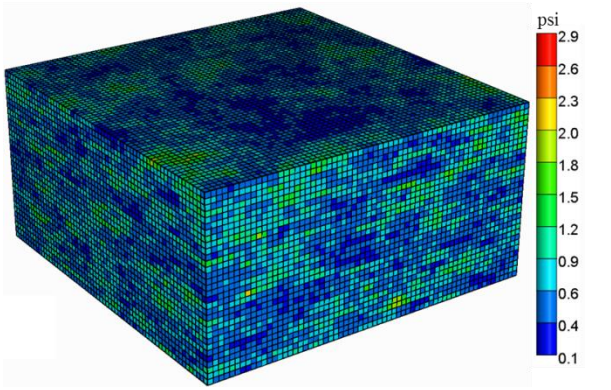

(c)

Fig. 7-1 Petrophysical fields of Hete5 in Table 7-1. (a) The permeability field. (b) The porosity field. (c) The capillary entry pressure field.

Here, we define two terms: the static LCT volume ratio and the dynamic LCT volume fraction. The differences between them are schematically shown in Fig. 7-2. The static LCT volume ratio is the number of LCT cells divided by the number of cells in a storage domain. The dynamic LCT volume fraction means the fraction of LCT cells in a CO_2 swept zone during injection. The physical implication of the static LCT volume ratio is the fraction of the pore space occupied by local capillary trapping in a storage domain, whereas, the dynamic LCT volume fraction is the fraction of CO_2 stored in local capillary trapping relative to the injected CO_2. Therefore, the former ratio is definite for a given reservoir while the latter changes with injection durations or injected volumes. However, the dynamic fraction would approach the static ratio as CO_2 injection continues, and they would be equal when CO_2 fully fills a storage domain.

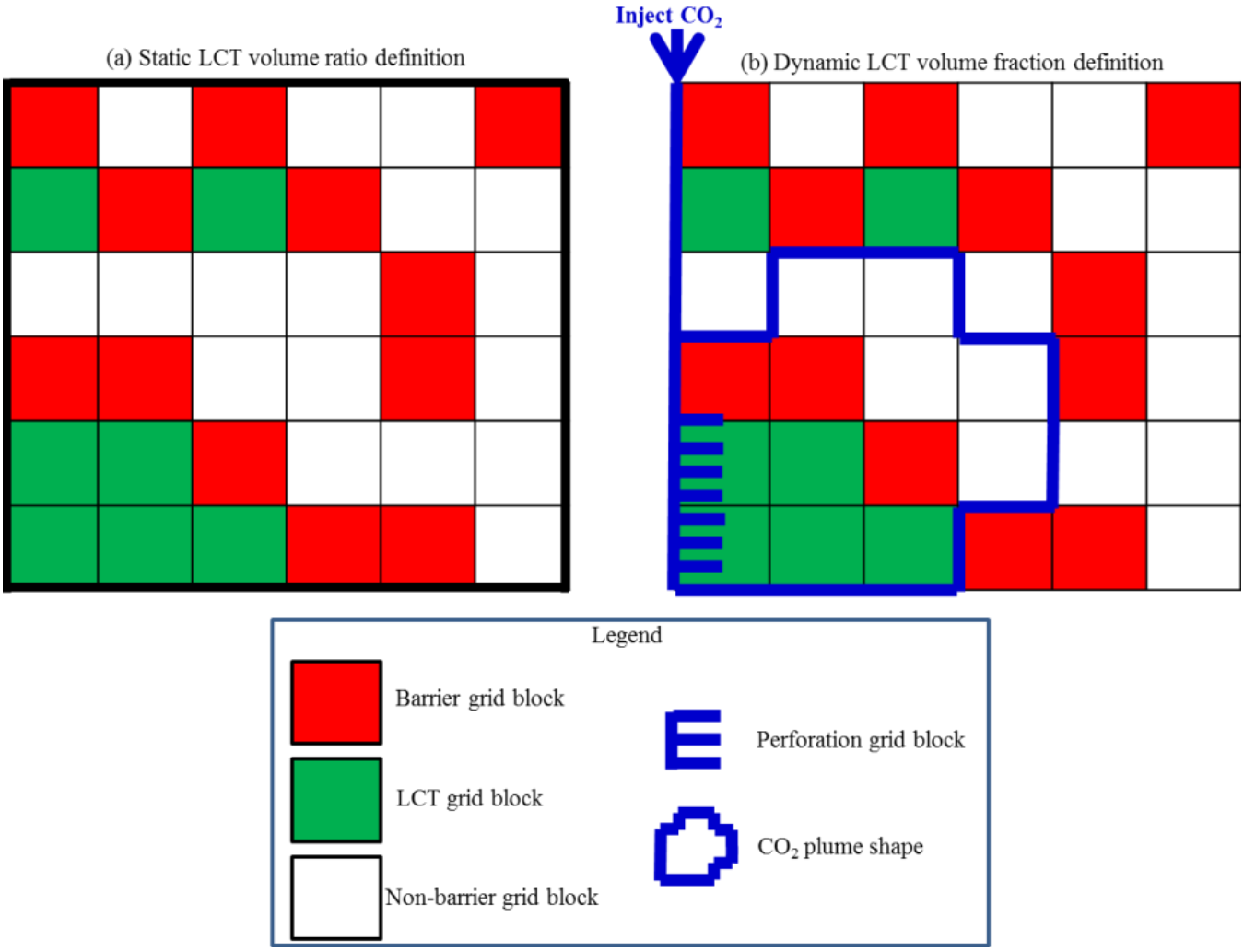

Fig. 7-2 Schematic illustration of the static LCT volume ratio and the dynamic LCT volume fraction. (a) The static ratio is the ratio of the number of green LCT cells over the total cells in a storage domain (the black square). (b) The dynamic fraction is the fraction of the number of green LCT cells in a CO_2 swept zone (the closed blue line) over the total cells in this zone.

7.3.1 Input settings in the connectivity analysis

In the connectivity analysis, we predict CO_2 plume shape mainly using permeability and porosity fields as input. Two other important parameters involved are the average CO_2 saturation and average CO_2 relative permeability. The average CO_2 saturation defines a magnitude of gas saturation, until which, CO_2 continuously fills in a given cell before moving into the adjacent cell. This is set to be equal to the average gas saturation as determined from a fractional flow

curve. Using the relative permeability curve in Fig. 7-3 and fluid properties in Table 7-2, we construct the fractional flow curve for CO_2 (see Fig. 7-4) without considering gravity, and then calculate the average gas saturation to be 0.54. The average gas relative permeability is set to be 0.86 (endpoint gas relative permeability).

Table 7-2. Parameter settings in the connectivity analysis. RC is the reservoir condition, and SC is the surface condition.

CO_2 volume ratio RC/SC	3.02E-3
CO_2 viscosity (RC, cp)	8.61E-2
CO_2 density (RC, kg/m^3)	618.70
Water density (RC, kg/m^3)	1024.60
Average CO_2 saturation	0.54
Endpoint CO_2 relative permeability	0.86

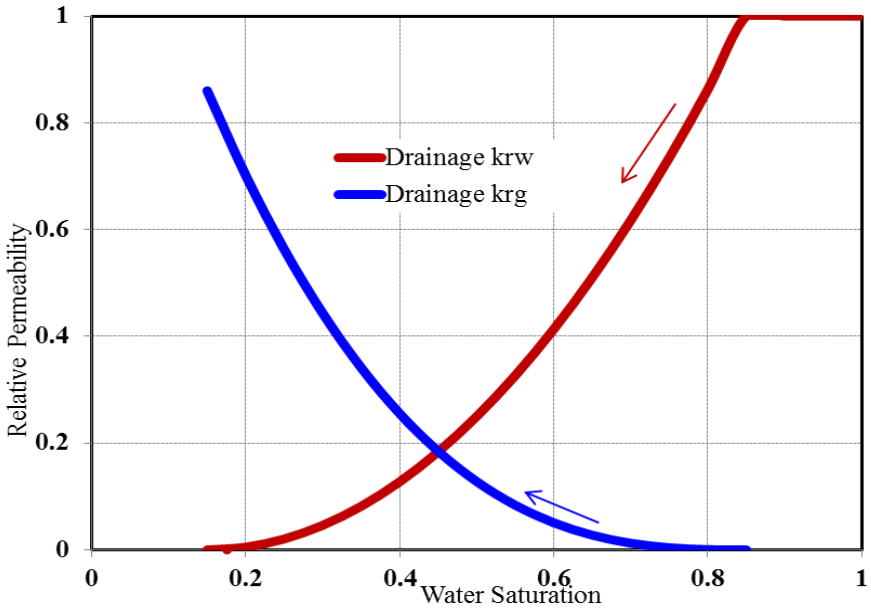

Fig. 7-3 Relative permeability curves used in the connectivity analysis.

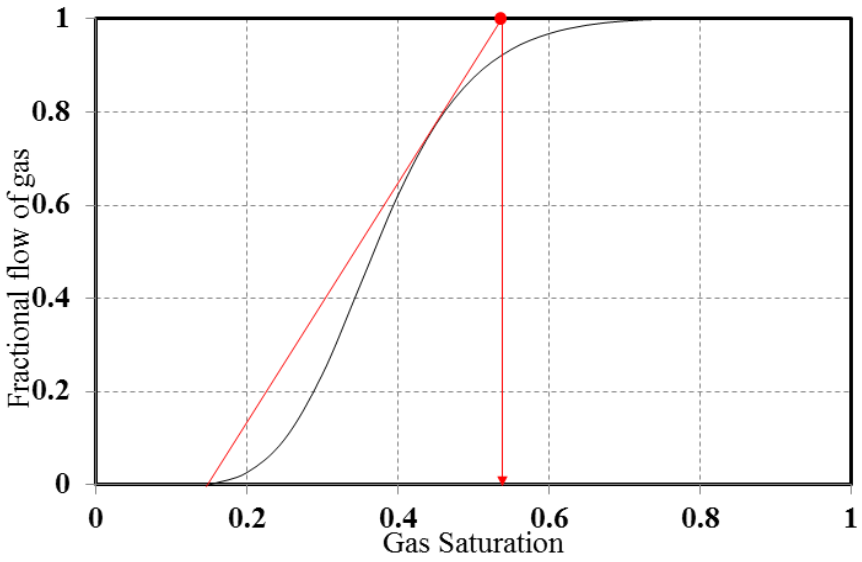

Fig. 7-4 Fractional flow curve of gas (CO_2).

In the connectivity analysis, six injection rates are selected: 8E+2, 8E+3, 8E+4, 8E+5, 8E+6, and 8E+7 MMScf/d. They cover the range of reported industrial CO_2 injection rates during geological carbon sequestration (IPCC 2005). The corresponding buoyancy number is calculated using Eq. 7.10 (Shook et al. 1992). In this equation, N_{gr} is the buoyancy number, $\Delta\rho$ is the density difference between brine and CO_2 (405.9 kg/m^3). g is gravitational constant (9.8 m/s). k_v is the mean of vertical permeability (refer to the 2nd column of Table 7-1). u is CO_2 flux penetrating a storage formation. μ_g is the viscosity of CO_2 (0.049 cp). α is the formation dip angle with respect to the horizontal direction. L and H are the reservoir length and perforation length, respectively.

$$N_{gr} = \frac{\Delta\rho g k_v H \cos\alpha}{u \mu_g L} \tag{7.10}$$

Table 7-3 shows injection settings and buoyancy numbers. Totally injected CO_2 volume is 1.6E+6 Scf, which is equivalent to about 0.14 pore volume of the storage domain. The injected volume is kept the same for different injection rates. This yields different injection durations in Table 7-3.

Table 7-3. Injection settings and buoyancy numbers in the connectivity analysis

Well type	Vertical injector					
Perforated cells	(29:31, 32, 32)					
Injection rate, Scf/d	8E+2	8E+3	8E+4	8E+5	8E+6	8E+7
Injection duration, day	2000	200	20	2	0.2	0.02
Buoyancy number	6E+1	6E+0	6E-1	6E-2	6E-3	6E-4

7.3.2 Input settings in the geologic criterion algorithm

Two important inputs involved in the algorithm are: (1) a capillary entry pressure field, it is correlated with the permeability field used in the above connectivity analysis. Table 7-1 lists properties of the input capillary entry pressure fields. (2) Critical capillary entry pressure (CCEP). CCEP is chosen to be at a threshold value as analyzed in chapter 4.

7.4 RESULTS

7.4.1 Effect of V_{dp} on the static LCT volume ratio

Figure 7-5 shows the impact of CCEP on the static LCT volume ratios in two different ranges of V_{dp}, i.e., 0.13~0.68 and 0.68~0.91. The former range represents homogenous and intermediately heterogeneous fields while the latter indicates highly heterogeneous fields. In the former fields, the point of the maximum static LCT volume ratio moves to the left side. This means threshold CCEP decreases with increasing V_{dp}. However, the highly heterogeneous fields show an opposite trend. This is because: at small V_{dp}, the mean of capillary entry pressure for these fields are close (refer to Table 7-1), the increasing standard deviation (through increasing V_{dp}) enhances the connectivity of LCT clusters, so threshold CCEP becomes small. However, at large V_{dp}, the mean of capillary entry pressure rapidly increases with V_{dp}. This trend protrudes the effect of the mean of capillary entry pressure on threshold CCEP. The values of threshold CCEP for all the fields are listed in Table 7-1.

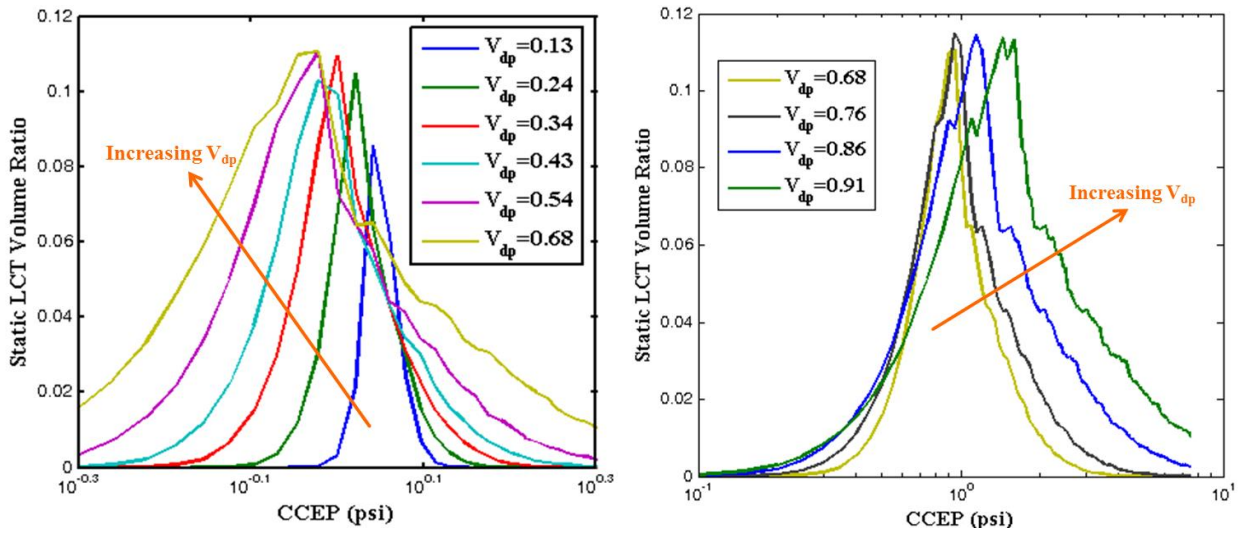

Fig. 7-5 Change of static LCT volume fractions with CCEP for different heterogeneous fields. Left: V_{dp}=0.13~0.68. Right: V_{dp}=0.68~0.91.

Figure 7-6 shows the maximum static LCT volume ratio versus V_{dp}. As V_{dp} increase, the maximum static LCT volume ratio first increases rapidly, followed by a leveling off. The inflection point occurs at V_{dp} around 0.3. This behavior can be explained through comparing the mean of capillary entry pressure to threshold CCEP. As shown in Table 7-1, when V_{dp} is less than 0.3, the threshold CCEP is close to the mean. Around this point, a small increase in standard deviation would cause a high possibility of forming local capillary traps. This explains the fast increase in the static LCT volume ratio. However, when V_{dp} is larger than 0.3, the threshold CCEP becomes much smaller than the mean. This gives rise to more barriers in a storage domain. On one hand, more connected barriers would surround more local capillary traps, so we see a small increase in the static LCT volume ratio. On the other hand, more barriers mean fewer flow paths; this decreases the number of local capillary traps. Therefore, the maximum static LCT volume ratios slightly fluctuate with V_{dp}.

For most of the reservoirs, V_{dp} typically ranges from 0.50 to 0.90 (Lake et al. 2014). In this range, the maximum static LCT volume ratio was around 11%. This can be considered the upper bound of LCT capacities in these capillary entry pressure fields.

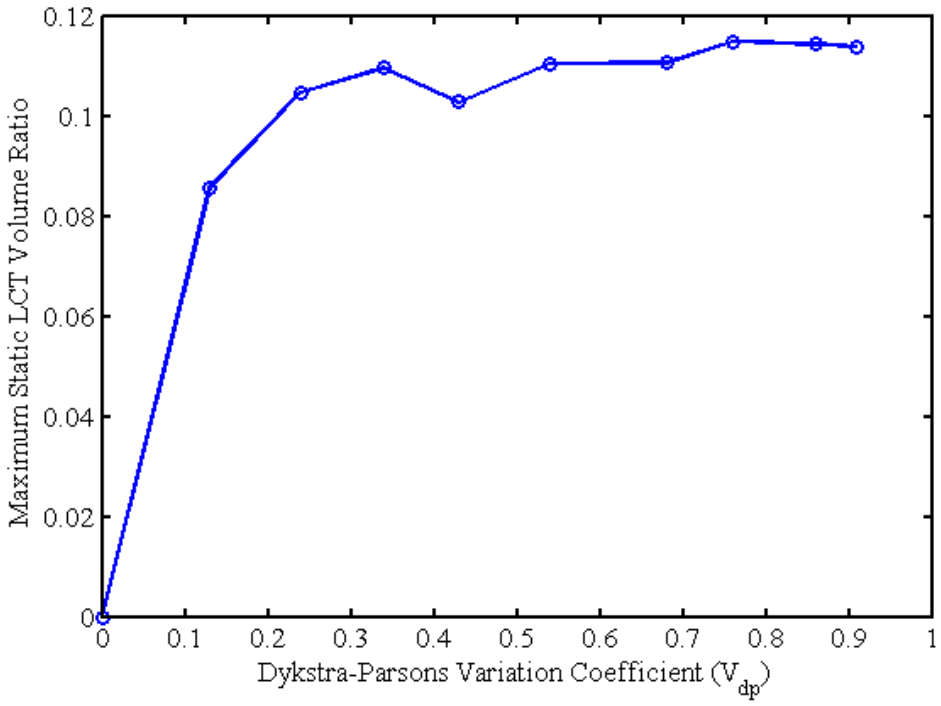

Fig. 7-6 Change of the maximum static LCT volume ratios with V_{dp}.

7.4.2 Effect of V_{dp} on the dynamic LCT volume fraction

Figure 7-7 shows the dynamic LCT volume fractions in different heterogeneous fields at the end of injection. In this figure, the flow regimes are categorized by the buoyancy number (N_{gr}): a viscous-dominated flow regime (N_{gr}<0.6), a buoyancy-dominated flow regime (N_{gr}>6), and a transient regime (0.6≤ N_{gr}≤ 6). In both the viscous-dominated and transient flow regimes, the fraction generally increases with V_{dp}. This trend is very similar to that of the static LCT ratio versus V_{dp} (refer to Fig. 7-6). In the buoyancy-dominated regime, however, the dynamic fraction is almost independent of V_{dp} in the interval of 0.25~0.68. For the typical range of V_{dp}, the dynamic LCT volume ratio varies from 8% to 28% that is subject to V_{dp} and injection rates. These fractions mean that local capillary trapping occupies a non-negligible portion of CO_2 plumes.

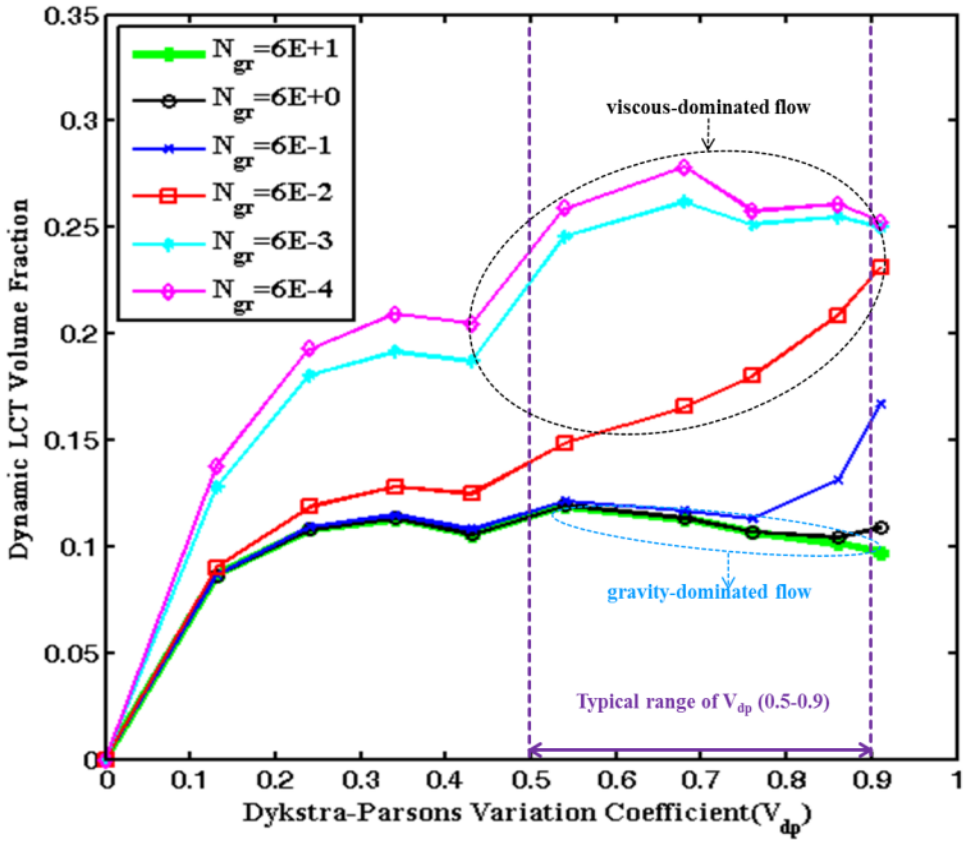

Fig. 7-7 Change of the dynamic LCT volume fractions with V_{dp} for different injection rates (buoyancy numbers). The two circled areas indicate viscous-dominated and buoyancy-dominated flow regimes. In between is the transient flow regime.

7.4.3 Effect of buoyancy number on the dynamic LCT volume fraction

Figure 7-7 shows the effect of buoyancy number (injection rate) on the dynamic LCT volume fractions. When a reservoir is relatively homogenous (V_{dp} <0.45), the fractions are independent of injection rates in the buoyancy-dominated and transient flow regimes. In the viscous-dominant regime, however, increasing the injection rate causes a large dynamic LCT volume fraction, and this effect is pronounced in heterogeneous reservoirs. Nevertheless, when the buoyancy number is less than 6E-4, the dynamic LCT volume fraction is insensitive to the injection rate. This is consistent with the core flooding observation by Shi (2011) that the influence of heterogeneity on the mean of CO_2 saturation profiles along a core become gradually diminished as the injection rate was increased in step to 3 cc/min (N_{gr}=6.4E-3).

To support the analyses, we show the spatial distribution of flooded LCT (LCT in the CO_2 plume), flooded non-LCT, and non-flooded LCT in storage formations (Fig. 7-8). Here, the flooded LCT and flooded non-LCT constitute CO_2 plume. Thus, the dynamic LCT volume fraction can be interpreted as the ratio of flooded LCT over the sum of both flooded LCT and flooded non-LCT. Figure 7-8 compares these three types of LCT in several layers # 8, 16, 24, and 32 and the cross section along the wellbore for two extreme heterogeneous reservoirs. One reservoir is almost homogeneous with V_{dp} equal to 0.13, and the other is the most heterogeneous with the largest V_{dp} of 0.91. Two extreme injection rates are shown, one rate is with the smallest N_{gr} of 6E-4, the other is with the largest N_{gr} of 6E+1. In the upper row of Fig. 7-8, the homogenous reservoir shows a good uniform sweep profile under the smallest injection rate (N_{gr}=60). This uniform profile causes less chance of CO_2 filling into the sparse local capillary traps. Therefore, a small dynamic LCT volume fraction is obtained in homogenous reservoirs (refer to Fig. 7-7). When a large injection rate is used for the homogeneous reservoirs, CO_2 sweeps more cells at the bottom of the domain. This is favorable to filling local capillary trap during the following buoyant flow as CO_2 migrates away from the wellbore. Therefore, when the reservoirs are relatively homogeneous (V_{dp} <0.45, refer to Fig. 7-7), increasing the injection rate still results in a small increase in the dynamic LCT volume fraction.

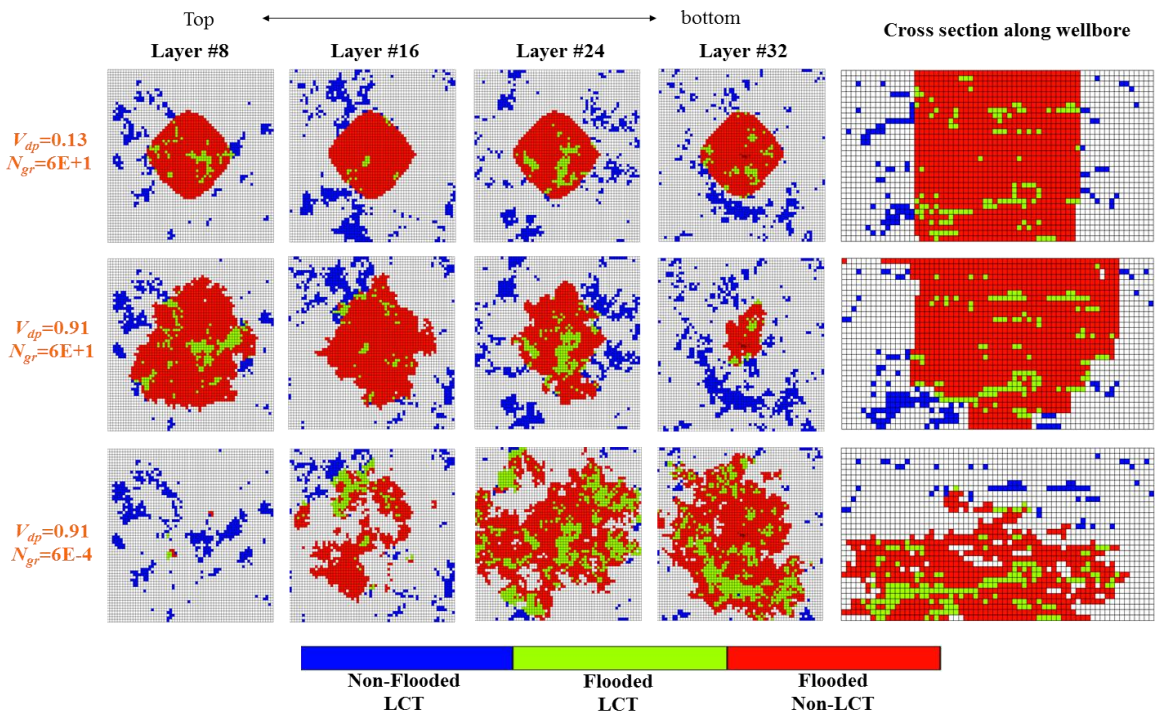

Fig. 7-8 The spatial distribution of flooded LCT, flooded non-LCT, and non-flooded LCT in different layers (#8, 16, 24, 32) and a cross section along a wellbore (XZ). Two limiting heterogeneous reservoirs are presented with two limiting injection rates (buoyancy numbers). Upper: V_{dp} =0.13, N_{gr}=6E+1; middle: V_{dp} =0.91, N_{gr}=6E+1; lower: V_{dp} =0.91, N_{gr}=6E-4. The layer is numbering from top to bottom of the domain.

For the heterogeneous reservoir (V_{dp}=0.91), at the smallest injection rate, CO_2 moves quickly to the top layer. This behavior causes limited filling of local capillary traps (N_{gr}=60, the middle row of Fig. 7-8). At the largest injection rate, however, CO_2 sweeps most of the cells at the bottom of the storage domain (N_{gr}=6E-4, the lower row of Fig. 7-8). As CO_2 moves far away from the wellbore, it would move along some specific paths with good connectivities. This kind of channeling increases the possibility of avoiding barriers and filling local capillary traps. Therefore, as reservoirs become heterogeneous, the dynamic LCT volume fraction becomes large under large injection rates (N_{gr}<0.6, refer to Fig. 7-7).

7.4.4 Effect of injected volume on the dynamic LCT volume fraction

Figure 7-9 shows the change of the dynamic LCT volume fractions with the injected volumes in different heterogeneous storage reservoirs. Four main observations can be made from the figure:

(1) An optimally injected volume exists, which yields the largest dynamic LCT volume fraction. For a heterogeneous reservoir, as the injected volume increases, the dynamic fraction first increases followed by a decrease. This is because, when the injected volume is small, CO_2 would not touch the top layer, so most of CO_2 migrates upward during the injection period. This is favorable to filling local capillary traps that are surrounded by barriers from top and sides. However, when the injected volume is large, CO_2 would accumulate in the upper portion of a domain, during which, CO_2 backfills local capillary traps. Since these traps are surrounded by barriers from the top and sides, CO_2 would avoid these barriers and move along flow paths. This causes a poor filling efficiency of local capillary traps, as compared to the upward migration.

(2) As a reservoir becomes heterogeneous (V_{dp} increases), the optimally injected volume decreases. Reservoir heterogeneity cause the channeling of CO_2, so CO_2 reaches the top layer at a small injected volume. As explained in the first point, the filling efficiency of local capillary traps during upward migration is better than that during backward movement (i.e., CO_2 moves downward after touching the top of the reservoir), so an early touch of a seal compromises the CO_2 filling of local capillary traps. Thus, the optimally injected volume becomes small as reservoirs become heterogeneous.

(3) At the optimally injected volume, the dynamic fraction increases with reservoir heterogeneity. This is because heterogeneity gives rise to more local capillary traps than homogeneity.

(4) When the net PV of CO_2 is 1, the dynamic fraction is equal to the static LCT volume ratio. Here, net PV of CO_2 = injected CO_2 volume / (PV × average CO_2 saturation). This equality is consistent with the above analysis of the interchangeability between the dynamic fraction and static ratio.

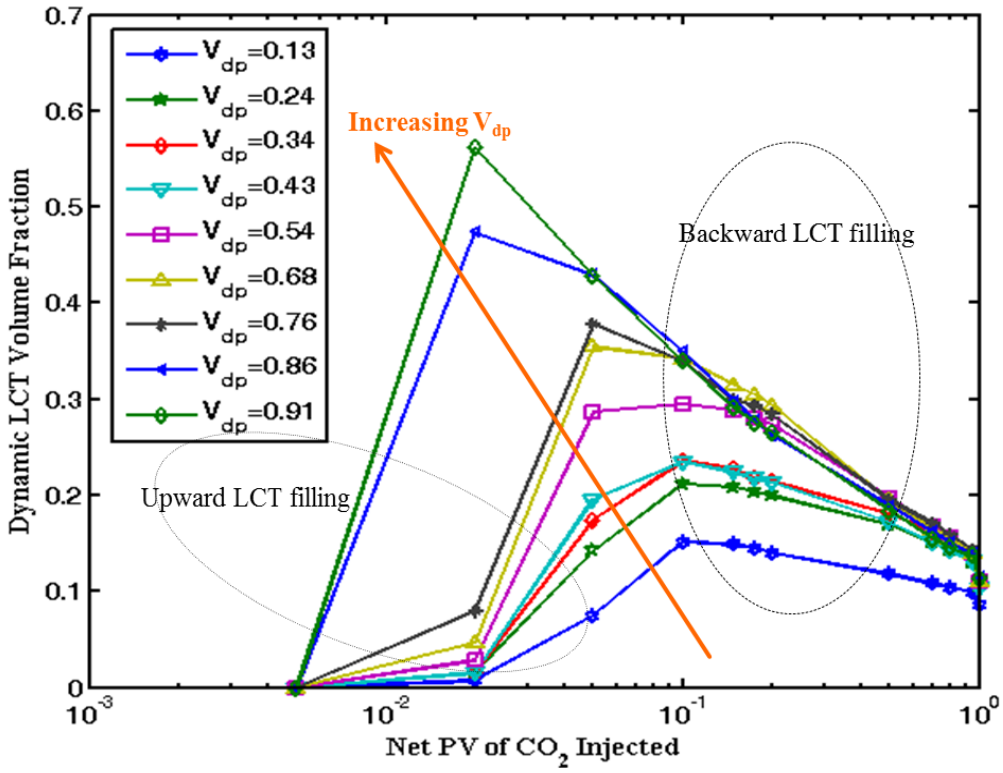

Fig. 7-9 Change of dynamic LCT volume fractions with injected volumes (at reservoir condition) in different heterogeneous reservoirs. The injected CO_2 volume is normalized by the pore volume (PV) of a reservoir. Net PV of CO_2 injected = injected CO_2 volume / (PV × average CO_2 saturation). When the net PV is 1, CO_2 fills all cells of a domain. N_{gr}=6E-4. The circle on the left side of curves represents filling local capillary traps during upward migration, whereas, the right circle shows filling local capillary traps during the backward process.

7.5 SUMMARY

In this chapter, we show the use of a fast simulation technique to model local capillary trapping during CO_2 injection. The modeling efforts are decoupled into two parts: (1) using a connectivity analysis to conduct flow simulation in a permeability field; (2) employing a geologic criterion to identify local capillary traps in a capillary entry pressure field. The former permeability field is correlated with the latter capillary entry pressure field using the Leverett j-function.

We employ the integrated simulation technique to quantify the amount of local capillary trapping. The effects of reservoir heterogeneity, injection rate, and injected volume are examined. We demonstrate the interplay between reservoir heterogeneity and injection rates impacts local capillary trapping during injection.

Both the geologic algorithm and the connectivity analysis are very fast; therefore, the integrated modeling technique can be used as a quick tool to estimate local capillary trapping storage capacity during geological carbon sequestration.

Nomenclature

Roman Symbols

A Contact area of the adjacent grid blocks, cm^2

C_t Reservoir total compressibility, 1/atm

$ED1$ Original edge weight, []

$ED2$ New edge weight, sec

g Gravity acceleration, $9.8m/s^2$

H_{re} Reservoir thickness, cm

h Height of CO_2 column, cm

$J(S_w)$ Leverett j-function, []

k Permeability, Darcy

k_v Mean of vertical permeability, Darcy

$\bar{k}$ Geometric average of permeability, Darcy

k_i Permeability in grid i, Darcy

k_j Permeability in grid j, Darcy

k_{rg} Relative permeability of CO_2, []

$\overline{k_g}$ Average relative permeability of CO_2, []

k_{50} 50 percentile permeability value, Darcy

$k_{84.1}$ 84.1 percentile permeability value, Darcy

L Length of grid block, cm

L_{pr} Reservoir perforation length, cm

p_c^{entry} Capillary entry pressure, psi

Q Well injection rate, cm^3/s

q_g CO_2 flow rate, cm^3/s

r_1 The radial distance of grid *i* from a wellbore, cm

r_2 The radial distance of grid *j* from a wellbore, cm

$\overline{S_g}$ Specific saturation at which a given grid is filled, []

T Transmissivity between the adjacent grid blocks, cm^3

t CO_2 injection duration, sec

u Total or Darcy velocity of CO_2, ft/day

V_{dp} Dykstra-Parsons variation coefficient, []

Vp_i Pore volume in grid i, cm^3

Vp_j Pore volume in grid j, cm^3

Greek Symbols

μ_g Viscosity of gas (CO_2), cp

μ_w Viscosity of brine, cp

ρ_g Density of CO_2, kg/m^3

σ Interfacial tension between CO_2 and brine, N/m

θ Contact angle, degree

ϕ Porosity, []

ϕ_i Porosity in grid i, []

ϕ_j Porosity in grid j, []

ΔP Viscous pressure difference, atm

$\Delta \rho$ Density difference between brine and CO_2, kg/m^3

Acronyms

CA Connectivity analysis

CCEP Critical capillary entry pressure

CMG Computer modeling group

GCS Geological carbon sequestration

LCT Local capillary trapping

RC Reservoir condition

SC Surface condition

Chapter 8: Analytical Modeling of Buoyant and Countercurrent Flow of CO_2 with Capillary Dispersion

This chapter describes an analytical model to accurately characterize CO_2 upward migration and backfilling inside a single-layer storage formation. This model is based on fractional flow theory. It can account for buoyant and countercurrent flow, vertical permeability and capillarity effects.

We present self-similar solutions of CO_2 saturation profiles (i.e., saturation versus distance) without considering capillarity and traveling wave solutions to capillary-dispersed profiles. All these solutions are given for both the upward migration and downward backfilling processes. Both water- and CO_2-wet reservoirs are examined at typical buoyant source fluxes. We demonstrate that the saturation wave types, CO_2 migration, and saturation profile are influenced by the buoyant flux, capillary pressure, wettability and relative permeability. The stabilized zone resulting from capillary dispersion inside the CO_2-wet reservoir generally extends longer than that for the water-wet reservoir.

Then, we demonstrate the transition from shocks to spreading waves because of the interaction between buoyancy and capillarity (i.e., Bond number). Finally, we discussed the application and limitation of the model.

8.1 PREVIOUS MODELS OF BUOYANT AND COUNTERCURRENT FLOW

Several buoyant and countercurrent flow work have been reported in the literature. Notably, Martin (1958) developed a mathematical model to study gravity segregation for oil/gas system. Following this, Siddiqui and Lake (1992) adapted the model to describe the secondary oil upward migration, backfilling, and trapping, and later it is extended to three-phase oil, gas, and water flow (Helset and Lake 1998).

Silin et al. (2009) developed a buoyancy-driven two-phase countercurrent flow model to study CO_2 leakage from deep geological carbon storage formations. Riaz and Tchelepi (2008) examined CO_2/brine dynamics of vertical displacement in 1D and 2D using numerical methods.

Hayek et al. (2009) studied possible CO_2 countercurrent flow and migration in a stratified system without considering capillarity and backfilling. Ngo et al. (2016) focused on buoyant flow of CO_2 through and around semi-permeability layer of finite extent using an extended capillary pressure function and graphically determining the saturation profile by using a capillary pressure continuity condition and buoyant flux continuity relationship. They do not explicitly consider capillary pressure in the flux-saturation profile.

8.2 THEORY AND APPROACH

The method of characteristics (MOC) has been routinely used to solve the partial differential equations that describe multiphase flow and reactive transport in porous media (Lake et al. 2014, Lake et al. 2003). The basic idea involved in the method is to transform the governing partial differential equations into a set of ordinary differential equations. The latter will then be solved using standard methods after incorporating the initial and boundary conditions. One notable example is the Buckley-Leverett approximate solution to the immiscible and cocurrent displacement equation, the derived saturation waves (e.g., shock or spreading wave) have been observed in the core flooding (Peters and Hardham 1990). It has been widely employed in interpreting laboratory and field production characteristics. More solutions derived using the MOC have been shown useful to describe the large-scale hydrocarbon charging process (Siddiqui and Lake 1997), vertical CO_2 plume migration (Silin et al. 2009, Hayek et al. 2009, Riaz and Tchelepi 2008) , saturation overshoot during water infiltration into soil (DiCarlo et al. 2012), and the propagation of chemical precipitation/dissolution waves (Bryant et al. 1986). These characteristic waves might be difficult to observe directly because of the heterogeneity of the porous media and complicated interaction between various types of waves.

The procedures of the mathematical formulation are shown below in detail. We first presented solutions to saturation profiles without capillary effect using the MOC. After incorporating capillary pressure, the traveling wave technique can be used to solve the partial differential equation as shown below. The equation derivation before incorporating capillary

pressure is very similar that originally proposed by Siddiqui and Lake (1992) with subtle changes shown below.

By assuming isothermal, incompressible, immiscible displacement, and one-dimensional flow in the homogenous porous media, material balance equations for CO_2 and brine phase in the vertical direction can be written as

$$\phi \frac{\partial S_g}{\partial t} + \frac{\partial u_g}{\partial z} = 0 \tag{8.1}$$

$$\phi \frac{\partial S_w}{\partial t} + \frac{\partial u_w}{\partial z} = 0 \tag{8.2}$$

Under countercurrent flow, the total flux should be zero

$$u_g + u_w = 0 \tag{8.3}$$

By assuming Darcy flow, the movement equations for the two phases are

$$u_g = -k_z \lambda_{rg} \left(\frac{dP_g}{dz} + \rho_g g\right) \tag{8.4}$$

$$u_w = -k_z \lambda_{rw} \left(\frac{dP_w}{dz} + \rho_w g\right) \tag{8.5}$$

After combining all the above equations, we get

$$u_g = \frac{k_z \lambda_{rg} \lambda_{rw}}{\lambda_{rg} + \lambda_{rw}} \left(\Delta\rho g - \frac{dP_c}{dz}\right) \tag{8.6}$$

In the above equations,

$$P_c = P_g - P_w \tag{8.7}$$

$$\Delta\rho = \rho_w - \rho_g \tag{8.8}$$

$$\lambda_{rw} = \frac{k_{rw}}{\mu_w} \tag{8.9}$$

$$\lambda_{rg} = \frac{k_{rg}}{\mu_g} \tag{8.10}$$

The CO_2 flux can be divided into two parts: a buoyant flux and a capillary flux,

$$u_g^b = \frac{k_z \lambda_{rg} \lambda_{rw}}{\lambda_{rg} + \lambda_{rw}} \left(\Delta\rho g\right) \tag{8.11}$$

$$u_g^c = \frac{k_z \lambda_{rg} \lambda_{rw}}{\lambda_{rg} + \lambda_{rw}} \left(-\frac{dP_c}{dz}\right) \tag{8.12}$$

Next, we will present the solutions to the cases without and with capillary pressure.

Case 1: w/o P_c

After neglecting capillary flux, the total flux reduces to the buoyant flux. We substitute the buoyant flux (Eq. 8.11) back into the material balance equation of CO_2 (Eq. 8.1),

$$\frac{\partial S_g}{\partial t} + \frac{\partial}{\partial z}\left(\frac{k_z \lambda_{rg} \lambda_{rw}}{\lambda_{rg} + \lambda_{rw}} \frac{\Delta \rho g}{\phi}\right) = 0 \tag{8.13}$$

The next step is to make the above equation dimensionless, by setting

$$z_D = \frac{z}{L} \tag{8.14}$$

$$t_D = \frac{k_z \Delta \rho g}{\mu_w \phi L (1 - S_{wr} - S_{gr})} t \tag{8.15}$$

We can re-write the time and space derivative terms as

$$\frac{\partial}{\partial z}\left(\frac{k_z \lambda_{rg} \lambda_{rw}}{\lambda_{rg} + \lambda_{rw}} \frac{\Delta \rho g}{\phi}\right) = \frac{\partial}{\partial z_D}\left(\frac{k_z \lambda_{rg} \lambda_{rw}}{\lambda_{rg} + \lambda_{rw}} \frac{\Delta \rho g}{\phi}\right) \frac{\partial z_D}{\partial z} = \frac{\partial}{\partial z_D}\left(\frac{k_z \lambda_{rg} \lambda_{rw}}{\lambda_{rg} + \lambda_{rw}} \frac{\Delta \rho g}{\phi L}\right) \tag{8.16}$$

$$\frac{\partial S_g}{\partial t} = \frac{\partial S_g}{\partial t_D} \frac{\partial t_D}{\partial t} = \frac{\partial S_g}{\partial t_D} \frac{k_z \Delta \rho g}{\mu_w \phi L (1 - S_{wr} - S_{gr})} \tag{8.17}$$

After substituting the above two terms back into Eq. 8.13, we get

$$\frac{\partial S_g}{\partial t_D} \frac{k_z \Delta \rho g}{\mu_w \phi L (1 - S_{wr} - S_{gr})} + \frac{\partial}{\partial z_D}\left(\frac{k_z \lambda_{rg} \lambda_{rw}}{\lambda_{rg} + \lambda_{rw}} \frac{\Delta \rho g}{\phi L}\right) = 0 \tag{8.18}$$

By assuming the vertical permeability, porosity, viscosity and density to be constant, Eq. 8.18 can be reduced to

$$\frac{1}{(1 - S_{wr} - S_{gr})} \frac{\partial S_g}{\partial t_D} + \frac{\partial}{\partial z_D}\left(\frac{\lambda_{rg} \lambda_{rw}}{\lambda_{rg} + \lambda_{rw}} \mu_w\right) = 0 \tag{8.19}$$

By setting

$$u_{gD} = \frac{\lambda_{rg} \lambda_{rw}}{\lambda_{rg} + \lambda_{rw}} \mu_w \tag{8.20}$$

$$S_{gD} = \frac{S_g - S_{gr}}{1 - S_{gr} - S_{wr}} \tag{8.21}$$

The derived dimensionless equation is

$$\frac{\partial S_{gD}}{\partial t_D} + \frac{\partial u_{gD}}{\partial x_D} = 0 \tag{8.22}$$

The relation between the dimensionless and dimensional buoyant flux can be written as

$$u_{gD}^{b} = u_{g}^{b} \frac{\mu_w}{k_z \Delta\rho g} \tag{8.23}$$

Equation 8.22 is hyperbolic and can be solved by the MOC (Lake et al. 2014) with the graphical saturation profile through the Welge (1952) tangential line construction.

We write the full derivatives of the S_{gD} term as,

$$dS_{gD} = \frac{\partial S_{gD}}{\partial x_D} dx_D + \frac{\partial S_{gD}}{\partial t_D} dt_D \tag{8.24}$$

For a constant S_{gD}

$$dS_{gD} = 0 \tag{8.25}$$

The velocity of a constant saturation becomes

$$v\Big|_{S_{gD}} = \left(\frac{dx_D}{dt_D}\right)\Big|_{S_{gD}} = -\left(\frac{\partial S_{gD}}{\partial t_D}\right) / \left(\frac{\partial S_{gD}}{\partial x_D}\right) \tag{8.26}$$

By substituting the dimensionless material balance equation into the above equation, we get

$$v\Big|_{S_{gD}} = \frac{1}{\phi} \frac{du_{gD}}{dS_{gD}} \tag{8.27}$$

Equation 9.26 means that the velocity of a specific saturation wave can be determined from the shape of u_{gD}-S_{gD} curve using the Welge tangential construction (Welge 1952) after incorporating boundary and initial conditions.

Case 2: w/ P_c

After adding capillary pressure, the material balance equation (Eq. 8.1) is changed from the hyperbolic to be parabolic. Before moving to the traveling wave solution for capillary dispersion, we make an analysis of the flux induced by capillarity. We re-write the capillary flux (Eq. 8.12) in the following form,

$$u_{g}^{c} = \frac{k_z \lambda_{rg} \lambda_{rw}}{\lambda_{rg} + \lambda_{rw}} \left(-\frac{dP_c}{dS_g} \frac{dS_g}{dz}\right) \tag{8.28}$$

Equation 8.28 indicates that capillary pressure will be non-negligible when

(1) Water saturation becomes residual under water-wet condition, capillary pressure would change steeply with water saturation (i.e., large dP_c/dS_g);

(2) Saturation shock forms with a large saturation step-change, this causes a large dS_g/dz;

(3) Saturation profile is not asymptotic to the distance axis as time proceeds; this is a general situation that gives rise to a large dS_g/dz. We will elaborate this point for the CO_2-wet reservoir in the following results.

Next, we employ the traveling wave technique to resolve into the shock region. Since the shock moves with a constant velocity, we introduce a new Z-coordinate system moving with such velocity (v). By doing this, we can write

$$Z = z - vt \tag{8.29}$$

The material balance equation (Eq. 8.1) is re-written in the z-coordinate system

$$\phi \left(\frac{\partial S_g}{\partial t} \right)_z + \left(\frac{\partial u_g}{\partial z} \right)_t = 0 \tag{8.30}$$

The total derivative for the S_g and Z term can be written as

$$dZ = \frac{\partial Z}{\partial z} dz + \frac{\partial Z}{\partial t} dt = dz - v dt \tag{8.31}$$

$$dS_g = \left(\frac{\partial S_g}{\partial z} \right)_t dz + \left(\frac{\partial S_g}{\partial t} \right)_z dt = \left(\frac{\partial S_g}{\partial Z} \right)_t dZ + \left(\frac{\partial S_g}{\partial t} \right)_Z dt \tag{8.32}$$

Substitute dZ equation into the dS_g equation and reorganize it, we get

$$\left(\frac{\partial S_g}{\partial t} \right)_z = \left(\frac{\partial S_g}{\partial t} \right)_Z - v \left(\frac{\partial S_g}{\partial Z} \right)_t \tag{8.33}$$

$$\left(\frac{\partial S_g}{\partial z} \right)_t = \left(\frac{\partial S_g}{\partial Z} \right)_t \tag{8.34}$$

Substitute the above time and space derivatives into Eq. 8.30, we can write

$$\phi \left(\frac{\partial S_g}{\partial t} \right)_Z - \phi v \left(\frac{\partial S_g}{\partial Z} \right)_t + \left(\frac{\partial u_g}{\partial Z} \right)_t = 0 \tag{8.35}$$

Equation 8.35 can be solved numerically to explore how the shock evolves with the time. Theoretically, the shock forming properties will come into balance with the mixing properties of capillary dispersion. Eventually, it will give rise to a saturation profile moving in pure translation

without change of shape (Lake et al. 2014). This means that the saturation profile is independent of time as time proceeds. Thus, Eq. 8.35 can be reduced to the ordinary different equation that can be directly integrated.

$$-\phi v\left(\frac{dS_g}{dZ}\right)_t + \left(\frac{du_g}{dZ}\right)_t = 0 \tag{8.36}$$

$$-\phi v S_g + u_g = C \tag{8.37}$$

In the above, v is the shock velocity, the constant C can be evaluated using the value at the endpoints of the buoyant shock. Equation 8.37 means that the traveling wave solution should have a flux that is linear with gas saturation.

We integrate Eq. 8.36 from the upstream of the shock to a general point,

$$-\phi v(S_g - S_g^+) + (u_g - u_g^+) = 0 \tag{8.38}$$

Then, the total flux can be re-written as

$$u_g = \phi v(S_g - S_g^+) + u_g^+ \tag{8.39}$$

Recall the buoyant flux in Eq. 8.11, the capillary flux can be written in a different form

$$u_g^c = u_g - u_g^b = \phi v(S_g - S_g^+) + u_g^+ - u_g^b \tag{8.40}$$

Recall the capillary flux in Eq. 8.12, then combining Eq. 8.40 and Eq. 8.12 yields,

$$\frac{dS_g}{dZ} = \frac{\phi v(S_g - S_g^+) + u_g^+ - u_g^b}{\frac{k_z \lambda_{rg} \lambda_{rw}}{\lambda_{rg} + \lambda_{rw}}(-P_c')} \tag{8.41}$$

Please note that, in Eq. 8.41, the derivative of P_c is with respect to gas saturation, rather than distance. Equation 8.41 can be also written as the derivative of the capillary pressure w.r.t. vertical distance.

$$\frac{dP_c}{dZ} = -(\phi v S_g - \phi v S_g^+ + u_g^+)\frac{\lambda_{rg} + \lambda_{rw}}{k_z \lambda_{rg} \lambda_{rw}} + \Delta\rho g \tag{8.42}$$

The length of the traveling-wave region can be calculated by numerically integrating either the above gas saturation (Eq. 8.41) or capillary pressure (Eq. 8.42) from upstream to downstream of the shock.

The transition zone where saturation distribution has the form of a traveling wave is traditionally called as the "stabilized zone" (Barenblatt et al. 1989). To be consistent, we will use this term in the following analysis. Many theoretical and core flooding experimental work (Lake et al. 2014, Barenblatt et al. 1989) has been focused on the development and length of the stabilized zone under *co-current and viscous* flow, which is motivated by the Buckley-Leverett problem (Buckley and Leverett 1942). However, the characteristic features of stabilized zone under *countercurrent* and *buoyant* flow would be different as analyzed below.

For the co-current flow, the spatial derivative of the saturation around the shock is shown below which is adapted from the work by DiCarlo et al. (2012).

$$\frac{dS_g}{dZ} = \frac{\phi v(S_g - S_g^+) - u_T(f_v - f_v^+)}{f_v k_z \lambda_{rw}(P_c')} \tag{8.43}$$

In the above, u_T is the total flux of the two phase, f_v is the viscous flux, f_v^+ is the upstream viscous flux, the other terms are named consistently with the above. By comparing the saturation derivative equations (Eq. 8.41 vs. 8.43) between *counter-current* and *co-current* flow, one can expect that

(1) The stabilized zone under the co-current flow tends to be suppressed by *viscous flow*, whereas, under *buoyant flow*, the gradient of capillary pressure is comparable to that of CO_2 buoyancy, which might give rise to a longer zone;

(2) The gas saturation is affected by both the water and gas mobility ratio under *counter-current* flow, whereas it is influenced only by the water mobility under *co-current* flow. Therefore, the stabilized zone would be theoretically different. Considering CO_2 injection into a saline aquifer, the viscosity of brine is about ten-fold larger than that of CO_2 in a typical storage formation (Paulsen 2014). When the shock has a large gas saturation and mobility ratio, the combined mobility ratio terms in the denominator of Eq. 8.41 for *countercurrent* flow would reduce to only water mobility for *co-current* flow (Eq. 8.43).

To implement the above model, we conceptualize CO_2 flow inside a homogenous domain with the closed upper boundary and a constant CO_2 flux on the lower boundary. The schematic

diagram is in Fig. 8-1. Both CO_2 and brine water are incompressible as assumed above; therefore, when CO_2 rises into the domain, brine falls down into the source area with equal and opposite flux. Two different source fluxes (Table 8-1) were selected for the analysis of saturation profile in both water and CO_2-wet reservoirs. Their magnitudes are comparable to the buoyant flux as observed from Sleipner field (Singh et al. 2010). Therefore, the analysis could represent the saturation evolution of the buoyant CO_2 flow, including time for the rising CO_2 to touch the top, CO_2 distribution in the vertical direction, and the differences between upward migration and backfilling behavior. All the source flux magnitudes, relative permeability model, capillary pressure model, fluid and porous media properties are summarized in Table 8-1. The relative permeability and capillary pressure curves are in Fig. 8-2.

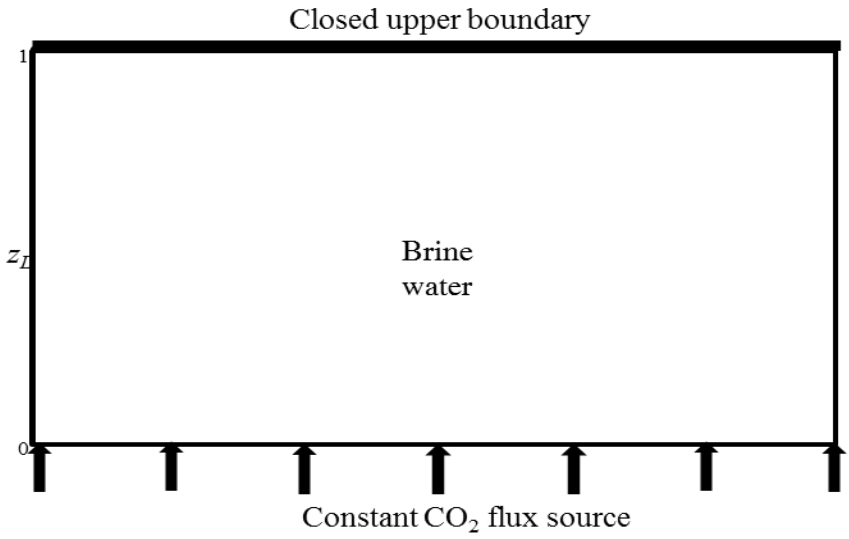

Fig. 8-1 Schematic domain for the model application. The height of the storage domain is made dimensionless, with the lower flux boundary as the starting point and upper closed boundary as the end point.

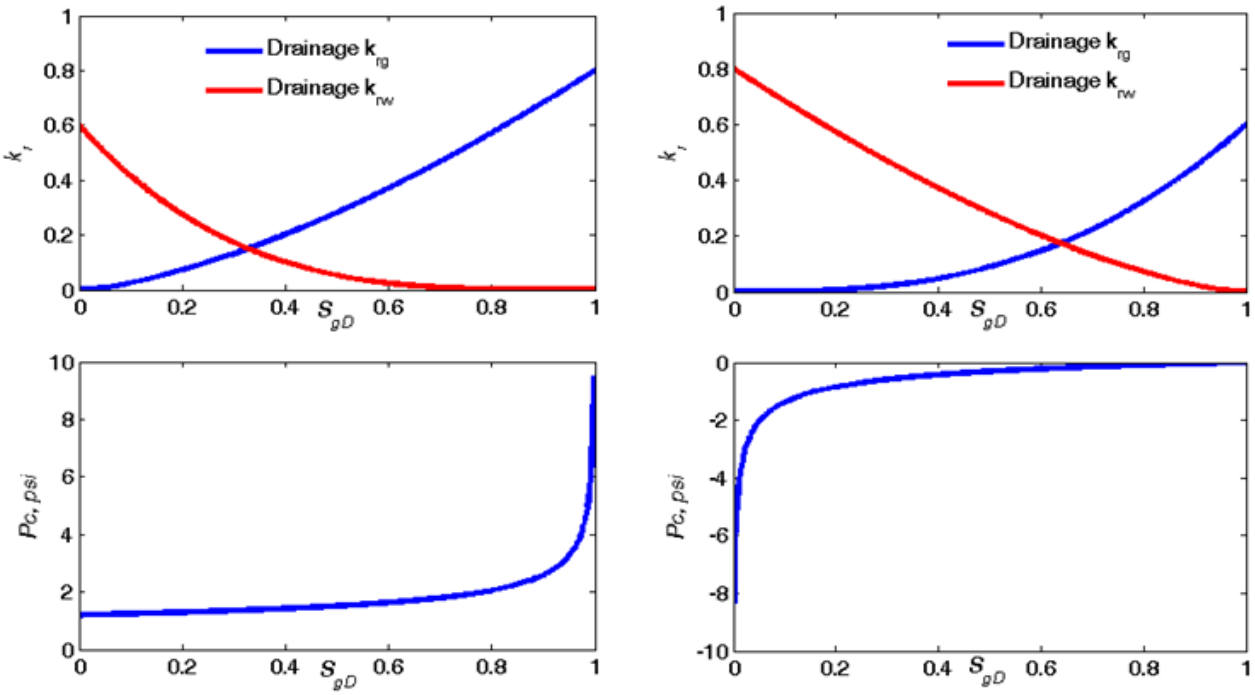

Fig. 8-2 The upper plots are the relative permeability curves, and the lower are the capillary pressure curves. The left column is for the water-wet reservoir and the right column for the CO_2-wet. Capillary pressure is defined as the difference between gas and water phase pressure.

Table 8-1. Reservoir and fluid properties for water-wet and CO_2-wet conditions

Parameters	**Water-wet**	**CO_2-wet**
Porosity (ϕ)	0.25	0.25
Permeability (k_z), Darcy	0.75	0.75
Brine water viscosity (μ_w), cp	0.55	0.55
CO_2 viscosity (μ_g), cp	0.085	0.085
Brine water density (ρ_w), kg/m^3	1024.6	1024.6
CO_2 density (ρ_g), kg/m^3	618.7	618.7
Residual water saturation (S_{wr})	0.20	0.20
Residual gas saturation (S_{gr})	0.20	0.20
[a] Water relative permeability (k_{wr})	$0.6(1-S_{gD})^{3.5}$	$0.8(1- S_{gD})^{1.5}$
[a] Gas relative permeability (k_{gr})	$0.8(S_{gD})^{1.5}$	$0.6(S_{gD})^{2.75}$
[b] Capillary pressure (P_c), psi	$P_{e1}\ (1-S_{gD})^{-1/3.0}$	$-P_{e1}\ [(S_{gD})^{-1/3.0}-1]$
Selected dimensionless source flux (U_{gD})	0.10, 0.17	0.10, 0.19
Corresponding dimensional source flux (U_g), m/yr	16.9, 28.7	16.9, 32.1

Note: [a] Brooks-Corey relative permeability model is used, $S_{gD}= (S_g- S_{gr})/(1- S_{wr}- S_{gr})$. [b] Brooks-Corey capillary pressure model is used (Brooks and Corey 1966).

8.3 RESULTS

We first analyze the small source flux case in the water-wet reservoir without considering capillary pressure. Then traveling wave solution around the shock area is introduced to demonstrate the capillary pressure effect. After that, we study how the magnitude of source flux influences the saturation profile by adopting a large flux (at the maximum point determined by the flux-saturation relationship). After analyzing the water-wet reservoir, a similar study is conducted for the CO_2-wet case, the impact of wettability on the saturation profile shape and capillary stabilized zone is emphasized. Finally, we demonstrate how buoyant force influences the shape of saturation wave.

8.3.1 Water-wet reservoir

8.3.1.1 Small flux

Figure 8-3a shows the buoyant flux-saturation relationship, time-distance diagram and saturation profiles at two different selected times. The capillary pressure is not considered. The change of buoyant flux with saturation is plotted using the dimensionless flux of Eq. 8.20 and multiphase flow properties in Table 8-1. A small flux (0.1) corresponding to the point *J* is selected as the source flux. The initial condition is at the point *I*. When such buoyant source flux comes into the domain, a saturation shock will occur and its velocity is determined by the chord *I*-*J*. When the upward shock with such a velocity encounters the upper closed boundary, it will be reflected and a new saturation shock is formed through the chord *J*-*T* followed by a rarefaction wave.

Correspondingly, in the time-distance diagram, the two blue lines represent the change of shock positions with time for upward and downward migration. The corresponding shock saturation and flux are in parenthesis.

The time-distance diagram is divided into three regions by the two blue lines. The upward left area is characterized by zero saturation and flux, this means CO_2 has not moved here at the corresponding time. The middle area is an upward shock with a saturation of 0.085 and flux of 0.1. The upper right is a combination of a downward shock with a saturation of 0.65 and a rarefaction wave represented by the green shaded area. The saturation of the rarefaction wave was from 0.65 to 1.00. The upward shock reached the impermeable upper boundary at t_D=0.86. The downward shock moved back to the lower boundary at t_D=7.51.

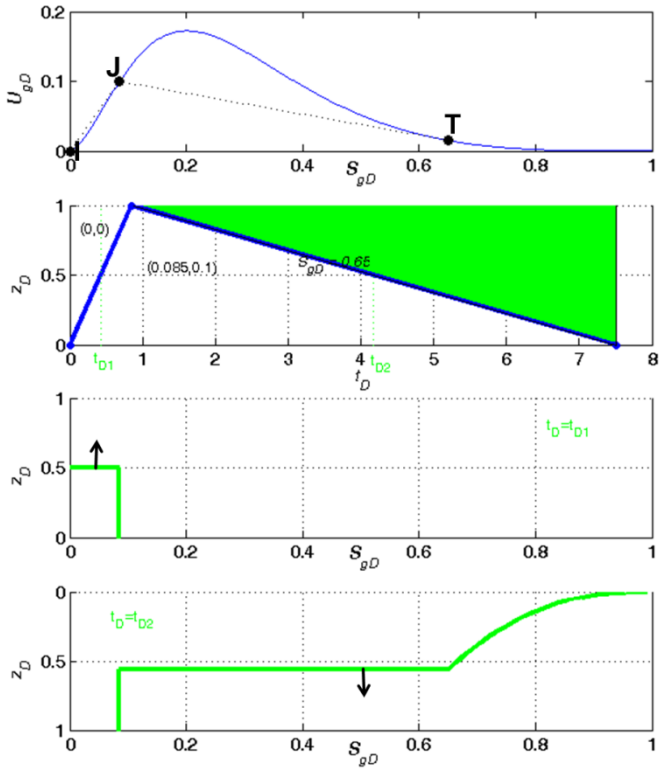

(a)

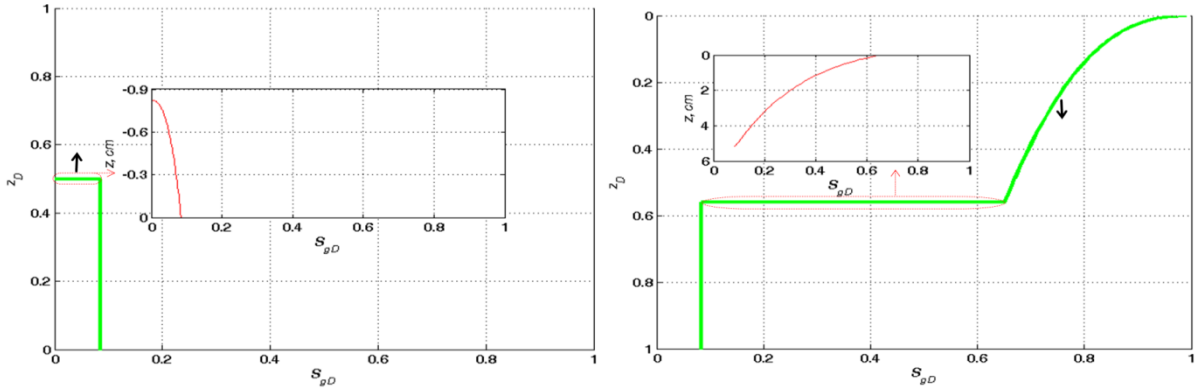

(b) (c)

Fig. 8-3 A small boundary flux is used in the water-wet reservoir. Subplots from top to bottom in (a) are: (1) U_{gD}-S_{gD} relationship; (2) Time-distance diagram; (3) Saturation profile at t_{D1} during upward migration; (4) Saturation profile at t_{D2} during backfilling. In the time-distance diagram, the green shaded area represents the spreading wave of CO_2 saturation. The insets show the resolution of the shock derived from the traveling wave solutions.

The corresponding upward and downward saturation profiles at the two selected times of t_{D1} and t_{D2} are shown below the time-distance diagram. The downward saturation profile shows the concave-down shape in the spreading region. This is similar to the typical shape of the Buckley-Leverett saturation profile (Lake et al. 2014). Mathematically, the shape (i.e., concave up or down) of the curve is determined by the second derivative of flux with respect to gas saturation as demonstrated below.

$$\frac{dz}{dS_{gD}} = \frac{vdt}{dS_{gD}} = \frac{d^2u_{gD}}{dS_{gD}^2}dt \tag{8.44}$$

The second derivative function is plotted in Fig. 8-4. The derivative decreases with increasing of gas saturation in the spreading saturation interval (0.65~1.0). Therefore, in the downward saturation profile of Fig. 8-3a, the slope of the saturation profile decreases with the gas saturation.

With capillary pressure, the shock is smoothed by the capillary dissipation effect. This can be observed from Fig. 8-3b and 8-3c. Insets show details of saturation profile around the shock area after incorporating capillary pressure. The length of the stabilized zone during upward migration was about 0.9 cm, whereas, the downward stabilized zone extends to about 6 cm. This is mainly because the downward shock velocity is much smaller than the upward shock as shown in Fig. 8-3a, thus, capillary dissipation effect is more pronounced in the former.

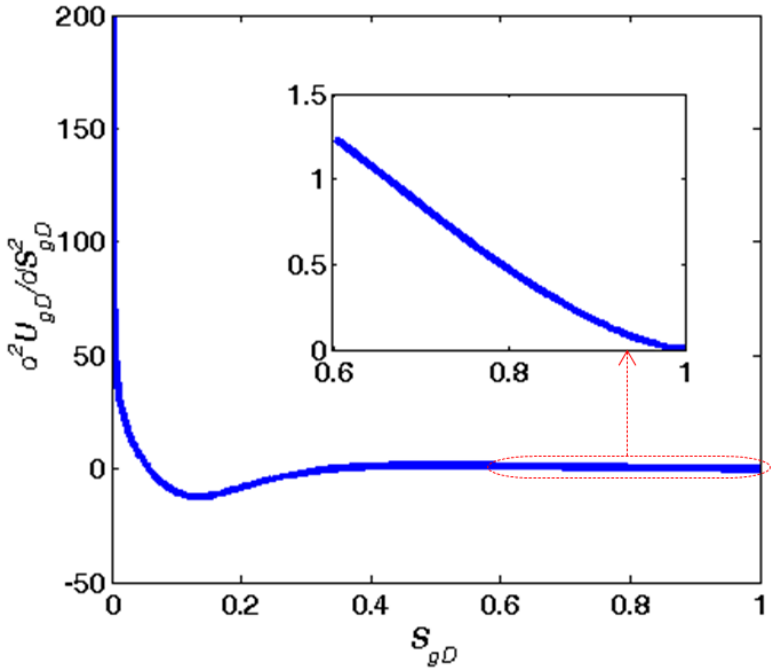

Fig. 8-4 The second derivative of U_{gD} with respect to S_{gD} for the water-wet reservoir. The inset shows the change of the derivative with gas saturation in the range of 0.6~1.0.

8.3.1.2 Large flux

To study the impact of boundary flux on CO_2 migration and saturation profile, a large source flux is selected that corresponds to the maximum point on the flux-saturation plot (refer to Fig. 8-5a). This causes the upward saturation wave to be a combination of shock and rarefaction wave. The shock saturation (S^*) was 0.10 and spreading wave saturation ranged from 0.1 to 0.2. The backward wave is also a mixed wave: the reflected shocks are bounded by the two dashed limiting shocks (Fig. 8-5a), and the rest of saturation (from the shock saturation to 1.0) waves are spreading.

Figure 8-5b is the time-distance diagram. It describes wave propagations for both the upward and downward shocks as well as several spreading saturations. For the upward migration, the shock is the fastest followed by the slow rarefaction waves. However, for the downward migration, the reflected shock with a large gas saturation (0.63) moves slower than the lately reflected wave with small saturation (0.52). The latter will, therefore, override the former after catching up at a specific time. This gives rise to the 'curved shock' (Lake et al.

2014) represented by the blue line. This kind of complicated wave interaction is because the upstream and downstream conditions are not constant. The curved shock touches the lower boundary at time t_D*. This time duration relates to an upward spreading wave with a specific saturation between 0.17 and 0.19, and the corresponding reflected shock informed from the specific saturation wave would be the smallest observable shock saturation. The limiting reflected shock related to point *J* will never occur because the velocity of the upward spreading wave with the saturation at that point is zero.

In the saturation profile of Fig. 8-5a, the upward saturation profile is comprised of shock and spreading part. This is different from the profile when using the small flux (refer to Fig. 8-3a). Notably, in Fig. 8-5a, the saturation profile is non-monotonic during backfilling because of the mixing of downward and upward saturation waves. One can expect that, as time proceeds, the shock saturation for the downward profile would be decreased to the smallest observable shock saturation as analyzed above.

Figures 8-5b and 8-5c show stabilized zones around shocks after adding capillary pressure. Intuitively, a large inlet flux would suppress capillary dissipation and, therefore, the stabilized zone should be shorter than that for the small flux. However, as shown in Eq. 8.41, the length of the stabilized zone is a complicated function of source flux magnitude, upstream and downstream saturation, shock velocity, and phase mobility ratio. When the inlet flux is increased, the upstream and downstream saturations are also changed simultaneously. Therefore, the impact of source flux magnitude on the stabilized zone development cannot be separately examined. In the following part, we will show an alternative way to study such effect by changing the buoyant force while keeping the boundary source flux constant.

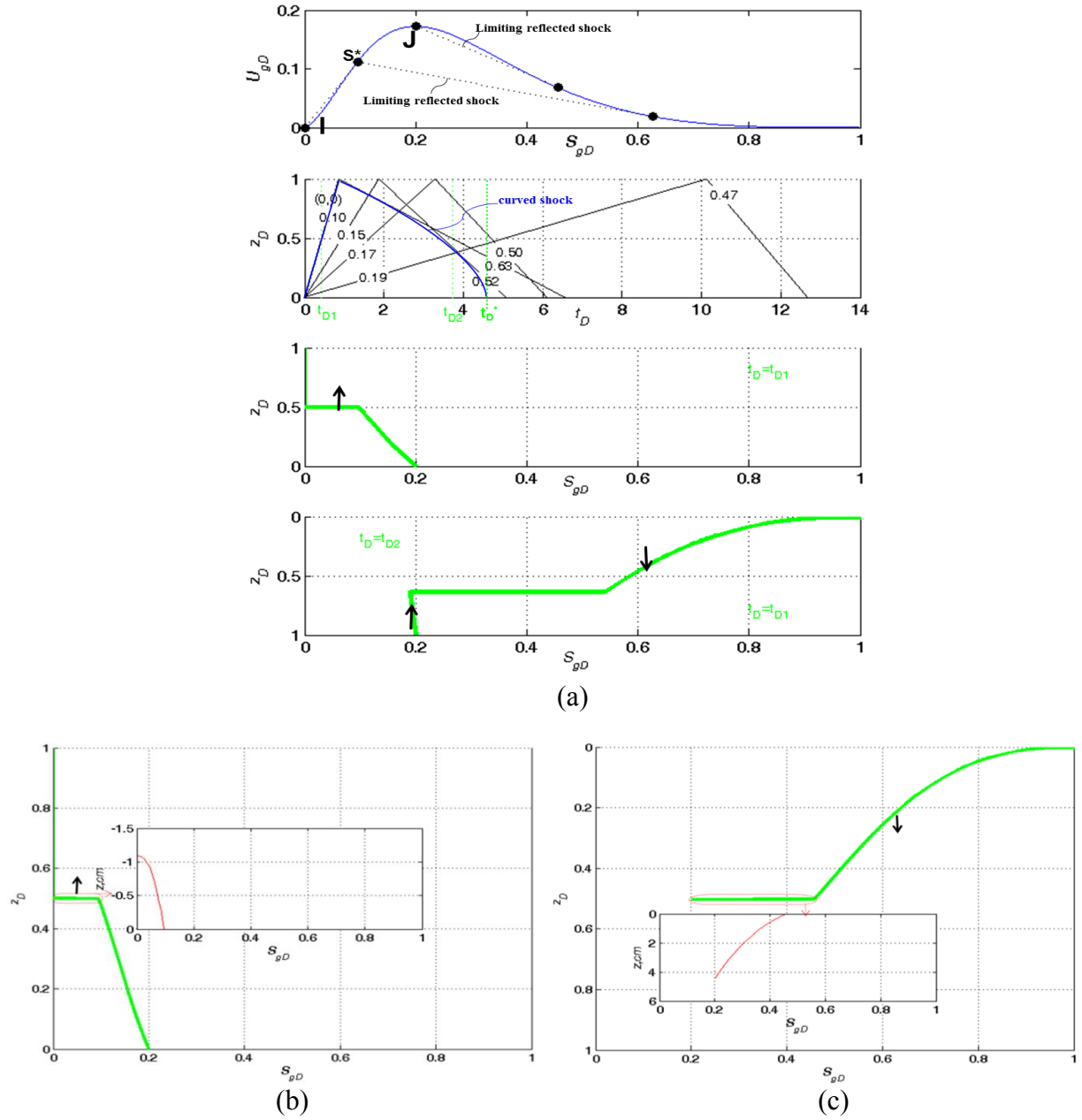

Fig. 8-5 A large boundary flux (corresponding to the maximum point) is employed in the water-wet reservoir. Subplots from top to bottom in (a) are: (1) U_{gD}-S_{gD} relationship; (2) Time-distance diagram; (3) Saturation profile at t_{D1} during upward migration; (4) Saturation profile at t_{D2} during backfilling. The insets show the resolution of the shocks from the traveling wave solution for the upward (b) and downward (c) saturation profile.

8.3.2 CO_2-wet reservoir

8.3.2.1 Small flux

Figure 8-6 shows U_{gD}-S_{gD} relationship, time-distance diagram, and saturation profiles for the CO_2-wet reservoir. When the reservoir becomes CO_2-wet, the U_{gD}-S_{gD} curve moves to the right and the maximum point occurs at a large gas saturation compared to the water-wet case (refer to Fig. 8-3). Therefore, it gives rise to large gas saturations of both the upward and downward shocks, and the saturation range of spreading wave is narrowed. The final backfilling time of the reflected shock was at t_D=9.95, which is larger than that for the water-wet reservoir. This is because of the relative permeability effect: the saturation shock under the CO_2-wet condition carries more CO_2 than that for the water-wet.

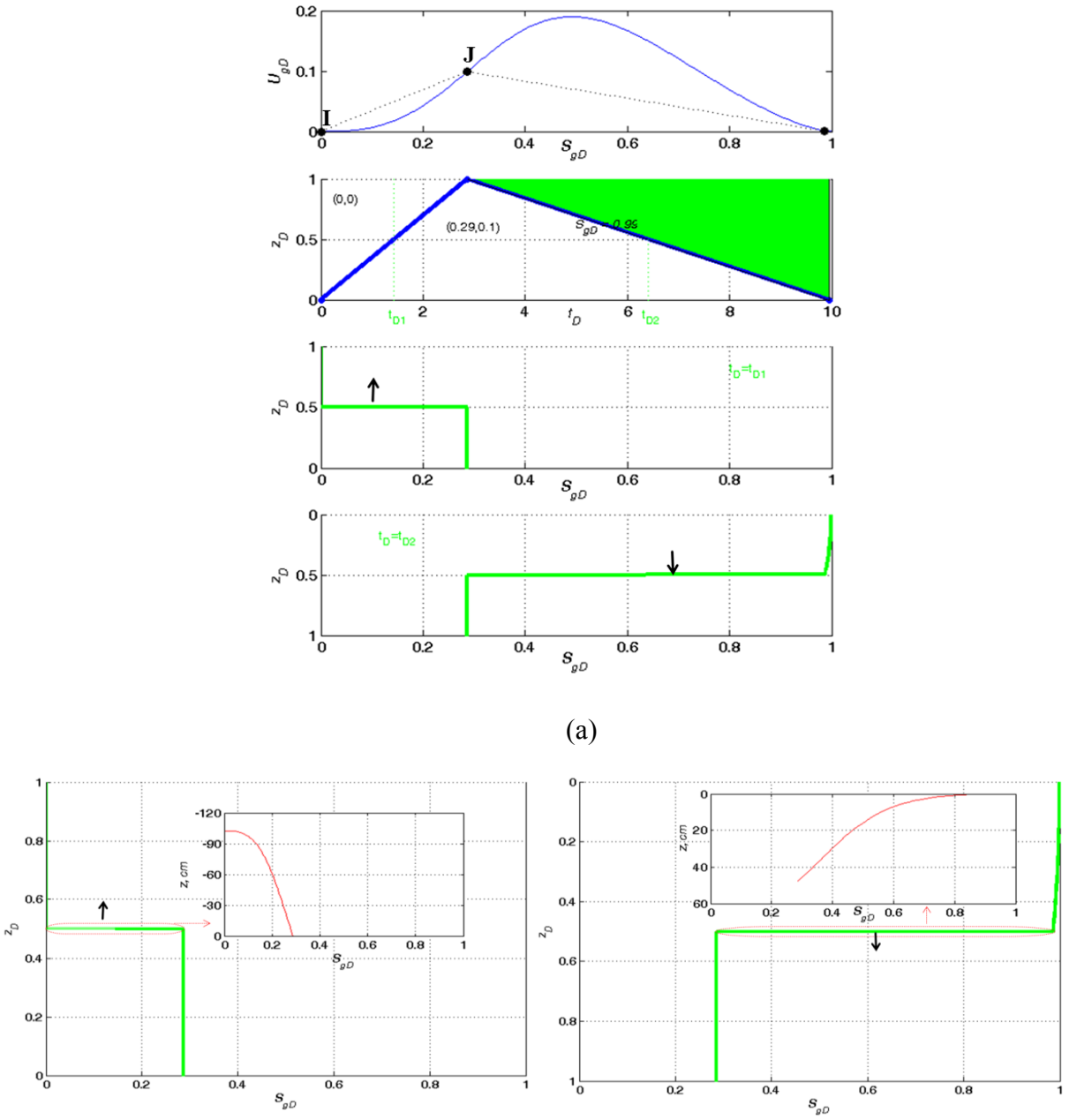

(a)

(b) (c)

Fig. 8-6 A small boundary flux is employed for a CO_2-wet reservoir. Subplots from top to bottom in (a) are: (1) U_{gD}-S_{gD} relationship; (2) Time-distance diagram; (3) Saturation profile at t_{D1} during upward migration; (4) Saturation profile at t_{D2} during backfilling. In the time-distance diagram, green shaded area represents spreading wave of CO_2 saturation. Insets in (b) and (c) show the resolution of the shock derived from the traveling wave solutions.

The saturation profile is similar to that for the water-wet case. A notable difference is the concave-up shape of the spreading part in the downward saturation profile as shown in the lowest subplot of Fig. 8-6a. As explained in the water-wet case, the concave-up shape is dictated by the second derivative of flux with respect to gas saturation, which is in Fig. 8-7. Obviously, the derivative increases with the gas saturation in the spreading saturation interval (0.99~1.00). Therefore, the slope of saturation profile becomes large as the gas saturation increases.

This observation has significant implications for the treatment of the capillary flux. As seen from Eq. 8.12, capillary flux is a function of the slope of saturation profile. If the slope decreases with increasing gas saturation as analyzed in the water-wet case, then capillary effect should be diminished as time proceeds. Therefore, for the water-wet reservoir, the above analysis of gas saturation evolution with no capillary flux is justifiable in approximating the long-term CO_2 migration behavior. However, for a CO_2-wet reservoir, capillary effect on the total flux would be pronounced because of concave-up shape of the saturation profile and because of the large-saturation shock.

This is also supported by Fig. 8-6a and 8-6c. They show stabilized zones around shocks after incorporating capillary pressure. Overall, the stabilized zone in the CO_2-wet case is longer than that for the water-wet. The upward stabilized zone can be well 100 cm. This suggests that, in a lab core flooding test, a long core would be necessary to assure that the stabilized zone could be fully developed under countercurrent flow for the CO_2-wet condition.

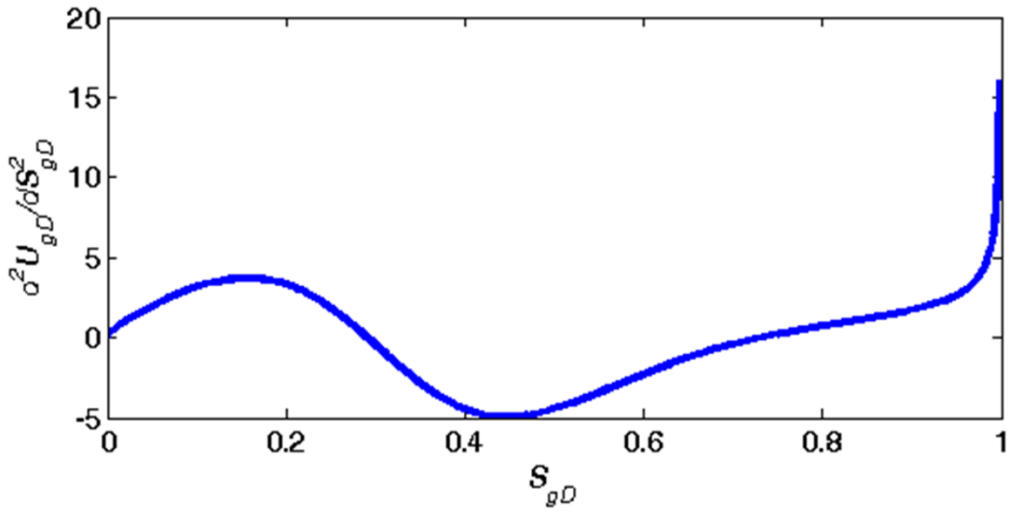

Fig. 8-7 The second derivative of U_{gD} with respect to S_{gD} for the CO_2-wet reservoir.

8.3.2.2 Large flux

Figure 8-8 shows U_{gD}-S_{gD} relationship, time-distance diagram, and gas saturation profiles for the CO_2-wet reservoir using the maximum inlet flux. Overall, they are similar to those for the water-wet case (refer to Fig. 8-5). Two notable differences can be observed after comparing Fig. 8-8 to Fig. 8-5: (1) in the CO_2-wet reservoir, although the upstream and downstream conditions are not constant for downward shocks, the curved shock is not formed. This is because velocities for the two limiting reflected shocks are very close and the reflected shocks move downward in sequence; (2) the stabilized zone for the CO_2-wet case is generally longer than that for the water-wet case with the maximum flux, particularly for the upward saturation profile (refer to Fig. 8-8b).

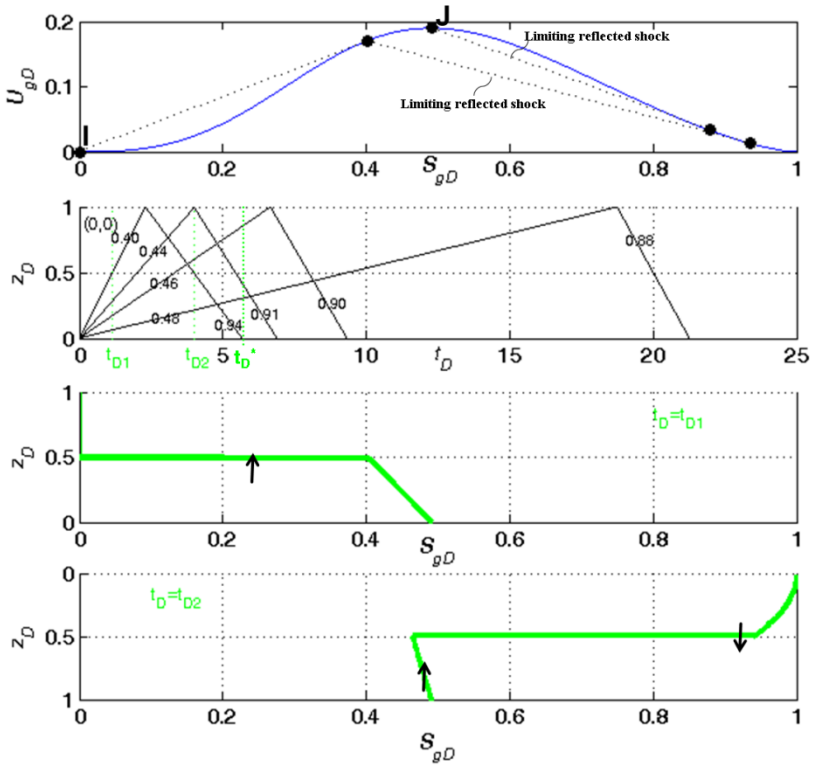

(a)

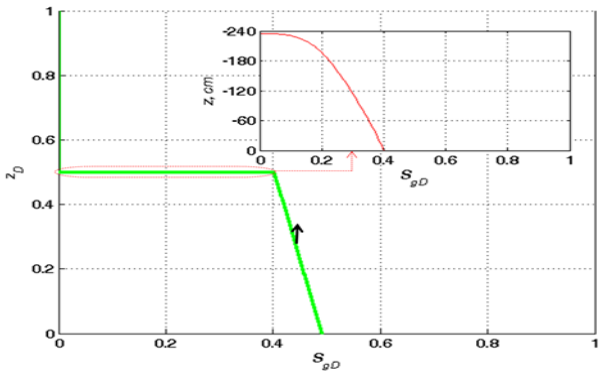

(b)

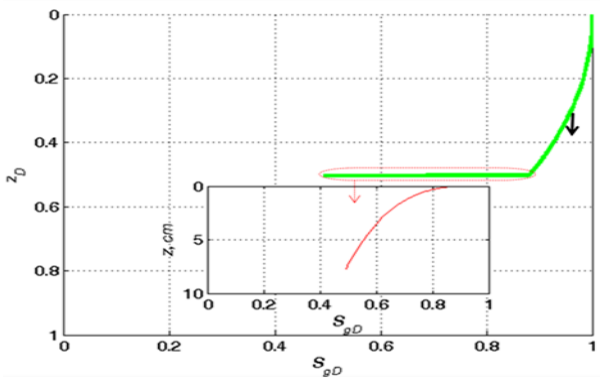

(c)

Fig. 8-8 A large boundary flux (corresponding to the maximum flux) is employed for the CO_2-wet reservoir. Subplots from top to bottom in (a) are: (1) U_{gD}-S_{gD} relationship; (2) Time-distance diagram; (3) Saturation profile at t_{D1} during upward migration; (4) Saturation profile at t_{D2} during backfilling. Insets in (b) and (c) show the resolution of shocks derived from the traveling wave solutions.

Compared to the small flux (Fig. 8-6), large flux gives a shorter time of upward migration and backfilling. In addition, large boundary source flux creates the mixed waves and non-monotonic saturation profile. In summary, the inlet boundary flux, wettability, and relative permeability essentially control the saturation wave development and migration.

8.4 THE IMPACT OF BOND NUMBER ON TRAVELING WAVE SHAPES

As explained above, capillary pressure is a dissipation effect that would smooth out shocks while buoyant force acts in the opposite way. Therefore, as the buoyant force increases, the size of the stabilized zone would be diminished. This is confirmed by Fig. 8-9a that shows the resolution of the upward saturation shocks in Fig. 8-3a. Different magnitudes of buoyancy are considered. The Bond number is used here to describe the relative importance of buoyancy to capillary pressure, and it is defined as $N_b=\Delta\rho g k_z/\sigma$. Where, σ is the interfacial tension between CO_2 and brine. Definitions of other parameters are the same as above. $\Delta\rho$ is set to be 1, 10, 100, and 1000 kg/m^3. Vertical permeability k_z is set to be 0.5 Darcy. Interfacial tension between CO_2 and brine is 4.9 mN/m. The calculated N_b ranged from 9.9e-10 to 9.9e-7. As N_b increases, the buoyant force converts the blunting stabilized zone into the discontinuous shock. For the given flux, at least, N_b>9.9e-8 was good enough to warrant the simple shock solution. N_b in Fig. 8-3a was 4.0e-7.

Meanwhile, as the buoyant force increases, Eq. 8.42 reduces to the capillary static equation,

$$\frac{dP_c}{dZ} = \Delta\rho g \tag{8.45}$$

Equation 8.45 means that capillary pressure varies linearly with vertical distance, which can be directly observed from Fig. 8-9b. As the Bond number increases (by increasing buoyancy), the Z-direction capillary pressure profile becomes straight.

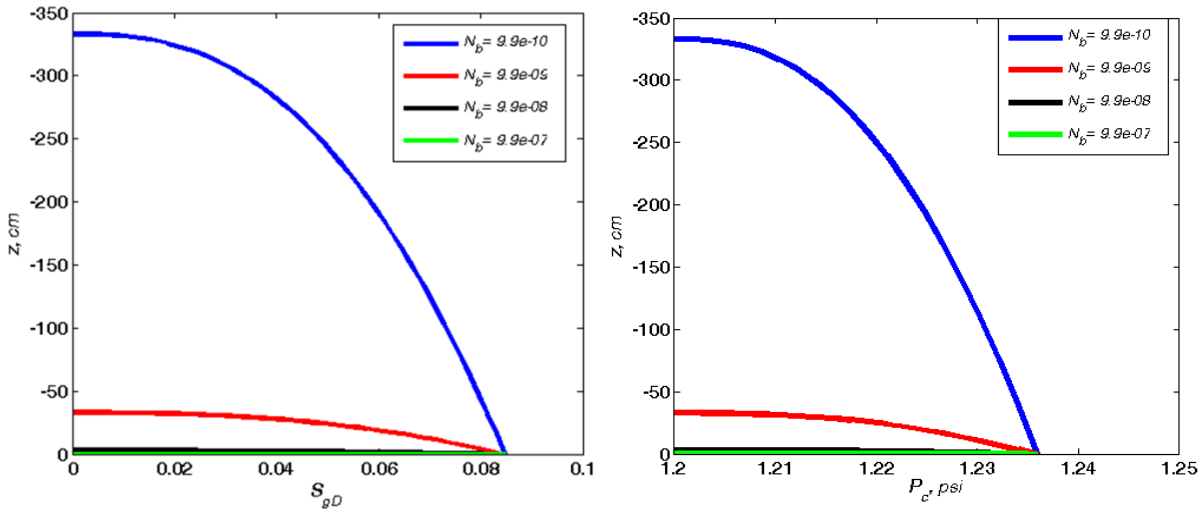

(a) (b)

Fig. 8-9 (a) The impact of Bond number (N_b) on saturation profiles. (b) The impact of Bond number on capillary pressure profiles (b).

8.5 APPLICATION AND LIMITATION

The above buoyant and countercurrent model predicts the exact time at which rising CO_2 reaches the top of the aquifer. A simple calculation is made on the Sleipner injection site. For the Utsira storage formation, the following reservoir and fluid phase properties are used (Singh et al. 2010, Taku Ide et al. 2007, Chadwick et al. 2005, Cavanagh 2013). The density difference between brine and CO_2 is 400 kg/m^3. Viscosity of brine is 1 cp. The formation thickness is 220 m. The porosity is 0.36. Both the residual water and residual CO_2 saturations are 0.1. A homogenous vertical permeability is assumed that ranges from 100 to 500 mD. Although the formation is comprised of several layers separated by shales, the shale is the intra-formation type rather than a complete shale layer (Singh et al. 2010). Meanwhile, the shale barriers are not perfect and maybe fractured (Cavanagh and Haszeldine 2014). All this information suggests that a homogeneous permeability field would be reasonable to represent the whole storage formation.

We directly employed the result for the water-wet reservoir. As shown in Fig. 8-3a, the dimensionless touching time was 0.85 when the dimensionless boundary flux was 0.10. By using Eq. 8.23 and the formation/fluid properties, the dimensional flux was between 1.2 and 6.1 m/yr.

By using Eq. 8.15, the time of reaching the top is determined to be between 0.88 and 4.4 yrs. Please note that it is the saturation wave velocity, rather than the flux, that determines the time of reaching the top or breakthrough (Buckley and Leverett. 1942). The field observed time was 2.5 yrs and our calculation is in between. Vertical permeability is the main uncertain parameter. Thus, the model gives a good estimation of bounding times of upward migration. Further, it could be used to guide the appropriate choice of injected CO_2 volume that prevent CO_2 reaching the seal system where it might be subject to leakage (Bryant et al. 2008).

Admittedly, the countercurrent model is subject to several limitations. First, the compressibility of CO_2 might not be negligible when gravity force dominates and the storage formation is very thick (Vilarrasa et al. 2010). Second, the model considers only buoyant flow during the post-injection period. The viscous pressure gradient during injection accelerates CO_2 upward migration. Thus, the model might overestimate the time of CO_2 reaching the seal system. However, in the long-term of geological sequestration and for most of the area away from the wellbore, buoyant flow dominates and, therefore, solutions presented in the paper could be used to approximate CO_2 upward migration and plume behavior.

8.6 SUMMARY

We adapt the model of describing the secondary oil migration proposed by Siddiqui and Lake (1992) to characterize CO_2 upward migration and backfilling behavior during countercurrent displacement in a saline aquifer. We examine both the water and CO_2-wet reservoirs at typical buoyant source fluxes. We present a self-similar solution of CO_2 saturation wave without capillary pressure effect and the traveling wave solution after capillarity incorporated. These solutions yield CO_2 saturation profiles (i.e., distance vs. time). The impact of saturation profile on capillary flux is highlighted here. Finally, we show the model prediction matches well with field observation. The model could also be used to assist in designing laboratory core-flooding tests on CO_2 buoyant flow.

Nomenclature

Roman Symbols

C	Constant
f	Fractional flow
g	Gravity acceleration [=] L/T^2
H	The height of storage domain [=] L
I	Initial condition
J	Injection condition
k_z	Vertical permeability [=] L^2
k_r	Relative permeability
L	Formation thickness [=] L
N	Bond number
P	Pressure [=] F/L^2
S	Phase saturation
T	Tangential point
t	Time [=] T
u	Phase flux [=] L/T
v	Velocity of the shock [=] L/T
z	Vertical Distance [=] L
Z	Traveling wave coordinate system [=] L

Greek Symbols

ϕ	Porosity
λ_r	Phase mobility ratio [=] $1/(T\text{-}F/L^2)$

ρ	Phase density [=] M/L^3
Δ	Difference
μ	Phase viscosity [=] $T\text{-}F/L^2$
σ	Interfacial tension [=] F/L

Subscripts

b	Bond
c	Capillary
D	Dimensionless
D_1	Dimensionless time point 1
D_2	Dimensionless time point 2
g	CO_2
r	Residual
T	Total
v	Viscous
w	Water
z	Vertical

Superscripts

b	Buoyant
c	Capillary
*	Shock saturation point or backfilling point of the fastest shock
+	Upstream

Chapter 9: Interplay between Capillary Trapping and Permeability-Retardation of Rising CO_2[4]

Previous chapters focus on the intra-layer capillary barrier in a single layer/formation. If multiple layers are involved in a CO_2 storage reservoir, then, both intra-layer and inter-layer capillary-barriers will emerge. We addressed questions associated with local capillary trapping caused by the former barrier in previous chapters. We study trapping behavior caused by the latter in this chapter.

Additionally, since capillary pressure is inversely correlated with permeability, a capillary barrier also acts as a permeability hindrance. Then both the capillary barrier and the permeability hindrance would delay CO_2 buoyant flow. However, it is not clear how permeability retardation and capillary-barrier trapping interact with each other during buoyant flow.

The above considerations epitomize the main objective of this chapter: to study these two accumulations separately under the condition of buoyant countercurrent flow. We build a one-dimensional multiphase and countercurrent flow model to describe CO_2 migration, accumulation, and trapping in a simplified domain comprised of a flow-barrier zone above a flow-path zone. We decouple the contributions of capillary-barrier and permeability-hindrance in the overall accumulation and systematically investigate interactions between the two in detail. The relative importance of these two accumulations is examined under various flow conditions (i.e., different buoyant source fluxes) and porous media properties (i.e., permeability contrast, wettability, and capillary pressure effect).

[4]Parts of this chapter is presented in the following conference: Ren, B., Delaney, J.M., Lake, L.W., Bryant, S.L. 2017. Maximizing CO_2 Accumulation in Storage Reservoirs: Interplay between Permeability Retardation and Capillary Trapping of Rising CO_2. Paper SPE-187356-MS presented at the SPE Annual Technical Conference and Exhibition, San Antonio, Texas, 9-11 October.

We demonstrate that CO_2 accumulation by the permeability retardation is possible because of a small relative permeability during countercurrent flow, and this accumulation is not dictated by wettability, which is the key to the capillary-barrier trapping. Although, in infinite time, the total accumulation would be reduced only to capillary-barrier trapping, the time-scale of the permeability-retardation can be significant. Therefore, neglecting permeability-retarded CO_2 would underestimate the overall safe storage capacity of CO_2 and overestimate the leakage risk of the geological carbon sequestration project. The results from the analytical study are confirmed using a full-physics simulation.

9.1 APPROACH

In this chapter, we extend the 1D countercurrent flow model in the chapter 8 to a two zones system. We solve the model analytically by the MOC when capillary pressure is not considered. Then, we add the capillary flux into the model and derive the approximate bounding solutions. Next, we employ it to analyze the accumulation caused by capillary trapping and permeability retardation and the relevant influential parameters. The procedures of the mathematical formulation has been shown in detail in the chapter 8. We reproduce some of the important equations here.

If we neglect the capillary flux, the total flux would be only the buoyant flux. The derived dimensionless equation is

$$\frac{\partial S_{gD}}{\partial t_D} + \frac{\partial u_{gD}}{\partial z_D} = 0 \tag{9.1}$$

In the above

$$z_D = \frac{z}{L} \tag{9.2}$$

$$t_D = \frac{k_z \Delta \rho g}{\mu_w \phi L (1 - S_{wr} - S_{gr})} t \tag{9.3}$$

$$u_{gD} = \frac{\lambda_{rg} \lambda_{rw}}{\lambda_{rg} + \lambda_{rw}} \mu_w \tag{9.4}$$

$$S_{gD} = \frac{S_g - S_{gr}}{1 - S_{gr} - S_{wr}} \tag{9.5}$$

$$u_{gD}^{b} = u_{g}^{b} \frac{\mu_w}{k_z \Delta \rho g} \tag{9.6}$$

A typical u_{gD}-S_{gD} curve is in Fig. 9-1. The CO_2 buoyant flux increases with gas saturation followed by a decrease. The flux decline at high gas saturation is attributed to the low water saturation that slows the migration of CO_2, as the flux of water is the same as that of CO_2 in the opposite direction under countercurrent flow. As analyzed in chapter 8, if the reservoir initial condition is at point *I*, and the injection boundary condition is at point *J*, then the saturation wave will be a shock with the velocity determined by the slope of the chord between *I* and *J*. If the injection boundary condition is at the point of (S^*_{gD}, u^*_{gD}), the saturation wave will be a combination of spreading wave and shock.

To simplify the analysis, we employ the blue lines to replace the real flux-saturation curve. The skeletonized straight lines are constructed using the two ends and the maximum point of the actual curve (see Fig. 9-1). The saturation wave is only the shock after using the skeletonized lines. This simplification removes many-detailed analyses on CO_2 migration/distribution in various saturation ranges, and meanwhile, it preserves the major characteristics of CO_2 plume migration.

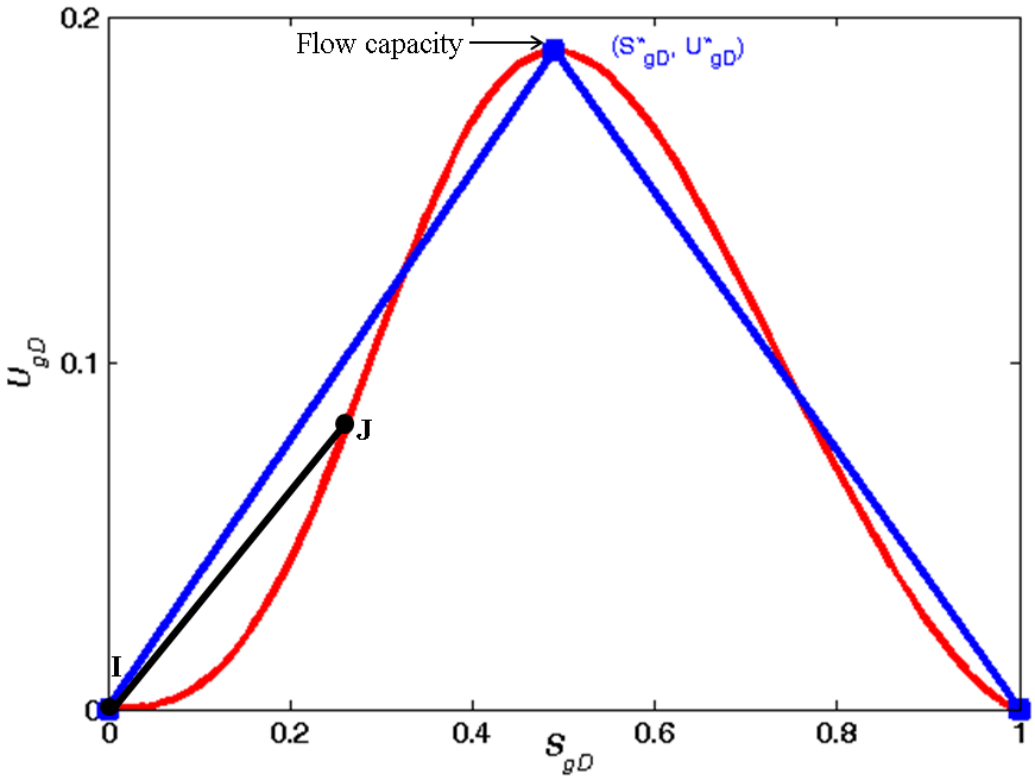

Fig. 9-1 Typical U_{gD}-S_{gD} relationship: the red curve is the actual buoyant flux at different gas saturations. The skeletonized curves (blue) are used for the following analysis. Points "I" and "J" represent the initial condition and injection condition, respectively.

The above solution to CO_2 saturation wave neglects the capillary flux. To add the capillary pressure effect, we follow Siddiqui and Lake (1997) to describe the capillary-barrier trapping. This modified way could give an accurate prediction of the phase saturation and trapping. In the result part, we will demonstrate how to graphically incorporate capillary pressure to characterize the capillary-barrier trapping.

We configure the problem domain with two parts: the bottom part is the flow path zone and the top is the barrier zone, as schematically show in Fig. 9-2. Both zones are inside a medium with the same thickness. They have the permeability of k_{z1} and k_{z2}, respectively. We consider two limiting permeability contrasts between barrier and flow path: the small contrast with k_{z1}=0.75 Darcy, k_{z2}=0.50 Darcy, and the large contrast with k_{z1}=0.75 Darcy, k_{z2}=0.05 Darcy

(see Table 9-1). The upper boundary is closed while the lowest boundary has a constant imposed flux.

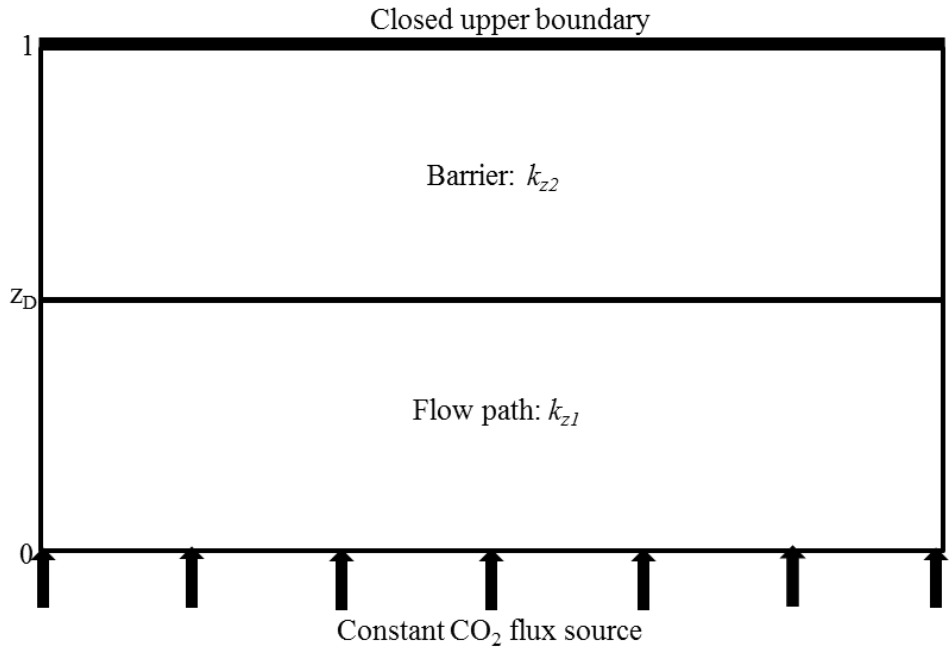

Fig. 9-2 Schematic configuration of the flow path and overlying barrier. The barrier has the same thickness as the flow path. The vertical axis is made dimensionless by scaling the individual thickness with respect to the total. A constant source flux is imposed at the lower boundary while the upper boundary is closed (no flow).

We present the results for two types of reservoir wettability: water-wet and CO_2-wet. We study two extreme magnitudes of source buoyant fluxes. They represent CO_2 fluxes in different portions of the reservoir at the end of injection. Considering CO_2 saturation around the wellbore would be larger than that in the region far away from the wellbore, a large CO_2 flux at the inlet (lower) boundary of the problem domain would correspond to the near wellbore and while a small flux would correspond to the far-away wellbore area. The two chosen fluxes, relative permeability, capillary pressure, and fluid properties under gas and water-wet conditions are summarized in Table 9-1.

Table 9-1. Reservoir and fluid properties for water-wet and CO_2-wet conditions

Parameters	**Water-wet**	**CO_2-wet**
Porosity	0.25	0.25
Permeability of flow path (k_1), Darcy	0.75	0.75
Permeability of barrier (k_2), Darcy	0.50, 0.05	0.05, 0.50
Capillary entry pressure of flow path (P_{e1}), psi	1.2	1.2
Water viscosity (μ_w), cp	0.55	0.55
CO_2 viscosity (μ_g), cp	0.085	0.085
Water density (ρ_w), kg/m^3	1024.6	1024.6
CO_2 density (ρ_g), kg/m^3	618.7	618.7
Residual water saturation (S_{wr})	0.20	0.20
Residual gas saturation (S_{gr})	0.20	0.20
[a] Water relative permeability (k_{wr})	$0.6(1\text{-}S_{gD})^{3.5}$	$0.8(1\text{-}S_{gD})^{1.5}$
Gas relative permeability (k_{gr})	$0.8(S_{gD})^{1.5}$	$0.6(S_{gD})^{2.75}$
Capillary pressure curve of flow path (P_{c1}), psi	$P_{e1}\ (1\text{-}S_{gD})^{-1/3.0}$	$-P_{e1}\ [(S_{gD})^{-1/3.0}\text{-}1]$
[b] Capillary entry pressure of barrier (P_{e2}), psi	$P_{e1}\ (k_1/k_2)^{0.5}$	$P_{e1}\ (k_1/k_2)^{0.5}$
Capillary pressure curve of barrier (P_{c2}), psi	$P_{e2}\ (1\text{-}S_{gD})^{-1/3.0}$	$-P_{e2}\ [(S_{gD})^{-1/3.0}\text{-}1]$
Total height of flow path and barrier, cm	200	200
[c] Height of static capillary trapping (H_g), cm	46.7, 147.7	0
Selected dimensionless buoyant fluxes	0.086, 0.144	0.086, 0.144

Note: [a] $S_{gD}= (S_g- S_{gr})/(1- S_{wr}- S_{gr})$; [b] the capillary entry pressure is calculated using the Leverett j-function; [c] the height of capillary trapping for the small permeability contrast case is calculated using the static capillary pressure equation. 46.7 cm and 147.7 cm correspond to the small and large permeable barrier, respectively.

9.2 RESULTS

In this part, we first show how the magnitude of the buoyant flux, permeability contrasts, and capillary pressure influence the two accumulation behaviors inside the water-wet reservoir. Then we conduct a similar analysis for the CO_2-wet reservoir and show the wettability effect. Finally, we discuss the results and the model.

9.2.1 Water-wet reservoir

9.2.1.1 Effect of the buoyant source flux magnitude

We first consider a relative homogenous water-wet reservoir; thus, the permeability contrast ratio between the flow barrier and flow path would be small and we set it to be 1.5 (Table 9-1). Capillary pressure is not considered. Figure 9-3 shows the impact of the buoyant flux magnitude on CO_2 migration and accumulation. Column A is for the small imposed boundary flux while the right for the large. The four subplots in each column are the flux-saturation relationship, time-distance diagram, saturation profile during CO_2 upward migration, and saturation profile during backfilling (i.e., CO_2 moves downward), respectively.

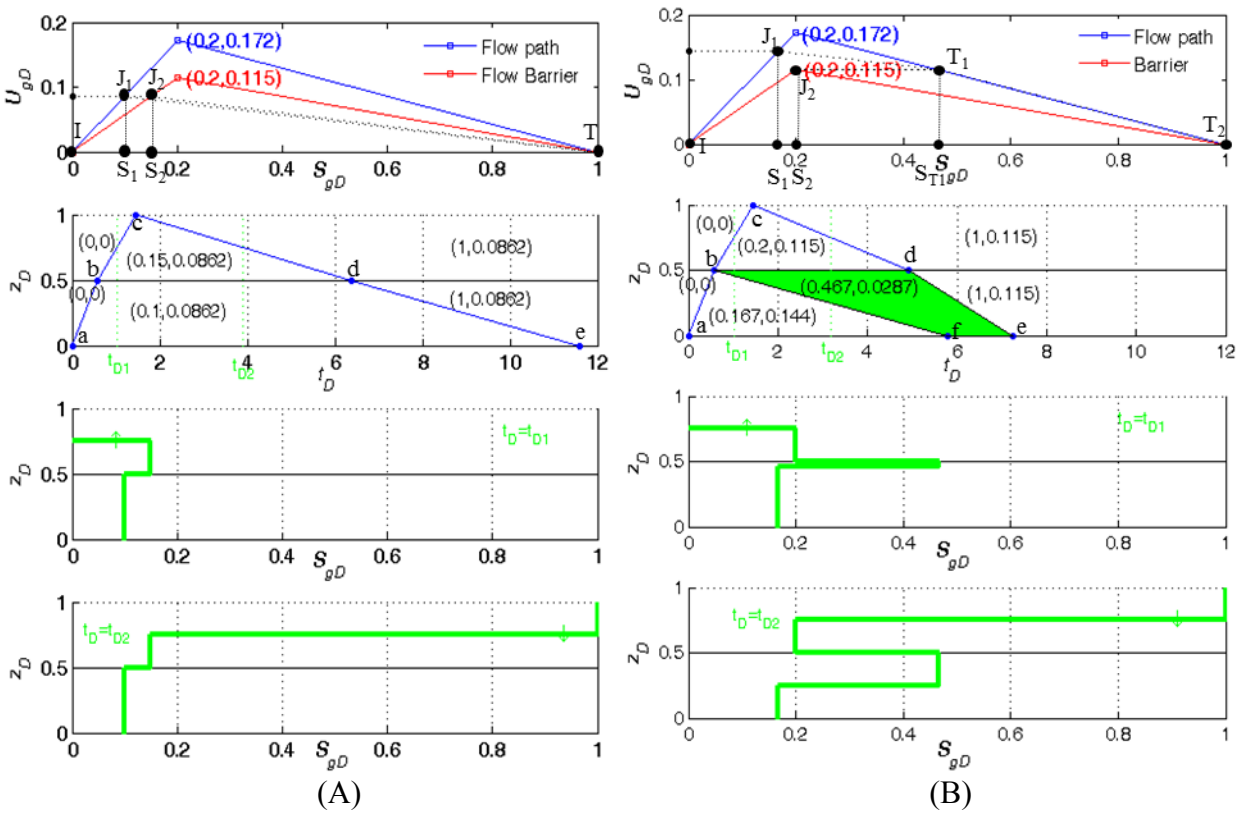

Fig. 9-3 Capillary pressure is not considered. Column A is for the inlet flux smaller than the capacity of the barrier, while column B is for the flux between the flow capacity of the barrier and flow path. The subplots from top to bottom are: (1) The U_{gD}-S_{gD} relationship for a small permeability contrast between barrier and flow path, the dashed line starts with a source flux smaller than the capacity of barrier, and then crosses the U_{gD}-S_{gD} lines for the flow path and barrier; (2) Time-distance diagram; (3) Saturation profile at t_{D1} during upward migration; (4) Saturation profile at t_{D2} during backfilling. In the time-distance diagram of the column B, the green shaded area indicates accumulation of CO_2.

We use the small flux case as an example to describe how to construct the subplots in Fig. 9-3A. By using the dimensionless flux equation U_{gD} and the relative permeability data in Table 9-1, we can obtain the U_{gD}-S_{gD} relationships for both flow path and barrier zones (subplot #1 in column A). We label the maximum flux and the corresponding saturation in the parenthesis (S^*_{gD}, U^*_{gD}). The small dimensionless buoyant flux was chosen to be 0.086, which is less than the maximum of barrier (equal to 0.115). When CO_2 with such a flux migrates into the flow path, the saturation wave is a shock with the saturation S_I and specific velocity determined by the slope of

the chord I-J_1. Then correspondingly, in the time-distance diagram, the migration starts from the origin (point *a*) and ends at the interface (point *b*) between barrier and flow path at a specific time t_D determined by the dimensionless distance and shock velocity. When CO_2 comes across the interface, the flux is continuous; this means the flux into the barrier should be the same as that in the flow path. Therefore, similar to the movement inside the flow path, CO_2 is carried by a new shock with the saturation S_2 and velocity equal to the slope I-J_2 (a slower velocity), it travels from point *b* to point *c*. When the wave touches the upper closed boundary, it will be reflected with the shock velocity determined by the chord J_2-T and moves from point *c* to point *d* as time proceeds. When CO_2 returns into the flow path zone, the shock velocity will be determined by the flow properties of the path and follow the slope of line J_1-T, and meanwhile it moves from point *d* toward to point *e* in the time-distance diagram.

According to the above analysis, the time-distance diagram can be divided into six regions separated by the blue lines, the barrier-flow path interface and boundaries. Each region is characterized by a distinct combination of flux and saturation shown in parenthesis (U_{gD}, S_{gD}). For example, the term (0.1, 0.0862) means that in the region surrounded by points *a*-*b*-*d*-*e*, the saturation is 0.1 and the dimensionless flux is 0.0862. The backfilling wave travels from point *c* through point *d* and *e*. As backfilling proceeds, the domain will be completely saturated with CO_2, therefore, the right two portions of the domain have a dimensionless CO_2 saturation equal to one. The final dimensionless backfilling time at point *e* was 11.6. By using the dimensionless time equation $t_D = k_z \Delta\rho g t/[\mu_w \phi L(1-S_{wr}-S_{gr})]$ and using properties of the flow path listed in Table 9-1, we can calculate the dimensional time t=0.11 day for the total height (L) of 0.1 m. The dimensional time linearly increases with the total height as indicated from the dimensionless equation.

We select two times t_{D1} and t_{D2} (dashed green lines in the subplot #2) to plot the saturation profile. The former time is before CO_2 touches the upper boundary, and the latter is during CO_2 backfilling. The corresponding saturation profiles are shown in subplots #3 and #4, respectively. During the upward migration, CO_2 saturation increases when moving into the

barrier because of its small permeability. This increased saturation is the contribution of the low permeability heterogeneity to the accumulation of CO_2. During the backfilling, the region swept is completely saturated with CO_2. In this sense, the accumulation is transient.

The above analysis is based on a small source flux. To explore the impact of large flux on CO_2 migration and accumulation, we increase the initial buoyant flux from 0.086 to 0.144, the latter is between flow capacity of the barrier zone and flow path zone (Fig. 9-3B). Here, the flow capacity corresponds to the maximum point in the U_{gD}-S_{gD} curve, and the capacity is determined by the mobility of CO_2 and water. When this buoyant flux comes into the flow path, a shock forms with the saturation of S_1 and velocity equal to the slope of I-J_1. As it crosses the interface, the CO_2 carried by this wave cannot be totally transmitted into the barrier because of its lower capacity. Continuity of the flux can only be satisfied when the flux into the barrier is reduced to the capacity of the barrier. This gives rise to a shock wave shaped by I-J_2 with the saturation of S_2. The remaining flux is retained into the flow path with a reflected shock wave determined by J_1-T_1, and the corresponding saturation is S_{T1}. The analysis on the backfilling saturation wave is similar to that using a small source flux.

In the time-distance diagram, we can see the reflected wave by the permeability hindrance moves from point *b* toward point *f* as time proceeds. CO_2 gradually accumulates inside the green region *b*-*d*-*e*-*f*. These accumulated would be in place as long as the source buoyant flux continues to move upward. If the source flux ceases, this accumulation would migrate into the barrier with the velocity that can be calculated in a similar way.

In the saturation profiles, the saturation distribution along the distance under a large buoyant flux is different from that for the small. The latter is monotonically increasing from the tail to the tip of CO_2 plume, while for the former, there is a region with an abrupt and large increase in CO_2 saturation below the path-barrier interface. This region is an accumulation of CO_2, and its height increases as the time proceeds from t_{D1} to t_{D2}. It should be indicated that allowing the downward shock to touch the inlet boundary might cause a boundary ambiguity as the inlet boundary condition is set to be the constant source flux. One might simply consider the

extra CO_2 that cannot be accommodated by the flow path drains back into the source area or moves laterally through the spill point in the space.

9.2.1.2 Effect of permeability contrast between the flow path and barrier zone

From the above analysis, there is no CO_2 accumulation under the small flux scenario when the permeability contrast between the flow path and the barrier is small (1.5). The increase in a permeability contrast influences only the upward and backfilling speed of CO_2 under the small source flux. However, the final backfilling time point will not be changed. This can be explained by the relationship of upward and downward shock velocity. Using Fig. 9-3A for example, the total time for the wave to travel inside the flow path can be expressed as the sum of upward time along the *a*-*b* line and downward time along the *d*-*e* line. The upward time is the ratio of the flow path zone height over the slope of line I-J_1, while the downward time is the ratio of flow path zone height over the slope of line J_1-T. The sum of the two times should be equal to the distance I-S_1 plus S_1-T, which is constant as long as the chosen flux is smaller than the capacity of the barrier.

Therefore, in the following analysis, we only consider the large flux case to study the effect of permeability contrast on the accumulation. Figure 9-4 shows the flow capacity, CO_2 migration and accumulation, saturation profile for the large source flux and large permeability contrast. The only difference between Fig. 9-3B and Fig. 9-4 is the permeability contrast: the former is 1.5 while the latter is 15.

Several observations can be made through comparing the two figures: (1) The accumulation speed of accumulation is faster for the large permeability contrast than that for the small contrast. This is because the carrying capacity of the barrier is decreased as its permeability decreases, and because the velocity of the reflected wave determined by the slope J_1-T_1 is larger than that for the small permeability contrast; (2) The saturation of the accumulated CO_2 was 0.947, which was much larger than the 0.467 for the small permeability contrast. More extra fluxes are reflected back into the path as the decrease of the flow capacity of the barrier; (3) The

final backfilling dimensionless time was 46.4, which increased more than six-fold compared with that for the small permeability contrast. The final filling time does not linearly change with the barrier permeability. This is because the change of barrier permeability influences the time of shock traveling inside both the barrier and flow path regions.

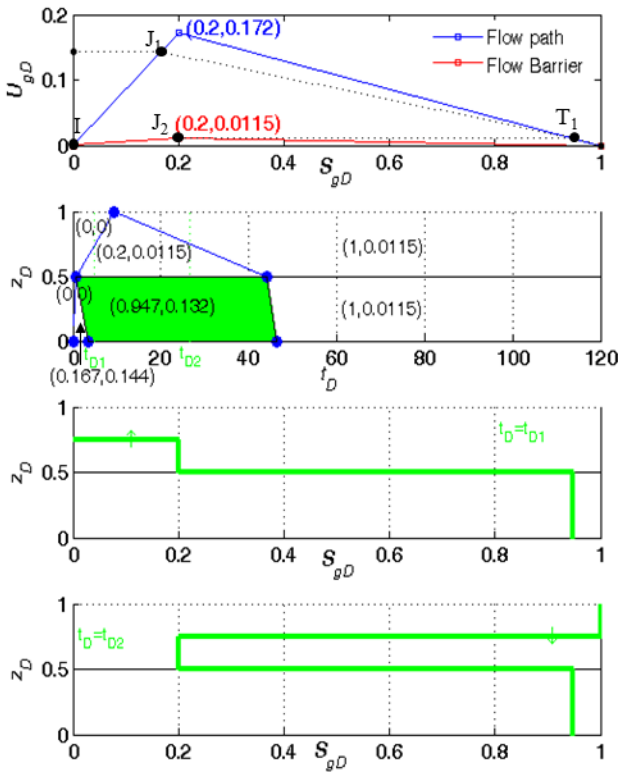

Fig. 9-4 Capillary pressure is not considered. A large source flux is used for a large permeability contrast configuration. Subplots from top to the bottom are: (1) The U_{gD}-S_{gD} relationship for the large permeability contrast inside the water-wet reservoir; (2) Time-distance diagram; (3) Saturation profile at t_{D1} during upward migration; (4) saturation profile at t_{D2} during backfilling. Note: in the time-distance diagram, the green shaded area represents accumulation of CO_2.

9.2.1.3 Effect of capillary pressure

We compare capillary trapping to permeability retardation for the two source fluxes with capillary pressure considered. For the small source flux, the capillary pressure curve, flux-

saturation relationship, and the time-distance diagram are shown in Fig. 9-5A. Figure 9-5B is for the large source flux.

We use the small flux case to demonstrate how to graphically incorporate capillary pressure into the estimation of CO_2 migration and accumulation. Subplot #1 is the capillary pressure curve generated by using the data in Table 9-1. As expected, the flow barrier has a larger capillary entry pressure than the flow path: the former is 1.47 *psi* and the latter is 1.20 *psi*. CO_2 saturation (S^*) in the flow path corresponding to the capillary entry pressure of the barrier was 0.456. As seen from subplot #2, the magnitude of CO_2 saturation carried by this shock was 0.1 (S_1) in the small buoyant flux case. When this CO_2 comes to the interface between the flow path and the barrier, it cannot instantly migrate into the barrier because of the capillary entry pressure effect. Instead, it accumulates below the barrier. When the saturation at the interface increases to 0.456 (point T_1), the leak into the barrier zone starts with the saturation of S_2 at the speed determined by the slope I-J_2. The decrease in the flux under the saturation S^* is attributed to the capillary effect.

Correspondingly, in the time-distance diagram, CO_2 upward and downward migration profile follow the points *a-b-c-d-e-f*. There is a time gap between point *b* and *c* at the interface. This is the time for CO_2 to accumulate untill the saturation achieves S^*, meanwhile, the accumulation height reaches the static capillary pressure height (height of the red area, refer to Table 9-1). Reservoir numerical simulation can be employed to determine the accurate leakage time. Here, we show an estimation on the lower-bound of leak time, which means the possible shortest time for CO_2 to accumulate.

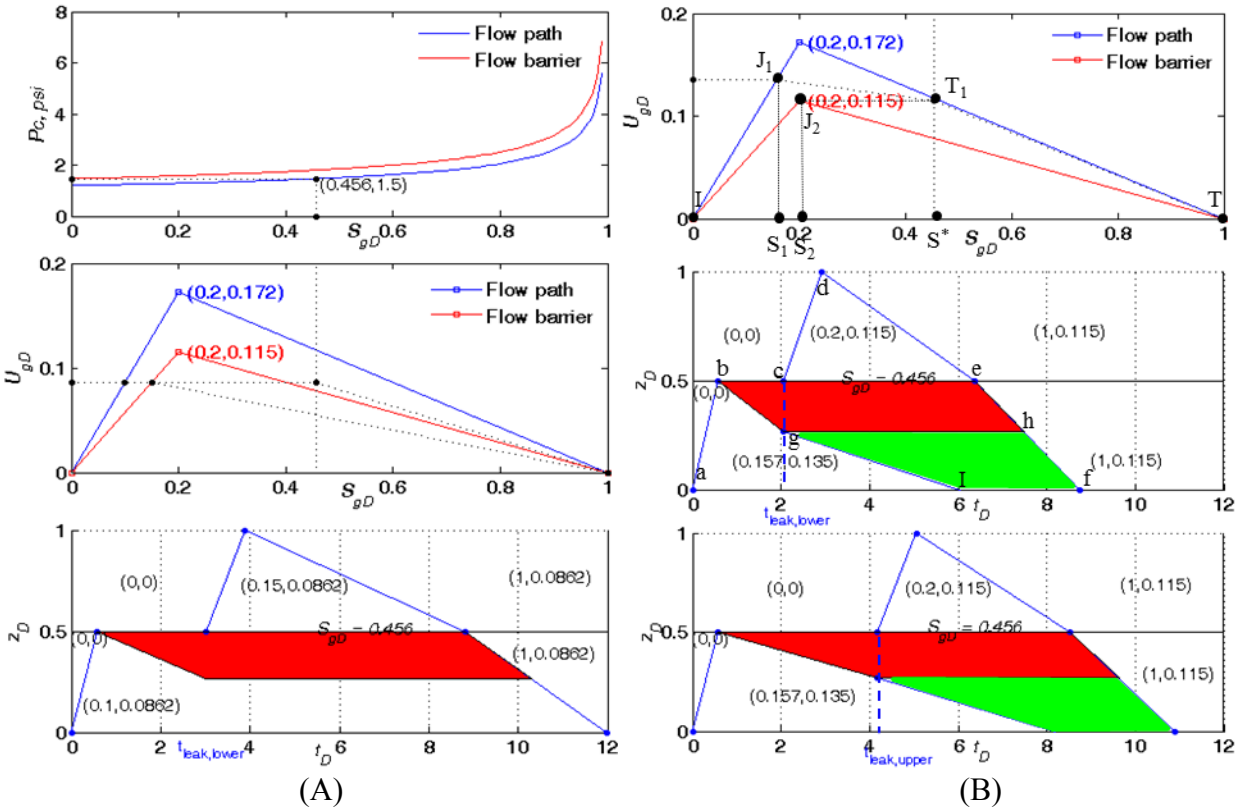

Fig. 9-5 Capillary pressure is considered. Column A is for the small flux, the subplots from top to the bottom are: (1) P_c-S_{gD} curve; (2) The U_{gD}-S_{gD} diagram for a small permeability contrast; (3) Time-distance diagram. Column B is for the large flux, the subplots from top to the bottom are: (1) The U_{gD}-S_{gD} diagram for a small permeability contrast; (2) Time-distance diagram for the lower-bounding leak time; (3) Time-distance diagram for the upper-bound leak time. The red shaded area is the capillary trapping, of which the height is constrained by the static capillary equation, while the green shaded area is the CO_2 accumulation induced by permeability retardation.

Suppose the upward shock in the flow path reflects instantly once it touches the interface, this is what happens under the scenario of no capillary effect. Then the reflected wave will move with the velocity calculated by the slope of line J_1-T, with the corresponding distance-time profile along the points *b*-*g*. This gives the fastest accumulation of CO_2 untill the static capillary height.

The flow in the red capillary trapping area is a spreading wave rather than a shock. The spreading portion has the saturation ranged from S^* to a larger value. We did not show saturation profiles as the saturation gradient could not be determined. Compared with the small

permeability contrast without capillarity (refer to Fig. 9-3), the capillary barrier always trap CO_2 even if the source buoyant flux is smaller than the capacity of barrier.

Similar to the small source flux, we analyzed the impact of capillary pressure on the accumulation behavior under the large source flux scenario (Fig. 9-5B). As expected, the capillary-barrier trapping is the same as that for the small flux; the only difference is the appearance of accumulation induced by both permeability retardation and the extra flux above the flow capacity of barrier zone. In the time-distance diagrams of Fig. 9-5B, the red area is the capillary barrier trapping while the green is CO_2 accumulation induced by permeability retardation.

The migration and accumulation behaviors are demonstrated using the bounding leak times. Subplot #2 in Fig. 9-5B shows time-distance diagram for the lower bound, and subplot #3 corresponds to an upper-bound estimation. By assuming an instant reflection of the shock inside the flow path, we can construct the distance-time profile along point *b*-*g* by using the velocity controlled by the chord J_l-T. This gives the lower-bound time estimation as shown in the middle right plot. If instant leakage into the barrier is assumed, then extra-flux will be carried by the saturation shock with the velocity equal to the slope of the chord J_l-T_l. For this assumption, the flux inside the flow path would be a lower bound estimation; therefore, the time the reflected wave takes to travel through the red region would be the upper limiting leak time. The exact leak time would be in between these two.

All the above analysis employs a small permeability contrast. For the large permeability contrast (by decreasing the barrier permeability), the observation would be qualitatively similar and the following quantitative differences would be expected: (1) The height of the capillary trapping would increase as the decrease of the barrier permeability, permeability retardation-induced accumulation would not occur if the column of flow path is less than the capillary trapping height. (2) The shock velocity would be changed for flow inside the barrier because the flux is a function of permeability. However, as the analysis in the above shows, the overall time-distance profile would be the same as that for the small permeability contrast scenario as long as

the imposed source flux is less than the capacity of barrier zone. (3) For the large permeability contrast, the leak time point would be narrowed if a large source flux were employed, as the velocity of the instantly reflected wave for the lower-bound estimation will be close to that with which the extra flux is carried under the upper-bound time scenario.

9.2.2 CO_2-WET RESERVOIR

9.2.2.1 Effect of buoyant source flux magnitude

Similar to the analysis on the water-wet reservoir, we first revoke capillary pressure to analyze the impact of flux magnitude and permeability contrast on the accumulation. Figures 9-6A and Fig. 9-6B show the flux-saturation relationship, time-distance diagram and saturation profiles for the small and large source flux, respectively. The chosen permeability contrast is 1.5. Overall, CO_2 migration and accumulation are qualitatively similar to that for the water-wet reservoir (refer to Fig. 9-3) for the same permeability contrast. But several notable differences can be made after careful comparison between Fig. 9-6B and Fig. 9-3B: (1) the saturation at the maximum flux moves to the right as a reservoir becomes CO_2-wet, this is obviously because the relative permeability is affected by the wettability; (2) the CO_2-wet reservoir tends to have a higher saturation of permeability-retarded accumulation than the water-wet one; (3) the permeability-retarded accumulation in the CO_2-wet reservoir is slower than that for the water-wet.

9.2.2.2 Effect of permeability contrast

If the permeability contrast between the flow path and barrier increases from 1.5 to 15, the arising influence on CO_2 migration and accumulation is similar to that for the water-wet reservoir. The enlarged permeability contrast gives rise to the higher CO_2 saturation of permeability-retarded accumulation when using a large source flux. However, as noted from Fig. 9-6B, the dimensionless CO_2 saturation of permeability-retarded accumulation can be as high as 0.66 in the CO_2-wet reservoir. This implies CO_2-wet reservoir requires less permeability contrast to create the same amount of permeability-retarded accumulation than the water-wet. This

suggests that, for the CO_2-wet reservoir, source flux magnitude would be more important than the permeability contrast in forming permeability-retarded accumulation.

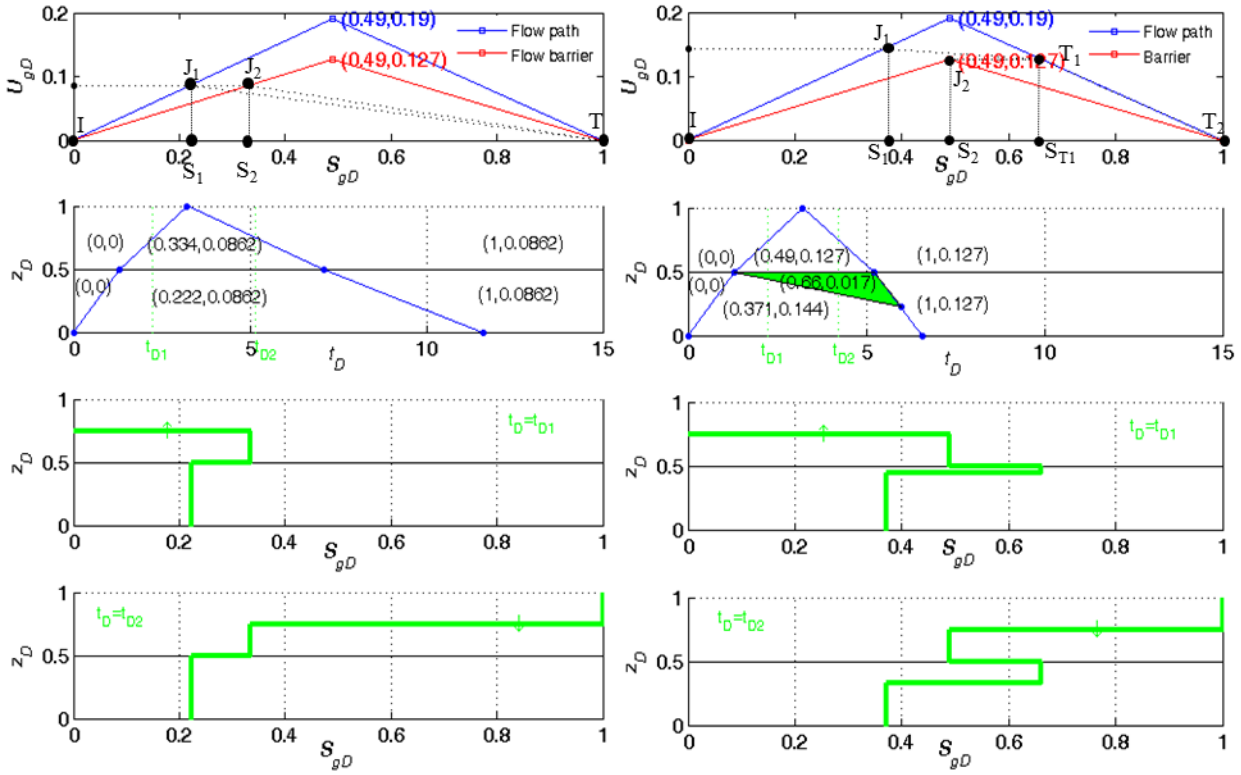

(A) (B)

Fig. 9-6 Capillary pressure is not considered. Column A is for the small flux while the column B for the large flux in the CO_2-wet reservoir. In each column, the subplots from top to the bottom: (1) The U_{gD}-S_{gD} relationship for a small permeability contrast inside the CO_2-wet reservoir; (2) Time-distance diagram; (3) Saturation profile at t_{D1} during upward migration; (4) Saturation profile at t_{D2} during backfilling. In the time-distance diagram, the green shaded area indicates permeability-retarded CO_2.

9.2.2.3 Effect of capillary pressure

Figures 9-7A and 9-7B show the capillary pressure curve, flux-saturation relationship, and time-distance diagram for the small and large source flux, respectively. Since we did not explicitly incorporate the capillary pressure into the flux equation, the time-distance profile is the same as that without capillary pressure term. Theoretically, capillary pressure in the CO_2-wet reservoir drives buoyant flow, therefore, it can be expected that the final backfilling time would

become small if the capillary dispersion were considered into the wave migration, and the time-distance relation would be nonlinear. Nevertheless, the evolution of permeability-retarded CO_2 would be qualitatively similar to those in Fig. 9-7.

We further compare Fig. 9-7 to Fig. 9-5 to explore the impact of wettability on CO_2 migration and accumulation. First, under the CO_2-wet condition, CO_2 instantly leaks into the barrier once it touches the interface. This change is also reflected in the final backfilling time point; it takes less time for CO_2 to completely saturate the CO_2-wet reservoir than the water-wet. Secondly, the capillary-barrier trapping does not develop in the CO_2-wet reservoir because capillary pressure is a driving force (i.e., pulling CO_2 into the rock instead of blocking it). Thirdly, the permeability-retarded accumulation remains in place irrespective of wettability condition, but its height and saturation are different for the varying wettability.

The increase in a permeability contrast would influence only permeability-retarded accumulation under the CO_2-wet condition. This is much different from the impact on the water-wet reservoir as analyzed above. Large permeability contrast would be more important for the CO_2-wet reservoir than the water-wet, as more permeability-retarded accumulation caused by a larger permeability contrast would compensate the loss of capillary-barrier trapping.

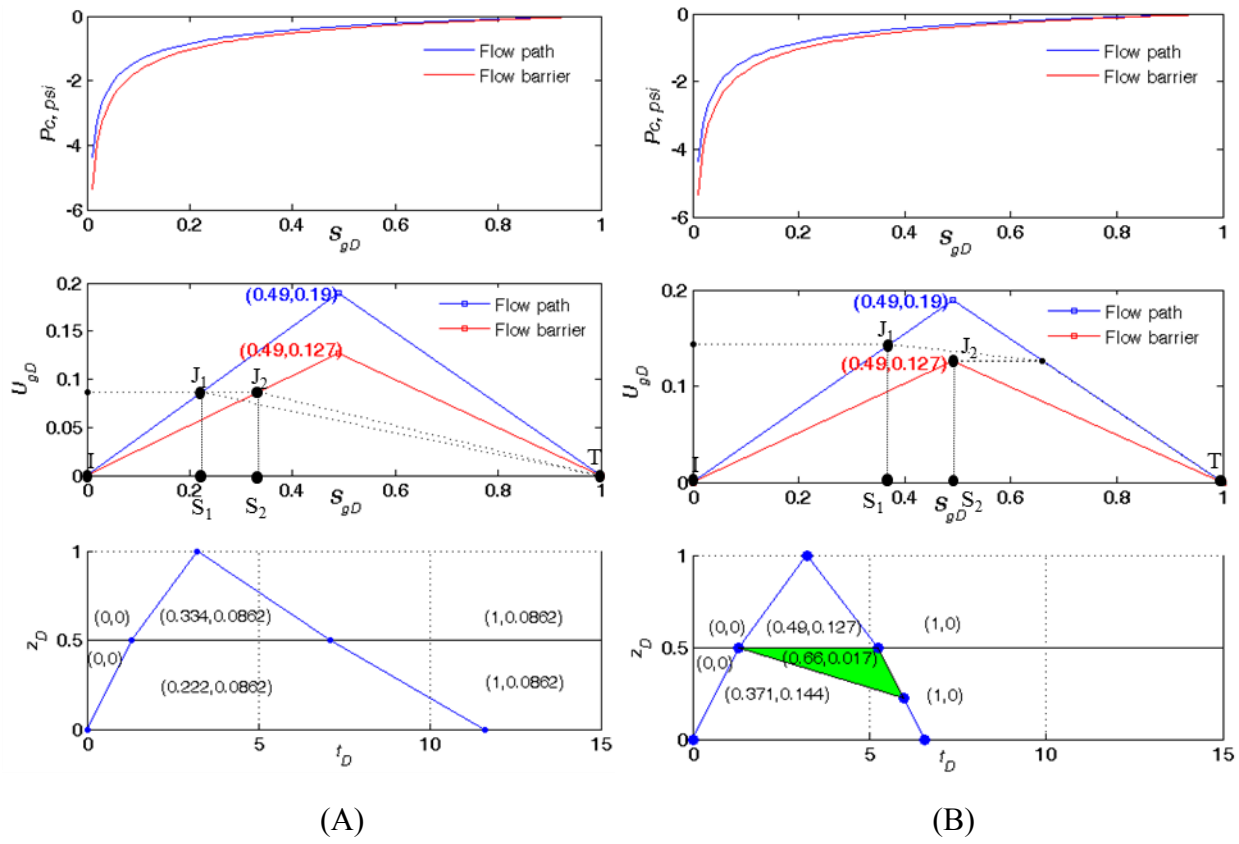

(A) (B)

Fig. 9-7 Capillary pressure is considered. The left column is for the small flux while the right for the large flux in the CO_2-wet reservoir. Subplots from top to bottom are: (1) P_c-S_g curve; (2) The U_g-S_g diagram for a small permeability contrast inside the CO_2-wet reservoir; (3) Time-distance diagram.

9.3 VALIDATIONS FROM FULL-PHYSICS SIMULATION

We validate the accumulations caused by permeability hindrances and capillary trapping using CMG-GEM (2012). A 1D domain was built with dimensions of 1×20 and grid size of 100×1 ft. As assumed in the analytical study, the upper barrier zone has the same thickness as the flow zone. Rock properties, fluid properties, relative permeability curve, and capillary pressure curves are the same as those in Table 9-1.

For each permeability contrast, first, simulations without capillary pressure was conducted to examine permeability-retarded accumulation. Then, capillary entry pressure effect (through using scaled capillary pressure curve) was considered to study CO_2 accumulation caused by both permeability and capillary-barrier. The capillary pressure curve was scaled using

procedures described in Chapter 3. The reservoir is set to be water-wet; the CO_2-wet case can be easily simulated in a similar way. Other inputs are the same as previous work (Ren et al. 2014, Saadatpoor 2009).

To obtain an equivalent buoyant driven flux in the simulation, a dimensionless flux is converted into a dimensional flux using the following equation, $U_g=U_{gD}\times k_z\times\Delta\rho\times g/\mu_w$. The two chosen dimensionless fluxes in the analytical study are 0.086 and 0.144. By using k_z=750 *mD*, $\Delta\rho$=406 kg/m^3, and μ_w=0.55 *cp*, the converted dimensional buoyant flux are 15.0 and 24.8 *m/yr*. We call these two as small and large flux in the following results. In CMG-GEM, Flow with the above dimensional buoyant fluxes lasts for 30 days. After that, fluxes are stopped and then purely buoyant flow is simulated, in order to examine the effect of source flux on CO_2 accumulation. The cases simulated are summarized in Table 9-2.

Table 9-2. Conditions for simulated cases in CMG-GEM

Case#	k_1, mD	k_2, mD	P_c curve	Inlet flux, m/yr	Figure
#1	750	500	w/o	15.0	9-8A
#2	750	500	w/o	24.8	9-8B
#3	750	50	w/o	24.8	9-8C
#4	750	500	Scaled P_c curve	15.0	9-9A
#5	750	500	Scaled P_c curve	24.8	9-9B
#6	750	50	Scaled P_c curve	24.8	9-9C

Figure 9-8 shows the evolution of saturation fields after 2, 6, 10 and 12 days of flow without capillary pressure effect. Figure 9-8A is for a combination of small permeability contrast and small inlet flux. In this column, as CO_2 moves upward, CO_2 crosses the middle interface between flow path and flow barrier. The permeability discontinuity does not result in CO_2 accumulations below the interface. This is because the buoyant flux can be accommodated by the flow capacity of the barrier zone. However, when a large inlet flux is used (in Fig. 9-8B) while

keeping the permeability contrast the same as that in column A, CO_2 accumulates in the flow zone when it encounters the permeability contrast. A large CO_2 saturation was observed below the flow barrier zone. As time proceeds, CO_2 finally accumulates below the top closed boundary. If a combination of large permeability contrast and large inlet flux is used, CO_2 accumulations are enhanced, as shown in Fig. 9-8C. These CO_2 accumulation behaviors can also be directly observed from the saturation profiles in Fig. 9-9.

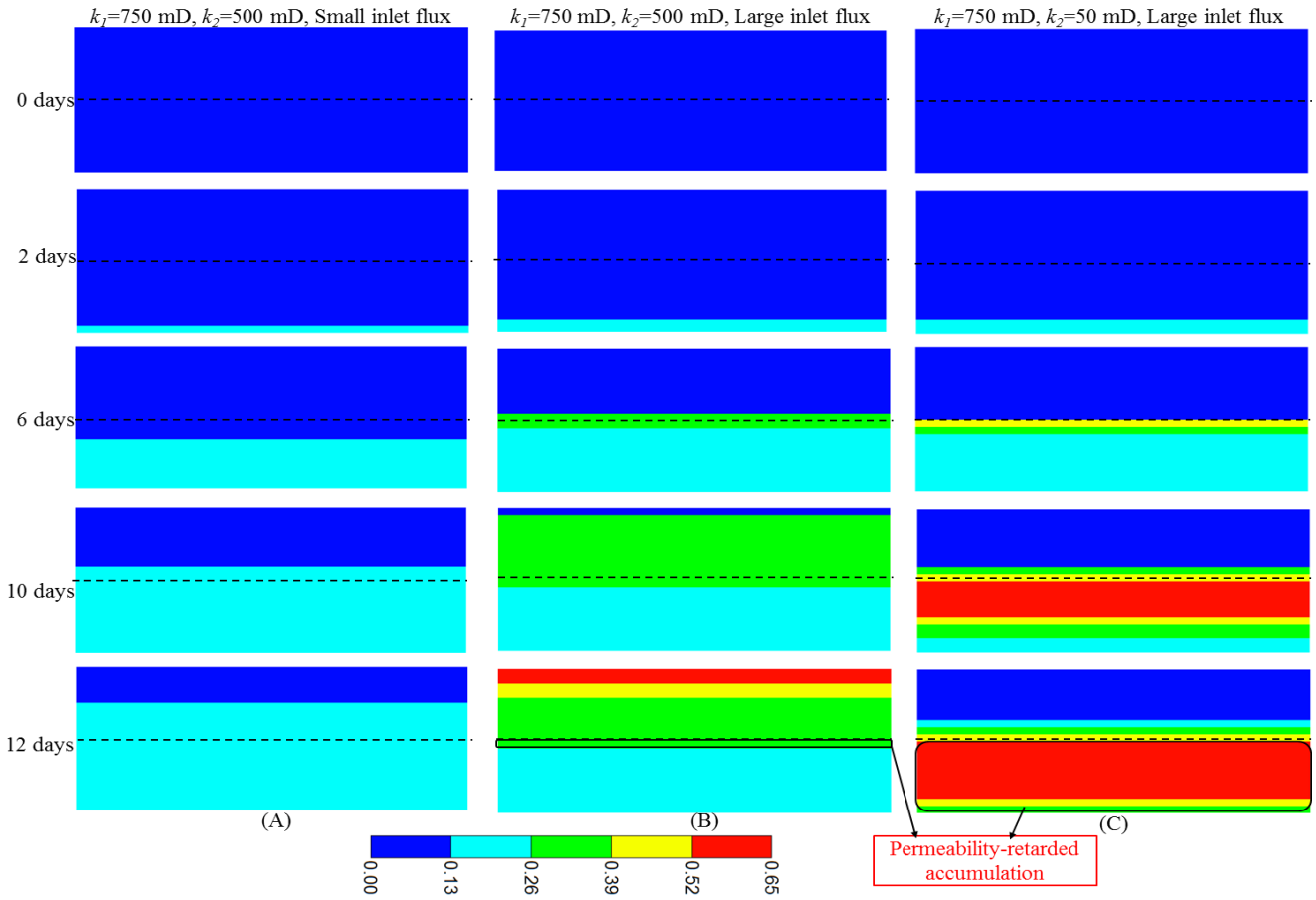

Fig. 9-8 The evolution of CO_2 saturation fields without capillary pressure effect. The row represents different time, and the column records different combinations of permeability contrast and inlet flux. Model size is 100 × 20 ft. Black dashes line represents the position of interface between a flow path zone and a flow barrier zone. Black rectangular area indicates CO_2 accumulation caused by the permeability hindrance.

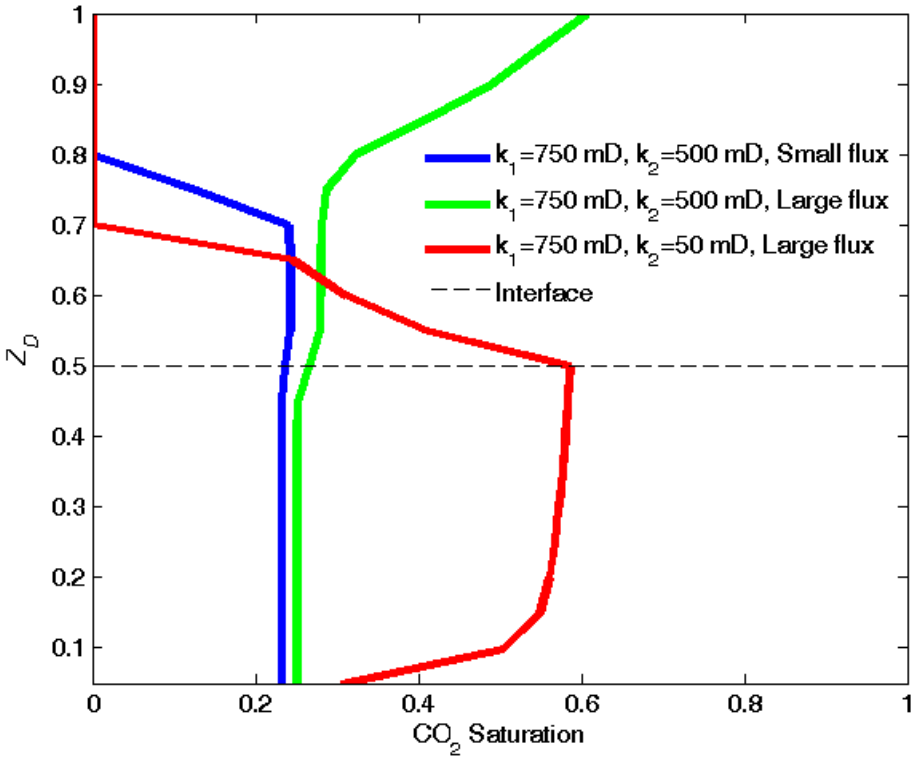

Fig. 9-9 CO_2 saturation profiles at 12 days of CO_2 flow. They are corresponding to the last row of Fig. 9-8. Capillary pressure is not considered.

Figure 9-8 is for cases without capillary pressure. Similar observation on the accumulation is made for the single capillary pressure curve, i.e., the flow path and barrier zone employs the same capillary pressure curve. The corresponding evolution of saturation fields is in Fig. 9-10, and the saturation profiles are in Fig. 9-11.

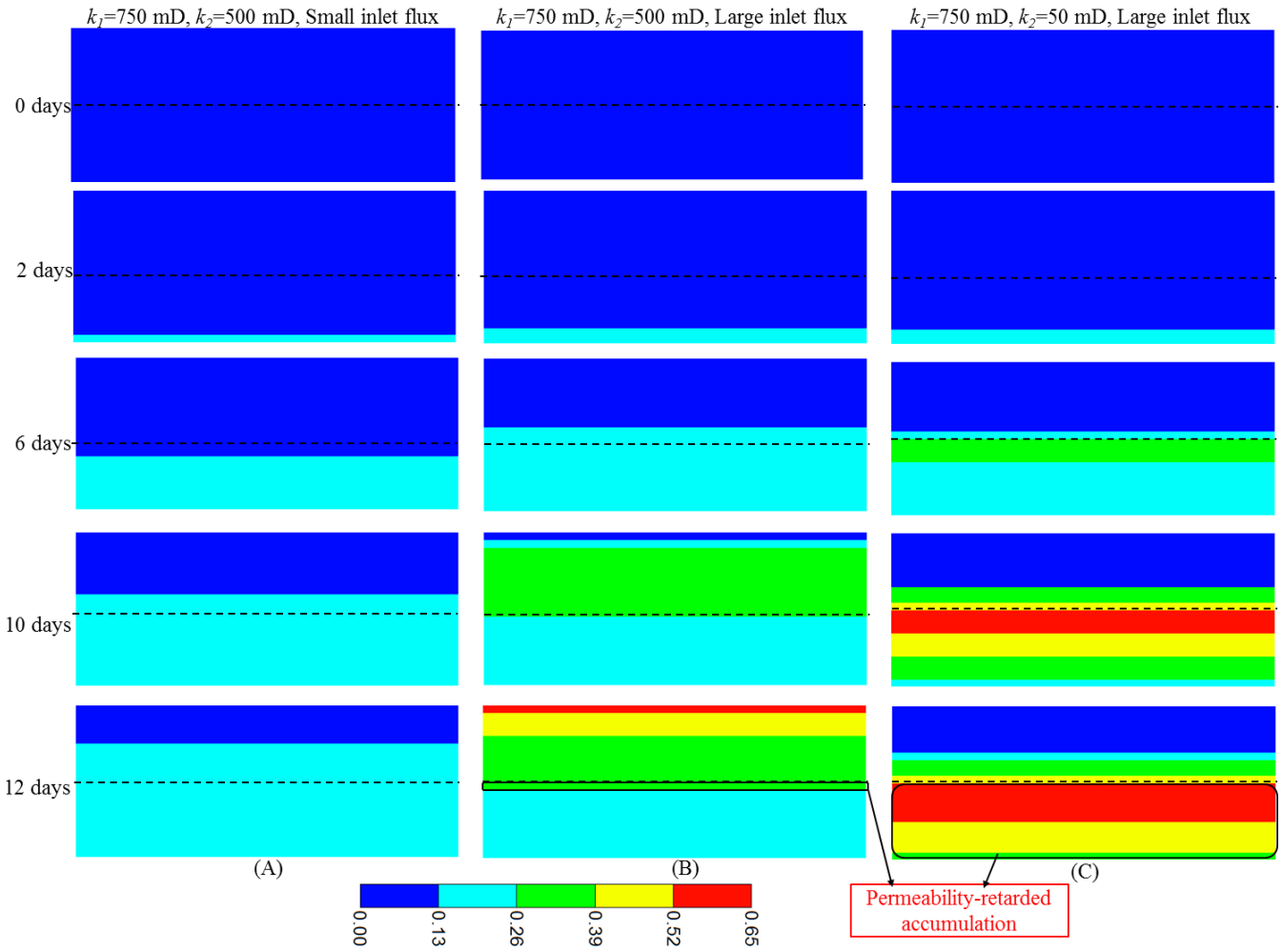

Fig. 9-10 The evolution of CO_2 saturation fields when using the single capillary pressure curve (the curve for the flow path zone). The row represents different time, and the column records different combinations of permeability contrast and inlet flux. Model size is 100 × 20 ft. Black dashes line represents the position of interface between a flow path zone and a flow barrier zone. Black rectangular area indicates CO_2 accumulation caused by the permeability hindrance.

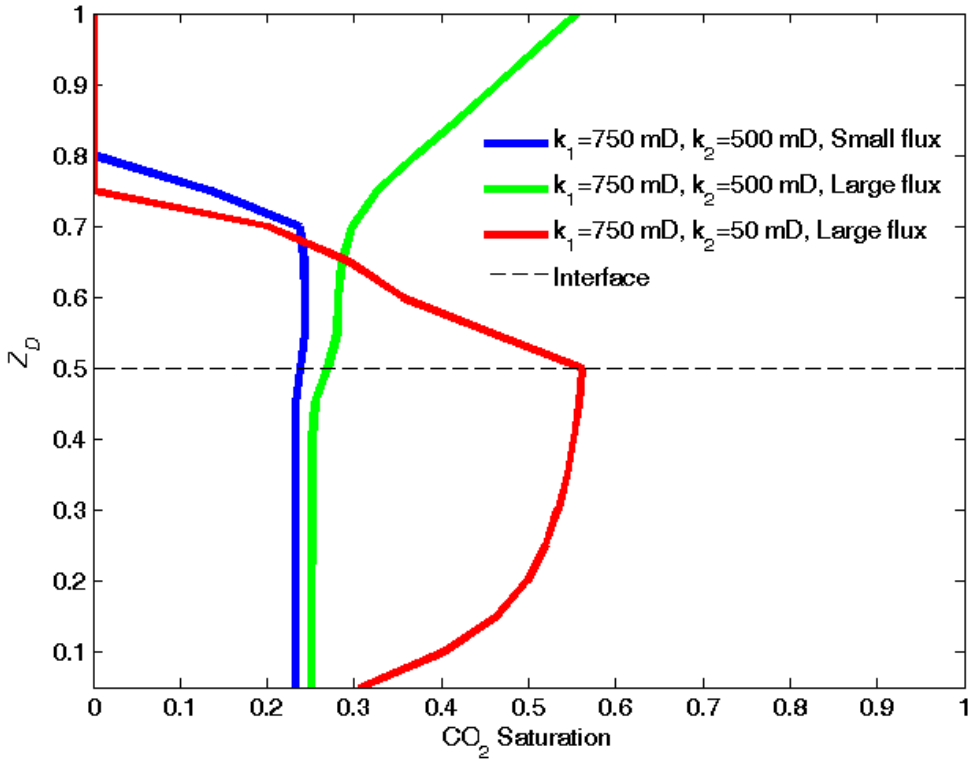

Fig. 9-11 CO_2 saturation profiles at 12 days of CO_2 flow. They are corresponding to the last row of Fig. 9-10. A single capillary pressure curve is used.

However, when scaled capillary pressure curve is used, flow path and flow barrier zone are assigned with different capillary entry pressure. Then, accumulation caused by both permeability-retardation and capillary-barrier would occur according to the analytical study. Therefore, the column of CO_2 accumulations would be higher than that without capillary pressure.

This can be seen from Fig. 9-12. It shows CO_2 saturation evolution with the capillary entry pressure effect. Combinations of different permeability contrasts and inlet fluxes are presented in the figure. For a combination of small permeability contrast and small flux (Fig. 9-12A), an accumulation of CO_2 is observed. This should be caused by the capillary barrier rather than the permeability hindrance, because CO_2 accumulation does not occur when capillary entry pressure is not considered (refer to Fig. 9-8A). The capillary trapping height as determined from

the static capillary pressure equation was 1.5 ft, which is the same as the observation in Fig. 9-12A.

However, when a large inlet flux is used (Fig. 9-12B), the CO_2 accumulation in Fig. 9-12B is higher than that of capillary-trapping accumulation in Fig. 9-12A. The total height is 6 ft while the static capillary-trapping height was only 1.5 ft. This means that the capillarity barrier is not sufficient to accommodate such a large column height, and the accumulation is caused by both the capillary barrier and the permeability hindrance. Further, if the permeability contrast is increased, one can expect the sustained CO_2 height should be much more than capillary static height. This is confirmed by Fig. 9-12C. Clearly, the red accumulated CO_2 should be comprised of both capillary trapping and permeability-retarded accumulation. The total height of the accumulation was 10 ft: capillary-barrier trapping accounts for 1.5 ft, and the remaining 8.5 ft should be the permeability-retarded accumulation. These CO_2 accumulation behaviors can also be directly observed from the saturation profiles in Fig. 9-13.

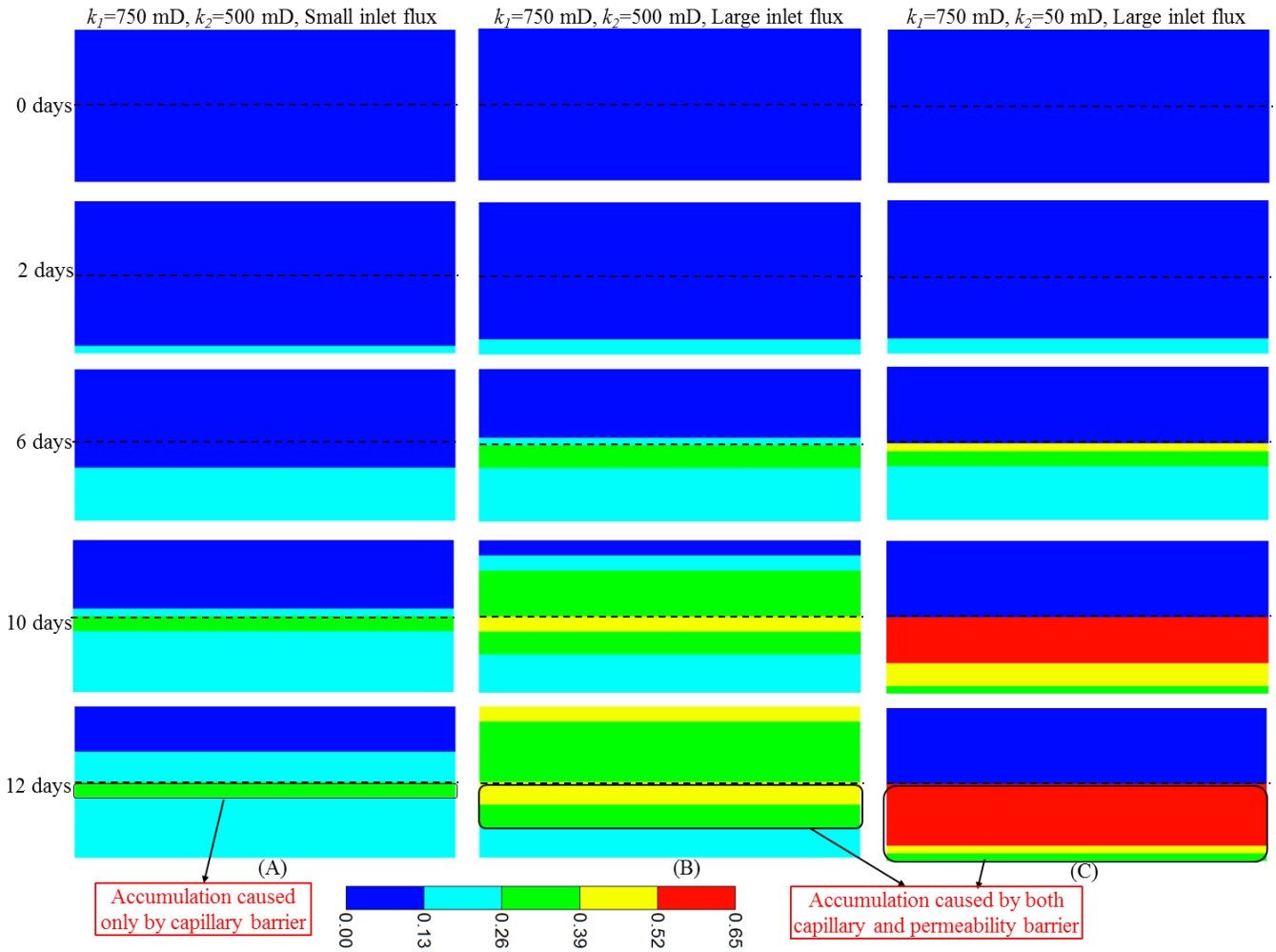

Fig. 9-12 The evolution of CO_2 saturation field with capillary entry pressure effect. The row represents different time, and the column records different combinations of permeability contrast and inlet flux. Model size is 100 × 20 ft. Black dashes line represents the position of interface between flow path and flow barrier zone. Black rectangular area indicates CO_2 accumulation caused by a capillary barrier (in column A) or caused by both the capillary barrier and the permeability hindrance (in column B and C).

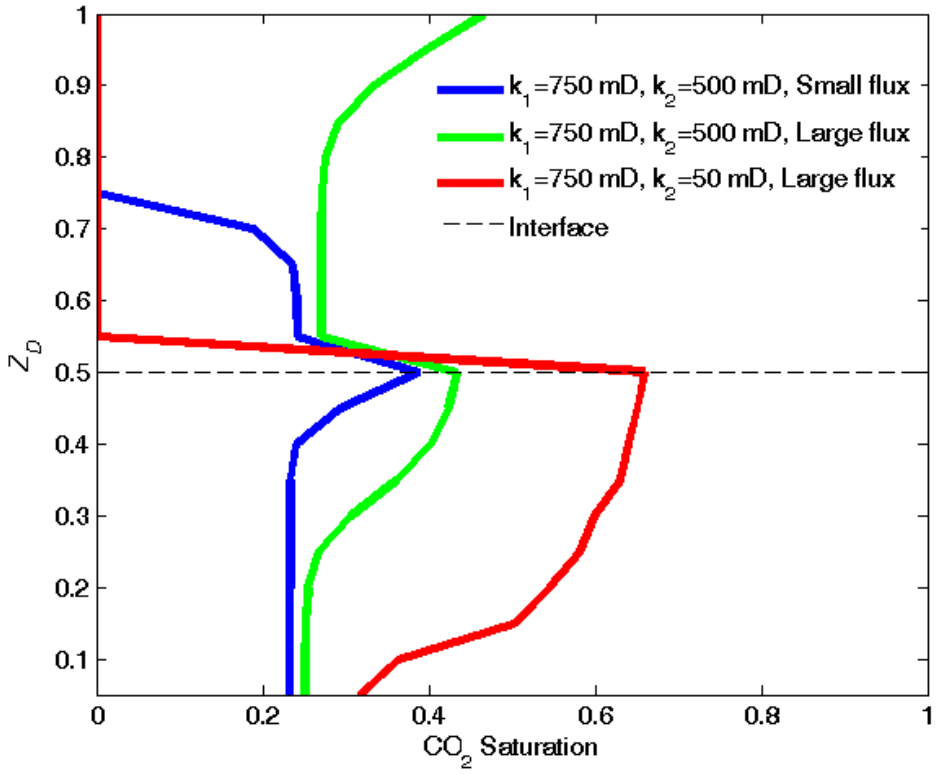

Fig. 9-13 CO_2 saturation profiles at 12 days of CO_2 flow. They are corresponding to the last row of Fig. 9-12. The capillary entry pressure effect is considered.

More importantly, after considering capillary entry pressure effect, leakage of CO_2 into the barrier zone is largely delayed. This can be observed from saturation evolution in Fig. 9-14. A combination of large permeability contrast and large flux is used, and a long time flow simulation is conducted with inlet flux stopped at 30 days. Without capillary entry pressure (Fig. 9-14A), most of the permeability-retarded CO_2 migrates into flow barrier zone at 180 days. However, after considering capillary entry pressure effect (Fig. 9-14B), negligible CO_2 is observed in the barrier zone at the same time. This is because of both capillary entry pressure and relative permeability effects: at the beginning of accumulation, capillary entry pressure creates a high saturation of CO_2 below the barrier compared with permeability-hindrance effect (Fig. 9-14A vs. 9-14B at 30 days). High CO_2 saturation causes slow upward migration, because the rate of CO_2 rising should be the same as the rate of water falling and the latter rate is small because of small water saturation. When the accumulation achieves the static capillary pressure height, the

following accumulation caused by permeability-retardation also moves upward slowly compared with the case without capillary entry pressure. That is, the high-saturation accumulation caused by capillary-barrier pronounces the permeability retardation effect. This ‘synergy effect’ greatly elongates the time-scale of CO_2 containment by permeability retardation inside the flow path zone. Even after 200 yrs of CO_2 flow, large CO_2 saturation still remain in the flow path zone because of the mixed effects of capillary entry pressure and permeability retardation (see Figs. 9-14 and 9-15).

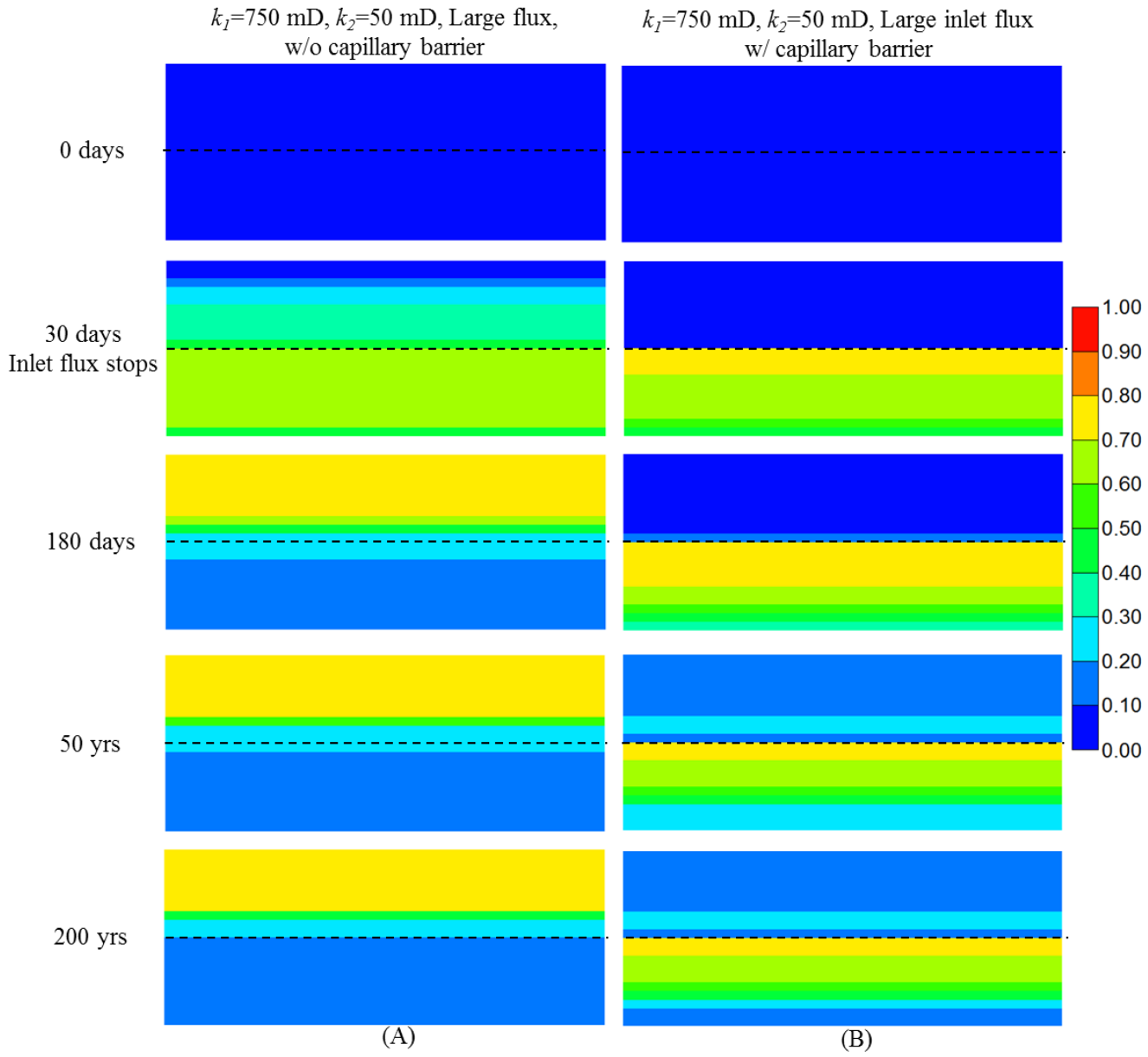

Fig. 9-14 The evolution of CO_2 saturation field with inlet flux stopped at 30 days followed by buoyant flow of CO_2. The row represents different time, and the column records different combinations of capillary entry pressure effect, permeability contrast, and inlet flux. Model size is 100 × 20 ft. Black dashes line represents the position of interface between flow path and flow barrier zone.

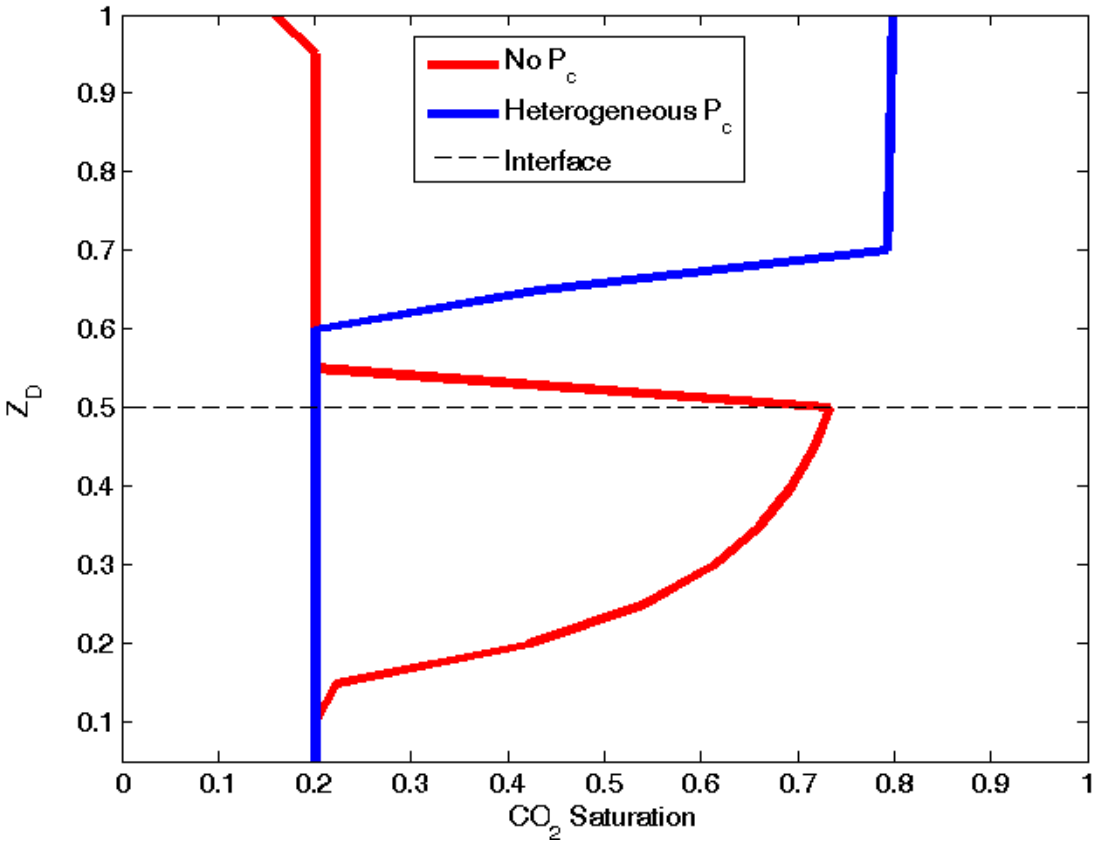

Fig. 9-15 CO_2 saturation profiles at 200 yrs of CO_2 flow. They are corresponding to the last row of Fig. 9-14.

9.4 DISCUSSION

9.4.1 Capillary-barrier trapping versus permeability-retarded accumulation

As shown above, these following conditions tend to give more permeability-retarded accumulation: (1) the source flux is larger than the capacity of barrier; (2) the flow path is thicker than the barrier; (3) large permeability contrast with small capillary entry pressure of the barrier; (4) the reservoir is less water-wet.

The permeability-hindrance manifests itself as accumulation of CO_2 at above residual saturation. Thus, it is analogous in its effect to capillary trapping. The essential difference is the time period during which the accumulations persist for each of the two processes. The capillary

trapping is permanent, while the time-scale of permeability-retarded accumulation is non-negligible. As shown in this above example, the permeability-retarded accumulation can be retained blow the flow barrier for a long time (~ hundreds of year), once inlet flux is halted. This is achieved through a combined effect of capillary entry pressure and relative permeability. Therefore, neglecting permeability-retarded accumulation might underestimate the overall amount of safe storage mode and overestimate the leakage risk.

More importantly, permeability-retarded accumulation does not depend on wettability although the latter influences relative permeability and subsequent height and saturation of the accumulation. On the other hand, wettability is a key for the capillary trapping as demonstrated here and other experimental work (Alyafei and Blunt 2016). Therefore, the importance of capillary trapping in ensuring safe storage of CO_2 would be seriously lessened as the reservoir tends to have an affinity to CO_2. However, capillary trapping is safer than permeability-retarded accumulation as the former is in place permanently. In addition, it is independent of the magnitude of CO_2 source flux.

9.4.2 Applicability and limitation

We employ a 1D model to characterize the migration, accumulation, and trapping in the domain with the flow path below the barrier. The inlet boundary condition is imposed with a constant source flux while the outlet boundary is closed. For the constant source flux boundary, it is applicable to the post-injection process of geologic carbon sequestration. During this period, the injected CO_2 at the bottom of the reservoir can be considered as the flux source. In fact, the observations of CO_2 accumulation are not subject to inlet boundary conditions (i.e., constant flux or constant pressure), rather, the key factor is the flow capacity as determined from the maximum point in a U_g-S_g curve. In other words, as long as the vertical CO_2 flux (realized by setting either a constant flux or constant pressure) below a permeability interface is larger than the flow capacity of a flow barrier zone, CO_2 accumulation will occur. Otherwise, CO_2 will not accumulate. Thus, the relative magnitude of vertical CO_2 flux in the *flow path zone* and the flow

capacity of the *flow barrier zone* control the occurrence of accumulation. The above two fluxes are specific to two different zones, and their magnitudes is dependent to the vertical permeability and CO_2/water relative permeability. For the upper outlet boundary, the closed boundary condition are applicable in small patches of a given storage aquifer. The small patch can be comprised of fine-grained cross-sets above the coarse-grained cross-sets (Gershenzon et al. 2015) with intra-reservoir shale located above. Many such sequences would be expected in a heterogeneous reservoir.

From our analysis on the permeability-retardation and capillary-barrier trapping, it could be deduced that the plume behavior estimation based only on the static capillary equation is insufficient to capture the full physics controlling CO_2 migration and accumulation. Therefore, using the invasion percolation approach (based on the gravity-capillary balance) to match CO_2 plume behavior might not accurately represent CO_2 migration and trapping inside the Sleipner saline aquifer (Cavanagh and Haszeldine 2014).

The results from 1D countercurrent flow model are subject to several simplifications. The handling of the flux and capillarity, the use of skeletonized lines, and bounding solutions would definitely affect the accuracy of evaluation on CO_2 migration and accumulation behavior. Therefore, the quantitative results might not be directly useful, but removing these simplifications will not change the conclusion on the accumulation by permeability-retardation and capillary trapping qualitatively. Particularly, the capillary pressure effect is considered in the wave migration estimation, but not in the flux calculation. This simplification is reasonable as explained below. Capillary pressure is a physical dissipation effect that would cause the shock to spread out. However, the spreading will grow exponentially to some asymptotic limit where it proceeds, without further growth, in simple translation (Lake et al. 2014). This means that capillary pressure affects only the wave shape before the asymptotic limit; it does not change the velocity of a wave. This suggests neglecting capillary pressure in the flux term might be reasonable.

9.5 SUMMARY

For safe CO_2 storage, it is essential to understand the spatial-temporal evolution of CO_2 accumulation and trapping. This chapter presents an integrated analytical and numerical study on the capillary-barrier trapping and permeability-retarded accumulation. Their relative importance are examined under the effects of source flux, capillary pressure, wettability, and permeability contrasts. Also, the mixed effects of capillary entry pressure and relative permeability on the delay of CO_2 upward migration are emphasized.

Nomenclature

Roman Symbols

g	Gravity acceleration [=] L/T^2
H	Height of capillary trapping [=] L
k	Permeability [=] L^2
k_z	Vertical permeability [=] L^2
k_r	Relative permeability
P	Pressure [=] F/L^2
L	Formation thickness [=] L
S	Phase saturation
t	Time [=] T
u	Phase flux [=] L/T
z	Distance [=] L

Greek Symbols

ϕ	Porosity
λ_r	Phase mobility ratio [=] $1/(T\text{-}F/L^2)$
ρ	Phase density [=] M/L^3
Δ	Difference
μ	Phase viscosity [=] $T\text{-}F/L^2$

Subscripts

1	Flow path zone
2	Flow barrier zone
c	Capillary
D	Dimensionless
D_1	Dimensionless time point 1
D_2	Dimensionless time point 2
e	Capillary entry pressure
g	CO_2
r	Residual
w	Water

Superscripts

b	Buoyant
*	Maximum or capillary entry pressure point

Chapter 10: Summary, Conclusions and Recommendations

10.1 SUMMARY AND CONCLUSIONS

The main objective of this dissertation is to understand local capillary trapping (LCT) and its effect on CO_2 migration, accumulation, and trapping during geologic carbon sequestration in saline aquifers. To achieve this objective, we

(1) explore the main physics of controlling LCT during injection and post-injection periods;

(2) quantify local capillary trap capacity in typical storage formations;

(3) characterize local capillary trap clusters;

(4) develop a fast simulation technique to predict LCT during CO_2 injection;

(5) study the interplay between capillary trapping and permeability retardation of rising CO_2.

Based on this work, the main conclusions are highlighted below:

(1). Full-physics simulations show that LCT dictate the final distribution of CO_2 inside a saline aquifer. In contrast to purely buoyant flow, viscous flow permits a full filling of local capillary traps in the near-wellbore region. Injection parameters (i.e., injection rate, injected volume, and injector well types) mainly influence the filling efficiency of local capillary traps. Aquifer static properties (i.e., formation dip angle, auto-correlation of capillary entry pressure fields, and standard deviation of capillary entry pressure) control the spatial configurations of LCT. Particularly, both dip angle and auto-correlation show substantial effects on the extent of LCT. Rock/fluid interaction parameters (i.e., relative permeability hysteresis, residual gas saturation, and capillary pressure hysteresis) primarily affect CO_2 saturation inside LCT.

(2). LCT is robust during leakage; locally trapped CO_2 does not escape from a storage formation even if a leak conduit is created along a wellbore. In addition, LCT persists under the effect of capillary hysteresis; the trapping is difficult to compromise even if capillary imbibition occurs.

(3). The geologic criterion algorithm can be extended to predict LCT that occurs when viscous flow is added to the modeling of sequestration. We demonstrate that, at a threshold critical capillary entry pressure, the algorithm gives both a close (compared to full-physics simulations) upper-bound estimation of LCT amount and a good prediction of LCT locations. Thus, this threshold critical capillary entry pressure is a physically representative value.

(4). Comparing a closed to a periodic LCT boundary in the geologic criteria algorithm shows that a closed boundary causes an overestimation of the LCT amount. For uncorrelated capillary entry pressure fields, this overestimation is removed when the system size is large enough. For auto-correlated fields, however, this overestimation always exists because of the interplay between LCT boundary conditions and auto-correlation.

Particularly, for the closed boundary, a massive overestimation occurs in auto-correlated systems with horizontal auto-correlation length λ_{Dx}=0.12~0.2. This is because of a layering effect. This layering effect enhances the lateral connectivity of flow paths. For a closed boundary, these flow paths are categorized as local capillary traps because lateral boundaries confine flow. For a periodic LCT boundary, however, part of these flow paths cannot act as local capillary traps because the periodic LCT boundary increases the vertical connectivity of flow paths meanwhile.

(5). Application of the geologic criterion algorithm in both synthetic media and realistic geologic models shows that spatial heterogeneity (i.e., auto-correlation length) of a capillary entry pressure field is a first order effect on the amount of LCT. The standard deviation of capillary entry pressure shows a minor effect. A simple counting argument is demonstrated to be useful for interpreting these results. Interpretations on the position of a threshold capillary entry pressure, its movement under the influence of heterogeneity, and the limiting volume fraction of LCT are consistent with predictions from the geologic criterion algorithm.

(6). Characterization of local capillary trap clusters shows that the wider frequency distribution (more heterogeneity) of capillary entry pressure yields more large clusters. In an auto-correlated system, auto-correlation displays an orientation effect on local capillary traps:

vertical auto-correlation length mainly influences the capacity of local capillary traps while horizontal auto-correlation length mostly affects the extent of the largest cluster. The horizontal auto-correlation effect causes the largest cluster to extend much wider than the auto-correlation length itself. There is a high chance that the largest cluster laterally spans a whole domain even when horizontal auto-correlation length is only 1/20 of domain width in 2D. Additionally, the largest cluster accommodates most of the LCT capacity in a 3D medium even when its horizontal auto-correlation length is 1/4 of the domain width.

(7). The integrated model of the geologic criterion and the connectivity analysis can be used as a quick tool to optimize LCT during CO_2 injection into a saline aquifer. For geologic features with fixed auto-correlation length, evaluation on the effect of injection strategies on LCT amount shows that: (a) for the static LCT capacity, i.e., LCT from only the geologic criterion, the capacity first increases with V_{dp} rapidly followed by a small augment; (b) for the dynamic LCT volume, i.e., LCT from both the geologic criterion and the connectivity analysis, viscous-dominated flow yields a larger LCT volume than buoyancy-dominated flow does, and this effect is enhanced in heterogeneous reservoirs. For buoyancy-dominated flow, LCT volume is almost constant; it is unaffected by reservoir heterogeneity in the typical rang of V_{dp}. (3) The optimal volume of injected CO_2, at which the maximum LCT volume is achieved, decreases as a reservoir becomes heterogeneous.

(8). Analytical modeling of buoyant and countercurrent flow of CO_2 in a single-layer formation demonstrates that the magnitude of buoyant source flux and flux-saturation relationship controls saturation wave types, upward migration, and backfilling behavior of CO_2. Wettability influences the relative permeability. This causes different gas saturations carried by waves for reservoirs with different wettability. This yields an earlier arrival of CO_2 at the top of a storage formation in wat-wet reservoirs than in CO_2-wet reservoirs if capillary pressure is not considered.

When capillary pressure is considered, it smears shocks. The stabilized zone caused by capillary dispersion is longer inside CO_2-wet reservoirs than water-wet reservoirs. This is mainly

because of different relative permeabilities. However, when capillary pressure is overridden by buoyant force, the stabilized zone shrinks, and traveling waves converge to shocks. This is consistent with the formation of saturation shocks in the case of no capillary pressure. Finally, we show that the prediction of CO_2 upward migration using the analytical model matches well with the field observation in the Sleipner.

(9). Capillary barriers interact with permeability hindrances in terms of CO_2 migration, accumulation, and trapping during buoyant countercurrent flow. Both capillary barriers and permeability hindrances cause CO_2 accumulations. These two accumulation mechanisms depend strongly but in qualitatively different ways upon the magnitude of the inlet flux, the permeability contrast between flow path and barrier, and capillary entry pressure. Specifically, the magnitude of source flux determines the occurrence of permeability-retarded accumulation, but not of the capillary trapping accumulation. As the source flux decreases, the permeability-retarded accumulation is diminished. The permeability contrast between a flow path and a flow barrier zone influences both capillary trapping and permeability-retarded accumulation in the aspects of accumulation rate, accumulation height, and CO_2 saturation. Both wettability and capillary pressure essentially control capillary trapping. As a reservoir becomes CO_2-wet, less capillary trapping would be obtained. Wettability also affects permeability-retarded accumulation as relative permeability is largely influenced by wettability.

10.2 RECOMMENDATIONS OF FUTURE WORK

1. Conventional reservoir simulations show a slow change of CO_2 saturation during the post-injection period. This prevents an accurate quantification of local capillary trapping from a CO_2 saturation field. It is recommended that further simulations should only consider capillary entry pressure point (without capillary transition zone); a flat capillary pressure curve is used. This would reduce the number of cells with transient gas saturation.

2. Further improvement of geologic criterion algorithm is needed: a) a cluster of local capillary traps determines a CO_2 column height. This column should be checked to see whether it

can be sustained by the corresponding cluster of capillary barriers; b) The effect of dip angle on local capillary trapping needs to be incorporated into the algorithm; c) the impact of imbibition (snap-off) on the size of local capillary trap clusters might merit further considerations.

3. The effect of critical capillary entry pressure on the selection of water alternating gas (WAG) ratio needs further study.

4. Examination of fractal behaviors of local capillary trap clusters is needed.

5. Further study is needed to examine whether local capillary trapping has a signature that could be detected with measurements such as seismic or electromagnetic tomography or induction logging.

6. Further improvement of the connectivity analysis is needed: a) a wellbore flow model needs to be incorporated into the connectivity analysis, to evaluate the effect of perforation interval length on local capillary trapping; b) the connectivity analysis should be extended to account for multiple wells in order to extensively evaluate storage efficiency and its impact on local capillary trapping; c) the applicability of the connectivity analysis to purely buoyant flow during the post-injection period should be further explored; d) adding capillary pressure term into the connectivity analysis is needed.

7. In the application of the integrated model (the geologic criterion and the connectivity analysis), other cases should be run to explore the interplay between auto-correlation and injection rate.

8. Other trapping mechanisms (e.g., dissolution trapping) might be necessary to be incorporated in the one-dimensional buoyant countercurrent flow model presented in chapter 8.

9. Further study on the interplay between capillary trapping and permeability retardation of rising CO_2 is needed: a) an analytical model could be developed to show that, at infinite time, the mixed accumulation would be reduced to only capillary trapping; b) the effect of permeability-retardation on CO_2 accumulation is observed in 1D, whether this is true in 2D merits further study; c) further study into the effect of boundary types (i.e., constant pressure vs. constant flux) on the permeability-retarded accumulation is needed.

Appendices

APPENDIX A: AN EXAMPLE OF INPUT FILE IN CMG-GEM

```
** Purpose: study Local capillary trapping when injection period incorporated
** All 40000 Grid Blocks have different Pc curves, scaled with J-Function
** A vertical well is put on the left side of the domain
RESULTS SIMULATOR GEM 201210
RANGECHECK ON
*INUNIT       *FIELD
*INTERRUPT          *INTERACTIVE
*XDR  *ON
*MAXERROR           20
*DIARY        *CHANGES
** Output Print File:
*WPRN         *GRID*TIME
*WPRN *ITER         *NONE
*OUTPRN       *GRID
                    **PRES        DROP  PCG     SATP
                    **KRG         KRO
                    **DENG        DENO RHOG RHOO MWG  MWO  VISG   VISO   FRG
                    SG            SO
                    **Z 'CO2'     Z 'H2O'
                    Y 'CO2'       Y 'H2O'
                    **X 'CO2'     X 'H2O'
                    **K 'CO2'     K 'H2O'
                    **SIG
                    **VELOCRC
** Simulation Results File:
```

```
*WSRF *GRID *TIME
*OUTSRF      *GRID
             *PRES DROP
             *PCG  SATP
             *KRG  KRO
             *DENG        DENO RHOG RHOO MWG  MWO  VISG   VISO   FRG
             *SG    SO    TSO
             *Z 'CO2'     Z 'H2O'
             *Y 'CO2'     Y 'H2O'
             *X 'CO2'     X 'H2O'
             *K 'CO2'     K 'H2O'
             *SIG
             *VELOCRC
*OUTSRF      *RES *ALL
** Restart File (To Restart at the last time step in RST File):
*WRST        100000
*REWIND 2
**********************************************************
** Aquifer details
*GRID*CART        400 1 100
*KDIR*DOWN
*DI    *CON 1
*DJ    *CON 1
*DK    *CON 1
*DEPTH       *TOP  200 1 1 5300.
*NULL        *CON 1
*POR  *MATRIX     *ALL
```

```
INCLUDE 'Phi_400x100.dat'
*VOLMOD *IJK 400 1 1:100 1.0E+7
** No Anisotropy:
*PERMI        *ALL
INCLUDE 'Perm_400x100.dat'
PERMJ EQUALSI
PERMK EQUALSI
**$  0 = pinched block, 1 = active block
PINCHOUTARRAY CON          1
*CPOR         MATRIX       3.0E-6
*PRPOR        MATRIX       14.7
**********************************************************
** Component properties for EOS model

*MODEL       *PR
*NC          2        2
*COMPNAME          'CO2'   'H2O'
*HCFLAG      0        0
*VISCOR      *PEDERSEN
*VISCOEFF    0.291
                    1.4
             0.0005747
              4.265
             1.0579
*MIXVC       1
*TRES         140.
*PCRIT        72.809000      217.754600
```

```
*TCRIT          304.12780       647.09440
*AC     0.223940    0.344000
*MW   44.01000    18.01500
*PCHOR          78.00000    52.00000
*SG     0.818000    1.000000
*TB     -109.21000      212.00000
*ZCRIT          0.274139    0.229409
*VISVC          0.094000    0.056000
*VSHIFT         0.024668    0.234867
*OMEGA        .457235530     .457235530
*OMEGB        .077796074     .077796074
*BIN
    -0.0576003
*PHASEID     *DEN
**************************************************************
** Relative permeability
*ROCKFLUID
RPT 1
** WATER OIL REL PERM TABLE : NOT USED IN SIMULATION
**$         Sw        krw       krow      Pcow
SWT
     0.000000   0.000000    1.000000  0.000000
    0.0524375  0.0008203  0.8400835  0.000000
     0.104875  0.0032813   0.6973033  0.000000
    0.1573125  0.0073828  0.5708514  0.000000
     0.209750   0.013125    0.4599021  0.000000
    0.2621875  0.0205078  0.3636104  0.000000
```

0.314625 0.0295313 0.2811098 0.000000

0.3670625 0.0401953 0.211510 0.000000

0.419500 0.052500 0.1538931 0.000000

0.4719375 0.0664453 0.1073101 0.000000

0.524375 0.0820313 0.0707757 0.000000

0.5768125 0.0992578 0.0432609 0.000000

0.629250 0.118125 0.0236831 0.000000

0.6816875 0.1386328 0.0108919 0.000000

0.734125 0.1607813 0.0036447 0.000000

0.7865625 0.1845703 0.0005609 0.000000

0.839000 0.210000 0.000000 0.000000

** OIL GAS REL PERM TABLE : USED IN SIMULATION

**	Sl	krg	krog	Pcog
	0.15	0.860969388	0	2.3
	0.2	0.7	0	1.687346405
	0.25	0.560459184	0.005102041	1.552352488
	0.3	0.440816327	0.020408163	1.478449735
	0.35	0.339540816	0.045918367	1.428158582
	0.4	0.255102041	0.081632653	1.39033085
	0.45	0.185969388	0.12755102	1.360168321
	0.5	0.130612245	0.183673469	1.335177351
	0.55	0.0875	0.25	1.313900644
	0.6	0.055102041	0.326530612	1.295414868
	0.65	0.031887755	0.413265306	1.27909927
	0.7	0.016326531	0.510204082	1.264517113
	0.75	0.006887755	0.617346939	1.251349854
	0.8	0.002040816	0.734693878	1.239358261

```
      0.85        0          0.862244898   1.228358254
       0.9        0          1             1.218205267
      0.95        0          1             1.208783762
         1        0          1             1.2
** MAX RESIDUAL GAS SATURATION VALUE
*HYSKRG     0.286
** End-point value to scale the relative permeability tables of each grid block
*SWCON      *CON  0
*PCGMAX     *ALL
INCLUDE 'PcScale_400x100.dat'
                *MOD *        2.291009
**********************************************************************
** Initial condition
*INITIAL
*USER_INPUT
*SW    *CON  0
*PRES *KVAR
*INCLUDE  'Hydrostatic Pressure.data'
ZGLOBALC 'H2O' CON          1
ZGLOBALC 'CO2' CON          0
**********************************************************************
** Numerical control

*NUMERICAL
MAXSTEPS 99999999
DTMAX   1.E-04
DTMIN        1.E-08
```

```
NORM PRESS 750
MAXCHANGE SATUR 0.5
MAXCHANGE GMOLAR 0.5
CONVERGE PRESS 0.514884
 ***********************************************************************
** Well and run details
*RUN
*DATE          2000 01 01
*WELL 'Inj-1'
*INJECTOR 'Inj-1'
*INCOMP SOLVENT  1.  0.
*OPERATE *STG 490573.82 *CONT
**$ UBA          ff  Status  Connection
**$          rad  geofac  wfrac  skin
GEOMETRY  K  0.1  0.35  1.  0.
PERF  GEOA  'Inj-1'
**$ UBA      ff  Status  Connection
   1 1 76:100          1.   OPEN
*DATE 2000 01 02
*DATE          2000 01 07
*DATE          2000 01 08
*TIME 7.3
*SHUTIN 'Inj-1'
*DATE          2000 01 09
*DATE          2000 01 10
*DTMAX 1
*DATE          2000 01 30
```

```
*DATE        2000 06 30
*DATE        2000 09 30
*WRST        *TNEXT
*DATE        2001 01 01
*DATE        2002 01 01
*DATE        2003 01 01
*DATE        2004 01 01
*WRST        *TNEXT
*DATE        2005 01 01
*DTMAX 2
*WRST        *TNEXT
*DATE        2010 01 01
*DATE        2020 01 01

*DTMAX 4
*WRST        *TNEXT
*DATE        2030 01 01
*DATE        2040 01 01
*DATE        2050 01 01
*STOP
```

APPENDIX B: USER'S GUIDE FOR JENNINGS' (2000) FAST FOURIER TRANSFORM PROGRAM

The FFT (Fast Fourier Transform) simulator is a stochastic permeability field generator. It is a type of spectral method, which represents a synthetic field with a Fourier Series. FFT starts with a Gaussian noise and does a moving average and Fourier filtering. The files ".dat" are test data sets. The files ".out" are output from the program using these test data sets. The program can be run with a Unix command like:

fft_sim < test1d1.dat > test1d1.out

Input:

Parameter	Description
Run type	Run type other than 1 produces no simulation, but rather a much bigger output file for plotting the covariance function, the power spectrum, and the amplitude spectrum.
Random number seed	The random number generator is built in and is machine portable. That means the same random number seed produces the same realization even when compiled on different computers.
Variogram window	Use zero. Non-zero values are for an expert user to try to damp covariance models with a Gaussian window in cases where the covariance would not otherwise decay enough within the grid.
X array size power, px	This is the power to base 2 for the number of grid blocks in the x-direction.
Y array size power, py	This is the power to base 2 for the number of grid blocks in the y-direction.
Z array size power, pz	This is the power to base 2 for the number of grid blocks in the z-direction.
X mesh spacing, dx	Size of x-directional grid block
Y mesh spacing, dy	Size of y-directional grid block
Z mesh spacing, dz	Size of z-directional grid block
Number of variogram structures	A covariance model can be built from a sum of any number of structures.
Variogram type	1 = stable 2 = J-bessel 3 = K-bessel
Variogram sill	Total variance
Alpha	1 = exponential variogram 2 = Gaussian variogram
X scale	Auto-correlation length (range) in x-direction
Y scale	Auto-correlation length (range) in y-direction
Z scale	Auto-correlation length (range) in z-direction

After compiling and running the program, test with the test data sets and compare to the results provided. The results should be identical except for round off and CPU time.

Sample input file:

1 1 0	run type, seed, window
3 3 3 1 1 1	px, py, pz, dx, dy, dz
1	number of variogram structures
1 1 1 0.5 0.5 0.5	variogram type, sill, alpha, x scale, y scale, z scale

Sample input file:

```
1 1 0
6 6 6 1 1 1
1
1 1 1 12 12 1
```

This file is for a 64× 64× 64 grid system. The grid size is 1 ft in each direction. An exponential variogram is used and the total variance is 1. The auto-correlation lengths are 12 ft in horizontal direction and 1 ft in vertical direction.

After the simulation, several statistics are displayed on the screen or written to the log file.

Some numbers to check:

•Smallest real part (power spectrum): This number should be positive. That confirms that the covariance model decays enough on the edges of the grid. When this number is positive none of the fixes are turned on and the covariance damping is not needed.

•Largest magnitude imaginary part: If this is ever non-zero something is broken in the code.

•Smallest real part (amplitude spectrum): This is another check for a sufficiently decayed covariance model. It should be positive. If any component of the power spectrum is negative the program applies an appropriate fix. This secondary check comes after the fix (if any).

•Adjustment factor: If any part of the power spectrum is negative and must be truncated, the variance will not come out as specified. The code will attempt an adjustment. The farther this number is from one, the more the possibility of something having gone wrong in the simulation.

Output:

The values are written to the output file in x, y, z order (x varies fastest). The output has a mean of zero and the variance that is specified in the input as the sill. Post-processing is needed to convert the column data into a matrix and also to convert these numbers to lognormal permeabilities. To convert these numbers to lognormal permeabilities with a specified mean add a constant and take the antilog. If the variogram model is normalized to a sill of one, the result should be scaled to get the actual variance.

$k(i,j,k) = \exp [\text{Meanln } k + \text{Stdevln}k \times K(i,j,k)]$

where, $k(i,j,k)$ is the log-normally distributed permeability; Meanln$k$ is the mean of the log normal permeability; Stdevln$k$ is the standard deviation of the log of the permeability; $K(i,j,k)$ is the output from FFT;If the sill of the variogram is already set to the actual variance, then no rescaling is required. Only the mean has to be added. $k(i,j,k) = \exp [\text{Meanln } k + K(i,j,k)]$ Note: be consistent with the use of the base of the logarithm. For the sample input file, we get the following output:

```
nx = 64, ny = 64, nz = 64, dx = 1.000000, dy = 1.000000, dz = 1.000000, seed = 1, nvar = 1
simulation
-3.98477e-001
-6.65854e-001
-1.48630e+000
-7.55874e-001
-3.29034e-001
-6.57017e-001
-5.67430e-001
-6.60170e-001
-1.50096e-001
-2.69492e-001
```

Sample post-processing program in Matlab

```
clc;
clear;
delimiter='';
R1=3;
C1=0;
fname = 'fftout.txt';
M = dlmread(fname, delimiter, R1, C1);
Mean=3.0;
Standard=2.0;
Variance=4.0;

AvglnPc=log(Mean/sqrt(1+Variance/(Mean^2)));
StdlnPc=sqrt(log(1+Variance/(Mean^2)));
Pc=exp(AvglnPc+StdlnPc.*M);
AvgPc=mean(Pc);
StdPc=std(Pc);

fid1=fopen('32x32x32_Pc.dat','wt');
fprintf(fid1,'%f\n',Pc);
fclose(fid1);
```

Sample post-processed output:

```
1.960329
1.666914
1.013544
1.578359
2.044642
1.675870
1.769432
1.672669
2.278987
2.119816
```

References

Alyafei, N., Blunt, M.J. 2016. The Effect of Wettability on Capillary Trapping in Carbonates. *Advances in Water Resources* **90**: 36-50. http://doi.org/10.1016/j.advwatres.2016.02.001

Anchliya, A., Ehlig-Economides, C.A., Jafarpour, B. 2012. Aquifer Management to Accelerate CO_2 Dissolution and Trapping. *SPE Journal* **17** (3): 805-816. https://doi.org/10.2118/126688-PA

Arts, R., Eiken, O., Chadwick, A., Zweigel, P., Van Der Meer, L., Zinszner, B. 2004. Monitoring of CO_2 Injected at Sleipner Using Time-Lapse Seismic Data. *Energy* **29** (9–10): 1383-1392. http://doi.org/10.1016/j.energy.2004.03.072

Aziz, K., Settari, A. 1978. *Petroleum Reservoir Simulation*. New York: Elsevier.

Bachu, S. 2008. CO_2 Storage in Geological Media: Role, Means, Status and Barriers to Deployment. *Progress in Energy and Combustion Science* **34** (2): 254-273. http://doi.org/10.1016/j.pecs.2007.10.001

Barenblatt, G.I., Entov, V.M., Ryzhik, V.M. 1989. *Theory of Fluid Flows through Natural Rocks*. Netherlands: Springer.

Beard, D., Weyl, P. 1973. Influence of Texture on Porosity and Permeability of Unconsolidated Sand. *AAPG bulletin* **57** (2): 349-369.

Behseresht, J., Bryant, S.L., Sepehrnoori, K. 2009. Infinite-Acting Physically Representative Networks for Capillarity-Controlled Displacements. *SPE Journal* **10** (04): 568-578. https://doi.org/10.2118/110581-PA

Behzadi, H., Alvarado, V. 2012. Upscaling of Upward CO_2 Migration in 2D System. *Advances in Water Resources* **46**: 46-54. http://doi.org/10.1016/j.advwatres.2012.06.003

Berg, R.R. 1975. Capillary Pressures in Stratigraphic Traps. *AAPG Bulletin* **59** (6): 939-956.

Birkholzer, J.T., Oldenburg, C.M., Zhou, Q. 2015. CO_2 Migration and Pressure Evolution in Deep Saline Aquifers. *International Journal of Greenhouse Gas Control* **40**: 203-220. http://dx.doi.org/10.1016/j.ijggc.2015.03.022.

Broadbent, S.R., Hammersley, J.M. 1957. Percolation Processes. *Mathematical Proceedings of the Cambridge Philosophical Society* **53** (03): 629-641. http://dx.doi.org/10.1017/S0305004100032680

Brooks, R.H., Corey, A.T. 1966. Properties of Porous Media Affecting Fluid Flow. *Journal of the Irrigation and Drainage Division Proceedings of the American Society of Civil Engineers* **IR2**: 61-88.

Bryant, S.L., Lakshminarasimhan, S., Pope, G.A. 2008. Buoyancy-Dominated Multiphase Flow and Its Effect on Geological Sequestration of CO_2. *SPE Journal* **13** (4): 447-454. http://dx.doi.org/10.2118/99938-MS.

Bryant, S.L., Schechter, R.S., Lake, L.W. 1986. Interactions of Precipitation/Dissolution Waves and Ion Exchange in Flow through Permeable Media. *AIChE Journal* **32** (5): 751-764. http://dx.doi.org/10.1002/aic.690320505.

Buckley, S.E., Leverett, M.C. 1942. Mechanism of Fluid Displacement in Sands. *Transactions of the AIME* **146**(01): 107-116. https://doi.org/10.2118/942107-G.

Burton, M., Kumar, N., Bryant, S.L. 2009. CO_2 Injectivity into Brine Aquifers: Why Relative Permeability Matters as Much as Absolute Permeability. *Energy Procedia* **1** (1): 3091-3098. https://doi.org/10.1016/j.egypro.2009.02.089.

Carruthers, D., Ringrose, P. 1998. Secondary Oil Migration: Oil-Rock Contact Volumes, Flow Behaviour and Rates. *Geological Society, London, Special Publications* **144** (1): 205-220. http://dx.doi.org/10.1144/GSL.SP.1998.144.01.16.

Carruthers, D.J., De Lind Van Wijngaarden, M. 2000. Modelling Viscous-Dominated Fluid Transport Using Modified Invasion Percolation Techniques. *Journal of Geochemical Exploration* **69–70**: 669-672. http://dx.doi.org/10.1016/S0375-6742(00)00138-2.

Carruthers, D.J.F. 1998. *Transport Modelling of Secondary Oil Migration Using Gradient-Driven Invasion Percolation Techniques*. Ph.D. Dissertation, Heriot-Watt University, Edinburgh, UK.

Carruthers, D.J.F. 2003. Modeling of Secondary Petroleum Migration Using Invasion Percolation Techniques: *AAPG/Datapages Discovery Series* **7**: 21-37.

Cavanagh, A. 2013. Benchmark Calibration and Prediction of the Sleipner CO_2 Plume from 2006 to 2012. *Energy Procedia* **37**: 3529-3545. http://dx.doi.org/10.1016/j.egypro.2013.06.246.

Cavanagh, A., Ringrose, P. 2011. Simulation of CO_2 Distribution at the inSalah Storage Site Using High-Resolution Field-Scale Models. *Energy Procedia* **4**: 3730-3737. http://dx.doi.org/10.1016/j.egypro.2011.02.306.

Cavanagh, A., Rostron, B. 2013. High-Resolution Simulations of Migration Pathways and the Related Potential Well Risk at the Ieaghg Weyburn–Midale CO_2 Storage Project. *International Journal of Greenhouse Gas Control* **16, Supplement 1**: S15-S24. http://dx.doi.org/10.1016/j.ijggc.2013.03.004.

Cavanagh, A.J., Haszeldine, R.S. 2014. The Sleipner Storage Site: Capillary Flow Modeling of a Layered CO_2 Plume Requires Fractured Shale Barriers within the Utsira Formation. *International Journal of Greenhouse Gas Control* **21**: 101-112. http://dx.doi.org/10.1016/j.ijggc.2013.11.017.

Cavanagh, A.J., Haszeldine, R.S., Blunt, M.J. 2010. Open or Closed? A Discussion of the Mistaken Assumptions in the Economides Pressure Analysis of Carbon Sequestration.

Journal of Petroleum Science and Engineering **74** (1–2): 107-110. http://doi.org/10.1016/j.petrol.2010.08.017.

Chadwick, R.A., Arts, R., Eiken, O. 2005. 4D Seismic Quantification of a Growing CO_2 Plume at Sleipner, North Sea. In: Dore, A. G. & Vining, B. A. (eds) Petroleum Geology: North-West Europe and Global Perspectives - Proceedings of the 6th Petroleum Geology Conference, 1385–1399

Chadwick, R.A., Noy, D., Arts, R., Eiken, O. 2009. Latest Time-Lapse Seismic Data from Sleipner Yield New Insights into CO_2 Plume Development. *Energy Procedia* **1** (1): 2103-2110. http://dx.doi.org/10.1016/j.egypro.2009.01.274.

CMG-GEM, 2012. GEM Users' Guide. Computer Modeling Group Ltd, Canada.

Court, B., Bandilla, K.W., Celia, M.A., Janzen, A., Dobossy, M., Nordbotten, J.M. 2012. Applicability of Vertical-Equilibrium and Sharp-Interface Assumptions in CO_2 Sequestration Modeling. *International Journal of Greenhouse Gas Control* **10**: 134-147. http://dx.doi.org/10.1016/j.ijggc.2012.04.015.

Dentz, M., Tartakovsky, D. 2009. Abrupt-Interface Solution for Carbon Dioxide Injection into Porous Media. *Transport in Porous Media* **79** (1): 15-27. http://dx.doi.org/10.1007/s11242-008-9268-y.

Dicarlo, D.A., Mirzaei, M., Aminzadeh, B., Dehghanpour, H. 2012. Fractional Flow Approach to Saturation Overshoot. *Transport in Porous Media* **91** (3): 955-971. http://dx.doi.org/10.1007/s11242-011-9885-8.

Doughty, C. 2007. Modeling Geologic Storage of Carbon Dioxide: Comparison of Non-Hysteretic and Hysteretic Characteristic Curves. *Energy Conversion and Management* **48** (6): 1768-1781. http://dx.doi.org/10.1016/j.enconman.2007.01.022.

Dykstra, H., Parsons, R.L. 1950. The Prediction of Oil Recovery by Waterflooding. In Secondary Recovery of Oil in the United States, second edition, 160-174. *Washington, DC*: API.

Ehlig-Economides, C., Economides, M.J. 2010. Sequestering Carbon Dioxide in a Closed Underground Volume. *Journal of Petroleum Science and Engineering* **70** (1–2): 123-130. http://dx.doi.org/10.1016/j.petrol.2009.11.002.

England, W.A., Mackenzie, A.S., Mann, D.M., Quigley, T.M. 1987. The Movement and Entrapment of Petroleum Fluids in the Subsurface. *Journal of the Geological Society* **144** (2): 327-347. http://dx.doi.org/10.1144/gsjgs.144.2.0327.

Exum, F.A., Harms, J.C. 1968. Comparison of Marine-Bar with Valley-Fill Stratigraphic Traps, Western Nebraska. *AAPG Bulletin* **52** (10):1851-1868.

Frisch, H., Hammersley, J. 1963. Percolation Processes and Related Topics. *Journal of the Society for Industrial and Applied Mathematics* **11** (4): 894-918. http://dx.doi.org/10.1137/0111066.

Ganesh, P.R. 2012. *Geologic Drivers Affecting Buoyant Plume Migration Patterns in Smallscale Heterogeneous Media: Characterizing Capillary Channels of Sequestered CO_2.* MS thesis, The University of Texas at Austin, Austin, Texas.

Garing, C., Voltolini, M., Ajo-Franklin, J. B., Benson, S. M. Pore-scale Evolution of Trapped CO_2 at Early Stages Following Imbibition using Micro-CT Imaging, to be published in Energy Procedia.

Gershenzon, N.I., Ritzi, R.W., Dominic, D.F., Soltanian, M., Mehnert, E., Okwen, R.T. 2015. Influence of Small-Scale Fluvial Architecture on CO_2 Trapping Processes in Deep Brine

Reservoirs. *Water Resources Research* **51** (10): 8240-8256. http://dx.doi.org/10.1002/2015WR017638.

Glass, R.J., Conrad, S.H., Peplinski, W. 2000. Gravity-Destabilized Nonwetting Phase Invasion in Macroheterogeneous Porous Media: Experimental Observations of Invasion Dynamics and Scale Analysis. *Water Resources Research* **36** (11): 3121-3137. http://dx.doi.org/10.1029/2000WR900152.

Glass, R.J., Yarrington, L. 2003. Mechanistic Modeling of Fingering, Nonmonotonicity, Fragmentation, and Pulsation within Gravity/Buoyant Destabilized Two-Phase/Unsaturated Flow. *Water Resources Research* **39** (3): 1058. http://dx.doi.org/10.1029/2002WR001542.

Guglielmi, Y., Elsworth, D., Cappa, F., Henry, P., Gout, C., Dick, P., Durand, J. 2015. In Situ Observations on the Coupling between Hydraulic Diffusivity and Displacements During Fault Reactivation in Shales. *Journal of Geophysical Research: Solid Earth* **120** (11): 7729-7748. http://dx.doi.org/10.1002/2015JB012158.

Guo, B., Bandilla, K.W., Doster, F., Keilegavlen, E., Celia, M.A. 2014. A Vertically Integrated Model with Vertical Dynamics for CO_2 Storage. *Water Resources Research* **50** (8): 6269-6284. http://dx.doi.org/10.1002/2013WR015215.

Hassanzadeh, H., Pooladi-Darvish, M., Keith, D.W. 2009. Accelerating CO_2 Dissolution in Saline Aquifers for Geological Storage - Mechanistic and Sensitivity Studies. *Energy & Fuels* **23** (6): 3328-3336. http://dx.doi.org/10.1021/ef900125m.

Hayek, M., Mouche, E., Mügler, C. 2009. Modeling Vertical Stratification of CO_2 Injected into a Deep Layered Aquifer. *Advances in Water Resources* **32** (3): 450-462. http://dx.doi.org/10.1016/j.advwatres.2008.12.009.

Helset, H.M., Lake, L.W. 1998. Three-Phase Secondary Migration of Hydrocarbon. *Mathematical Geology* **30** (6): 637-660. http://dx.doi.org/10.1023/A:1022339201394.

Hesse, M.A., Orr, F.M., Tchelepi, H.A. 2008. Gravity Currents with Residual Trapping. *Journal of Fluid Mechanics* **611**: 35-60. https://doi.org/10.1017/S002211200800219X

Hesse, M.A., Woods, A.W. 2010. Buoyant Dispersal of CO_2 During Geological Storage. *Geophysical Research Letters* **37**, L01403. https://doi.org/10.1029/2009GL041128.

Hirsch, L.M., Schuette, J.F.1999. Graph Theory Applications to Continuity and Ranking in Geologic Models. *Computers & Geosciences* **25** (2): 127-139.

Holtz, M.H. 2002. Residual Gas Saturation to Aquifer Influx: A Calculation Method for 3-D Computer Reservoir Model Construction. SPE Gas Technology Symposium, Calgary, Alberta, Canada, 30 April-2 May. https://doi.org/10.2118/75502-MS.

Iglauer, S., Wülling, W., Pentland, C.H., Al-Mansoori, S.K., Blunt, M.J. 2011. Capillary-Trapping Capacity of Sandstones and Sandpacks. *SPE Journal* **16** (4): 778-783. https://doi.org/10.2118/120960-PA.

IPCC (Intergovernmental Panel on Climate Change). 2005. IPCC special report on carbon dioxide capture and storage. Cambridge University Press, Cambridge, UK, pp. 195-276.

Javaheri, M., Jessen, K. 2011. Residual Trapping in Simultaneous Injection of CO_2 and Brine in Saline Aquifers. SPE Western North American Region Meeting, Anchorage, Alaska, USA, 7-11 May. https://doi.org/10.2118/144613-MS.

Jennings, J.W., Ruppel, S.C., Ward, W.B. 2000. Geostatistical Analysis of Permeability Data and Modeling of Fluid-flow Effects in Carbonate Outcrops. *SPE Reservoir Evaluation and Engineering* **3** (04): 292-303. http://dx.doi.org/10.2118/65370-PA.

Jeong, H. 2016. *Fast Assessment of Uncertainty in Buoyant Fluid Displacement Using a Connectivity-Based Proxy*. Ph.D. Dissertation, The University of Texas at Austin, Austin, Texas.

Jeong, H., Srinivasan, S. 2016. Fast Assessment of CO_2 Plume Characteristics Using a Connectivity Based Proxy. *International Journal of Greenhouse Gas Control* **49**: 387-412. http://dx.doi.org/10.1016/j.ijggc.2016.03.001.

Juanes, R., Spiteri, E.J., Orr, F.M., Blunt, M.J. 2006. Impact of Relative Permeability Hysteresis on Geological CO_2 Storage. *Water Resources Research* **42**, W12418. http://dx.doi.org/10.1029/2005wr004806.

Kong, X., Delshad, M., Wheeler, M.F. 2014. History Matching Heterogeneous Coreflood of CO_2/Brine by Use of Compositional Reservoir Simulator and Geostatistical Approach. *SPE Journal* **20** (02): 267-276. http://dx.doi.org/10.2118/163625-PA.

Krause, M.H. 2012. Modeling and Investigation of the Influence of Capillary Heterogeneity on Relative Permeability. SPE Annual Technical Conference and Exhibition, San Antonio, Texas, USA, 8-10 October. https://doi.org/10.2118/160909-STU.

Krause, M.H., Perrin, J.-C., Benson, S.M. 2011. Modeling Permeability Distributions in a Sandstone Core for History Matching Coreflood Experiments. *SPE Journal* **16** (4): 768-777. http://dx.doi.org/10.2118/126340-PA.

Krevor, S.C.M., Pini, R., Li, B., Benson, S.M. 2011. Capillary Heterogeneity Trapping of CO_2 in a Sandstone Rock at Reservoir Conditions. *Geophysical Research Letters* **38**, L15401. http://dx.doi.org/10.1029/2011GL048239.

Kumar, A., Noh, M.H., Ozah, R.C., Pope, G.A., Bryant, S.L., Sepehrnoori, K., Lake, L.W. 2005. Reservoir Simulation of CO_2 Storage in Deep Saline Aquifers. *SPE Journal* **10** (3): 336-348. http://dx.doi.org/10.2118/89343-pa.

Kumar, N., Bryant, S. 2008. Optimizing Injection Intervals in Vertical and Horizontal Wells for CO_2 Sequestration. SPE Annual Technical Conference and Exhibition, Denver, Colorado, USA, 21-24 September,. http://dx.doi.org/10.2118/116661-MS.

Kuo, C.-W., Perrin, J.-C., Benson, S.M. 2010. Effect of Gravity, Flow Rate, and Small Scale Heterogeneity on Multiphase Flow of CO_2 and Brine. SPE Western Regional Meeting, Anaheim, California, USA, 27-29 May. http://dx.doi.org/10.2118/132607-MS.

Lake, L.W., Johns, R., Rossen, B., Pope, G. 2014. *Enhanced oil recovery*, fourth edition. Richardson TX: Soceity of Petroleum Engineers.

Lake, L.W., Bryant, S.L., Araque-Martinez, A.N. 2003. *Geochemistry And Fluid Flow*, first edition. Amsterdam: Elsevier.

Land, C.S. 1968. Calculation of Imbibition Relative Permeability for Two- and Three-Phase Flow from Rock Properties. *SPE Journal* **8** (02): 149-156. https://doi.org/10.2118/1942-PA

Lasseter, T.J., Waggoner, J.R., Lake, L.W. 1986. Reservoir Heterogeneities and Their Influence on Ultimate Recovery. In *Reservoir Characterization*, ed. Lake, L.W., Carroll, H, B. 545-559. Academic Press.

Lengler, U., De Lucia, M., Kühn, M. 2010. The Impact of Heterogeneity on the Distribution of Co2: Numerical Simulation of CO_2 Storage at Ketzin. *International Journal of Greenhouse Gas Control* **4** (6): 1016-1025. http://dx.doi.org/10.1016/j.ijggc.2010.07.004.

Lenormand, R., Touboul, E., Zarcone, C. 1988. Numerical Models and Experiments on Immiscible Displacements in Porous Media. *Journal of Fluid Mechanics* **189**: 165-187. http://dx.doi.org/10.1017/S0022112088000953.

Leonenko, Y., Keith, D.W. 2008. Reservoir Engineering to Accelerate the Dissolution of CO_2 Stored in Aquifers. *Environmental Science & Technology* **42** (8): 2742-2747. http://dx.doi.org/10.1021/es071578c.

Leverett, M.C. 1941. Capillary Behavior in Porous Solids. *AIME Petroleum Transactions* **142**: 152-169. https://doi.org/10.2118/941152-G.

Li, B., Benson, S.M., Tchelepi, H.A. 2012. Modelling Fine-Scale Capillary Heterogeneity in Multphase Flow of CO_2 and Brine in Sedimentary Rocks. XIX International Conference on Water Resources, University of Illinois at Urbana-Champaign, June 17-22.

Luo, X. 2011. Simulation and Characterization of Pathway Heterogeneity of Secondary Hydrocarbon Migration. *AAPG Bulletin* **95** (6): 881-898. https://doi.org/10.1306/11191010027.

Macminn, C.W., Szulczewski, M.L., Juanes, R. 2010. CO_2 Migration in Saline Aquifers. Part 1. Capillary Trapping under Slope and Groundwater Flow. *Journal of Fluid Mechanics* **662**: 329-351. https://doi.org/10.1017/S0022112010003319.

Macminn, C.W., Szulczewski, M.L., Juanes, R. 2011. CO_2 Migration in Saline Aquifers: Regimes in Migration with Dissolution. *Energy Procedia* **4**: 3904-3910. https://doi.org/10.1016/j.egypro.2011.02.328.

Martin, J.C. 1958. Some Mathematical Aspects of Two-Phase Flow with Applications to Flooding and Gravity Segregation Problems. *Producer Monthly* **22** (2): 22-35. https://doi.org/10.1007/BF00893752.

Meckel, T.A. 2013. Digital Rendering of Sedimentary-Relief Peels: Implications for Clastic Facies Characterization and Fluid Flow. *Journal of Sedimentary Research* **83** (6): 495-501. https://doi.org/10.2110/jsr.2013.43.

Meckel, T.A., Bryant, S.L., Ravi Ganesh, P. 2015. Characterization and Prediction of CO_2 Saturation Resulting from Modeling Buoyant Fluid Migration in 2D Heterogeneous Geologic Fabrics. *International Journal of Greenhouse Gas Control* **34**: 85-96. http://dx.doi.org/10.1016/j.ijggc.2014.12.010.

Mijic, A., Laforce, T.C. 2012. Spatially Varying Fractional Flow in Radial CO_2-Brine Displacement. *Water Resources Research* **48**, W09503. http://dx.doi.org/10.1029/2011WR010961.

Mijic, A., Laforce, T.C., Muggeridge, A.H. 2014. CO_2 Injectivity in Saline Aquifers: The Impact of Non-Darcy Flow, Phase Miscibility, and Gas Compressibility. *Water Resources Research* **50** (5): 4163-4185. http://dx.doi.org/10.1002/2013WR014893.

Mo, S., Akervoll, I. 2005. Modeling Long-Term CO_2 Storage in Aquifer with a Black-Oil Reservoir Simulator. SPE-93951 presented at the SPE/EPA/DOE Exploration and Production Environmental Conference, Galveston, Texas, 7-9 March. http://dx.doi.org/10.2118/93951-MS.

Mouche, E., Hayek, M., Mügler, C. 2010. Upscaling of CO_2 Vertical Migration through a Periodic Layered Porous Medium: The Capillary-Free and Capillary-Dominant Cases. *Advances in Water Resources* **33** (9): 1164-1175. http://dx.doi.org/10.1016/j.advwatres.2010.07.005.

Na, Z., Suekane, T., Hosokawa, T., Inaoka, S., Wang, Q. 2011. In-Situ Capillary Trapping of CO_2 by Co-Injection. *Transport in Porous Media* **90** (2): 575-587. http://dx.doi.org/10.1007/s11242-011-9800-3.

Nghiem, L., Shrivastava, V., Kohse, B., Hassam, M., Yang, C. 2010. Simulation and Optimization of Trapping Processes for CO_2 Storage in Saline Aquifers. *Journal of Canadian Petroleum Technology* **49** (8): 15-22. http://dx.doi.org/10.2118/139429-PA.

Nghiem, L., Yang, C., Shrivastava, V., Kohse, B., Hassam, M., Card, C. 2009. Risk Mitigation through the Optimization of Residual Gas and Solubility Trapping for CO_2 Storage in Saline Aquifers. *Energy Procedia* **1** (1): 3015-3022. http://dx.doi.org/10.1016/j.egypro.2009.02.079.

Ngo, T.D., Mouche, E., Audigane, P. 2016. Buoyant Flow of CO_2 Through and Around a Semi-Permeable Layer of Finite Extent. *Journal of Fluid Mechanics* **809**: 553-584. https://doi.org/10.1017/jfm.2016.684.

Noh, M.H., Lake, L.W., Bryant, S.L., Araque-Martinez, A.N. 2007. Implications of Coupling Fractional Flow and Geochemistry for CO_2 Injection in Aquifers. *SPE Reservoir Evaluation and Engineering* **10** (04): 406-414. http://dx.doi.org/10.2118/89341-PA.

Nordbotten, J., Celia, M., Bachu, S. 2005. Injection and Storage of CO_2 in Deep Saline Aquifers: Analytical Solution for CO_2 Plume Evolution During Injection. *Transport in Porous Media* **58** (3): 339-360. http://dx.doi.org/10.1007/s11242-004-0670-9.

Oruganti, Y.D., Mishra, S. 2013. An Improved Simplified Analytical Model for CO_2 Plume Movement and Pressure Buildup in Deep Saline Formations. *International Journal of Greenhouse Gas Control* **14** (0): 49-59. http://dx.doi.org/10.1016/j.ijggc.2012.12.024.

Paulsen, V.H. 2014. An Experimental Study of CO_2 Sequestration in Saline Aquifers and Gas Hydrates. MS thesis, The University of Bergen, Bergen, Norway.

Peters, E.J., Hardham, W.D. 1990. Visualization of Fluid Displacements in Porous Media Using Computed Tomography Imaging. *Journal of Petroleum Science and Engineering* **4** (2): 155-168. http://dx.doi.org/10.1016/0920-4105(90)90023-V.

Pruess, K., Xu, T., Apps, J., Garcia, J. 2003. Numerical Modeling of Aquifer Disposal of CO_2. *SPE Journal* **8** (1): 49-60. http://dx.doi.org/10.2118/66537-MS.

Qi, R., Laforce, T., Blunt, M. 2009. Design of Carbon Dioxide Storage in Aquifers. *International Journal of Greenhouse Gas Control* **3** (2): 195-205. http://dx.doi.org/10.1016/j.ijggc.2008.08.004.

Rabinovich, A., Itthisawatpan, K., Durlofsky, L.J. 2015. Upscaling of CO_2 Injection into Brine with Capillary Heterogeneity Effects. *Journal of Petroleum Science and Engineering* **134**: 60-75. http://doi.org/10.1016/j.petrol.2015.07.021.

Ren, B., Bryant, S.L., Lake, L.W. 2015. Fast Modeling of Local Capillary Trapping During CO_2 Injection into a Saline Aquifer. CMTC-439486 presented at the Carbon Management Technology Conference, Sugar Land, Texas, 17-19 November, http://dx.doi.org/10.7122/439486-MS.

Ren, B., Sun, Y., Bryant, S. 2014. Maximizing Local Capillary Trapping During CO_2 Injection. *Energy Procedia* **63**: 5562-5576. http://dx.doi.org/10.1016/j.egypro.2014.11.590.

Riaz, A., Tchelepi, H.A. 2008. Dynamics of Vertical Displacement in Porous Media Associated with CO_2 Sequestration. *SPE Journal* **13** (3): 305-313. http://dx.doi.org/10.2118/103169-PA.

Roof, J.G. 1970. Snap-Off of Oil Droplets in Water-Wet Pores. *SPE Journal* **10** (01): 85-90. http://dx.doi.org/10.2118/2504-PA.

Saadatpoor, E. 2009. *Effect of Capillary Heterogeneity on Buoyant Plumes: New Trapping Mechanism in Carbon Sequestration*. MS thesis, The University of Texas at Austin, Austin, Texas.

Saadatpoor, E. 2012. *Local Capillary Trapping in Geological Carbon Storage*. Ph.D. Dissertation, The University of Texas at Austin, Austin, Texas.

Saadatpoor, E., Bryant, S.L., Sepehrnoori, K. 2009a. New Trapping Mechanism in Carbon Sequestration. *Transport in Porous Media* **82** (1): 3-17. http://dx.doi.org/10.1007/s11242-009-9446-6.

Saadatpoor, E., Bryant, S.L., Sepehrnoori, K. 2009b. Upscaling Local CO_2 Trapping During Buoyancy Driven Flow. SPE-124846 presented at the Annual Technical Conference and Exhibition, New Orleans, Louisiana, 4-7 October. http://dx.doi.org/10.2118/124846-MS.

Saripalli, P., Mcgrail, P. 2002. Semi-Analytical Approaches to Modeling Deep Well Injection of CO_2 for Geological Sequestration. *Energy Conversion and Management* **43** (2): 185-198. http://dx.doi.org/10.1016/S0196-8904(01)00017-6.

Shi, J.-Q., Xue, Z., Durucan, S. 2011. Supercritical CO_2 Core Flooding and Imbibition in Tako Sandstone—Influence of Sub-Core Scale Heterogeneity. *International Journal of Greenhouse Gas Control* **5** (1): 75-87. http://dx.doi.org/10.1016/j.ijggc.2010.07.003.

Shook, M., Li, D., Lake, L.W. 1992. Scaling Immiscible Flow through Permeable Media by Inspectional Analysis. *In Situ* **16** (4): 311-350.

Siddiqui, F.I., Lake, L.W. 1997. A Comprehensive Dynamic Theory of Hydrocarbon Migration and Trapping. SPE-38682 presented at the Annual Technical Conference and Exhibition, San Antonio, Texas, 5-8 October. http://dx.doi.org/10.2118/38682-MS.

Silin, D., Patzek, T.W., Benson, S.M. 2009. A One-Dimensional Model of Vertical Gas Plume Migration through a Heterogeneous Porous Medium. *International Journal of Greenhouse Gas Control* **3** (3): 300-310. http://dx.doi.org/10.1016/j.ijggc.2008.09.003.

Singh, V.P., Cavanagh, A., Hansen, H., Nazarian, B., Iding, M., Ringrose, P.S. 2010. Reservoir Modeling of CO_2 Plume Behavior Calibrated against Monitoring Data from Sleipner, Norway. SPE-134891 presented at the Annual Technical Conference and Exhibition, Florence, Italy, 19-22 September. http://dx.doi.org/10.2118/134891-MS.

Spiteri, E.J., Juanes, R. 2006. Impact of Relative Permeability Hysteresis on the Numerical Simulation of Wag Injection. *Journal of Petroleum Science and Engineering* **50** (2): 115-139. http://dx.doi.org/10.1016/j.petrol.2005.09.004.

Stauffer, D., Aharony, A. 1992. *Introduction to Percolation Theory*, 2nd edition. London: Taylor & Francis.

Sun, Y.H. 2014. *Investigation of Buoyant Plumes in a Quasi-2D domain Characterizing the Influence of Local Capillary Trapping and Heterogeneity on Sequestered CO_2: A Bench Scale Experiment*. MS thesis, The University of Texas at Austin, Austin, Texas.

Swickrath, M.J., Mishra, S., Ravi Ganesh, P. 2016. An Evaluation of Sharp Interface Models for CO_2-Brine Displacement in Aquifers. *Groundwater* **54** (3): 336-344. http://dx.doi.org/10.1111/gwat.12366.

Sylta, Ø., Pedersen, J.I., Hamborg, M. 1998. On the Vertical and Lateral Distribution of Hydrocarbon Migration Velocities During Secondary Migration. *Geological Society,*

London, Special Publications **144** (1): 221-232. http://dx.doi.org/10.1144/GSL.SP.1998.144.01.17.

Taku Ide, S., Jessen, K., Orr, F.M. 2007. Storage of CO_2 in Saline Aquifers: Effects of Gravity, Viscous, and Capillary Forces on Amount and Timing of Trapping. *International Journal of Greenhouse Gas Control* **1** (4): 481-491. http://dx.doi.org/10.1016/s1750-5836(07)00091-6.

Tao, Q. 2012. *Modeling CO_2 Leakage from Geological Storage Formation and Reducing the Associated Risk*. Ph.D. Dissertation, The University of Texas at Austin, Austin, Texas.

Tao, Q., Bryant, S. 2014. Optimization of Injection/Extraction Rates for Surface-Dissolution Process. *SPE Journal* **19** (04): 598-607. http://dx.doi.org/10.2118/167256-PA.

Trevisan, L., Cihan, A., Fagerlund, F., Agartan, E., Mori, H., Birkholzer, J.T., Zhou, Q., Illangasekare, T.H. 2014. Investigation of Mechanisms of Supercritical CO_2 Trapping in Deep Saline Reservoirs Using Surrogate Fluids at Ambient Laboratory Conditions. *International Journal of Greenhouse Gas Control* **29**: 35-49. http://dx.doi.org/10.1016/j.ijggc.2014.07.012.

Trevisan, L., Krishnamurthy, P.G., Meckel, T.A. 2017. Impact of 3D Capillary Heterogeneity and Bedform Architecture at the Sub-Meter Scale on CO_2 Saturation for Buoyant Flow in Clastic Aquifers. *International Journal of Greenhouse Gas Control* **56**: 237-249. http://dx.doi.org/10.1016/j.ijggc.2016.12.001.

Van Valkenburg, M.E. and Annable, M.D. 2002. Mobilization and Entry of DNAPL Pools into Finer Sand Media by Cosolvents: Two-dimensional Chamber Studies. *Journal of Contaminant Hydrology* **59**(3-4): 211-230.

Vilarrasa, V., Bolster, D., Dentz, M., Olivella, S., Carrera, J. 2010. Effects of CO_2 Compressibility on CO_2 Storage in Deep Saline Aquifers. *Transport in Porous Media* **85** (2): 619-639. http://dx.doi.org/10.1007/s11242-010-9582-z.

Waggoner, J.R., Castillo, J.L., Lake, L.W. 1992. Simulation of EOR Processes in Stochastically Generated Permeable Media. *SPE Formation Evaluation* **7** (02): 173-180. http://dx.doi.org/10.2118/21237-PA.

Wang, S., Feng, Q., Javadpour, F., Yang, Y.B. 2016. Breakdown of Fast Mass Transport of Methane through Calcite Nanopores. *The Journal of Physical Chemistry C* **120** (26): 14260-14269. http://dx.doi.org/10.1021/acs.jpcc.6b05511.

Wei, N., Gill, M., Crandall, D., Mcintyre, D., Wang, Y., Bruner, K., Li, X., Bromhal, G. 2014. CO_2 Flooding Properties of Liujiagou Sandstone: Influence of Sub-Core Scale Structure Heterogeneity. *Greenhouse Gases: Science and Technology* **4** (3): 400-418. http://dx.doi.org/10.1002/ghg.1407.

Welge, H.J. 1952. A Simplified Method for Computing Oil Recovery by Gas or Water Drive. *Journal of Petroleum Technology* **4** (04): 91-98. http://dx.doi.org/10.2118/124-G.

Wilkinson, D. 1984. Percolation Model of Immiscible Displacement in the Presence of Buoyancy Forces. *Physical Review A* **30** (1): 520-531. http://link.aps.org/doi/10.1103/PhysRevA.30.520.

Woods, A.W., Espie, T. 2012. Controls on the Dissolution of CO_2 Plumes in Structural Traps in Deep Saline Aquifers. *Geophysical Research Letters* **39**, L08401. http://dx.doi.org/10.1029/2012GL051005.

Zhang, G., Taberner, C., Cartwright, L., Xu, T. 2011. Injection of Supercritical CO_2 into Deep Saline Carbonate Formations: Predictions from Geochemical Modeling. *SPE Journal* **16** (4): 959-967. http://dx.doi.org/10.2118/121272-PA.

Vita

Bo Ren was born in Xintai, Shandong Province, China. He graduated from Xintai No. 1 High School in 2005. He got a B.S. and M.S. degree in Petroleum Engineering in 2009, and 2012 respectively, both from China University of Petroleum (East). Bo began his graduate studies in Petroleum Engineering at the University of Texas at Austin in September of 2012, under the supervision of Dr. Larry Lake and Dr. Steven Bryant. Bo likes to volleyball and poker.

Permanent email address: boren@utexas.edu

This dissertation was typed by the author.